UNIVERSITY OF CALIFORNIA, SAN DIEGO

Motion Planning for 3D Navier Stokes Equations and Stability of Nonholonomic Source Seeking Algorithms

A Dissertation submitted in partial satisfaction of the requirements for the degree Doctor of Philosophy

in

Engineering Sciences (Mechanical Engineering)

by

Jennie Eleanor Cochran

Committee in charge:

Professor Miroslav Krstić, Chair
Professor Thomas Bewley
Professor William Helton
Professor Sonia Martínez
Professor Ruth Williams

2008

The Dissertation of Jennie Eleanor Cochran is approved, and it is acceptable in quality and form for publication on microfilm:

_____

_____

_____

_____

_____
Chair

University of California, San Diego

2008

To my family.

TABLE OF CONTENTS

Signature Page . . . iii

Dedication . . . iv

Table of Contents . . . v

List of Figures . . . viii

Acknowledgements . . . xii

Vita . . . xiv

Abstract of the Dissertation . . . xv

1 Introduction . . . 1
1.1 Motion Planning for the Navier Stokes System . . . 1
1.2 Source Seeking with Nonholonomic Vehicles . . . 2

2 Motion Planning and Trajectory Tracking for 3-D Poiseuille Flow . . . 4
2.1 Abstract . . . 4
2.2 Introduction . . . 5
2.3 System Model . . . 8
2.4 Motion Planning . . . 11
2.4.1 Proof of Theorem 2.1 and Construction of Open Loop Control 16
2.4.2 Simulation Results on Motion Planning . . . 20
2.5 Stabilization . . . 21
2.6 Closed-Form Solutions to the Kernel PDEs . . . 32
2.7 Inherent Difficulty Increases with Reynolds and Wave Numbers . . . 35
2.8 Conclusion . . . 40
2.9 Further Remarks On The Stabilizing Controller . . . 40
2.10 Acknowledgments . . . 41

3 Nonholonomic Source Seeking With Tuning of Angular Velocity . . . 42
3.1 Abstract . . . 42
3.2 Introduction . . . 43
3.3 Vehicle Model and Extremum Seeking Controller . . . 45
3.4 Closed Loop Stability . . . 48
3.4.1 Stability Theorem . . . 49
3.4.2 Collocated Sensor . . . 59
3.4.3 Unstable Solutions . . . 63
3.4.4 Effect of the d Parameter . . . 66

3.5 System Properties With $d = 0$ . . . 70
3.5.1 Circular Level Sets . . . 71
3.5.2 Elliptical Level Sets . . . 72
3.6 System Properties with Elliptical Level Sets and $d > 0$ . . . 75
3.7 Conclusion . . . 76
3.8 Acknowledgements . . . 80

4 Applications of Nonholonomic Source Seeking With Tuning of Angular Velocity . . . 81
4.1 Abstract . . . 81
4.2 Introduction . . . 81
4.3 Overview of Extremum Seeking for Autonomous Vehicles . . . 84
4.4 Diffusive Source . . . 86
4.5 Level Sets . . . 87
4.6 Actuated Sensor . . . 89
4.7 Conclusions and Future Work . . . 91

5 GPS Denied Source Seeking For Underactuated Autonomous Vehicles in 3D 97
5.1 Abstract . . . 97
5.2 Introduction . . . 98
5.3 Overview of Source Seeking in 2D . . . 99
5.4 Vehicle Model . . . 100
5.5 VYPa Vehicles . . . 102
5.6 Convergence of VYPa Vehicle . . . 104
5.7 Illustration of VYPa Vehicle Behavior . . . 113
5.8 VeRa Vehicles . . . 117
5.9 Other Applications . . . 125
5.10 Conclusions . . . 126

6 Fish Locomotion . . . 128
6.1 Abstract . . . 128
6.2 Introduction . . . 129
6.3 Review of Source Seeking with a Nonholonomic Unicycle . . . 131
6.4 Equations of Motion in a Perfect Fluid . . . 133
6.5 Locomotion and Source Seeking for a Three Link Fish . . . 135
6.5.1 ODE Model with an Infinite Dimensional Output Map for a Three Link Fish in a Potential Flow . . . 137
6.5.2 Reciprocal Motion . . . 141
6.5.3 Basic Gaits for Three Link Fish . . . 144
6.5.4 Source Seeking With a Three Link Fish . . . 147
6.5.5 Path Following for a Three Link Fish . . . 148
6.6 Locomotion and Source Seeking for a Joukowski Foil Fish . . . 149

6.6.1 ODE Model With an Infinite Dimensional Output Map for a Joukowski foil fish in a Potential Flow with Point Vortices . . 150
6.6.2 Basic Gaits of the Joukowski Foil Fish 155
6.6.3 Source Seeking for a Joukowski Foil Fish 155
6.6.4 Path Following for a Joukowski foil fish. 158
6.7 Conclusions 158
6.8 Acknowledgments 160

A Full Expressions for w_i and w_{si}. 161

Bibliography 163

LIST OF FIGURES

Figure 2.1: 3-D Channel Flow. 8
Figure 2.2: The structure of the input-output relationship $\mathcal{U} \mapsto \mathcal{Y}$ and a description of the types of problems that are solved in constructing the input $\mathcal{U}$ for a given reference output $\mathcal{Y}$. 15
Figure 2.3: The string of (invertible) transformations involved in solving the full-state motion planning problem. 16
Figure 2.4: Snapshots of the desired skin friction spatio-temporal profile (reference output trajectory). Time proceeds left to right and top to bottom. Arrows indicate direction and magnitude. 22
Figure 2.5: Snapshots of the desired pressure spatio-temporal profile (reference output trajectory). Time proceeds left to right and top to bottom. Blue indicates low pressure while red indicates high pressure. 24
Figure 2.6: Snapshots in time of the input reference trajectory for stream- and span-wise velocity. Time proceeds left to right and top to bottom. Arrows indicate direction and magnitude. 26
Figure 2.7: Snapshots in time of the input reference trajectory for normal velocity. Time proceeds left to right and top to bottom. Blue indicates negative velocity while red indicates positive velocity. 28
Figure 2.8: $\max_t \left\{ \left| u^r|_{y=1} \right| \right\}$ growing in k_z and k_x forced by $u^r_y|_{y=0} = \sin(t)$. 35
Figure 2.9: $\max_t \left\{ \left| W^r|_{y=1} \right| \right\}$ growing in k_z and k_x forced by $u^r_y|_{y=0} = \sin(t)$. 36
Figure 2.10: (a) $\max_t \left\{ \left| u^r|_{y=1} \right| \right\}$ and (b) $\max_t \left\{ \left| W^r|_{y=1} \right| \right\}$ growing in Re forced by $u^r_y|_{y=0} = \sin(t)$. 36
Figure 2.11: $\max_t \left\{ \left| u^r|_{y=1} \right| \right\}$ growing in k_z and k_x forced by $p^r|_{y=0} = \sin(t)$. 37
Figure 2.12: $\max_t \left\{ \left| W^r|_{y=1} \right| \right\}$ growing in k_z and k_x forced by $p^r|_{y=0} = \sin(t)$. 37
Figure 2.13: (a) $\max_t \left\{ \left| u^r|_{y=1} \right| \right\}$ and (b) $\max_t \left\{ \left| W^r|_{y=1} \right| \right\}$ growing in Re forced by $p^r|_{y=0} = \sin(t)$. 38
Figure 2.14: $\max_t \left\{ \left| u^r|_{y=1} \right| \right\}$ growing in k_z and k_x forced by $p^r|_{y=0} = \frac{1}{\pi^3} \mathrm{e}^{-\frac{k_x^2}{\pi^2} - \frac{k_z^2}{\pi^2}} \sin(t)$. 39
Figure 2.15: $\max_t \left\{ \left| W^r|_{y=1} \right| \right\}$ growing in k_z and k_x forced by $p^r|_{y=0} = \frac{1}{\pi^3} \mathrm{e}^{-\frac{k_x^2}{\pi^2} - \frac{k_z^2}{\pi^2}} \sin(t)$. 39

Figure 3.1: The notation used in the model of vehicle sensor and center dynamics. 46

Figure 3.2: Block diagram of source seeking via tuning of angular velocity, $\dot{\theta}$, of the vehicle. The sensor at the position r_s is at a distance R from the vehicle center at r_c. 47
Figure 3.3: Vehicle following a moving source whose map has elliptical level sets. 48
Figure 3.4: Source emits a signal with circular level sets. 56
Figure 3.5: Source with elliptical level sets. 57
Figure 3.6: Effect of the parameter a on the motion of the vehicle center. 58
Figure 3.7: Block diagram of source seeking via tuning of angular velocity when the sensor is collocated with the vehicle center. 60
Figure 3.8: A simulation with a collocated sensor ($R = 0$) and $\epsilon = .001$. . 64
Figure 3.9: An unstable solution. 65
Figure 3.10: Set of unstable solutions. 66
Figure 3.11: Root locus of parameter d when (a) $\frac{V_c}{R} > h$ and (b) $\frac{V_c}{R} < h$. . . 68
Figure 3.12: Phase portrait of averaged system with d small 69
Figure 3.13: Phase portrait of averaged system with d large 69
Figure 3.14: Both (a) and (b) show the trajectory of a vehicle with the same initial conditions and same parameters. 70
Figure 3.15: Phase portrait of averaged system with $d = 0$ 71
Figure 3.16: Trajectory of the averaged system and the original system with $d = 0$. 73
Figure 3.17: Initial conditions and attractors. 75
Figure 3.18: System attractors as d progresses. 77
Figure 3.19: Initial conditions and attractors. 78
Figure 3.20: System attractors as V_c progresses. 79

Figure 4.1: Basic vehicle configuration. 85
Figure 4.2: Sequence of images from a vehicle employing extremum seeking to tracking a diffusive signal. 88
Figure 4.3: Sequence of images from a vehicle tracking a diffusive signal. . 92
Figure 4.4: (a) Trajectory of a vehicle employing extremum seeking to trace an elliptical level set. (b) Evolution of the map value at the vehicle center. 93
Figure 4.5: Trajectories of vehicles tracing level sets and the evolution of map values at the vehicle center. 94
Figure 4.6: Vehicle configuration for decoupled sensor and center. θ_s is the angle between the sensor and the vehicle centerline. 95
Figure 4.7: Trajectory of vehicle with coupled center and sensor dynamics. 95
Figure 4.8: Trajectory of vehicle with decoupled center and sensor dynamics. 96
Figure 4.9: Distance between the center of the vehicle and the target. . . . 96

Figure 5.1: (a) Pictorial drawing of the 3D vehicle. (b) Graphical interpretation of vehicle in 3D. 101

Figure 5.2: Block diagram of ES control applied to the pitch and yaw velocities of the VYPa. 103
Figure 5.3: Vehicle locating a static source which creates a signal field with spherical level sets. 114
Figure 5.4: Attractors resulting from different parameter configurations. . 114
Figure 5.5: Vehicle locating a target from a signal field with ellipsoidal level sets. 115
Figure 5.6: The vehicle follows the moving source which creates a signal field with spherical level sets which move with the target. 115
Figure 5.7: Vehicle locates a source. 116
Figure 5.8: Vehicle locates a source. 116
Figure 5.9: Vehicle does not locate the source – parameters produce an unstable result. 117
Figure 5.10: Block diagram of ES control applied to the roll velocity of the VeRa. 118
Figure 5.11: VeRa locates a static source. 122
Figure 5.12: VeRa distance to source. 123
Figure 5.13: VeRa tracking a static source. 123
Figure 5.14: Trajectory of the center of a VeRa vehicle tracking a moving source. 124
Figure 5.15: Motion of vehicle front, r_f, during transitive journey toward the source. 125
Figure 5.16: Trajectories of the center of vehicles tracing level sets are shown.126

Figure 6.1: A snapshow in time showing (a) the three link fish moving in a potential flow and (b) a Joukowski foil fish moving in a potential flow with point vortices. 132
Figure 6.2: A typical trajectory of a fish-like vehicle seeking the source of some signal and being driven by our extremum seeking based control law. 132
Figure 6.3: Configuration of the three link fish model. 136
Figure 6.4: Reciprocal motion of the three link fish: $\beta_0 = 1$, $\theta_1|_{t=0} = 0$, $\theta_2|_{t=0} = 0$. 141
Figure 6.5: Reciprocal motion of the three link fish: $\beta_0 = -1$, $\theta_1|_{t=0} = 0$, $\theta_2|_{t=0} = 0$. 142
Figure 6.6: Reciprocal motion of the three link fish: $\beta_0 = 1/2$, $\theta_1|_{t=0} = 0$, $\theta_2|_{t=0} = 0$. 142
Figure 6.7: Snapshots in time of reciprocal motion. 143
Figure 6.8: Forward gaits of a three link fish. $\beta = 0$. 145
Figure 6.9: Turning gaits of a three link fish. $a = 1$, $\omega = 10$. 145
Figure 6.10: Snapshots in time of the fish moving forward. 146
Figure 6.11: Source seeking for a three link fish. 148
Figure 6.12: Three link fish following a predetermined path. 149

Figure 6.13: Forward gait for Joukowski foil fish. $\beta = 0$. 156
Figure 6.14: Turning gait for Joukowski foil fish. $a = .1$, $\omega = 15$. 156
Figure 6.15: Snapshots in time of a Joukowski foil fish moving forward. . . 157
Figure 6.16: Source seeking for a Joukowski foil fish. 158
Figure 6.17: Source seeking for a Joukowski foil fish. 159
Figure 6.18: Joukowski foil fish following a predetermined path. 159

ACKNOWLEDGEMENTS

I would like to thank my parents, Anne and Tony Cochran, my sisters, Allison and Elizabeth Cochran and my brothers Rob and Harry Cochran for the years and years of their unending support and love.

I would like to sincerely thank my advisor, Miroslav Krstic, for letting me run with the source seeking topic and for everything he has taught me. His guidance and mentorship have been integral to the success of this work.

I would like to thank Tom Bewley for introducing me to the world of CFD and flow control and for always being willing and eager to explain things.

I would like to thank the members of my committee for their helpful comments and questions.

I would like to thank my fellow graduate students Antranik Siranosian, Nima Ghods, Andrey Smyshlyaev, Rafael Vazquez, Jamie Gray, Paul Frihauf, James Krieger and Gideon Prior for being wonderful people to work with day in and day out. A special thanks goes to Antranik and Nima for putting up with me in such close proximity for so long.

I would like to thank my friends Nicole Herbold, Eric Herbold, Ben Maurer and Claire Debever for making me laugh and smile.

I would like to thank Sandi and Dennis Chinn for their support.

I would like to thank Stephanie Hope for her listening ear, her witty conversation and for always helping me put things in perspective.

Lastly I would like to thank my fiance Brian Chinn for the sacrifices he has made so we could be together while I finished my degree and for his unending support and love.[1]

This dissertation includes reprints of the following papers:

J. Cochran and M. Krstic, "Motion Planning and Trajectory Tracking for 3-D Poiseuille Flow," *Journal of Fluid Mechanics*, under review. (Chapter 2)

J. Cochran and M. Krstic, "Nonholonomic Source Seeking With Tuning of Angular Velocity," *IEEE Transactions on Automatic Control*, to appear (Chapter 3)

[1]HE IS THE BEST EVER.

J. Cochran, A. Siranosian, N. Ghods, and M. Krstic, "Source Seeking with a Nonholonomic Unicycle without Position Measurements and with Tuning of Angular Velocity — Part II: Applications," *Proceedings of IEEE Conference on Decision and Control*, 2007. (Chapter 4)

J. Cochran, A. Siranosian, N. Ghods, and M. Krstic, "GPS Denied Source Seeking For Underactuated Autonomous Vehicles in 3D," *IEEE Transactions on Robotics*, to appear. (Chapter 5)

J. Cochran, E. Kanso, S. D. Kelly, H. Xiong, and M. Krstic, "Source Seeking for Two Nonholonomic Models of Fish Locomotion," *IEEE Transactions on Robotics*, under review. (Chapter 6)

The dissertation author was the primary investigator and author of these publications.

VITA

2003	B.S. in Computer Science and Engineering, Massachusetts Institute of Technology
2004	M.Eng. in Computer Science and Electrical Engineering, Massachusetts Institute of Technology
2006-2007	Teaching Assistant, Department of Mechanical Engineering, University of California, San Diego
2005-2008	NDSEG Research Fellow, University of California, San Diego
2008	Ph.D. in Engineering Sciences (Mechanical Engineering), University of California, San Diego

PUBLICATIONS

J. Cochran and M. Krstic, "Nonholonomic Source Seeking With Tuning of Angular Velocity," *IEEE Transactions on Automatic Control*, to appear.

J. Cochran and M. Krstic, "Motion Planning and Trajectory Tracking for 3-D Poiseuille Flow," *Journal of Fluid Mechanics*, to appear.

J. Cochran, A. Siranosian, N. Ghods, and M. Krstic, "GPS Denied Source Seeking For Underactuated Autonomous Vehicles in 3D," under review.

J. Cochran, and M. Krstic, "Source Seeking for Two Nonholonomic Models of Fish Locomotion," *IEEE Transactions on Robotics*, being prepared.

ABSTRACT OF THE DISSERTATION

Motion Planning for 3D Navier Stokes Equations
and
Stability of Nonholonomic Source Seeking Algorithms

by

Jennie Eleanor Cochran
Doctor of Philosophy in Engineering Sciences (Mechanical Engineering)
University of California San Diego, 2008
Professor Miroslav Krstić, Chair

Two different problems are discussed: Motion planning and trajectory generation for the 3D Navier Stokes system and then source seeking with nonholonomic vehicles that have no position information.

Taking ideas from robotics, motion planning for the Navier Stokes system of PDEs is examined. In the context of a channel flow, the problem consists of finding the reference velocity input for all time, for each point in space at one wall that guarantees desired output reference skin friction and pressure trajectories (also for all time and for each point in space) at the other wall. In addition to the open loop reference velocity input that depends on a specific initial condition, a feedback component that augments the open loop reference velocity input and stabilizes the system about the entire reference state trajectory is also designed. This controller, which was developed using PDE backstepping, is different from previously developed controllers in that it was developed for the full infinite dimensional system instead of a discretized version of the system and it is explicit with symbolically computed gains.

For use in environments where position information is unavailable, the extremum seeking method is applied to autonomous vehicles as a means of navigating to find the source of some signal which the vehicles can measure locally. The signal is

maximum at the source and decreases with distance away from the source. This work is distinct from previous work in that the vehicles have no position information, no communication and are nonholonomic. Detailed convergence analysis and full characterization of vehicle behavior for the method applied to nonholonomic 2D and 3D vehicles are provided. All vehicles are based on the 2D unicycle with constant forward velocity and actuated angular velocity. Using these ideas, the extremum seeking method is also applied to vehicles which are modeled as either three-link fish or Joukowski airfoils. A control law, based on extremum seeking, guides the biomimetic vehicle to seek the source of a signal, to move to a point in space and to follow a predetermined path.

1

Introduction

This work consists of two separate topics: flow control and navigation of nonholonomic vehicles. Thus this dissertation is divided into self-contained chapters which each contain abstract, introduction, results and conclusion sections. I first address motion planning for the 3D Navier Stokes system using the PDE backstepping method and then continue the rest of the dissertation by addressing source seeking with nonholonomic vehicles using the extremum seeking method.

1.1 Motion Planning for the Navier Stokes System

I first started working on this topic by developing a controller to stabilize the 3D Navier Stokes system around the parabolic Poiseuille velocity profile in a channel flow. Vazquez [80] had previously designed a controller for the 2D system using the PDE backstepping method [72]. This controller is different from previously developed controllers in that it was developed for the full infinite dimensional system instead of a discretized version of the system and it is explicit with symbolically computed gains. After extending this controller to three dimensions, I started looking at motion planning and developed open and closed loop controllers which are presented in Chapter 2. Though stabilization for turbulence suppression is an active area of research in fluid dynamics [34, 16, 7, 1, 9, 6, 11, 30, 83, 10, 66, 31, 81, 29, 64, 85, 2],

motion planning is not a common concept in fluid dynamics. It is, however, a central subject in robotics. I take ideas from this area and apply them to the Navier Stokes system of PDEs. Motion planning has been considered for other systems modeled by partial differential equations, [47, 46, 59, 68, 54] though it has not been considered for the Navier Stokes system in the sense that I examine it[1]. In the context of a channel flow, infinite in the streamwise and spanwise directions and bounded in the normal direction, I study the problem of finding the reference velocity input for all time, for each point in space at one wall that guarantee desired output reference skin friction and pressure trajectories (also for all time and for each point in space) at the other wall. We chose skin friction and pressure as the output variables as they are linked to aerodynamics quantities of interest such as forces and moments exerted on vehicles. In the process of finding the reference input velocities, I find the unique functions that govern the entire velocity field (reference state trajectory) and ensure the output reference skin friction and pressure trajectories.

In addition to the open loop reference velocity input that depends on a specific initial condition, I also design a feedback component that augments the open loop reference velocity input and stabilizes the system about the entire reference state trajectory. I then go on to examine more closely particular closed form solutions and the behavior of the solution as wavenumbers grows or the Reynolds number grows.

1.2 Source Seeking with Nonholonomic Vehicles

This work started with the idea of applying the extremum seeking method [5] to autonomous vehicles as a means of navigating without the use of position information. This is a useful concept in environments where GPS is unavailable and inertial navigation is too expensive, such as urban environments, under water, under ice and in caves. It was first applied to vehicles modeled as point masses whose goal is finding the source of some signal which the vehicles can measure locally [87].

[1]While the work presented here gives the first solution for motion planning for a broad family of time-varying trajectories at the boundary of the channel flow system, [79] solves the problem of moving the system from rest to a given Poiseuille profile (equilibrium-to-equilibrium transfer).

We assume the signal is maximum at the source and decreases with distance away from the source. The control law guides the vehicle up the gradient of the signal to find the source. The method was then extended to the nonholonomic unicycle with a constant angular velocity and a forward velocity tuned by extremum seeking [86]. I started working on this topic when we extended the method to the unicycle with a constant forward velocity and an angular velocity that is tuned by extremum seeking.

I start examining this topic in Chapter 3 where I discuss a modification of the previously employed control law and the proof that, when guided by this new control law, the 2D unicycle with a constant forward velocity and a tuned angular velocity locally exponentially converges to an annulus around the source. I examine both the case where the vehicle center and sensor are not collocated and the case where they are. In addition, I provide full characterizations of the vehicle behavior. I continue in Chapter 4 with further applications of extremum seeking to the 2D unicycle such as tracking diffusive sources, tracing level sets, and implementing decoupled extremum seeking. Chapter 5 extends the method to two different vehicles which operate in three dimensions. I include a stability analysis for the control law applied to one vehicle and simulation results for the control law applied to the other vehicle. Finally, I use ideas from Chapters 3, 4 and 5 to apply the extremum seeking method to vehicles which are modeled as either a three-link fish or a Joukowski airfoil. I show how to apply extremum seeking to guide the vehicle to a point in space or along a predetermined path.

2

Motion Planning and Trajectory Tracking for 3-D Poiseuille Flow

2.1 Abstract

We present the first solution to a boundary motion planning problem for the Navier Stokes equations, linearized around the parabolic equilibrium in a 3-D channel flow. The pressure and skin friction at one wall are chosen as the reference outputs as they are the most readily measurable "wall-restricted" quantities in experimental fluid dynamics and also because they play a special role as performance metrics in aerodynamics. The reference velocity input is applied at the opposite wall. We find the exact (method independent) solution to the motion planning problem using the PDE backstepping theory. The motion planning solution results in open-loop controls, which produce the reference output trajectories only under special initial conditions for the flow velocity field. To achieve convergence to the reference trajectory from other (nearby) initial conditions, we design a feedback controller. We also present a detailed examination of the closed form solutions for gains and the behavior of the motion planning solution as the wavenumbers grow or the Reynolds number grows. Numerical results are shown for the motion planning problem.

2.2 Introduction

What is Motion Planning? Motion planning, or trajectory generation, is not a common concept in fluid dynamics. However, it is a central subject in another area of mechanics—robotics. By motion planning we are referring to the following problem. Suppose one is interested in producing a particular spatio-temporal waveform on a flow boundary for some specific flow variables. Such variables may be skin friction and pressure, which are linked to aerodynamic quantities of interest such as forces and moments exerted on an aerial vehicle. These boundary flow variables are referred to as *output* variables, and their desired profile is referred to as the *reference output*. Now suppose a part of the flow boundary is instrumented with actuators such as velocity actuators. The actuated quantities, in this case the velocities at the boundary, are referred to as the flow *inputs* and their evolution over time is likewise called the *reference input*. Motion planning is defined as the problem of determining the spatio-temporal functions governing the reference inputs that generate the reference output. In our example this means determining how to actuate the velocities at the flow boundary to enforce specific skin friction and pressure output profiles. To find the functions that govern the flow input, one must first find the unique functions that govern the entire velocity field. This solution is referred to as the *state reference trajectory* as it defines the trajectory (for all space and time) that the system states (the velocity field) must take in order to satisfy the system equations and the reference output. From this solution one finds the reference input.

The solution of a motion planning problem formulated in this way could be used to produce the exact temporal profiles of forces and moments acting on an aerial vehicle, using flow actuators (rather than moving flaps). Such capability is of interest for achieving low radar detectability of aircraft, but it is of just as much interest in its own right, as a fundamental problem in fluid mechanics and control theory.

As the solution to the motion planning problem is defined for all time, at the specific time $t = 0$, the velocity field needs to have a particular spatial profile in order for the reference input to produce the reference output. This is almost never going to be the case, as the initial velocity cannot be chosen by the designer, it is

given. For this reason, the *open-loop* reference inputs designed to solve the motion planning problem cannot be used alone. The reference trajectory of the system state needs to be stabilized by adding a *feedback* component to the (open-loop) reference input. The design of the feedback component of the controller is referred to as *trajectory tracking*.

The two problems, motion planning design and trajectory tracking design, are independent. The solution to the former is a function (vector-valued) of time and of the spatial coordinates, whereas the solution to the latter is a function of the spatial coordinates only. This function is referred to as a *gain function* and multiplies the (time-dependent) velocity field in the feedback law. Even for *linearized* Navier-Stokes equations (around an equilibrium profile), and even for a simple geometry as the channel flow, motion planning and trajectory tracking are extremely challenging problems. Since the objective in the motion planning problem is exact, its solution is unique — and thus method independent — whereas the solution to the trajectory tracking problem is not unique and thus is method dependent. This chapter presents motion planning and trajectory tracking designs for skin friction and pressure at the wall opposite to the actuated wall.

Relation to Flow Control for Stabilization. Most of the research on model-based flow control so far has been on problems of stabilization type. The channel flow geometry has occupied a special place in this research. The work on feedback design for turbulence suppression in channel flow by boundary control was initiated with the papers by [34] and [16], which employed linear quadratic optimal control techniques, and was followed by the work by [7] and [1], which employed Lyapunov techniques. This topic continues to enjoy interest, as reflected through the steady improvement of the available results [9, 6, 11, 30, 83, 10, 66, 31, 81, 80]. In parallel, stabilization problems in other (non-channel) geometries are being pursued, such as, for example, in [29, 64, 85, 2].

Designs for stabilization are of "feedback" type and do not solve the main problem that we consider here—the motion planning problem. Motion planning, though new for Navier-Stokes systems, has already been considered for more accessible types of systems modeled by partial differential equations, particularly those of parabolic

type studied by [47, 46, 59, 68, 54]. While this chapter presents the first solution for motion planning for a broad family of time-varying trajectories at the boundary of the channel flow system, [79] solve the problem of moving the system from rest to a given Poiseuille profile (equilibrium-to-equilibrium transfer).

The "Backstepping" Approach. The approach that we consider here is generally referred to as "backstepping for PDEs" and it was introduced for 1-D parabolic PDEs in the work by [72]. In the work by [81, 80] this method was extended to linearized Navier-Stokes equations, at arbitrary Reynolds numbers, which we use as a starting point for our efforts in developing motion planning. Backstepping is an approach that employs a particular form of a Volterra transformation in the spatial variable(s) and in a boundary control law. The combination of the transformation and the boundary control allow one to transform the system being controlled, which is typically complex, into a simple "target" system. The basic heat equation PDE is often employed as the target system. By employing the backstepping approach, we reduce the motion planning problem for the 3-D Navier-Stokes channel problem to a motion planning problem for two 1-D heat equations. In this way, backstepping finds the unique solution to the motion planning problem. Backstepping is also employed to solve the trajectory tracking problem.

Organization of the Chapter. We start by reviewing the 3-D channel flow linearized model and giving an informal argument explaining why the solution to the motion planning problem is unique in Section 2.3. We then state and prove the solution to the motion planning problem in Section 2.4. The solution relies on several changes of variable, including the 2D Fourier transform, the change to normal velocity and vorticity for variables, and, most importantly, the PDE backstepping transformations. A control law which stabilizes the system around the desired trajectory is introduced and discussed in Section 2.5. We then go on to look more closely at particular closed form solutions in Section 2.6 and then the behavior of the solution as the wavenumbers grow or Reynolds number grows in Section 2.7. We conclude in Section 2.8.

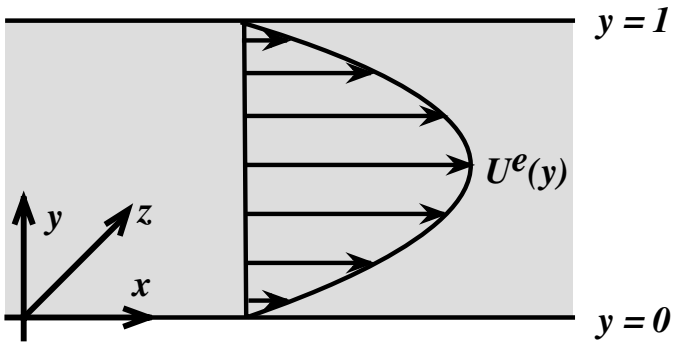

Figure 2.1: 3-D Channel Flow.

2.3 System Model

We consider the 3-D channel flow that is infinite in the x and z directions and bounded by walls at $y = 0$ and $y = 1$ as seen in Figure 2.1. The governing equations for the dimensionless velocity field of the incompressible channel flow are the Navier Stokes equations

$$\mathbf{U}_t = \frac{1}{Re}\triangle\mathbf{U} - \mathbf{U}\cdot\nabla\mathbf{U} - \nabla P \tag{2.1}$$

$$\nabla\cdot\mathbf{U} = 0 \tag{2.2}$$

where $\mathbf{U} = (U, W, V)$ and $U(y, x, z, t)$ is the streamwise velocity, $W(y, x, z, t)$ is the spanwise velocity, $V(y, x, z, t)$ is the wall-normal velocity, $P(y, x, z, t)$ is the pressure and Re is the Reynolds number. The velocities at far wall $y = 0$ satisfy the standard no-slip no penetration boundary condition,

$$\mathbf{U}|_{y=0} = 0. \tag{2.3}$$

These equations are linearized around the equilibrium parabolic Poiseuille profile

$$U^e = 4y(1-y) \tag{2.4}$$

$$W^e = V^e = 0 \tag{2.5}$$

$$P^e = P_0 - \frac{8}{Re}x\,. \tag{2.6}$$

After defining the fluctuation variables

$$u = U - U^e\,, \qquad p = P - P^e \tag{2.7}$$

the linearized system is

$$
\begin{aligned}
u_t &= \frac{1}{Re}\triangle u - U^e u_x - U^e_y V - p_x && (2.8)\\
W_t &= \frac{1}{Re}\triangle W - U^e W_x - p_z && (2.9)\\
V_t &= \frac{1}{Re}\triangle V - U^e V_x - p_y && (2.10)\\
& u_x + V_y + W_z = 0 && (2.11)\\
u|_{y=0} &= 0 \qquad W|_{y=0} = 0 \qquad V|_{y=0} = 0\,. && (2.12)
\end{aligned}
$$

The Dirichlet conditions at the far wall $y = 0$ satisfy the standard no-slip and no-penetration boundary conditions. However, it is the Neumann boundary variables at the same wall that are used as the *reference outputs*. They are denoted by $\mathcal{Y}$ and given by the desired skin friction and pressure trajectories, $u^r_y(0, x, z, t)$, $W^r_y(0, x, z, t)$, $p^r(0, x, z, t)$. We must solve for the reference inputs, denoted by $\mathcal{U}$, and given by $u^r(1, x, z, t)$, $W^r(1, x, z, t)$, $V^r(1, x, z, t)$. These inputs are actuated at the near wall $y = 1$.

We assume all three velocities to be actuated. We stress that there is no consensus in the literature as to which velocities are physically reasonable or mathematically necessary to actuate. The possibility of both wall-normal and tangential ("lateral") air injection using synthetic jets is discussed in [26]. We emphasize that the three velocity components at the boundary that our control laws command are neither mutually independent nor arbitrary but satisfy the Navier-Stokes PDEs.

It is important to understand what type of a mathematical problem one is facing when trying to find $\mathcal{U}$ for a given $\mathcal{Y}$. If we exchange the role of t and y, then the equations, expressed in terms of u, W, p, are

$$
\begin{aligned}
u_{yy} &= -u_{xx} - u_{zz} + Re\left(u_t + U^e u_x + U^e_y V + p_x\right) && (2.13)\\
W_{yy} &= -W_{xx} - W_{zz} + Re\left(W_t + U^e W_x + p_z\right) && (2.14)\\
p_{yy} &= -p_{xx} - p_{zz} + 2U^e_y V_x\,. && (2.15)
\end{aligned}
$$

Note that the left side is a partial derivative of order two in y and on the right the partial derivatives with respect to t, x, z are of order two or less. The now "initial conditions" at $y = 0$ are given by $\mathcal{Y}$, the no slip condition ($u = W = 0$) and

$p_y|_{y=0} = -\frac{1}{Re}\frac{\partial}{\partial x}u_y|_{y=0} - \frac{1}{Re}\frac{\partial}{\partial z}W_y|_{y=0}$, (where $u_y|_{y=0}, W_y|_{y=0}$ are again given by $\mathcal{Y}$). Set up in this way, this is a problem of Cauchy/Kowalevski type. As such we can expand the PDE using a formal power series in y and define recurrence relations for the coefficients (as functions of the remaining independent variables). As the first and second coefficients of this series are given through the "initial conditions", the recurrence relations define the series without any ambiguity. The normal velocity V is also defined without ambiguity through $V_y = -u_x - W_z$ and $V|_{y=0} = 0$. Therefore, if the series converges, we have a solution to u, W, V, p given $\mathcal{Y}$ and that solution is unique.

As standard for channel flow, we make use of the 2D Fourier Transform in the x and z directions to reduce the spatial dimension of the system from three to one. It results in a continuum of 1-D systems, each paramaterized by k_x and k_z, the wavenumbers in the x and z directions respectively. As the 3D PDE system is linear, each 1-D system is uncoupled from the others, though the subsystems within the 1-D system remain coupled. As the transformation between Fourier/wave space and physical space is standard, we continue the rest of the chapter (unless explicitly stated) in wavespace. For convenience we drop the dependence on k_x and k_z in the functions. The equations that result from the transformation are (in wavespace)

$$u_t = \frac{1}{Re}\triangle_k u - 2\pi i k_x U^e u - U^e_y V - 2\pi i k_x p \tag{2.16}$$

$$W_t = \frac{1}{Re}\triangle_k W - 2\pi i k_x U^e W - 2\pi i k_z p \tag{2.17}$$

$$V_t = \frac{1}{Re}\triangle_k V - 2\pi i k_x U^e V - p_y \tag{2.18}$$

$$2\pi i k_x u + 2\pi i k_z W + V_y = 0 \tag{2.19}$$

$$u|_{y=0} = 0 \qquad W|_{y=0} = 0 \qquad V|_{y=0} = 0 \tag{2.20}$$

where $\triangle_k = \frac{\partial^2}{\partial y^2} - \alpha^2$ and $\alpha^2 = 4\pi^2(k_x^2 + k_z^2)$. The velocities $u(y,t)$, $W(y,t)$, $V(y,t)$ and pressure $p(y,t)$, as well as the reference output trajectories $u^r_y|_{y=0}$, $W^r_y|_{y=0}$, $p^r|_{y=0}$ are parameterized by the wavenumbers k_x and k_z.

2.4 Motion Planning

The desired reference output $\mathcal{Y} = \left\{ u_y^r|_{y=0},\, W_y^r|_{y=0},\, p^r|_{y=0} \right\}$ for the skin friction and pressure is chosen within the following class of functions of (t, k_x, k_z):

$$u_y^r|_{y=0} \;=\; \sum_m A_m \mathrm{e}^{\varphi_m t}, \qquad W_y^r|_{y=0} \;=\; \sum_m B_m \mathrm{e}^{\varphi_m t} \tag{2.21}$$

$$p^r|_{y=0} \;=\; \sum_m C_m \mathrm{e}^{\varphi_m t} \tag{2.22}$$

where A_m, B_m, C_m and φ_m can all depend on the wavenumbers k_x, k_z. Indeed, φ_m can be complex - thus any sinusoid can be represented by (2.21)–(2.22).

In general these sums must be chosen such that

$$\sum_m X_m \sqrt{\frac{\epsilon}{\varphi_m}} \sinh\left(\sqrt{\frac{\varphi_m}{\epsilon}}\right) \mathrm{e}^{\varphi_m t} \;<\; \infty \qquad \forall k_x, k_z$$

where $X_m \in \{A_m, B_m, C_m\}$. If $\varphi_m = im\varphi_0$, then X_m must be the Fourier coefficients of a function that is smooth and periodic in t. In addition the terms $X_m(k_x, k_z)$ need to decay "fast enough" in k_x, k_z, for example, to be square integrable in k_x, k_z (in which case they correspond to the Fourier Transform of square integrable functions in x, z). We will discuss this more in Section 2.7 where we analyze the growth of the motion planning solution.

Before stating the main result of this chapter, we introduce Volterra operators and other notation. The Volterra operator is a "spatially causal" or lower triangular change of variable which starts from the lower wall $y = 0$ and is marched forward continuously in space towards the near wall $y = 1$. This type of approach has been effective in control of finite-dimensional nonlinear systems such as robotics and flight dynamics and it is known under the names of feedback linearization [33], dynamic inversion, and integrator backstepping [45]. The extension to infinite-dimensional systems was developed recently and results in explicit formulae for the gain functions [72]. This method is based on a functional transformation $\boldsymbol{f} \mapsto \boldsymbol{g}$,

$$\boldsymbol{f}(y) \;=\; \boldsymbol{g}(y) - \int_0^y K(y,\eta)\boldsymbol{g}(\eta)d\eta\,,$$

where the second term is a Volterra integral operator with a kernel $K(y, \eta)$. This transformation is invertible and its inverse involves another Volterra operator,

$$\boldsymbol{g}(y) \;=\; \boldsymbol{f}(y) + \int_0^y L(y,\eta)\boldsymbol{f}(\eta)d\eta\,,$$

where the kernels $L(y,\eta)$ and $K(y,\eta)$ are related through a (non-Volterra type) integral equation

$$L(y,\eta) \;=\; K(y,\eta) + \int_\eta^y K(y,\sigma)L(\sigma,\eta)d\sigma\,.$$

We introduce a compact Volterra operator notation as

$$\mathcal{V}\left(K,f\right)(y) \;=\; \int_0^y K(y,\eta)f(\eta)d\eta$$

where the operator output is a function of y, the upper limit of integration is the first argument of the first function, and the integration is over the second argument of the first function and the first argument of the second function. (If the second function has more than one argument, such as time or wavenumbers, all but the first are ignored as far as the integration is concerned.) We also define

$$\mathcal{W}_\eta^y\,(K,L) \;=\; \int_\eta^y K(y,\sigma)L(\sigma,\eta)d\sigma$$

which is similar to $\mathcal{V}\,(\cdot,\cdot)$ except that 1) the lower limit of integration is the second argument of the second function and 2) the operator output is a function of both y and η.

Next we present the main result of the chapter — the full reference trajectory (for input and state), valid for all individual wavenumbers, satisfying the reference output profiles for the skin friction and pressure at the far wall (2.21)-(2.22), and consisting of a linear combination of two Volterra integrals of explicit functions with spatial gain kernels. The linear combination results from the use of the normal velocity and vorticity while the Volterra operators arise from the use of PDE backstepping theory. [1]

Theorem 2.1 *The PDE system* (2.16)–(2.20) *with desired output* (2.21)–(2.22) *is satisfied by the following functions defined for* $(y,t)\in[0,1]\times[0,\infty)$,

$$u^r \;=\; \frac{-1}{2\pi i}\frac{k_xY^r+k_z\omega^r}{k_x^2+k_z^2} \tag{2.23}$$

$$W^r \;=\; \frac{-1}{2\pi i}\frac{k_zY^r-k_x\omega^r}{k_x^2+k_z^2} \tag{2.24}$$

$$V^r(y,t) \;=\; \int_0^y Y^r(\eta,t)d\eta \;=\; \mathcal{V}\,(1,Y^r) \tag{2.25}$$

[1] The solution is method independent – we simply employ backstepping to find it. Therefore, the pattern of dependence on Reynolds and wave numbers (which is examined in Section 2.7) is not a result of the method but is inherent to the motion planning problem itself.

where $Y^r(y,t)$ *and* $\omega^r(y,t)$ *are*

$$\begin{aligned} Y^r &= \Psi^r - F + \mathcal{V}\left(L, \Psi^r - F\right) && (2.26)\\ \omega^r &= \Omega^r - G + \mathcal{V}\left(\Phi, \Omega^r - G\right) + \mathcal{V}\left(\Theta, \Psi^r - F\right), && (2.27) \end{aligned}$$

the functions $\Psi^r(y,t), \Omega^r(y,t), F(y,t), G(y,t)$ *are defined by*

$$\begin{aligned} \Psi^r &= -2\pi i \sum_m (k_x A_m + k_z B_m) \mathrm{e}^{\varphi_m t} \sqrt{\frac{\epsilon}{\varphi_m}} \sinh\left(\sqrt{\frac{\varphi_m}{\epsilon}} y\right) && (2.28)\\ \Omega^r &= -2\pi i \sum_m (k_z A_m - k_x B_m) \mathrm{e}^{\varphi_m t} \sqrt{\frac{\epsilon}{\varphi_m}} \sinh\left(\sqrt{\frac{\varphi_m}{\epsilon}} y\right) && (2.29)\\ F &= -\sum_m C_m \mathrm{e}^{\varphi_m t} \mathcal{V}\left(\sigma_m, \mathcal{V}\left(K, q_p\right) - q_P\right) && (2.30)\\ G &= -\sum_m C_m \mathrm{e}^{\varphi_m t} \mathcal{V}\left(\sigma_m, \mathcal{V}\left(\Gamma, q_p\right)\right) && (2.31) \end{aligned}$$

where $\sigma_m(y,\eta) = \frac{\sinh(\sqrt{\frac{\varphi_m}{\epsilon}}(y-\eta))}{\sqrt{\varphi_m \epsilon}}$ *and the kernels* $L(y,\eta)$, $\Theta(y,\eta)$, $\Phi(y,\eta)$, $K(y,\eta)$, $\Gamma(y,\eta)$ *are defined by the following well-posed PDEs [72] in the region* $\left\{(y,\eta) : 0 \le \eta \le y \le 1\right\}$

$$\begin{aligned} \epsilon L_{yy} &= \epsilon L_{\eta\eta} - \phi(y) L - f \qquad & \epsilon K_{yy} &= \epsilon K_{\eta\eta} + \phi(\eta) K - f \\ &\quad - \mathcal{W}_\eta^y\left(f, L\right) & &\quad + \mathcal{W}_\eta^y\left(K, f\right) && (2.32)\\ \epsilon L|_{\eta=y} &= -\frac{1}{2}\mathcal{V}\left(1, \phi\right) - g(0) & \epsilon K|_{\eta=y} &= -\frac{1}{2}\mathcal{V}\left(1, \phi\right) - g(0) && (2.33)\\ \epsilon L|_{\eta=0} &= -g(y) & \epsilon K|_{\eta=0} &= \mathcal{V}\left(K, g\right) - g(y) && (2.34) \end{aligned}$$

$$\begin{aligned} \epsilon \Theta_{yy} &= \epsilon \Theta_{\eta\eta} - \phi(y) \Theta - h \qquad & \epsilon \Gamma_{yy} &= \epsilon \Gamma_{\eta\eta} + \phi(\eta) \Gamma - h \\ &\quad - \mathcal{W}_\eta^y\left(h, L\right) & &\quad + \mathcal{W}_\eta^y\left(\Gamma, f\right) + \mathcal{W}_\eta^y\left(\Pi, h\right) && (2.35)\\ \epsilon \Theta|_{\eta=y} &= 0 & \epsilon \Gamma|_{\eta=y} &= 0 && (2.36)\\ \epsilon \Theta|_{\eta=0} &= 0 & \epsilon \Gamma|_{\eta=0} &= \mathcal{V}\left(\Gamma, g\right) && (2.37) \end{aligned}$$

$$\begin{aligned} \epsilon \Phi_{yy} &= \epsilon \Phi_{\eta\eta} - \phi(y) \Phi & \epsilon \Pi_{yy} &= \epsilon \Pi_{\eta\eta} + \phi(\eta) \Pi && (2.38)\\ \epsilon \Phi|_{\eta=y} &= -\frac{1}{2}\mathcal{V}\left(1, \phi\right) & \epsilon \Pi|_{\eta=y} &= -\frac{1}{2}\mathcal{V}\left(1, \phi\right) && (2.39)\\ \epsilon \Phi|_{\eta=0} &= 0 & \epsilon \Pi|_{\eta=0} &= 0 && (2.40) \end{aligned}$$

where

$$\begin{aligned}
\epsilon &= \frac{1}{Re} && (2.41)\\
\phi(y) &= 8\pi i k_x y(y-1) - \epsilon\alpha^2 && (2.42)\\
f(y,\eta) &= 8\pi i k_x(2y-1) - 32\pi i \frac{k_x}{\alpha}\sinh\Big(\alpha(y-\eta)\Big) \\
&\quad -16\pi i k_x(2\eta-1)\cosh\Big(\alpha(y-\eta)\Big) && (2.43)\\
g(y) &= -\epsilon\alpha\sinh(\alpha y) && (2.44)\\
q_P(y) &= -\alpha^2\cosh(\alpha y) && (2.45)\\
h(y,\eta) &= 8\pi k_z i(1-2y)\,. && (2.46)
\end{aligned}$$

The reference input is given by $u^r|_{y=1}, W^r|_{y=1}$ *and*

$$\begin{aligned}
V^r|_{y=1} &= \mathrm{e}^{-\frac{\alpha^2}{Re}t}\int_0^t \mathrm{e}^{\frac{\alpha^2}{Re}\tau}\Bigg(\frac{Y^r_y|_{y=1}}{Re} - \cosh(\alpha)\frac{Y^r_y|_{y=0}}{Re} \\
&\quad +4\pi i k_x\frac{\cosh(\alpha y)}{\sinh(\alpha)}\int_0^1 V^r(\eta,\tau)U^e_y(\eta)\cosh\Big(\alpha(1-\eta)\Big)d\eta \\
&\quad -\alpha\sinh(\alpha)\sum_m C_m\mathrm{e}^{\varphi_m\tau}\Bigg)d\tau + \mathcal{V}\left(1, Y^r|_{t=0}\right)|_{y=1}. \qquad (2.47)
\end{aligned}$$

We prove Theorem 2.1 by construction in Section 2.4.1 to help the reader gain insight into the design aspects and the structure of the solution. The structure of the problem is pictorially represented in Figure 2.2. We start with the linearized Navier Stokes equations (2.16)–(2.20) and forcing trajectories (2.21)–(2.22) and perform several transformations, shown in Figure 2.3, to divide the problem into several tractable problems. After solving these simpler motion planning problems, we transform the solutions back to the velocity variables. The steps are summarized as follows:

1) Solve for the pressure and find a (open loop) normal velocity controller to reduce the open-loop problem from three velocity variables and one pressure variable down to three velocity variables.

2) Employ a transformation that reduces the model with three velocity variables to a model with only two variables in the normal direction – the normal vor-

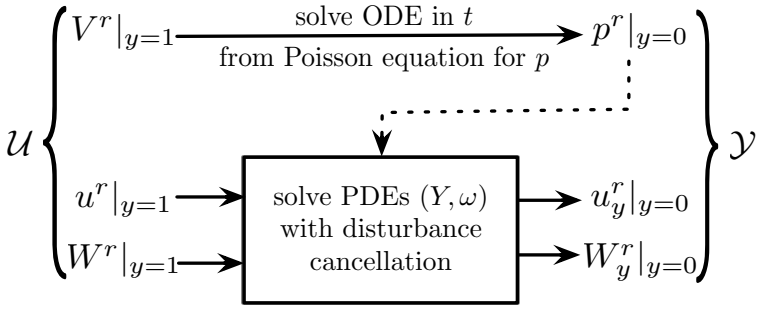

Figure 2.2: The structure of the input-output relationship $\mathcal{U} \mapsto \mathcal{Y}$ and a description of the types of problems that are solved in constructing the input $\mathcal{U}$ for a given reference output $\mathcal{Y}$.
Finding $V^r|_{y=1}$ is "easy" — it involves only a solution to an ODE in the time variable, given the pressure reference $p^r|_{y=0}$. Finding $u^r|_{y=1}$ and $W^r|_{y=1}$ is more complicated as it involves solving the Cauchy-Kowalevski problem for two coupled PDEs with a given output reference $u^r_y|_{y=0}, W^r_y|_{y=0}$, combined with solving an exact disturbance cancellation problem, where the pressure reference $p^r|_{y=0}$ acts as a known disturbance.

ticity ω^r and the derivative of the normal velocity in the normal direction $Y^r = V^r_y$.

3) Use the PDE backstepping transformation (employing Volterra integral operators and kernels K, Π, Γ) to transform the more complex model (Y^r, ω^r) to simple heat equations for (Ψ^r, Ω^r) and (F, G).

4) Solve the heat equations which define Ψ^r, Ω^r. These are forced at the boundary by $u^r_y|_{y=0}, W^r_y|_{y=0}$.

5) Solve the heat equations which define F, G. These are forced internally by $p^r|_{y=0}$.

6) Use the inverse transformation (also employing Volterra integral operators and kernels L, Φ, Θ) to transform back from Ψ^r, Ω^r and F, G to Y^r, ω^r.

7) A linear combination of Y^r and ω^r gives us u^r, W^r, V^r.

$$\Big\{u, W, V, p\Big\} \;\leftrightarrows\; \Big\{Y, \omega\Big\} \quad \underset{K,\Pi,\Gamma}{\overset{L,\Phi,\Theta}{\Longleftrightarrow}} \quad \Big\{\Psi - F, \Omega - G\Big\}$$

Figure 2.3: The string of (invertible) transformations involved in solving the full-state motion planning problem.

2.4.1 Proof of Theorem 2.1 and Construction of Open Loop Control

Solve for the full pressure reference trajectory. Rather than working with four different variables (three velocity variables and one pressure variable — which is further complicated by a nondynamic constraint), we instead use only two variables in the normal direction. Before stating the system equations for these two variables, we identify the input velocity trajectory in the normal direction $V^r|_{y=1}$ that ensures that the output pressure trajectory $p^r|_{y=0}$ is satisfied (exactly, i.e., for all time). The explicit solution to the elliptic PDE for p,

$$\begin{aligned}
\triangle_k p &= -4\pi i k_x U_y^e V \\
p_y|_{y=0} &= -2\pi i \frac{k_x u_y|_{y=0} + k_z W_y|_{y=0}}{Re} \\
p_y|_{y=1} &= \frac{-2\pi i \left(k_x u_y|_{y=1} + k_z W_y|_{y=1}\right) - \alpha^2 V|_{y=1}}{Re} - V_t|_{y=1}
\end{aligned}$$

is

$$\begin{aligned}
p \;=\; \frac{1}{\alpha}\Bigg\{ & -4\pi i k_x \mathcal{V}\Big(U_y^e(\eta)\sinh\Big(\alpha(y-\eta)\Big), V\Big) \\
& +4\pi i k_x \frac{\cosh(\alpha y)}{\sinh(\alpha)} \int_0^1 V(\eta,t) U_y^e(\eta)\cosh\Big(\alpha(1-\eta)\Big) d\eta \\
& -\frac{\cosh\Big(\alpha(1-y)\Big)}{\sinh(\alpha)} \frac{(-2\pi i)(k_x u_y|_{y=0} + k_z W_y|_{y=0})}{Re} \\
& +\frac{\cosh(\alpha y)}{\sinh(\alpha)} \Big(\frac{(-2\pi i)(k_x u_y|_{y=1} + k_z W_y|_{y=1}) - \alpha^2 V|_{y=1}}{Re} - V_t|_{y=1} \Big) \Bigg\}. \qquad (2.48)
\end{aligned}$$

By choosing the open-loop control $V^r|_{y=1} = \mathcal{N}$, where $\mathcal{N}$ verifies

$$\mathcal{N}_t \;=\; -\frac{\alpha^2}{Re}\mathcal{N} + \frac{(-2\pi i)(k_x u_y|_{y=1} + k_z W_y|_{y=1})}{Re}$$

$$
\begin{aligned}
&- \cosh(\alpha)\frac{(-2\pi i)(k_x u_y|_{y=0} + k_z W_y|_{y=0})}{Re} \\
&+4\pi i k_x \frac{\cosh(\alpha y)}{\sinh(\alpha)} \int_0^1 V^r(\eta,t) U_y^e(\eta) \cosh\Big(\alpha(1-\eta)\Big) d\eta \\
&-\alpha \sinh(\alpha) \sum_m C_m \mathrm{e}^{\varphi_m t}\,, \qquad (2.49)
\end{aligned}
$$

i.e., when $V^r|_{y=1}$ is defined as (2.47), we arrive at the motion planning solution for p^r:

$$
\begin{aligned}
p^r \;=\; \frac{1}{\alpha}\Bigg\{ &- 4\pi i k_x \boldsymbol{\mathcal{V}}\Big(U_y^e(\eta)\sinh\Big(\alpha(y-\eta)\Big), V^r\Big) \\
&+ \sinh(\alpha y)\frac{(-2\pi i)(k_x u_y|_{y=0} + k_z W_y|_{y=0})}{Re} + \alpha\cosh(\alpha y)\sum_m C_m \mathrm{e}^{\varphi_m t}\Bigg\}, \qquad (2.50)
\end{aligned}
$$

where $p^r|_{y=0}$ is exactly (2.22). The control (2.49) conveniently absorbs the nonstrict feedback (spatially non-causal) term – the integral from zero to one – into the normal velocity reference input, allowing for the rest of the motion planning problem (for u^r and W^r) to be approached using the backstepping method.

Reduce system to two variables in the normal direction. As is standard, we make use of the continuity equation and work with a variant of the normal velocity and the normal vorticity:

$$
\begin{aligned}
Y^r &= V_y^r = -2\pi i(k_x u^r + k_z W^r) \qquad (2.51)\\
\omega^r &= -2\pi i(k_z u^r - k_x W^r)\,. \qquad (2.52)
\end{aligned}
$$

We see from a first glance at the evolution equations

$$
\begin{aligned}
Y_t^r &= \frac{1}{Re}\triangle_k Y^r - 2\pi i k_x U^e Y^r + 2\pi i k_x U_y^e \boldsymbol{\mathcal{V}}(1, Y^r) - \alpha^2 p^r \qquad (2.53)\\
\omega_t^r &= \frac{1}{Re}\triangle_k \omega^r - 2\pi i k_x U^e \omega^r + 2\pi i k_z U_y^e \boldsymbol{\mathcal{V}}(1, Y^r) \qquad (2.54)
\end{aligned}
$$

(where we have used the fact that V has a homogeneous Dirichlet boundary condition at $y = 0$ to inversely relate V to Y)that we must solve for p^r if we wish to retain two second order subsystems instead of the fourth order and second order subsystem seen in the Orr-Sommerfeld equations.

At this point we know p^r and $V^r|_{y=1}$ and may now take these into account to construct the rest of the motion planning solution. Substituting (2.50) into (2.53)

the full "cascade" system for the two variables Y^r, ω^r is:

$$
\begin{aligned}
Y^r_t &= \epsilon Y^r_{yy} + \phi(y) Y^r + g(y) Y^r_y|_{y=0} + \mathcal{V}(f, Y^r) + q_P(y) \sum_m C_m \mathrm{e}^{\varphi_m t} && (2.55)\\
\omega^r_t &= \epsilon \omega^r_{yy} + \phi(y) \omega^r + \mathcal{V}(h, Y^r) && (2.56)\\
Y^r|_{y=0} &= 0 \qquad Y^r_y|_{y=0} = -2\pi i \sum_m (k_x A_m + k_z B_m) \mathrm{e}^{\varphi_m t} && (2.57)\\
\omega^r|_{y=0} &= 0 \qquad \omega^r_y|_{y=0} = -2\pi i \sum_m (k_z A_m - k_x B_m) \mathrm{e}^{\varphi_m t} && (2.58)
\end{aligned}
$$

where we use the homogeneous Neumann boundary condition for V in the boundary conditions for Y. By "cascade" we mean that Y^r feeds into the w^r equation but not the other way around, which will be exploited in our design. Note also that the Y^r equation is forced by the pressure output trajectory.

Construct the forward PDE backstepping transformation. This step employs the PDE backstepping method. This method for finding stabilizing boundary controllers for parabolic PDE systems is introduced and explained in [72]. In this chapter, though we do use the method to find *stabilizing* controllers, its main use is in breaking up the entire *motion planning* problem into solvable steps and finding the full spatio-temporal reference trajectory. It is important to note that this solution is method independent — we simply take advantage of backstepping to find it constructively.

The backstepping method exploits the invertibility of transformations that employ a shift by a Volterra operator, which has a triangular structure. We start with the block-triangular transformation $(Y^r, \omega^r) \mapsto (\Psi^r - F, \Omega^r - G)$ given by

$$
\begin{aligned}
\Psi^r - F &= Y^r + \mathcal{V}(K, Y^r) && (2.59)\\
\Omega^r - G &= \omega^r + \mathcal{V}(\Gamma, Y^r) + \mathcal{V}(\Pi, \omega^r) && (2.60)
\end{aligned}
$$

where Ψ^r, Ω^r and F, G are defined next. The forcing term $q_P(y) \sum_m C_m \mathrm{e}^{\varphi_m t}$ in (2.55), which comes from the pressure reference, complicates the motion planning problem for the streamwise and spanwise wall shear stress output trajectories, $u^r_y|_{y=0}, W^r_y|_{y=0}$. This pressure term acts as a known disturbance that needs to be cancelled by the controls $u^r|_{y=1}, W^r|_{y=1}$, which have a simultaneous task of also generating the output trajectory $u^r_y|_{y=0}, W^r_y|_{y=0}$. The (main) motion planning part of the state trajectory is (Ψ_r, Ω^r), whereas the disturbance cancellation part is (F, G). We first decide how

we want Ψ^r and Ω^r to behave and from there we then define the gain kernels K, Π, Γ and find the equations that govern F, G. We set the boundary conditions of Ψ^r, Ω^r to match the boundary conditions of Y^r, ω^r and set the boundary conditions of F, G to zero. We also want the simplest parabolic PDE the method will allow to govern the behavior of Ψ^r and Ω^r – arriving at uncoupled forced heat equations:

$$\Psi^r_t = \epsilon \Psi^r_{yy} \qquad \Omega^r_t = \epsilon \Omega^r_{yy} \tag{2.61}$$

$$\Psi^r|_{y=0} = 0 \qquad \Omega^r|_{y=0} = 0 \tag{2.62}$$

$$\Psi^r_y|_{y=0} = -2\pi i \sum_m (k_x A_m + k_z B_m) \mathrm{e}^{\varphi_m t} \quad \Omega^r_y|_{y=0} = -2\pi i \sum_m (k_z A_m - k_x B_m) \mathrm{e}^{\varphi_m t}\,. \tag{2.63}$$

The gain kernels K, Π, Γ which allow the transformation (2.59)–(2.60) to decouple the cascade system (2.55)–(2.58) and transform it to the uncoupled system (2.61)–(2.63) are defined by the hyperbolic PDEs (2.32)–(2.40). These PDEs can be solved numerically or symbolically using an equivalent integral equation formualtion that can be solved via a successive approximation series [72]. The procedure to find the PDEs which govern the gain kernels can be found in [44]. This procedure extends easily allowing us to find the governing equations for F and G:

$$F_t = \epsilon F_{yy} + \Big(\mathcal{V}(K, q_P) - q_P(y)\Big) \sum_m C_m \mathrm{e}^{\varphi_m t} \tag{2.64}$$

$$G_t = \epsilon G_{yy} + \mathcal{V}(\Gamma, q_P) \sum_m C_m \mathrm{e}^{\varphi_m t} \tag{2.65}$$

$$\begin{aligned} F_y(0) &= 0, \quad G_y(0) = 0 \\ F(0) &= 0, \quad G(0) = 0\,. \end{aligned} \tag{2.66}$$

Solve for Ψ^r, Ω^r. The motion planning problem for Ψ^r, Ω^r defined by (2.61)–(2.63) can be solved by representing Ψ^r or Ω^r as a power series expansion in y – i.e. $\Psi^r = \sum_l^\infty a_l(t) \frac{y^l}{l!}$. After solving for $a_l(t)$, the resulting series can be explicitly summed as the sinh function seen in the solution (2.28)–(2.29).

Solve for F, G. The equations governing F, G can be solved by taking the Laplace transform in y and then solving the resulting first order ordinary differential equation in t. The inverse Laplace transform results in the solution (2.30)–(2.31).

Find the inverse of the PDE backstepping transformation. After breaking the full problem down to simpler motion planning problems and a number of PDE equations

governing gain kernels, we must inversely relate Ψ^r, Ω^r and F, G to Y^r, ω^r. This inverse relationship (2.26)–(2.27) also uses Volterra integrals, this time with gain kernels L, Θ, Φ. The gain kernels are defined by (2.32)–(2.40) and can be related to the forward transform gain kernels through the following integral equations

$$\begin{aligned} L &= K + \mathcal{W}_\eta^y (K, L) \\ \Phi &= \Pi + \mathcal{W}_\eta^y (\Pi, \Phi) \\ \Theta &= \Gamma + \mathcal{W}_\eta^y (\Gamma, L) + \mathcal{W}_\eta^y (\Pi, \Theta) \ . \end{aligned}$$

Retrieve u^r, W^r, V^r. The two velocity variables u^r, W^r are recovered through the linear combinations of the two variables Y^r, ω^r (2.23)–(2.24), while V^r is recovered as the integral of Y^r, (2.25).

2.4.2 Simulation Results on Motion Planning

We illustrate the motion planning solution that results when choosing a specific spatio-temporal waveform for the skin friction and pressure at the far wall (a reference output trajectory) and applying the techniques presented in this chapter to obtain the exact initial conditions plus the exact input velocity (reference input) trajectories at the near wall. The figures show motion planning results for the following spatio-temporal output reference trajectory

$$u_y^r|_{y=0} = \begin{cases} \mathrm{e}^{-\frac{16\pi^2}{25}\left(\frac{k_x^2}{100}+\frac{k_z^2}{9}\right)} \sin\Big((4\pi k_x + 1/2)t\Big), & k_z \geq 0 \\ 0, & k_z < 0 \end{cases} \tag{2.67}$$

$$W_y^r|_{y=0} = \begin{cases} \mathrm{e}^{-\frac{32\pi^2}{25}\left(\frac{k_x^2}{100}+\frac{k_z^2}{9}\right)} i \sin\Big((4\pi k_x + 1/2)t\Big), & k_z \geq 0 \\ 0, & k_z < 0 \end{cases} \tag{2.68}$$

$$p^r|_{y=0} = \begin{cases} 4\pi\Big(i\frac{k_x}{10} + \frac{k_z}{3}\Big)\mathrm{e}^{-\frac{32\pi^2}{25}\left(\frac{k_x^2}{100}+\frac{k_z^2}{9}\right)} \sin\Big((4\pi k_x + 1/2)t\Big), & k_z \geq 0 \\ 0, & k_z < 0 \end{cases} \tag{2.69}$$

written in wavespace. We emphasize that the figures show the exact solution and include no feedback component — in other words, we did not simulate the linearized Navier Stokes equations, instead we computed the solution (2.23)–(2.25).

To show the general applicability of the method toward possibly complex problems, the output reference trajectory (2.67)–(2.69) is chosen as more complex than any particular physical application that we can think of would call for.

Figures 2.4 and 2.5 showsnap shots in time of the spatio-temporal profile (2.67)–(2.69) in physical space. The arrows in Figure 2.4 indicate the direction and magnitude of the output skin friction at the far wall $y = 0$. The colors in Figure 2.5 indicate the output pressure at $y = 0$ with blue being low pressure and red being high pressure. Time proceeds left to right and top to bottom in all figures.

Figures 2.6 and 2.7 result from applying the solution at $Re = 20$ to the above profile. The figures show snapshots in time of the exact input velocities that must be actuated at the near wall $y = 1$ to obtain the trajectories seen in Figures 2.4 and 2.5. The arrows in Figure 2.6 indicate the direction and magnitude of the (u^r, W^r) reference input velocity vector. The colors in Figure 2.7 represent the value of the normal velocity reference input with blue denoting negative velocities and red denoting positive velocities.

2.5 Stabilization

As one cannot choose the initial conditions of the flow, we must look to the addition of a feedback component to the reference input. Toward this end, we present a feedback law that accomplishes the stabilization of the linearized Navier Stokes system about the trajectory (2.23)–(2.25). Similarly to the motion planning solution, the feedback law is derived using the PDE backstepping method. However, unlike the motion planning solution which is unique, the choice of a stabilizing feedback is not. While previous optimal control designs required actuation of only the normal or only the tangential component of velocity, but at both walls, our approach employs actuation of all three velocity components but only at the far wall, $y = 1$. One of the advantages of the backstepping approach over optimal control approaches, when applied to the channel flow, is that it is not necessary to solve high-dimensional Riccati equations, and the backstepping gains (the kernels) are explicit (symbolically computable) functions of the Reynolds number and the

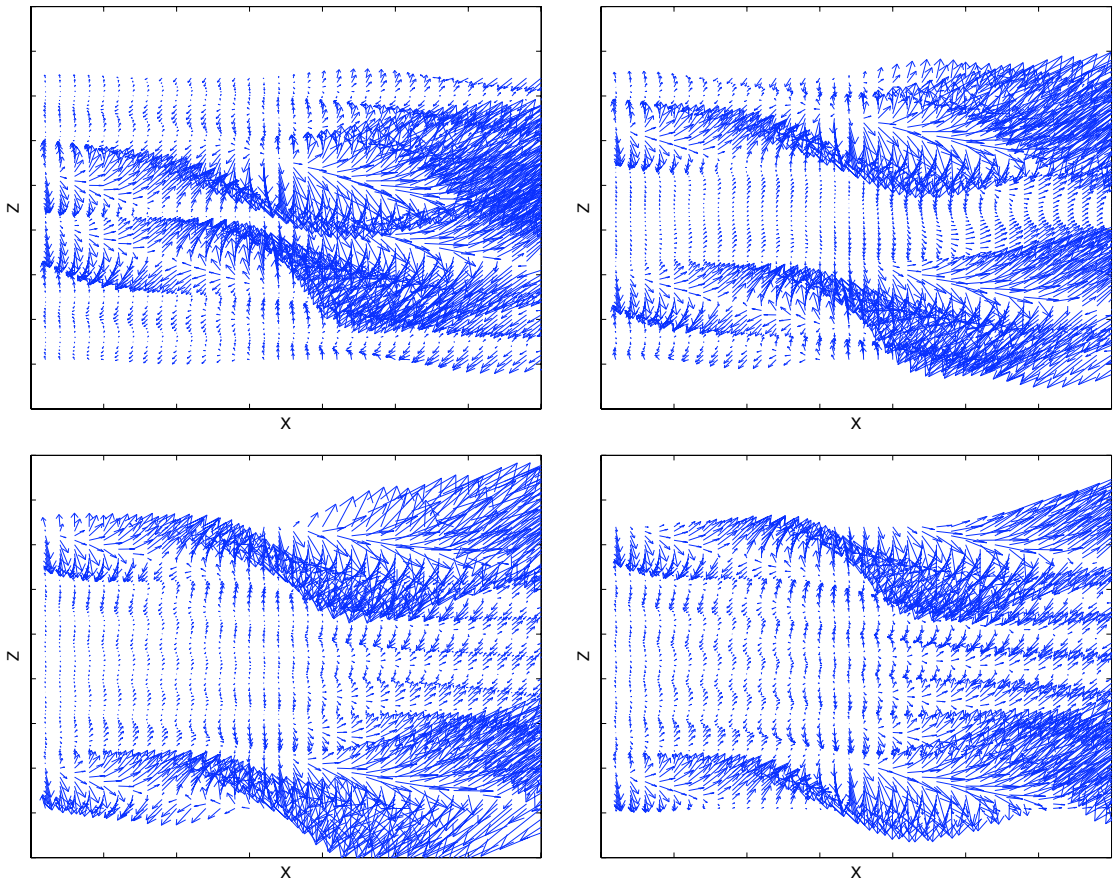

Figure 2.4: Snapshots of the desired skin friction spatio-temporal profile (reference output trajectory). Time proceeds left to right and top to bottom. Arrows indicate direction and magnitude.

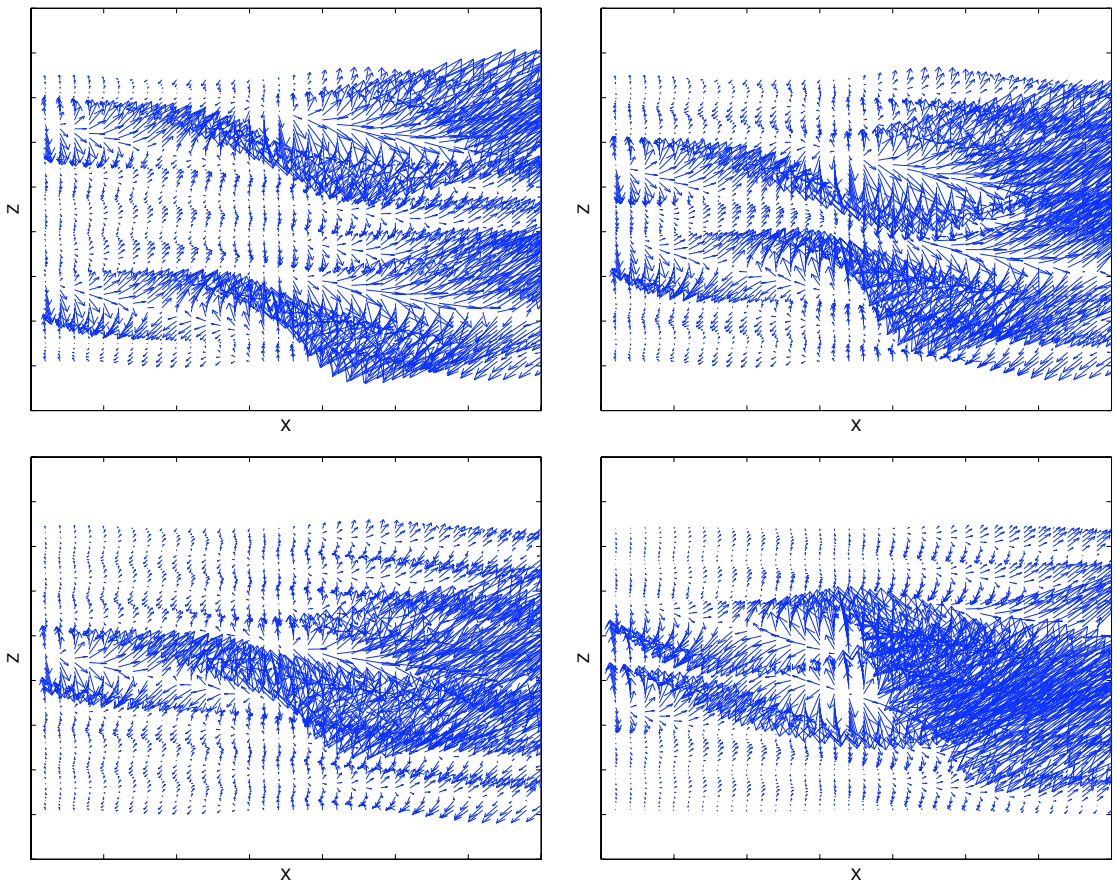

Figure 2.4. Snapshots of the desired skin friction spatio-temporal profile (reference output trajectory). Time proceeds left to right and top to bottom. Arrows indicate direction and magnitude.

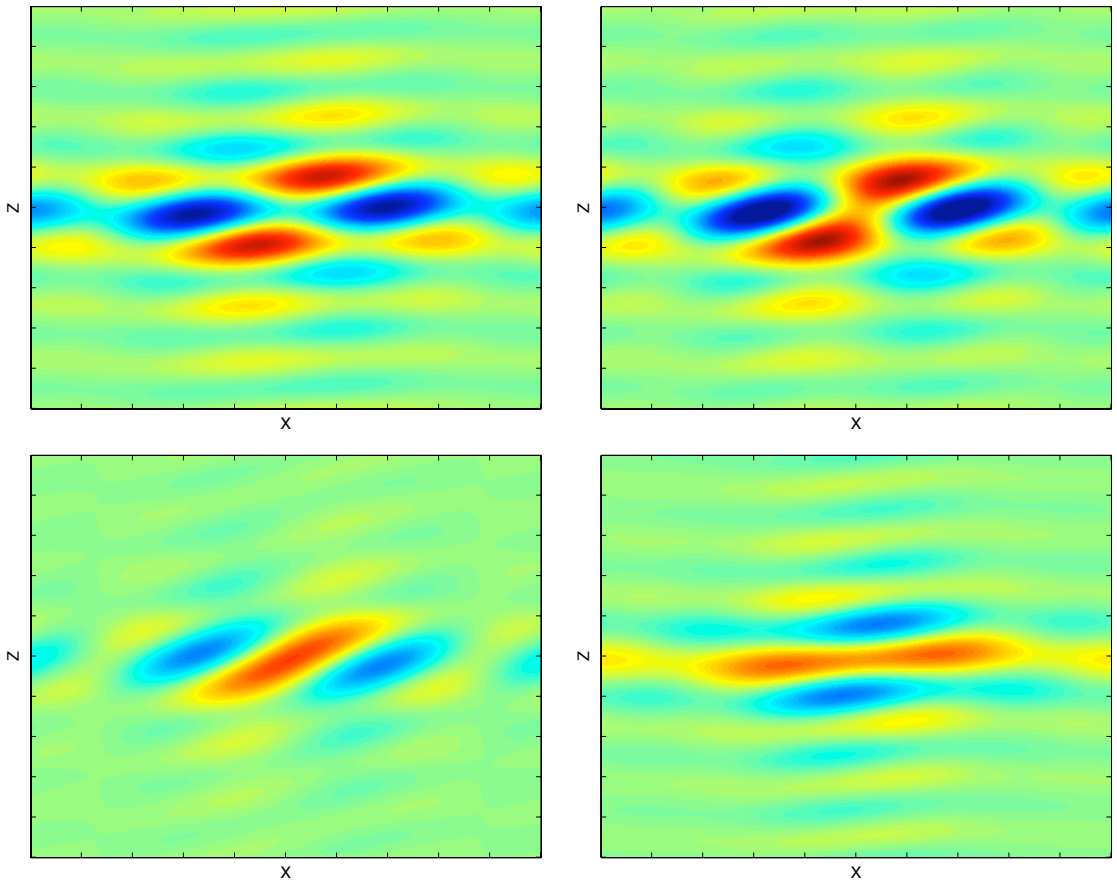

Figure 2.5: Snapshots of the desired pressure spatio-temporal profile (reference output trajectory). Time proceeds left to right and top to bottom. Blue indicates low pressure while red indicates high pressure.

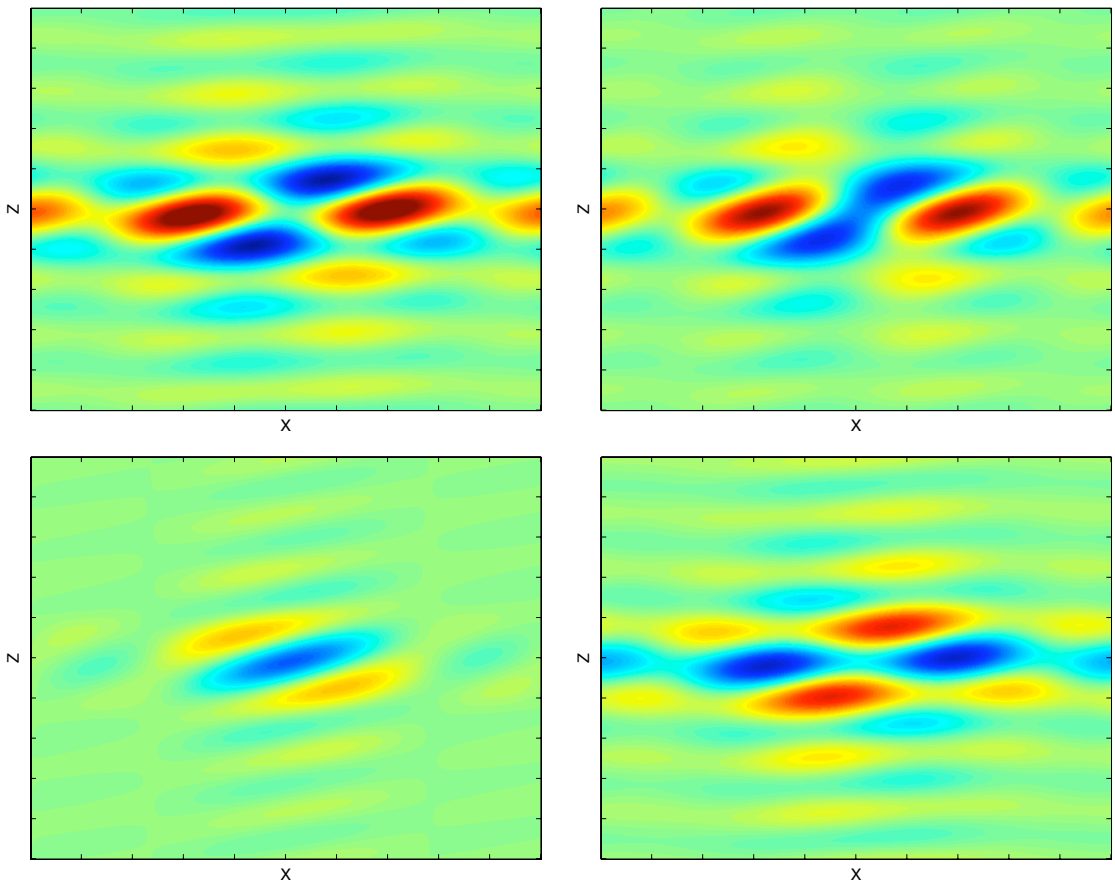

Figure 2.5. Snapshots of the desired pressure spatio-temporal profile (reference output trajectory). Time proceeds left to right and top to bottom. Blue indicates low pressure while red indicates high pressure.

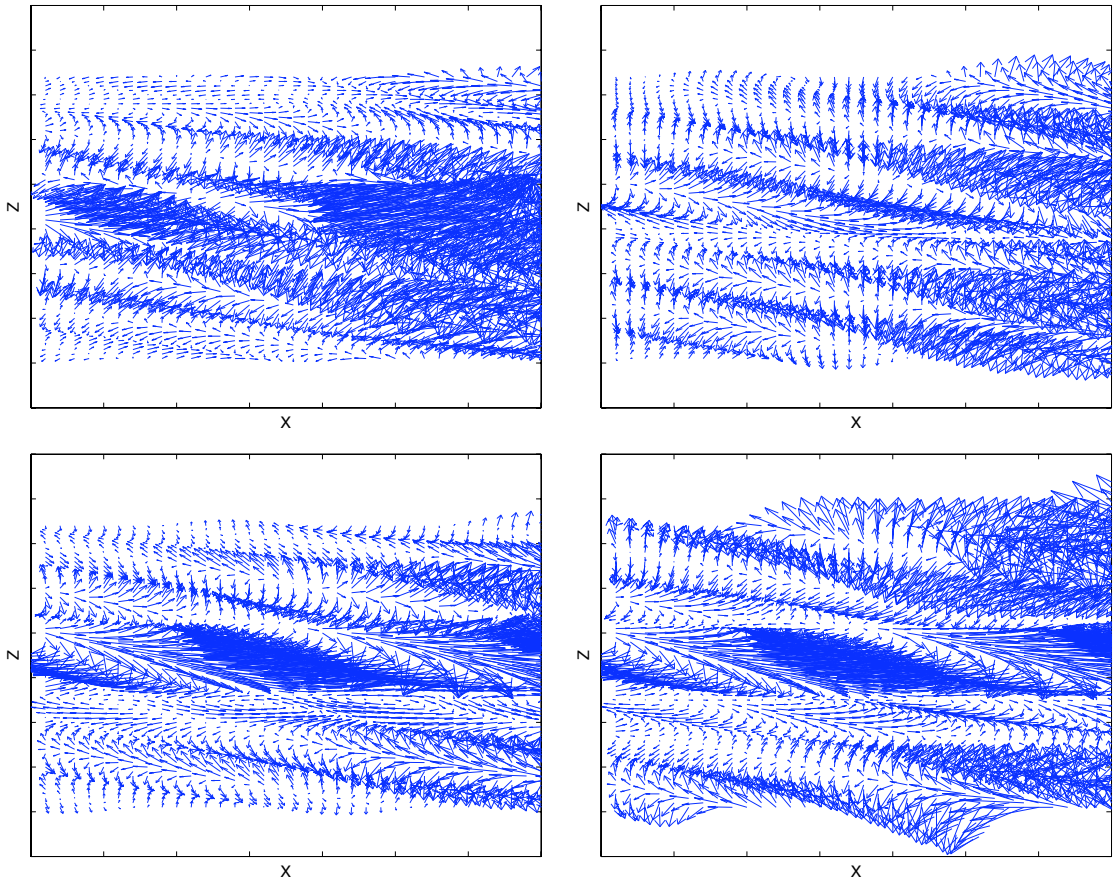

Figure 2.6: Snapshots in time of the input reference trajectory for stream- and span-wise velocity. Time proceeds left to right and top to bottom. Arrows indicate direction and magnitude.

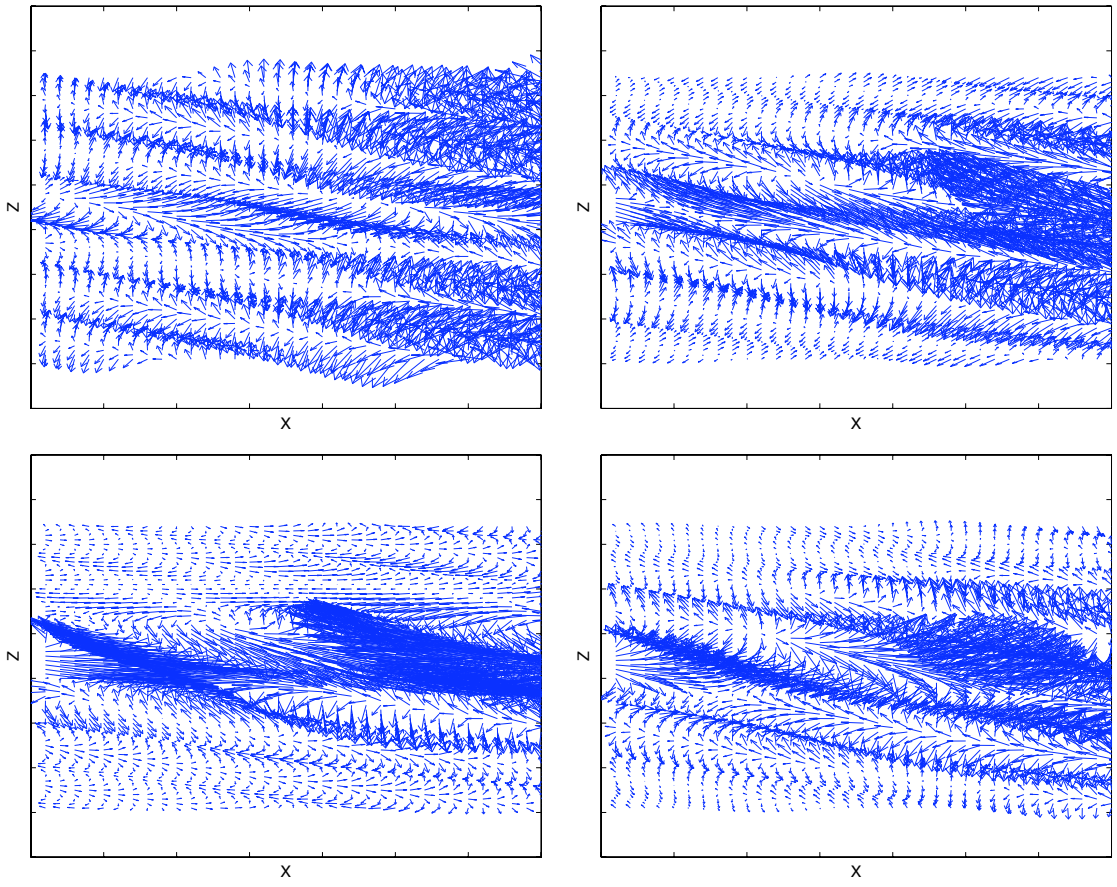

Figure 2.6. Snapshots in time of the input reference trajectory for stream- and span-wise velocity. Time proceeds left to right and top to bottom. Arrows indicate direction and magnitude.

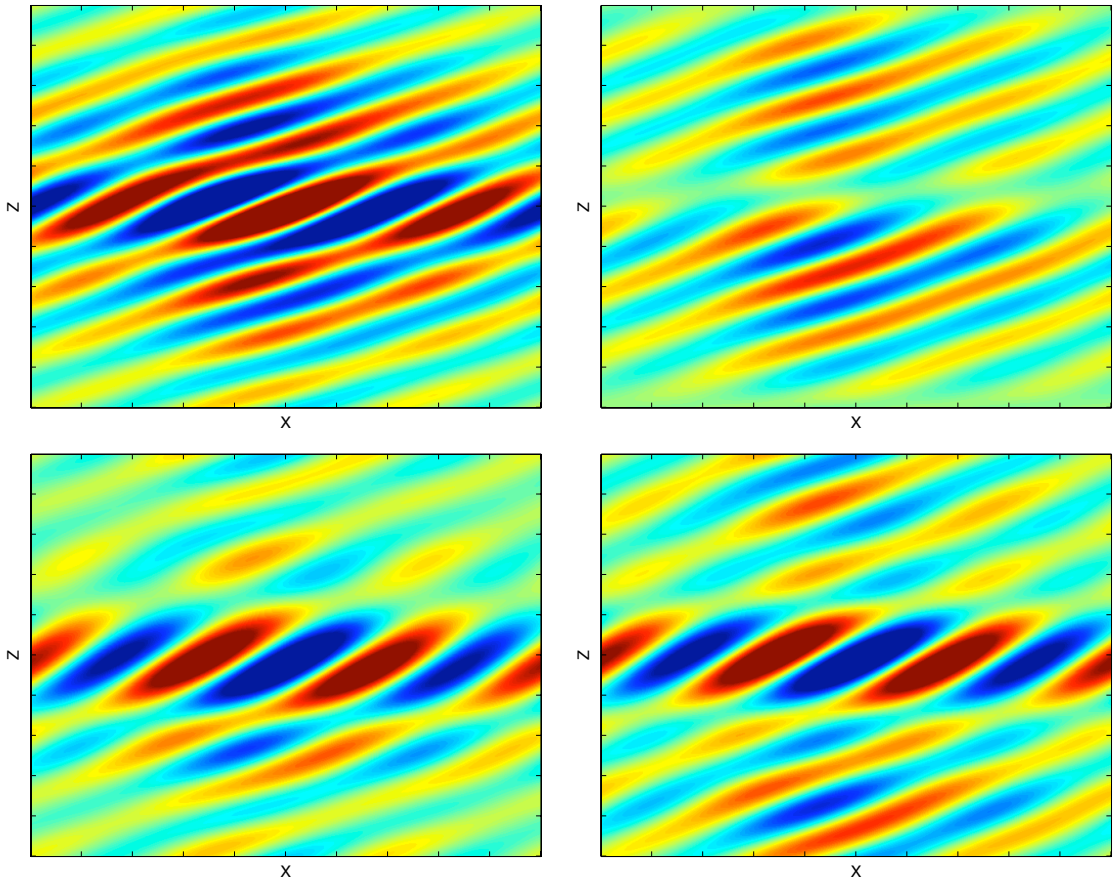

Figure 2.7: Snapshots in time of the input reference trajectory for normal velocity. Time proceeds left to right and top to bottom. Blue indicates negative velocity while red indicates positive velocity.

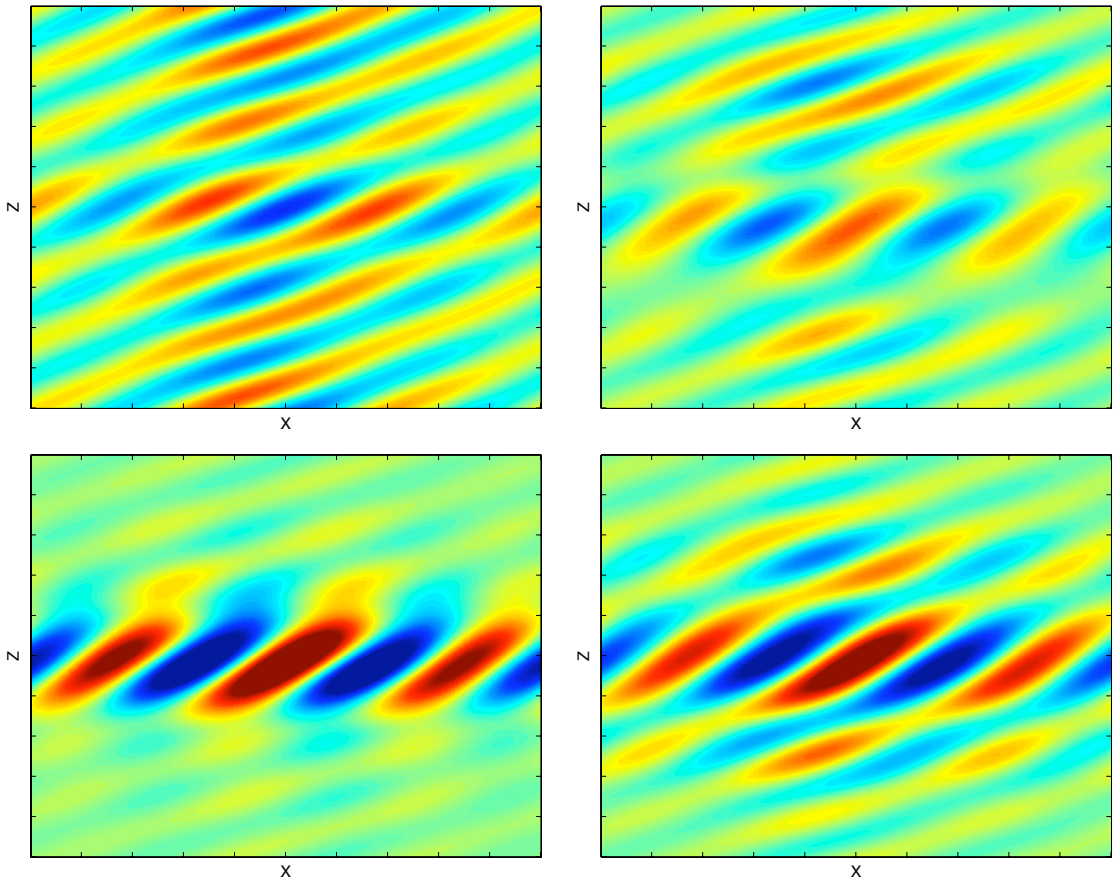

Figure 2.7. Snapshots in time of the input reference trajectory for normal velocity. Time proceeds left to right and top to bottom. Blue indicates negative velocity while red indicates positive velocity.

wavenumbers. Though the feedback law that we present here employs full state feedback, an observer developed in [82] allows us to implement the controller by measuring only the pressure and the skin friction at the same wall as the output reference, $y = 0$.

Theorem 2.2 *The feedback boundary controller, actuating the three velocities at the near wall* $y = 1$,

$$\begin{aligned}
u|_{y=1} &= \sum_m A_m \mathrm{e}^{\varphi_m t}\sqrt{\frac{\epsilon}{\varphi_m}}\sinh\left(\sqrt{\frac{\varphi_m}{\epsilon}}\right) + \mathcal{V}\left(\frac{k_x^2 K + k_z^2\Pi + k_z k_x \Gamma}{k_x^2+k_z^2}, u\right)\Big|_{y=1} \\
&\quad + \mathcal{V}\left(\frac{k_x k_z K - k_z k_x \Pi + k_z^2\Gamma}{k_x^2+k_z^2}, W\right)\Big|_{y=1} - \frac{1}{2\pi i}\frac{k_x F|_{y=1} + k_z G|_{y=1}}{k_x^2+k_z^2} \qquad (2.70) \\
W|_{y=1} &= \sum_m B_m \mathrm{e}^{\varphi_m t}\sqrt{\frac{\epsilon}{\varphi_m}}\sinh\left(\sqrt{\frac{\varphi_m}{\epsilon}}\right) + \mathcal{V}\left(\frac{k_z k_x K - k_x k_z \Pi - k_x^2\Gamma}{k_x^2+k_z^2}, u\right)\Big|_{y=1} \\
&\quad + \mathcal{V}\left(\frac{k_z^2 K + k_x^2\Pi - k_x k_z \Gamma}{k_x^2+k_z^2}, W\right)\Big|_{y=1} - \frac{1}{2\pi i}\frac{k_z F|_{y=1} - k_x G|_{y=1}}{k_x^2+k_z^2} \qquad (2.71) \\
V(t,1)_t &= \mathrm{e}^{-\frac{\alpha^2}{Re}t}\int_0^t \mathrm{e}^{\frac{\alpha^2}{Re}\tau}\left(\frac{2\pi i}{Re}\Big(\cosh(\alpha)\Big(k_x u_y|_{y=0} + k_z W_y|_{y=0}\Big)\right. \\
&\quad -\Big(k_x u_y|_{y=1} + k_z W_y|_{y=1}\Big)\Big) \\
&\quad + 4\pi i k_x \frac{\cosh(\alpha y)}{\sinh(\alpha)}\int_0^1 V(\eta,\tau)U_y^e(\eta)\cosh\Big(\alpha(1-\eta)\Big)d\eta \\
&\quad \left. -\alpha\sinh(\alpha)\sum_m C_m \mathrm{e}^{\varphi_m\tau}\right)d\tau \qquad (2.72)
\end{aligned}$$

exponentially stabilizes the system (2.16)–(2.20) *about the solution* (2.23)–(2.25) *in the* L_2 *sense:*

$$\begin{aligned}
&\int_0^1 \Big(|u-u^r|^2 + |W-W^r|^2 + |V-V^r|^2\Big)dy \\
&\quad \le \; C\mathrm{e}^{-\epsilon t}\int_0^1 \left(\Big|u|_{t=0} - u^r|_{t=0}\Big|^2 + \Big|W|_{t=0} - W^r|_{t=0}\Big|^2 + \Big|V|_{t=0} - V^r|_{t=0}\Big|^2\right)dy
\end{aligned} \qquad (2.73)$$

where $\epsilon = 1/Re$ *and*

$$\begin{aligned}
C &= (1+\alpha^2)(1+||L||_\infty)^2(1+||K||_\infty)^2 \\
&\quad \times\Big((1+||\Phi||_\infty)^2 + ||\Theta||_\infty\,(1+||\Phi||_\infty + ||\Theta||_\infty)\Big)
\end{aligned}$$

$$\times \left((1 + ||\Pi||_\infty)^2 + ||\Gamma||_\infty (1 + ||\Pi||_\infty + ||\Gamma||_\infty) \right) \tag{2.74}$$

$$||\cdot||_\infty = \sup_{0 \le \eta \le y \le 1} \{\cdot\}. \tag{2.75}$$

Proof: To prove stability about the solution (2.23)–(2.25), we first note that the pressure is still defined by (2.48) and becomes (2.50) when the normal velocity component of the feedback is defined as in (2.72). We then write the system in terms of Y and ω. The error system ($\tilde{Y} = Y - Y^r, \tilde{\omega} = \omega - \omega^r$) then has the following dynamics

$$\tilde{Y}_t = \epsilon \tilde{Y}_{yy} + \phi(y)\tilde{Y} + g(y)\tilde{Y}_y(0) + \mathcal{V}\left(f, \tilde{Y}\right) \tag{2.76}$$

$$\tilde{\omega}_t = \epsilon \tilde{\omega}_{yy} + \phi(y)\tilde{\omega} + \mathcal{V}\left(h, \tilde{Y}\right) \tag{2.77}$$

$$\tilde{Y}|_{y=1} = \mathcal{V}\left(K, \tilde{Y}\right)|_{y=1} \tag{2.78}$$

$$\tilde{\omega}|_{y=1} = \mathcal{V}(\Pi, \tilde{\omega})|_{y=1} + \mathcal{V}\left(\Gamma, \tilde{Y}\right)|_{y=1} \tag{2.79}$$

$$\tilde{Y}|_{y=0} = 0 \qquad \tilde{\omega}|_{y=0} = 0 \tag{2.80}$$

where we made use of (2.59), (2.60) to determine the value of the $Y^r|_{y=1}, \omega^r|_{y=1}$. Using the standard backstepping transformation

$$\tilde{\Psi} = \tilde{Y} - \mathcal{V}\left(K, \tilde{Y}\right) \tag{2.81}$$

$$\tilde{\Omega} = \tilde{\omega} - \mathcal{V}(\Pi, \tilde{\omega}) - \mathcal{V}\left(\Gamma, \tilde{Y}\right) \tag{2.82}$$

where $K(y,\eta)$, $\Pi(y,\eta)$, $\Gamma(y,\eta)$ are still defined by (2.32)–(2.40), we arrive at the dynamics for the backstepping error variables

$$\begin{aligned} \tilde{\Psi}_t &= \epsilon \tilde{\Psi}_{yy} & \tilde{\Omega}_t &= \epsilon \tilde{\Omega}_{yy} \\ \tilde{\Psi}|_{y=0} &= 0 & \tilde{\Omega}|_{y=0} &= 0 \\ \tilde{\Psi}|_{y=1} &= 0 & \tilde{\Omega}|_{y=1} &= 0 \end{aligned} \tag{2.83}$$

which are uncoupled heat equations. The use of the backstepping transformation (2.81),(2.82) shifts the coupling effects of the cascade system (2.76)–(2.80) to the boundary. These coupling effects (related to the nonnormality of the Orr -Sommerfeld/Squire operator) cause small time algebraic growth in the Squire equation. To deal with this the boundary control law cancels them. The variables $\tilde{\Psi}$ and

$\tilde{\Omega}$ can be bounded as follows

$$\int_0^1 |\tilde{\Psi}|^2 dy \leq \mathrm{e}^{-\epsilon t} \int_0^1 \left|\tilde{\Psi}|_{t=0}\right|^2 dy \tag{2.84}$$

$$\int_0^1 |\tilde{\Omega}|^2 dy \leq \mathrm{e}^{-\epsilon t} \int_0^1 \left|\tilde{\Omega}|_{t=0}\right|^2 dy\,. \tag{2.85}$$

Thus we can bound the L_2 norm of the error system as in (2.73) by using the forward and inverse transformations (2.26)–(2.27) and (2.59)–(2.60).

■

Note that this controller and stability theorem are defined for any wavenumber though the control is not actually meant to be applied for high wavenumbers as the inverse Fourier Transform would not converge in that case. When using this control law to stabilize the reference solution, the functions $A_m(k_x, k_z)$, $B_m(k_x, k_z)$, $C_m(k_x, k_z)$ should have compact (though arbitrarily large) support set $\mathcal{S}$ in (k_x, k_z), whereas the control law (2.70)–(2.72) should be applied for a sufficiently large disk $\mathcal{D}$ (around the origin) in wavenumber space (k_x, k_z), where $\mathcal{S} \subset \mathcal{D}$. The uncontrolled wavenumber set $\Re^2 \backslash \mathcal{D}$ takes advantage of the stability of these wavenumber pairs around a zero velocity profile. Details about this can be found in [44].

2.6 Closed-Form Solutions to the Kernel PDEs

The kernel PDEs (2.32)–(2.40) can be solved numerically, by using a modified Ablowitz-Kruskal-Ladik scheme [3], or symbolically, by using the method of successive approximations [72]. In certain cases we can find the solutions in closed form. Setting the streamwise wavenumber k_x to zero is one such case. In terms of control of channel flow turbulence, this is an important scenario as it is the case where the transient growth is the largest [69, 8, 15, 35], thus it is of interest that we can find closed form solutions for this case.

Theorem 2.3 *The PDE systems*

$$\epsilon L_{yy} = \epsilon L_{\eta\eta} + \epsilon\kappa^2 L \qquad \epsilon K_{yy} = \epsilon K_{\eta\eta} - \epsilon\kappa^2 K \tag{2.86}$$

$$\epsilon L|_{\eta=0} = -g(y) \qquad \epsilon K|_{\eta=0} = \mathcal{V}(K, g) - g(y) \tag{2.87}$$

$$\epsilon L|_{\eta=y} = \epsilon\frac{\kappa^2 y}{2} \qquad \epsilon K|_{\eta=y} = \epsilon\frac{\kappa^2 y}{2} \tag{2.88}$$

$$\begin{aligned}\epsilon\Theta_{yy} &= \epsilon\Theta_{\eta\eta} + \epsilon\kappa^2\Theta - h \\ &\quad - \mathcal{W}_\eta^y\left(h, L\right)\end{aligned} \qquad \begin{aligned}\epsilon\Gamma_{yy} &= \epsilon\Gamma_{\eta\eta} - \epsilon\kappa^2\Gamma - h \\ &\quad + \mathcal{W}_\eta^y\left(\Pi, h\right)\end{aligned} \tag{2.89}$$

$$\epsilon\Theta|_{\eta=0} = 0 \qquad \epsilon\Gamma|_{\eta=0} = \mathcal{V}\left(\Gamma, g\right) \tag{2.90}$$

$$\epsilon\Theta|_{\eta=y} = 0 \qquad \epsilon\Gamma|_{\eta=y} = 0 \tag{2.91}$$

$$\epsilon\Phi_{yy} = \epsilon\Phi_{\eta\eta} + \epsilon\kappa^2\Phi \qquad \epsilon\Pi_{yy} = \epsilon\Pi_{\eta\eta} - \epsilon\kappa^2\Pi \tag{2.92}$$

$$\epsilon\Phi|_{\eta=0} = 0 \qquad \epsilon\Pi|_{\eta=0} = 0 \tag{2.93}$$

$$\epsilon\Phi|_{\eta=y} = \epsilon\frac{\kappa^2 y}{2} \qquad \epsilon\Pi|_{\eta=y} = \epsilon\frac{\kappa^2 y}{2} \tag{2.94}$$

are satisfied by the functions

$$L = \kappa\sinh(\kappa(y-\eta)) + \Phi + \mathcal{W}_\eta^y\left(\kappa\sinh(\kappa(y-\eta)), \Phi\right) \tag{2.95}$$

$$\Theta = \Theta_1 + \mathcal{W}_\eta^y\left(\Theta_1, \Phi\right) \tag{2.96}$$

$$\Phi = \kappa^2\eta\frac{I_1(\sqrt{\kappa^2(y^2-\eta^2)})}{\sqrt{\kappa^2(y^2-\eta^2)}} \tag{2.97}$$

$$\Theta_1 = \frac{2i}{\epsilon\kappa}\eta\Big(\kappa(2y-\eta-1)\sinh(\kappa(y-\eta)) - \cosh(\kappa(y-\eta)) + 1\Big) \tag{2.98}$$

$$K = \kappa^2(y-\eta) + \Pi - \mathcal{W}_\eta^y\left(\Pi, \kappa^2(y-\eta)\right) \tag{2.99}$$

$$\Gamma = \Gamma_1 - \mathcal{W}_\eta^y\left(\Pi, \Gamma_1\right) \tag{2.100}$$

$$\Pi = \kappa^2\eta\frac{J_1(\sqrt{\kappa^2(y^2-\eta^2)})}{\sqrt{\kappa^2(y^2-\eta^2)}} \tag{2.101}$$

$$\begin{aligned}\Gamma_1 = {} & \frac{\kappa i}{\epsilon}\eta(y-\eta)(3y-\eta-2) \\ & -\frac{2i}{3\epsilon\kappa^2}\Big(6\kappa + 12\kappa(y-\eta) + 3\kappa^3(y-\eta)^2 - 2\kappa^3(y-\eta)^3 \\ & -6\kappa\cosh(\kappa(y-\eta)) - 24\sinh(\kappa(y-\eta)) \\ & +12\kappa(y-\eta)\cosh(\kappa(y-\eta))\Big)\end{aligned} \tag{2.102}$$

where $\kappa = 2\pi k_z$, I_1 is a modified Bessel function of the first kind and J_1 is a Bessel function of the first kind.

Proof: The solutions (and their derivations) to (2.92)–(2.94) can be found in [72]. Once Φ is found, Π is simply $-\Phi$ with κ^2 replaced with $-\kappa^2$. Also using

methods from [72] we write L, K, Θ, Γ as

$$L = L_1 + \Phi + \mathcal{W}_\eta^y(L_1, \Phi) \tag{2.103}$$

$$K = K_1 + \Pi - \mathcal{W}_\eta^y(\Pi, K_1) \tag{2.104}$$

$$\Theta = \Theta_1 + \mathcal{W}_\eta^y(\Theta_1, \Phi) \tag{2.105}$$

$$\Gamma = \Gamma_1 - \mathcal{W}_\eta^y(\Pi, \Gamma_1) \tag{2.106}$$

where L_1, K_1, Θ_1, Γ_1 are defined by

$$\epsilon L_{1yy} = \epsilon L_{1\eta\eta} \qquad \epsilon K_{1yy} = \epsilon K_{1\eta\eta} \tag{2.107}$$

$$\epsilon L_1|_{\eta=0} = -g(y) \qquad \epsilon K_1|_{\eta=0} = \mathcal{V}(K_1, g) - g(y) \tag{2.108}$$

$$\epsilon L_1|_{\eta=y} = -g(0) \qquad \epsilon K_1|_{\eta=y} = 0 \tag{2.109}$$

$$\epsilon\Theta_{1yy} = \epsilon\Theta_{1\eta\eta} - h - \mathcal{W}_\eta^y(h, L_1) \qquad \epsilon\Gamma_{1yy} = \epsilon\Gamma_{1\eta\eta} - h \tag{2.110}$$

$$\epsilon\Theta_1|_{\eta=0} = 0 \qquad \epsilon\Gamma_1|_{\eta=0} = \mathcal{V}(\Gamma_1, g) \tag{2.111}$$

$$\epsilon\Theta_1|_{\eta=y} = 0 \qquad \epsilon\Gamma_1|_{\eta=y} = 0 \tag{2.112}$$

By inspection we find $L_1 = -\frac{g(y-\eta)}{\epsilon}$. By using the transformation $K_1(y,\eta) = F_K(y-\eta)$ we change the K_1 system to an integral system in F_K: $\epsilon F_K(y) = \int_0^y F_K(\eta)g(y-\eta)d\eta - g(y)$. Then, by noting that $g(y)'' = k^2 g(y)$, we can rearrange the F_K system into a solvable second order ordinary differential equation: $F_K'' = 0, F_K(0) = 0, F_K'(0) = \kappa^2$ and find $K_1 = \kappa^2(y-\eta)$. To find Θ_1, use the change of variables $\left(\xi = y+\eta, \zeta = y-\eta, T(\xi,\zeta) = \Theta_1(y,\eta)\right)$ to obtain a PDE in T: $T_{\xi\zeta} = -\frac{1}{4\epsilon}h(\frac{\xi+\zeta}{2})\cosh(\kappa\zeta), T(\xi,\xi) = 0, T(\xi,0) = 0$. T is then found by integrating the forcing function first with respect to ζ from zero to ζ and then with respect to ξ from ζ to ξ. Similarly, to find Γ_1, again use the change of variables $\left(\xi = y+\eta, \zeta = y-\eta, \Sigma(\xi,\zeta) = \Gamma_1(y,\eta)\right)$ to obtain a PDE in Σ: $\Sigma_{\xi\zeta} = -\frac{1}{4\epsilon}h(\frac{\xi+\zeta}{2}), \Sigma(\xi,0) = 0, \epsilon\Sigma(\xi,\xi) = \int_0^\xi \Sigma(\xi+\tau, \xi-\tau)g(\tau)d\tau$. Again, integrate $\Sigma_{\xi\zeta}$ first with respect to ζ from zero to ζ and then with respect to ξ from ζ to ξ to obtain a forced integral equation for Σ. As the forcing is a function of both ξ and ζ whereas the integral part of solely a function of ζ, designate the integral part as $\Delta(\zeta)$ and find the integral equation for Δ that is only in ζ. This integral equation can then be turned into a solvable second order ordinary differential equation by again noting that $g(y)'' = \kappa^2 g(y)$. ■

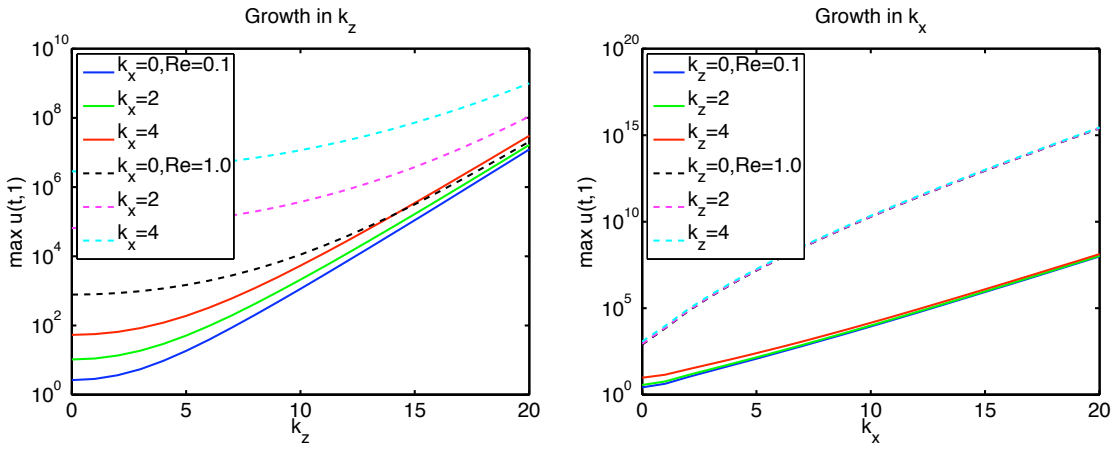

Figure 2.8: $\max_t \left\{ \left| u^r|_{y=1} \right| \right\}$ growing in k_z and k_x forced by $u_y^r|_{y=0} = \sin(t)$.

2.7 Inherent Difficulty Increases with Reynolds and Wave Numbers

One natural question to ask of the reference solution (2.23)–(2.25), is how it grows or decays as either the wavenumbers grow or as the Reynolds number grows. We consider both cases in this section. The growth that is demonstrated in this section is inherent to the problem as the solution itself is unique and method independent. Thus large controls are primarily the result of an overly ambitious choice of reference trajectory.

The following figures examine the portion of the motion planning solution due solely to a streamwise output friction trajectory of $u_y^r|_{y=0} = \sin(t)$. They show the maximum absolute value of the input reference trajectory, $\max_t \left\{ \left| u^r|_{y=1} \right| \right\}$, $\max_t \left\{ \left| W^r|_{y=1} \right| \right\}$, given different system parameters when the output trajectory is as stated $\left(u_y^r|_{y=0} = \sin(t), W_y^r|_{y=0} = 0, p^r|_{y=0} = 0 \right)$. Figures 2.8 and 2.9 show the growth of the input reference as the wavenumbers grow, while figure 2.10 demonstrates the growth as the Reynolds number grows.

The exponential growth of the motion planning solution in both wavenumber and Reynolds number is also seen when the solution is forced by only the spanwise friction output trajectory $W_y^r|_{y=0} = \sin(t)$ or by the output pressure trajectory

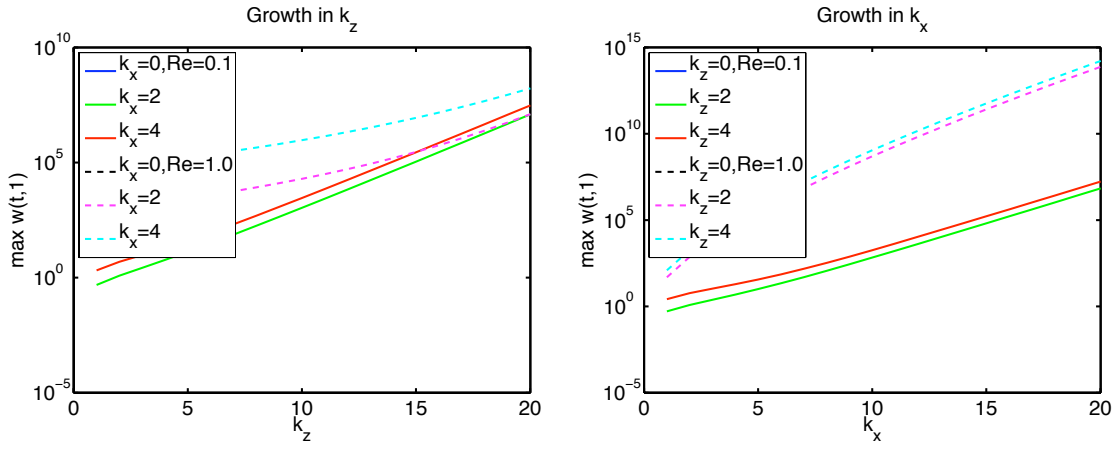

Figure 2.9: $\max_t \left\{ \left| W^r|_{y=1} \right| \right\}$ growing in k_z and k_x forced by $u^r_y|_{y=0} = \sin(t)$.

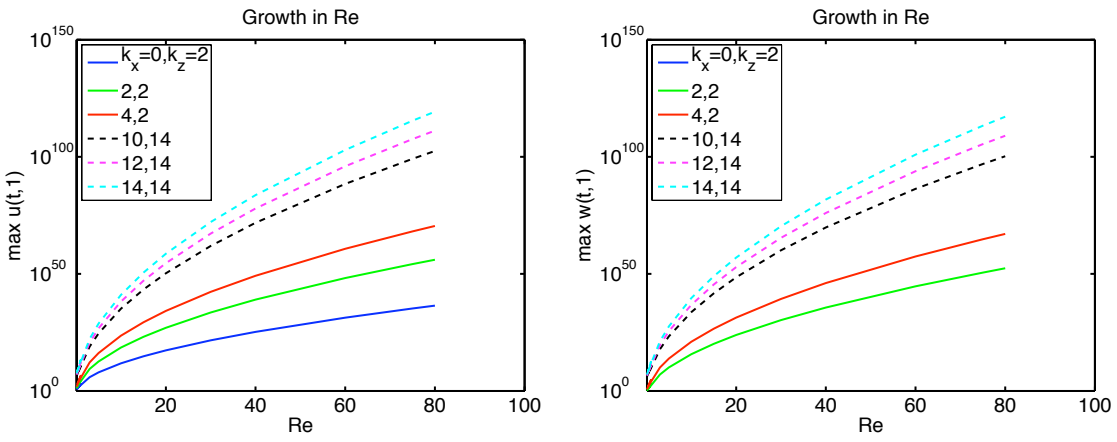

(a) (b)

Figure 2.10: (a) $\max_t \left\{ \left| u^r|_{y=1} \right| \right\}$ and (b) $\max_t \left\{ \left| W^r|_{y=1} \right| \right\}$ growing in Re forced by $u^r_y|_{y=0} = \sin(t)$.

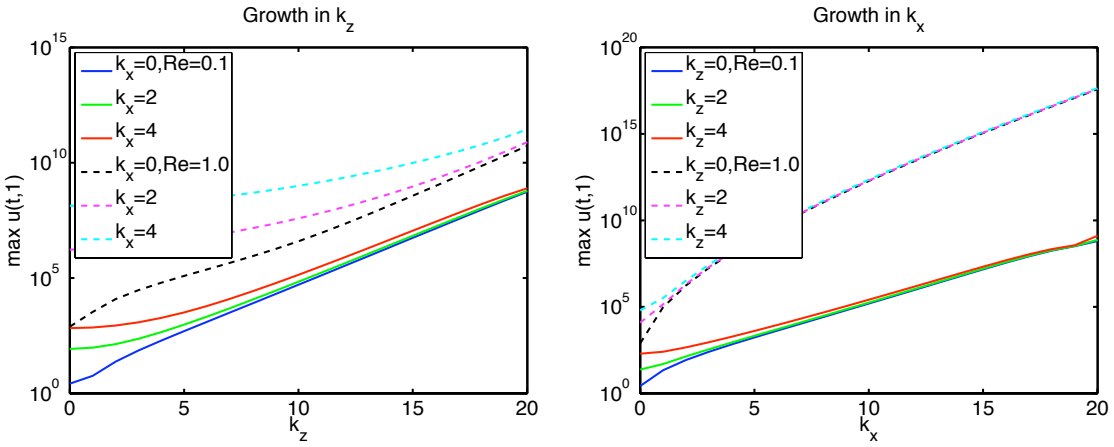

Figure 2.11: $\max_t \left\{ \left| u^r|_{y=1} \right| \right\}$ growing in k_z and k_x forced by $p^r|_{y=0} = \sin(t)$.

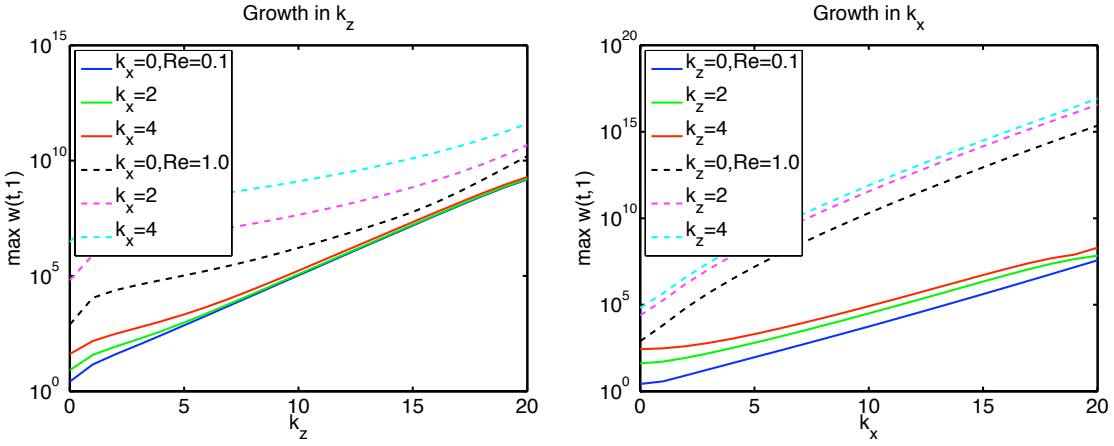

Figure 2.12: $\max_t \left\{ \left| W^r|_{y=1} \right| \right\}$ growing in k_z and k_x forced by $p^r|_{y=0} = \sin(t)$.

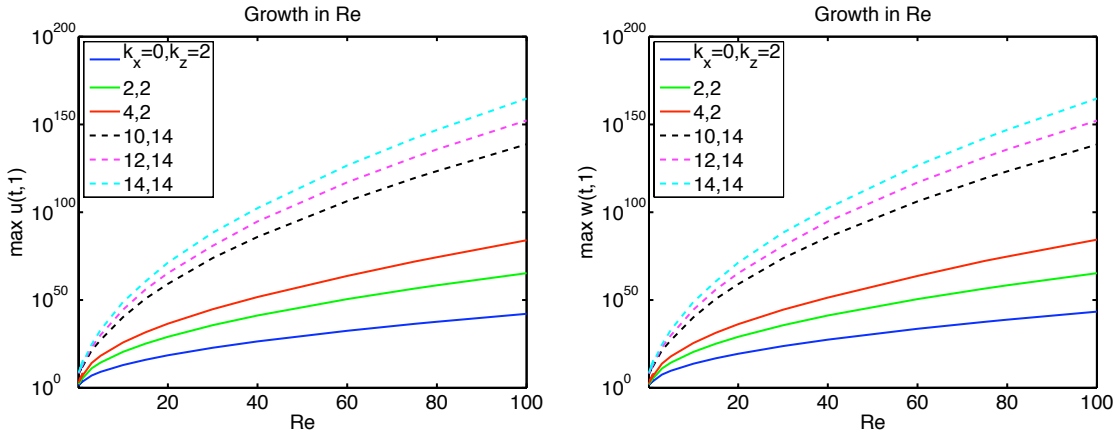

(a) (b)

Figure 2.13: (a) $\max_t \left\{ \left| u^r|_{y=1} \right| \right\}$ and (b) $\max_t \left\{ \left| W^r|_{y=1} \right| \right\}$ growing in Re forced by $p^r|_{y=0} = \sin(t)$.

$p^r|_{y=0} = \sin(t)$ as shown in Figures 2.11 and 2.12, while Figure 2.13 demonstrates the growth as the Reynolds number grows.

These figures show the need to carefully chose the amplitudes (and frequencies which affect the growth similarly to the Reynolds number) of the output trajectories so that the use of the inverse Fourier transform to transform the system back to physical space converges. It is important when choosing the amplitude functions to take advantage of their dependence on wavenumber as opposed to blindly choosing a constant value for all wavenumber pairs. Examples include choosing only a finite number of frequencies and choosing Gaussian functions in k_x and k_z as the amplitude functions.

It makes sense that more energy is required to generate high frequencies than low frequencies. To counter the growth due to high wavenumbers, one must decrease the amplitude at high wavenumbers. Figures 2.14 and 2.15 show how the growth changes once the amplitude of the output reference trajectory depends on wavenumber – they show the growth of the input reference due to an output reference of $p^r|_{y=0} = \mathcal{F}\{e^{-\pi^4 x^2 - \pi^4 z^2}\} \sin(t) = \frac{1}{\pi^3} e^{-\frac{k_x^2}{\pi^2} - \frac{k_z^2}{\pi^2}} \sin(t)$. The dependence seen in these figures is much more acceptable.

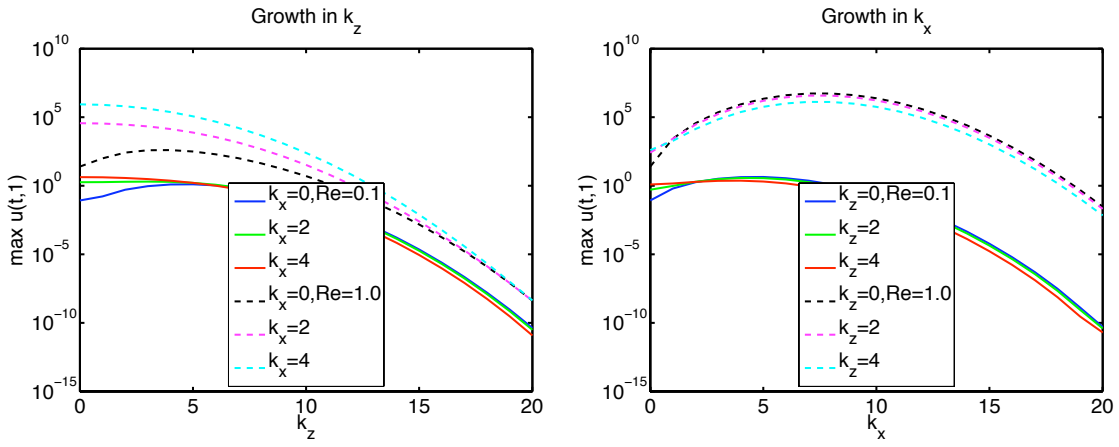

Figure 2.14: $\max_t \left\{ \left| u^r|_{y=1} \right| \right\}$ growing in k_z and k_x forced by $p^r|_{y=0} = \frac{1}{\pi^3} \mathrm{e}^{-\frac{k_x^2}{\pi^2} - \frac{k_z^2}{\pi^2}} \sin(t)$.

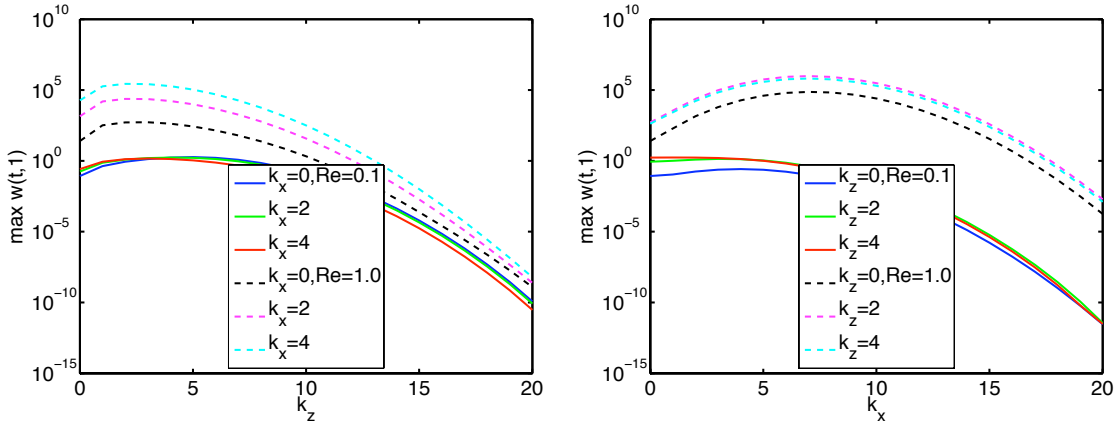

(a) (b)

Figure 2.15: $\max_t \left\{ \left| W^r|_{y=1} \right| \right\}$ growing in k_z and k_x forced by $p^r|_{y=0} = \frac{1}{\pi^3} \mathrm{e}^{-\frac{k_x^2}{\pi^2} - \frac{k_z^2}{\pi^2}} \sin(t)$.

2.8 Conclusion

The PDE backstepping theory enables the synthesis of the exact solution to the motion planning problem for skin friction and pressure for the 3D linearized Navier Stokes equations modeling channel flow. This is the first such result in the field of flow control. The PDE backstepping theory also allows us to stabilize the system about the reference solution, and thus achieve trajectory tracking for skin friction and pressure outputs. We hope to expand this study to state prediction and aircraft maneuverability with fluidic actuators.

The growth of the solution due to the Reynolds number serves to actually encourage us to turn to the fully nonlinear Navier Stokes equations for motion planning purposes. As the only way to move energy in the linearized equations is through the diffusive properties tied to the Reynolds number, as the Reynolds number goes up, the energy needed to affect the far wall increases - as seen in the figures in the chapter. However, the convective terms in the nonlinear equations could be useful for motion planning.

Motion planning for *boundary layer flows* is of great physical relevance. However, due to the collocated input-output structure, this system is not differentially flat and is likely to have unstable inverse dynamics at high Reynolds numbers. Future research should focus on identifying collocated flow problems that allow motion planning.

2.9 Further Remarks On The Stabilizing Controller

The feedback part of the controller (2.70)–(2.72) can be used alone to stabilize the system to a zero profile. This stabilizing controller,

$$u|_{y=1} = \mathcal{V}\left(\frac{k_x^2 K + k_z^2 \Pi + k_z k_x \Gamma}{k_x^2 + k_z^2}, u\right)\Big|_{y=1} + \mathcal{V}\left(\frac{k_x k_z K - k_z k_x \Pi + k_z^2 \Gamma}{k_x^2 + k_z^2}, W\right)\Big|_{y=1} \tag{2.113}$$

$$W|_{y=1} = \mathcal{V}\left(\frac{k_z k_x K - k_x k_z \Pi - k_x^2 \Gamma}{k_x^2 + k_z^2}, u\right)\Big|_{y=1} + \mathcal{V}\left(\frac{k_z^2 K + k_x^2 \Pi - k_x k_z \Gamma}{k_x^2 + k_z^2}, W\right)\Big|_{y=1} \tag{2.114}$$

$$V(t,1)_t = \mathrm{e}^{-\frac{\alpha^2}{Re}t}\int_0^t \mathrm{e}^{\frac{\alpha^2}{Re}\tau}\left(\frac{2\pi i}{Re}\Big(\cosh(\alpha)\Big(k_x u_y|_{y=0} + k_z W_y|_{y=0}\Big) - \Big(k_x u_y|_{y=1} + k_z W_y|_{y=1}\Big)\Big) + 4\pi i k_x \frac{\cosh(\alpha y)}{\sinh(\alpha)}\int_0^1 V(\eta,\tau)U_y^e(\eta)\cosh\Big(\alpha(1-\eta)\Big)d\eta\right)d\tau \tag{2.115}$$

found by setting $A_m = B_m = C_m = 0$ (i.e. $U^r = W^r = V^r = 0$), is, in theory, an elegant solution to the stabilization problem. However, it is not very practical and other stabilization methods perform better. When using this controller at reasonable Reynolds numbers the magnitudes of the velocity inputs are huge — many times that of the flow itself. This occurs because the controller takes advantage of the diffusive property of the flow. When the Reynolds number increases, though, diffusion is negligible and thus the controller must work extremely hard. In fact, the magnitude of the velocity input grows exponentially with Reynolds number. We attempted to simulate the stabilization of the channel flow with this stabilizing controller. We could only do so with extremely small Reynolds numbers $Re < 20$ before the computer could not handle the large numbers.

2.10 Acknowledgments

The authors gratefully acknowledge discussions with Rafael Vazquez, Andrey Smyshlyaev and Tom Bewley.

This chapter is in part a reprint of the material as it will appear in:
J. Cochran and M. Krstic, "Motion Planning and Trajectory Tracking for 3-D Poiseuille Flow," *Journal of Fluid Mechanics*, under review.

The dissertation author was the primary investigator and author of this publication.

3

Nonholonomic Source Seeking With Tuning of Angular Velocity

3.1 Abstract

We consider the problem of seeking the source of a scalar signal using an autonomous vehicle modeled as the nonholonomic unicycle. The vehicle does not have the capability of sensing its position or the position of the source but is capable of sensing the scalar signal originating from the source. The signal field is assumed to decay away from the position of the source but the vehicle does not have the knowledge of the functional form of the field. We employ extremum seeking to steer the vehicle to the source. Our control strategy keeps the forward velocity constant and tunes the angular velocity, a setting suitable for most autonomous vehicles, including aerial ones. Because of the constant forward velocity constraint, after it has converged near the source, the vehicle exhibits extremely interesting and complex motions. Using averaging theory, we prove local exponential convergence to an "orbit-like" attractor around the source. We also present a thorough analysis of non-local behaviors and attractors that the vehicle can exhibit near the source. The richness and complexity of behaviors makes only some of them amenable to analysis, whereas others are illustrated through a carefully laid out simulation study.

3.2 Introduction

In the literature on coordinated motion control and autonomous agents, deprivation of position information is an area of rapidly growing interest. The applications where this might occur are many, and include vehicles operating under water, under ice, in caves or in urban environments where GPS is unavailable, and applications where INS systems are too costly.

In [86] we considered the problem of seeking the source of a scalar signal using a nonholonomic vehicle with no position information. Specifically, we considered a unicycle with a constant angular velocity and a controlled forward velocity and showed local convergence to the source of a signal. For some vehicles, including fixed-wing aircraft, the approach in [86], which requires motion both forward and in reverse, cannot realistically be applied. In this chapter we consider the complementary case of a unicycle with a constant forward velocity and tuned angular velocity. The approach in this chapter is applicable to a broader class of vehicles, including aircraft, and also produces a more efficient method of locomotion than in [86]—the vehicle heads directly toward the source instead of doing so in the form of drifting triangles, rhombi, or stars [86].

In the scenario we consider, the vehicle, modeled as a nonholonomic unicycle, senses some scalar signal which emanates from the source it seeks. This signal could be the concentration of a chemical or biological agent, or it could also be an electromagnetic, acoustic, thermal or radar signal. The strength of the signal is assumed to decay away from the source through diffusion or other physical processes. Other information about the spatial distribution of the signal is not available to the vehicle. Throughout the scenario, the seeking vehicle senses only the strength of the signal at the location of its sensor. To find the source, we employ the extremum seeking method, [5], which uses non-model based gradient estimation. The controller jointly estimates the gradient (using the motion of the vehicle's sensor in space) and drives the vehicle toward the source. We present a stability proof for the scheme with a static source, further analysis of non-local aspects of the closed-loop dynamics, and simulation results for both static and moving sources. The simulations show that tuning the angular velocity produces much more realistic vehicle trajectories

compared to tuning the forward velocity [86].

While other groups have considered source seeking problems, [62] and [58], this work is different in that the vehicle has no knowledge of its position or the position of the source, there is no communication between it and other entities, and it has nonholonomic dynamics. Many groups have also employed unicycle models in their work, including [36], [43], and [51], while others have also used the extremum seeking method in their work outside of the field of autonomous vehicles, including [61], [60], [17], [73], [41], [14], [74], [28], [48] and [88]. The main novelty of this result is in simultaneously solving a nonholonomic steering problem and an adaptive optimization problem.

Unlike the design in [86], the present design is for a system that is not small-time locally controllable. Furthermore, while the objectives of converging rapidly and directly towards the source (on average) and entering a quasi-steady motion near the source are not contradictory with the actuation configuration in [86], with the actuation configuration in the present chapter they are in fact hard to achieve simultaneously. We reconcile the seeming contradiction between convergence to and settling around the source by proposing a modification to the basic extremum seeking algorithm, which employs a quadratic feedback of the output of the washout filter (to be referred to as the d term). This term, in a rather non-obvious way, stabilizes an otherwise marginally stable non-periodic solution around the source (without actually altering this solution). As a consequence, a much more delicate stability analysis emerges in this chapter. Averaging is still the main tool. However, while the system's right-hand side is periodic, the system's attractor is in fact not periodic; It involves the frequencies of both extremum seeking and of the revolution around the source. These frequencies cannot be guaranteed to be commensurate because the latter depends on the parameter of the unknown signal field. We ascertain the existence and exponential stability of this attractor (characterizing it explicitly to an arbitrary level of accuracy in terms of the control parameters). This is clearly of practical significance as it ensures that the vehicle will not only converge towards the source but also establish a sustainable motion near the source. A further degree of difficulty in this problem over [86] is that with vehicles controlled

through the heading rate a topological obstacle exists that creates a set of unstable trajectories. These trajectories correspond to converging perfectly to the source and not being able to decide whether to turn the vehicle back in the clockwise or the counter-clockwise direction. We characterize these trajectories. We also study two fundamentally different implementations, one with a sensor that is non-collocated with the center of the vehicle and another that is collocated. The latter situation requires parameter choices that induce three time scales, such that the analysis employs both averaging and singular perturbation methods.

We start the chapter in Section 3.3 with a description of the vehicle model and extremum seeking scheme. We prove local exponential convergence to an "orbit-like" attractor around the source for both noncollocated and collocated vehicle center and sensor in Section 3.4. We also characterize non-local behaviors and attractors that the vehicle can exhibit near the source as a result of the forward velocity constraint, including a zero-measure set of unstable trajectories. This analysis of the complex motions displayed by the vehicle continues in Section 3.5 where we fully examine the effect of a specific controller parameter. We present a carefully constructed simulation study in Section 3.6 which highlights the variety and complexity of the vehicle behaviors that are not amenable to analysis. We discuss our parallel research efforts in Section 3.7.

3.3 Vehicle Model and Extremum Seeking Controller

We consider a mobile agent modeled as a unicycle with a sensor mounted at a distance R away from the center. The diagram in Figure 3.1 depicts the position, heading, angular and forward velocities for the center and sensor. The equations of motion for the vehicle center are

$$\dot{r}_c = v\mathrm{e}^{j\theta} \tag{3.1}$$

$$\dot{\theta} = \Omega \tag{3.2}$$

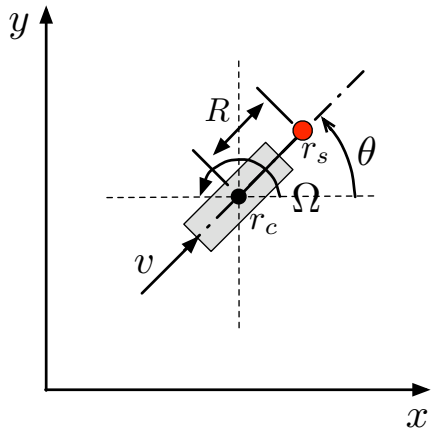

Figure 3.1: The notation used in the model of vehicle sensor and center dynamics.

where r_c is the center of the vehicle, θ is the orientation and v, Ω are the forward and angular velocity inputs. The sensor is located at $r_s = r_c + R\mathrm{e}^{j\theta}$.

The task of the vehicle is to seek a source that emits a signal which decays as a function of distance away from the source. We assume this signal field is distributed according to an unknown nonlinear map $J = f\Big(r(x, y)\Big)$ which has an isolated local maximum $f^* = f(r^*)$ where r^* is the location of the local maximum. We design a controller that achieves local convergence to r^* without knowledge of the shape of f, using only the measurement of J at the vehicle sensor.

If both the shape of f and the position, r_c, of the vehicle were known, and if the vehicle were fully actuated in both x and y directions, then we could design a control law to force the vehicle's trajectory to evolve according to the gradient dynamical system $\dot{r}_c = -\nabla f$. In that case the trajectory of r_c would asymptotically converge to the set of stationary points of f where $\nabla f(r^*) = 0$. However, in the absence of this knowledge, we employ techniques of non-model-based optimization. This task becomes even more complex as we consider a kinematically constrained vehicle.

To accomplish the task, we employ extremum seeking to tune the angular velocity (Ω) while keeping the forward velocity, v, constant. This scheme is depicted by the block diagram in Figure 3.2. The forward velocity, v, of the unicycle is set to the

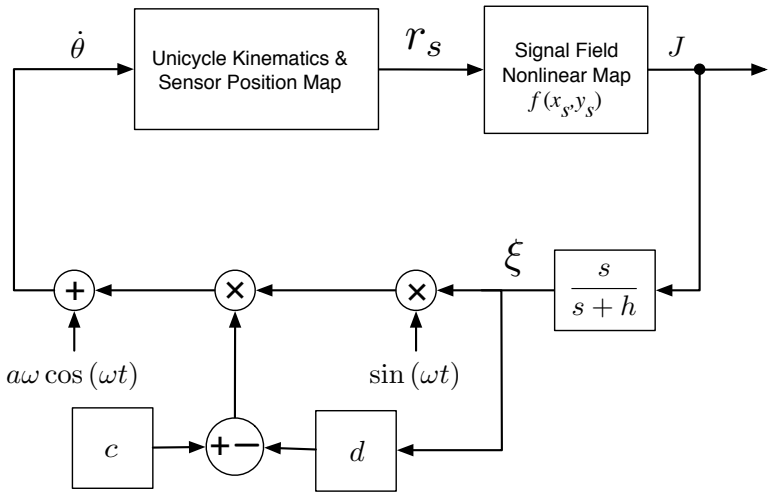

Figure 3.2: Block diagram of source seeking via tuning of angular velocity, $\dot{\theta}$, of the vehicle. The sensor at the position r_s is at a distance R from the vehicle center at r_c.

constant, V_c, while $\dot{\theta}$ is tuned by the extremum seeking control law

$$\dot{\theta} = a\omega\cos(\omega t) + c\xi\sin(\omega t) - d\xi^2\sin(\omega t) \tag{3.3}$$

where ξ is the output of the washout filter. The performance can be influenced by the parameters a, c, d, R, V_c, h and ω. The last term, $-d\xi^2\sin(\omega t)$, which we shall refer to as the d term, is not part of the basic extremum seeking tuning law. We added this term in order to achieve exponential convergence to an "orbit-like" solution that exists around the source but happens to be only marginally stable (for $d = 0$). The practical problem that the d term addresses is that the vehicle, having a constant forward velocity, cannot stop once it has reached the source. It must overshoot it and turn around. To counter this, the d term partly sacrifices the gradient extraction and actually pushes the vehicle a bit off the trajectory that would take it directly toward the source. However, in doing so the d term allows the vehicle to settle into a motion close to the target after it has reached the target.

This scheme was designed with both static and moving sources in mind. Figure 3.3 shows a source moving in a figure-eight that is first found, "caught up to" and then followed by the vehicle. While the simulation shows that the scheme works well

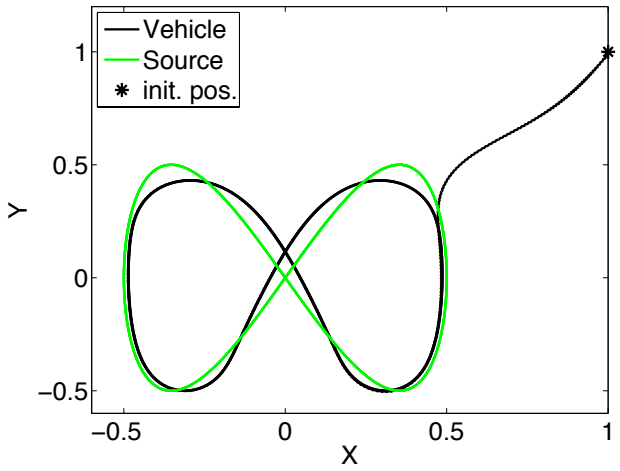

Figure 3.3: Vehicle following a moving source whose map has elliptical level sets. The simulation parameters are $V_c = 0.1, c = 100, d = 10, a = 0.5, \omega = 40, R = 0.1, h = 1, f^* = 0, q_r = 1.5, q_p = 0.25$. The source moves according to $x_{src}(t) = 0.5\sin(0.13t), y_{src}(t) = 0.5\sin(0.26t)$.

with a moving source, in the next section we present a stability result that focuses on static sources.

3.4 Closed Loop Stability

In this section we present and prove a local stability theorem for the vehicle and control scheme presented in Section 3.3.

The dynamics of the closed loop system are very intricate, despite the fact that the system has only four states (three states of the vehicle and one filter state). The complexity comes from the nonlinearities (trigonometric nonlinearities in the vehicle model and the polynomial nonlinearity in the signal map) and also from the time-varying forcing applied by extremum seeking.

We first prove the stability result for a vehicle with a noncollocated center and sensor, followed by a discussion of a similar result for a collocated center and sensor. As we use the averaging method to prove stability of an error system, we also discuss the properties of the averaged error system. In particular, we explain the relation between the equilibrium of the averaged error system and the corresponding

solutions in physical space, the unstable solutions of the averaged error system, and the effect of the control parameter d.

3.4.1 Stability Theorem

We assume that the nonlinear map defining the distribution of the signal field is quadratic and takes the form $J = f(r_s) = f^* - q_r|r_s - r^*|^2$ where r^* is the unknown maximizer, $f^* = f(r^*)$ is the unknown maximum and q_r is an unknown positive constant. We define an output error variable

$$e = \frac{h}{s+h}[J] - f^* \tag{3.4}$$

which allows us to express ξ, the signal after the washout filter, as $\xi = \frac{s}{s+h}[J] = J - \frac{h}{s+h}[J] = J - f^* - e$, noting also that $\dot{e} = h\xi$.

Theorem 3.1 *Consider the following system*

$$\dot{r}_c = V_c \mathrm{e}^{j\theta} \tag{3.5}$$

$$\dot{\theta} = a\omega\cos(\omega t) + c\xi\sin(\omega t) - d\xi^2\sin(\omega t) \tag{3.6}$$

$$\dot{e} = h\xi \tag{3.7}$$

$$\xi = -(q_r|r_s - r^*|^2 + e) \tag{3.8}$$

$$r_s = r_c + R\mathrm{e}^{j\theta} \tag{3.9}$$

where $c, d, h, R, V_c, q_r > 0$*, the parameter* a *is chosen such that* $J_1(a), J_0(a), J_1(2a) > 0$*, the parameter* h *is chosen such that* $2V_cJ_0(a) > hR(2J_0(a) - J_1(2a)/J_1(a)$ *and where* $J_0(a)$ *and* $J_1(a)$ *are Bessel functions of the first kind. For sufficiently large* ω*, if the initial conditions* $r_c(0)$*,* $\theta(0)$*,* $e(0)$ *are such that the following quantities are sufficiently small,*

$$||r_c(0) - r^*| - \rho|\,, \qquad \left|e(0) + q_rR^2 + \tfrac{V_cJ_0(a)}{2cRJ_1(a)}\right|\,, \tag{3.10}$$

$$\textit{either } \left|\theta(0) - \arg(r_c(0) - r^*) + \tfrac{\pi}{2}\right| \textit{ or } \left|\theta(0) - \arg(r_c(0) - r^*) - \tfrac{\pi}{2}\right| \tag{3.11}$$

where

$$\rho = \sqrt{\frac{V_cJ_0(a)}{2cq_rRJ_1(a)}}\,, \tag{3.12}$$

then the trajectory of the vehicle center, $r_c(t)$, locally exponentially converges to, and remains in, the annulus

$$\rho - O\left(1/\omega\right) \leq |r_c - r^*| \leq \rho + O\left(1/\omega\right) \tag{3.13}$$

and the sensor reading $J(t)$ converges exponentially to a periodic function within $O(1/\omega)$ of

$$f^* - q_r R^2 - \frac{V_c J_0(a)}{2cRJ_1(a)}\,. \tag{3.14}$$

For the ease of interpreting the results, the reader is reminded that $J_1(a)/J_0(a) = a/2 + O(a^3)$.

Furthermore, the vehicle center locally exponentially converges to a solution of either the form

$$\begin{aligned} x_c^{\mathrm{attr}_1}(t) &= x^* - \left(\rho + \tilde{r}_\mu^{\mathrm{eq}_1} + \tilde{r}_{c_0}^{\frac{2\pi}{\omega}\,\mathrm{eq}_1}(t)\right) \\ &\quad \times \cos\left(\frac{V_c}{\rho}(1+\alpha_\mu^{\mathrm{eq}_1})t + \frac{V_c}{\rho}\beta_0^{\frac{2\pi}{\omega}\,\mathrm{eq}_1}(t) + \gamma^{\mathrm{eq}_1}\right) \qquad (3.15) \\ y_c^{\mathrm{attr}_1}(t) &= y^* + \left(\rho + \tilde{r}_\mu^{\mathrm{eq}_1} + \tilde{r}_{c_0}^{\frac{2\pi}{\omega}\,\mathrm{eq}_1}(t)\right) \\ &\quad \times \sin\left(\frac{V_c}{\rho}(1+\alpha_\mu^{\mathrm{eq}_1})t + \frac{V_c}{\rho}\beta_0^{\frac{2\pi}{\omega}\,\mathrm{eq}_1}(t) + \gamma^{\mathrm{eq}_1}\right) \qquad (3.16) \end{aligned}$$

or the form

$$\begin{aligned} x_c^{\mathrm{attr}_2}(t) &= x^* - \left(\rho + \tilde{r}_\mu^{\mathrm{eq}_2} + \tilde{r}_{c_0}^{\frac{2\pi}{\omega}\,\mathrm{eq}_2}(t)\right) \\ &\quad \times \cos\left(\frac{V_c}{\rho}(1+\alpha_\mu^{\mathrm{eq}_2})t + \frac{V_c}{\rho}\beta_0^{\frac{2\pi}{\omega}\,\mathrm{eq}_2}(t) + \gamma^{\mathrm{eq}_2}\right) \qquad (3.17) \\ y_c^{\mathrm{attr}_2}(t) &= y^* - \left(\rho + \tilde{r}_\mu^{\mathrm{eq}_2} + \tilde{r}_{c_0}^{\frac{2\pi}{\omega}\,\mathrm{eq}_2}(t)\right) \\ &\quad \times \sin\left(\frac{V_c}{\rho}(1+\alpha_\mu^{\mathrm{eq}_2})t + \frac{V_c}{\rho}\beta_0^{\frac{2\pi}{\omega}\,\mathrm{eq}_2}(t) + \gamma^{\mathrm{eq}_2}\right) \qquad (3.18) \end{aligned}$$

where $\tilde{r}_\mu^{\mathrm{eq}_i}$ is $O(1/\omega)$, $\tilde{r}_{c_0}^{\frac{2\pi}{\omega}\,\mathrm{eq}_i}(t)$ is periodic with frequency ω, is zero mean and is $O(1/\omega)$, $\alpha_\mu^{\mathrm{eq}_i}$ is $O(a^2)+O(1/\omega)$, $\beta_0^{\frac{2\pi}{\omega}\,\mathrm{eq}_i}(t)$ is periodic with frequency ω, is zero mean and is $O(a^2)+O(1/\omega)$, and γ^{eq_i} is a constant.

Proof: We start the proof by defining the shifted variables

$$\hat{r}_c = r_c - r^* \tag{3.19}$$
$$\hat{\theta} = \theta - a\sin(\omega t) \tag{3.20}$$
$$\tau = \omega t\,, \tag{3.21}$$

and a map between $\hat{r}_c$ and a new quantity θ^* given by

$$-\hat{r}_c = |\hat{r}_c|e^{j\theta^*} \tag{3.22}$$
$$\theta^* = -\frac{j}{2}\ln\left(-\frac{\hat{r}_c}{\bar{\hat{r}}_c}\right) = \arg(r^* - r_c)\,, \tag{3.23}$$

where θ^* represents the heading angle towards the source located at r^* when the vehicle is at r_c. Using these definitions, the expression for ξ is

$$\begin{aligned}\xi &= -\Big(q_r|r_c + Re^{j\theta} - r^*|^2 + e\Big)\\ &= -\Big(q_r|Re^{j\theta} + \hat{r}_c|^2 + e\Big)\\ &= -\Big(q_r\Big(R^2 + |\hat{r}_c|^2 - 2R|\hat{r}_c|\cos(\hat{\theta} - \theta^* + a\sin(\tau))\Big) + e\Big)\,.\end{aligned} \tag{3.24}$$

The dynamics of the shifted system are

$$\frac{d\hat{r}_c}{d\tau} = \frac{1}{\omega}\Big\{V_c e^{j(\hat{\theta} + a\sin(\tau)}\Big\} \tag{3.25}$$
$$\frac{d\hat{\theta}}{d\tau} = \frac{1}{\omega}(c - d\xi)\xi\sin(\tau) \tag{3.26}$$
$$\frac{de}{d\tau} = \frac{1}{\omega}h\xi\,. \tag{3.27}$$

We next define error variables $\tilde{r}_c$ and $\tilde{\theta}$ which represent the distance to the source, and the difference between the vehicle's heading and the optimal heading, respectively,

$$\tilde{r}_c = |\hat{r}_c| \tag{3.28}$$
$$\tilde{\theta} = \hat{\theta} - \theta^*\,. \tag{3.29}$$

The resulting dynamics for the error variables are

$$\begin{aligned}
\frac{d\tilde{r}_c}{d\tau} &= \frac{d|\hat{r}_c|}{d\tau} = \frac{d\sqrt{\hat{r}_c\bar{\hat{r}}_c}}{d\tau} = \frac{1}{2|\hat{r}_c|}\left(\frac{d\hat{r}_c}{d\tau}\bar{\hat{r}}_c + \hat{r}_c\frac{d\bar{\hat{r}}_c}{d\tau}\right) \\
&= -\frac{V_c}{\omega}\cos(\tilde{\theta} + a\sin(\tau)) \qquad (3.30) \\
\frac{d\tilde{\theta}}{d\tau} &= \frac{d\hat{\theta}}{d\tau} - \frac{d\theta^*}{d\tau} = \frac{d\hat{\theta}}{d\tau} + \frac{j}{2}\frac{1}{|\hat{r}_c|^2}\left(\frac{d\hat{r}_c}{d\tau}\bar{\hat{r}}_c - \hat{r}_c\frac{d\bar{\hat{r}}_c}{d\tau}\right) \\
&= \frac{1}{\omega}(c - d\xi)\xi\sin(\tau) + \frac{V_c}{\omega}\frac{\sin(\tilde{\theta} + a\sin(\tau))}{\tilde{r}_c} \qquad (3.31) \\
\frac{de}{d\tau} &= \frac{1}{\omega}h\xi \qquad (3.32) \\
\xi &= -\Big(q_r\Big(R^2 + \tilde{r}_c^2 - 2R\tilde{r}_c\cos(\tilde{\theta} + a\sin(\tau))\Big) + e\Big). \qquad (3.33)
\end{aligned}$$

Note that going from the previous shifted system (3.25)–(3.27) to the error system (3.30)–(3.32) involves moving from a four state system to a three state system by replacing the complex valued $\hat{r}_c$ by its real valued modulus $\tilde{r}_c$ and combining the heading of the vehicle θ and the optimal heading of the vehicle θ^* into their difference $\tilde{\theta}$.

As the system equations are periodic in 2π, the average error system[1] is

$$\begin{aligned}
\frac{d\tilde{r}_c^{\text{ave}}}{d\tau} &= -\frac{V_c J_0(a)}{\omega}\cos(\tilde{\theta}^{\text{ave}}) \qquad (3.34) \\
\frac{d\tilde{\theta}^{\text{ave}}}{d\tau} &= \frac{1}{\omega}\sin(\tilde{\theta}^{\text{ave}})\left\{\frac{V_c J_0(a)}{\tilde{r}_c^{\text{ave}}} - 2q_r R J_1(a)\tilde{r}_c^{\text{ave}}\left(c + 2d\left(q_r(R^2 + \tilde{r}_c^{\text{ave}^2}) + e^{\text{ave}}\right)\right)\right\} \\
&\quad + \frac{1}{\omega}2dq_r^2R^2\tilde{r}_c^{\text{ave}^2}J_1(2a)\sin(2\tilde{\theta}^{\text{ave}}) \qquad (3.35) \\
\frac{de^{\text{ave}}}{d\tau} &= \frac{h}{\omega}\left(2q_rR\tilde{r}_c^{\text{ave}}J_0(a)\cos(\tilde{\theta}^{\text{ave}}) - q_rR^2 - q_r\tilde{r}_c^{\text{ave}^2} - e^{\text{ave}}\right). \qquad (3.36)
\end{aligned}$$

The average error system (3.34)–(3.36) has two equilibria defined by

$$\begin{aligned}
\left[\tilde{r}_c^{\text{ave}^{\text{eq}_1}}, \tilde{\theta}^{\text{ave}^{\text{eq}_1}}, e^{\text{ave}^{\text{eq}_1}}\right] &= \left[\rho, +\frac{\pi}{2}, -q_r(R^2 + \rho^2)\right] \qquad (3.37) \\
\left[\tilde{r}_c^{\text{ave}^{\text{eq}_2}}, \tilde{\theta}^{\text{ave}^{\text{eq}_2}}, e^{\text{ave}^{\text{eq}_2}}\right] &= \left[\rho, -\frac{\pi}{2}, -q_r(R^2 + \rho^2)\right]. \qquad (3.38)
\end{aligned}$$

[1] During the calculations for the average system we use Bessel integral equalities $\frac{1}{2\pi}\int_0^{2\pi} \mathrm{e}^{ja\sin(t)}dt = J_0(a)$ and $\frac{1}{2\pi}\int_0^{2\pi} \mathrm{e}^{ja\sin(t)}\sin(t)dt = J_1(a)$ which can be derived from Taylor series approximations and are also found in [4].

The two equilibria (3.37) and (3.38) have the corresponding Jacobians

$$A^{\text{eq}_1} = -\frac{1}{\omega}\begin{bmatrix} 0 & -V_c J_0(a) & 0 \\ 4\gamma J_1(a)(c+2dq_r\rho^2) & 4d\gamma^2 J_1(2a)\rho^2 & 4d\gamma J_1(a)\rho^2 \\ 2hq_r\rho & 2h\gamma J_0(a)\rho & h \end{bmatrix} \tag{3.39}$$

and

$$A^{\text{eq}_2} = \frac{1}{\omega}\begin{bmatrix} 0 & -V_c J_0(a) & 0 \\ 4\gamma J_1(a)(c+2dq_r\rho^2) & -4d\gamma^2 J_1(2a)\rho^2 & 4d\gamma J_1(a)\rho^2 \\ -2hq_r\rho & 2h\gamma J_0(a)\rho & -h \end{bmatrix} \tag{3.40}$$

where $\gamma = q_r R$. The characteristic polynomial for both Jacobians is

$$\begin{aligned} 0 = {} & (\omega s)^3 + h(\omega s)^2 + \frac{2V_c^2 J_0(a)^2}{\rho^2}\omega s + h\frac{2V_c^2 J_0(a)^2}{\rho^2} \\ & +4d\rho^2 q_r^2 R\Bigg(RJ_1(2a)(\omega s)^2 + \Big(2V_c J_0(a)J_1(a) \\ & +hR\Big(J_1(2a) - 2J_0(a)J_1(a)\Big)\Big)\Big(\omega s\Big)\Bigg). \end{aligned} \tag{3.41}$$

According to the Routh-Hurwitz criterion, to guarantee that the roots of the polynomial have negative real parts, each coefficient must be greater than zero and the product of the s^2 and s^1 coefficients must be greater than the s^0 coefficient. The first criterion is satisfied by the assumptions in Theorem 3.1. In addition, given these assumptions, the product of the s^2 and s^1 coefficients minus the s^0 coefficient is $\Big(d4\rho^2 q_r^2 R^2 J_1(2a)\Big)\Big(\frac{2V_c^2 J_0(a)^2}{\omega^3\rho^2}\Big)$ plus a nonnegative term. As this difference is always positive, the second criterion is also satisfied. Therefore the Jacobians (3.39) and (3.40) are Hurwitz given the assumptions in Theorem 3.1. As such, both equilibria (3.37) and (3.38) are exponentially stable. By applying Theorem 10.4 from [40] to this result, we conclude that the error system (3.30)–(3.32) has two distinct, exponentially stable periodic solutions within $O(1/\omega)$ of the equilibria (3.37) and (3.38) defined by

$$\tilde{r}_c^{\text{attr}_i}(\tau) = \rho + \tilde{r}_c^{2\pi^{\text{eq}_i}}(\tau) \tag{3.42}$$

$$\tilde{\theta}^{\text{attr}_i}(\tau) = (-1)^{(i-1)}\frac{\pi}{2} + \tilde{\theta}^{2\pi^{\text{eq}_i}}(\tau) \tag{3.43}$$

$$e^{\text{attr}_i}(\tau) = -q_r(R^2+\rho^2) + e^{2\pi^{\text{eq}_i}}(\tau) \tag{3.44}$$

for $i \in \{1,2\}$ where $\tilde{r}_c^{2\pi^{\mathrm{eq}_i}}(\tau)$, $\tilde{\theta}^{2\pi^{\mathrm{eq}_i}}(\tau)$, $e^{2\pi^{\mathrm{eq}_i}}(\tau)$ are periodic with period 2π and are $O(1/\omega)$. This indicates that the distance between the vehicle center r_c and the source r^* converges to within $O(1/\omega)$ of the value $\rho = \sqrt{\frac{V_c J_0(a)}{2cq_r RJ_1(a)}}$, defining the annulus in Theorem 3.1. As the attractive solution of e is a periodic function within $O(1/\omega)$ of $-q_r R^2 - \frac{V_c J_0(a)}{2cRJ_1(a)}$, the sensor reading $J(t)$ converges to a periodic function within $O(1/\omega)$ of $f^* - q_r R^2 - \frac{V_c J_0(a)}{2cRJ_1(a)}$. To prove the last part of the theorem, we first note that, while the error system (3.30)–(3.30) has three states, the (shifted) physical system from which the error system was derived has four, the complex valued $\hat{r}$ and the real valued $\hat{\theta}$ and e. To study the attractive solutions of $\hat{r}_c$, and thus x_c and y_c, we recall $\hat{r}_c = -\tilde{r}_c \exp^{j\theta^*}$ and thus we start by determining first the θ^* part of the attractor solution from

$$\frac{d\theta^*}{d\tau} = -\frac{V_c}{\omega}\frac{\sin(\tilde{\theta} + a\sin(\tau))}{\tilde{r}_c}. \tag{3.45}$$

We substitute the attractor solution (3.42)–(3.44) of the error system[2] and find

$$\begin{aligned}
\frac{d\theta^{*^{\mathrm{attr}_1}}}{d\tau} &= -\frac{V_c}{\omega}\frac{\sin(\frac{\pi}{2} + \tilde{\theta}^{2\pi^{\mathrm{eq}_1}}(\tau) + a\sin(\tau))}{\rho + \tilde{r}_c^{2\pi^{\mathrm{eq}_1}}(\tau)} && (3.46)\\
&= -\frac{1}{\omega}\frac{V_c}{\rho}\left(1 + \left(\cos\left(\tilde{\theta}^{2\pi^{\mathrm{eq}_1}}(\tau) + a\sin(\tau)\right) - 1\right)\right)\left(1 - \frac{\tilde{r}_c^{2\pi^{\mathrm{eq}_1}}}{\rho + \tilde{r}_c^{2\pi^{\mathrm{eq}_1}}}\right) && (3.47)\\
&= -\frac{1}{\omega}\frac{V_c}{\rho}\left(1 + \left(\cos\left(\tilde{\theta}^{2\pi^{\mathrm{eq}_1}}(\tau) + a\sin(\tau)\right) - 1\right) - \frac{\tilde{r}_c^{2\pi^{\mathrm{eq}_1}}}{\rho + \tilde{r}_c^{2\pi^{\mathrm{eq}_1}}}\right.\\
&\quad \left. -\frac{\tilde{r}_c^{2\pi^{\mathrm{eq}_1}}}{\rho + \tilde{r}_c^{2\pi^{\mathrm{eq}_1}}}\left(\cos\left(\tilde{\theta}^{2\pi^{\mathrm{eq}_1}}(\tau) + a\sin(\tau)\right) - 1\right)\right) && (3.48)\\
&= -\frac{1}{\omega}\frac{V_c}{\rho}\left(1 + \alpha^{2\pi^{\mathrm{eq}_1}}(\tau)\right) && (3.49)
\end{aligned}$$

where

$$\begin{aligned}
\alpha^{2\pi^{\mathrm{eq}_1}}(\tau) &= -2\sin^2\left(\frac{\tilde{\theta}^{2\pi^{\mathrm{eq}_1}}(\tau) + a\sin(\tau)}{2}\right)\\
&\quad -\frac{\tilde{r}_c^{2\pi^{\mathrm{eq}_1}}}{\rho + \tilde{r}_c^{2\pi^{\mathrm{eq}_1}}}\cos\left(\tilde{\theta}^{2\pi^{\mathrm{eq}_1}}(\tau) + a\sin(\tau)\right) && (3.50)
\end{aligned}$$

[2]We substitute only the solution around the first equilibrium (3.37) as the derivation with the use of the other solution is nearly identical.

is a periodic function with period 2π and is $O\Big(\Big(O(1/\omega)+a\Big)^2\Big)+O(1/\omega)=O(a^2)+O(1/\omega)$. Therefore

$$\begin{aligned}
\theta^{*\text{attr}_1}(t) &= -\int_0^t \frac{V_c}{\rho}d\hat{t} - \frac{V_c}{\rho}\int_0^t \alpha^{\frac{2\pi}{\omega}\text{eq}_1}(\hat{t})d\hat{t} - \gamma^{\text{eq}_1} && (3.51)\\
&= -\frac{V_c}{\rho}t - \frac{V_c}{\rho}\int_0^t \alpha^{\frac{2\pi}{\omega}\text{eq}_1}(\hat{t})d\hat{t} - \gamma^{\text{eq}_1} && (3.52)\\
&= -\frac{V_c}{\rho}t - \frac{V_c}{\rho}\int_0^t \Big(\alpha_\mu^{\text{eq}_1} + \alpha_0^{\frac{2\pi}{\omega}\text{eq}_1}(\hat{t})\Big)d\hat{t} - \gamma^{\text{eq}_1} && (3.53)\\
&= -\frac{V_c}{\rho}(1+\alpha_\mu^{\text{eq}_1})t - \frac{V_c}{\rho}\beta_0^{\frac{2\pi}{\omega}\text{eq}_1}(t) - \gamma^{\text{eq}_1} && (3.54)
\end{aligned}$$

where γ^{eq_1} is a constant, $\alpha_\mu^{\text{eq}_1} = \frac{1}{2\pi}\int_0^{2\pi}\alpha^{2\pi\text{eq}_1}(\tau)d\tau$ is the mean of $\alpha^{\frac{2\pi}{\omega}\text{eq}_1}(t)$ and is $O(a^2)+O(1/\omega)$, $\alpha_0^{\frac{2\pi}{\omega}\text{eq}_1}(t) = \alpha^{\frac{2\pi}{\omega}\text{eq}_1}(t) - \alpha_\mu^{\text{eq}_1}$ is the zero-mean part of $\alpha^{\frac{2\pi}{\omega}\text{eq}_1}(t)$, and $\beta_0^{\frac{2\pi}{\omega}\text{eq}_1}(t)$ is the integral of $\alpha_0^{\frac{2\pi}{\omega}\text{eq}_1}(t)$, is periodic with frequency ω and is zero mean. Both $\alpha_0^{\frac{2\pi}{\omega}\text{eq}_1}(t)$ and $\beta_0^{\frac{2\pi}{\omega}\text{eq}_1}(t)$ are $O(a^2)+O(1/\omega)$. The corresponding solution to the movement of the vehicle center $\hat{r}_c(t)$ is

$$\hat{r}_c^{\text{attr}_1}(t) = -(\rho + r_\mu^{\text{eq}_1} + \tilde{r}_{c0}^{\frac{2\pi}{\omega}\text{eq}_1}(t))\exp^{j\left(-\frac{V_c}{\rho}(1+\alpha_\mu^{\text{eq}_1})t - \frac{V_c}{\rho}\beta_0^{\frac{2\pi}{\omega}\text{eq}_1}(t) - \gamma^{\text{eq}_1}\right)} \quad (3.55)$$

where $r_\mu = \frac{1}{2\pi}\int_0^{2\pi}\tilde{r}^{2\pi\text{eq}_1}(\tau)d\tau$ is the mean of $\tilde{r}_c^{\frac{2\pi}{\omega}\text{eq}_1}(t)$ and is $O(1/\omega)$, $\tilde{r}_{c0}^{\frac{2\pi}{\omega}\text{eq}_1}(t) = \tilde{r}_c^{\frac{2\pi}{\omega}\text{eq}_1} - r_\mu^{\text{eq}_1}$ is zero mean and $O(1/\omega)$. As $x_c + jy_c = r^* + \hat{r}_c$ the attractive solutions noted in (3.42)–(3.44) are derived from (3.55). ■

Simulations: Figure 3.4 depicts four trajectories of the center of a vehicle starting from two different initial positions. The source produces a map with circular level sets. In all cases the vehicle converges to an annulus that encircles the source. The difference in the convergence of the trajectories to the annulus is due to the value of the d parameter. The radius of the convergent annulus is about 0.14 which corresponds to estimated ρ value of 0.1392. Even though our main theorem is for maps with circular level sets, the same source seeking scheme works well also for maps with elliptical level sets, as shown in Figure 3.5. As in the case of circular level sets, the d value affects the solution to which the vehicle will be attracted. In the case of circular level sets, the value of d affects whether the vehicle ultimatly goes clockwise or counter clockwise around the source. However, unlike the case of the circular level sets, the d value affects both the shape and number of attractors. More details can be found in Section 3.6.

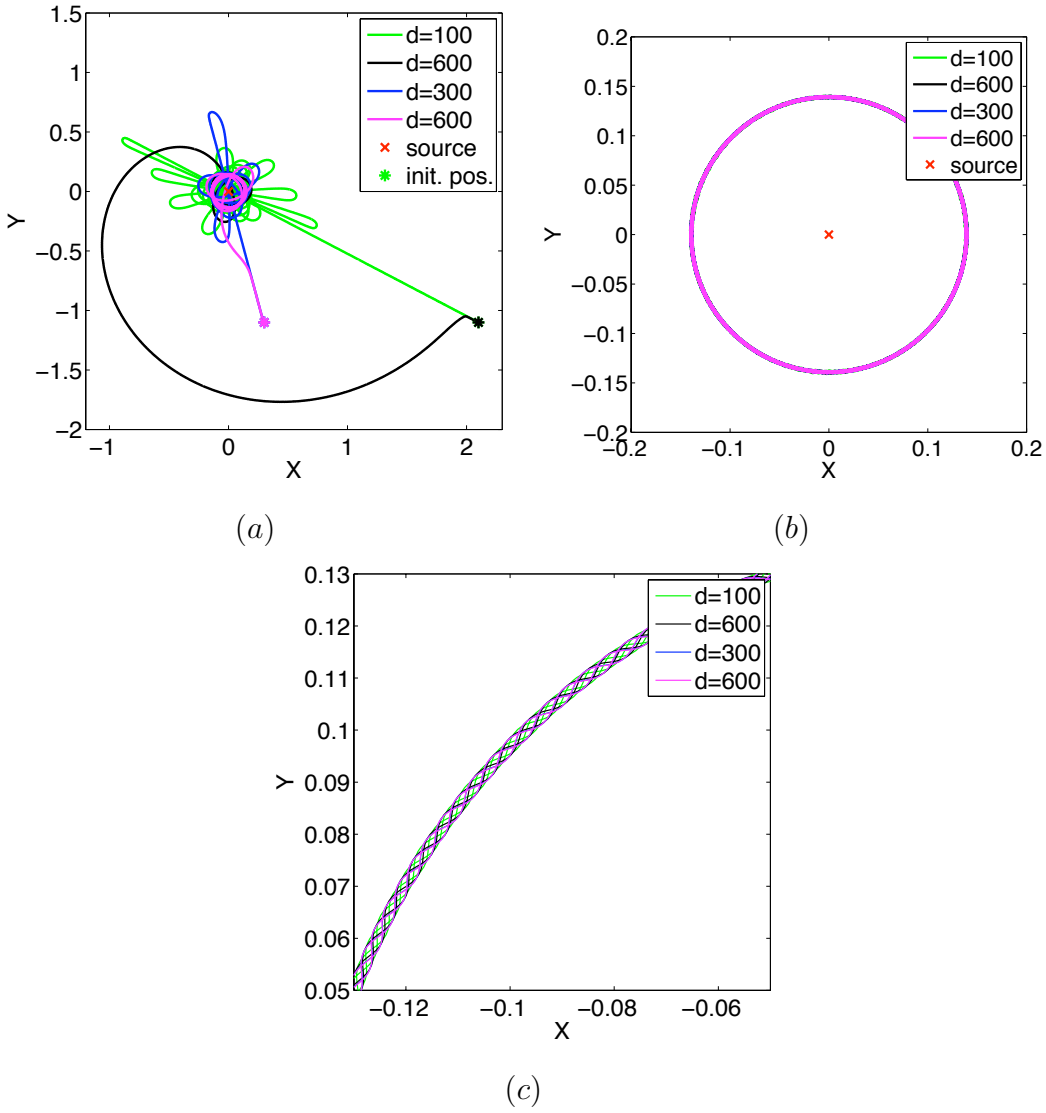

Figure 3.4: Source emits a signal with circular level sets.
(a) Four trajectories of the vehicle center are shown starting from two different initial conditions. All trajectories converge to the annulus shown in (b). The sinusoidal path that the vehicle center follows is clearly seen in the close up (c). For all simulations $V_c = 0.1, c = 100, a = 0.5, \omega = 40, R = 0.1, h = 1, f^* = 0, q_r = 1$.

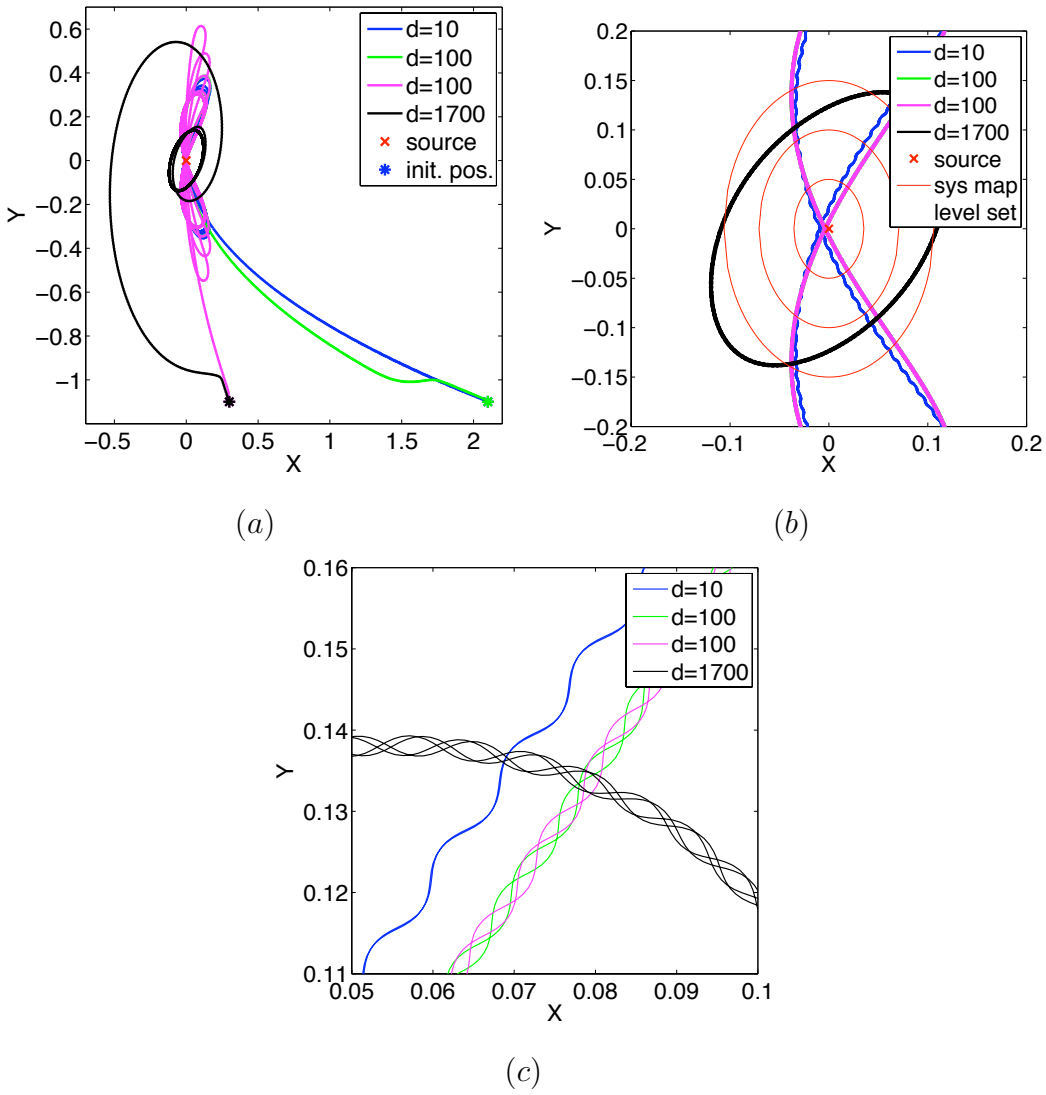

Figure 3.5: Source with elliptical level sets.
(a) Four trajectories of the vehicle center are shown starting from different initial conditions. The trajectories converge to either of the two attractors shown in (b) (The other two attractors of the system are the mirror images of the two shown). The sinusoidal path of the vehicle center is seen in the zoomed in (c). Increases in the value of d cause the change in the shape of the attractor from twisted figure eight to rotated ellipse. For all simulations $V_c = 0.1$, $c = 100$, $a = 0.5$, $\omega = 40$, $R = 0.1$, $h = 1$, $f^* = 0$, $q_r = 1.5$, $q_p = 0.25$.

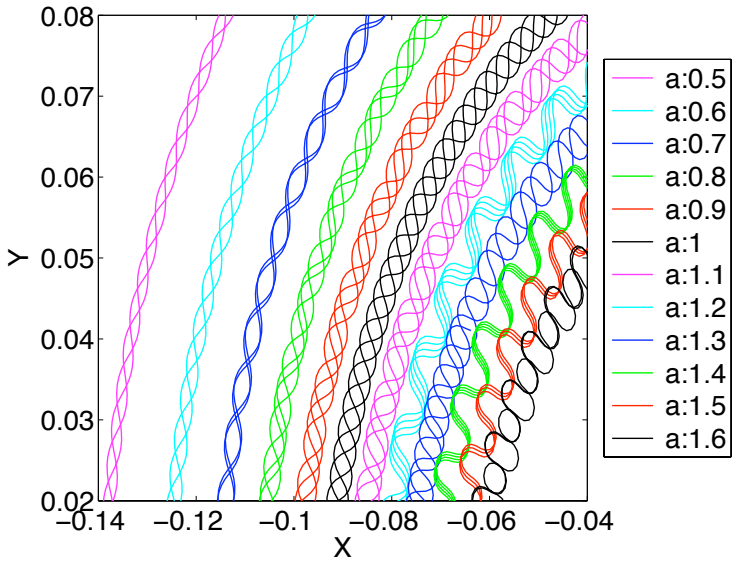

Figure 3.6: Effect of the parameter a on the motion of the vehicle center. The vehicle center makes sharper and more pronounced turns when it moves along the attractor as the parameter a is increased. The radius of the attractor ρ also decreases slightly. The other simulation parameters are $V_c = -.1, c = 100, d = 600, \omega = 40, R = 0.1, h = 1. f^* = 0, q_r = 1$.

The a parameter, which governs the amplitude of the probing signal, has a subtle effect on the motion of the center. While increasing a makes the sensor swing wider, it does not have such a dramatic effect on the center movement. A higher a results in a slightly smaller attractor radius ρ and causes the vehicle center to make sharper and more pronounced turns instead of gently swaying while moving forward as seen in Figure 3.6.

Remark 3.1: Figure 3.4 clearly displays two distinct behaviors of the source seeking scheme. For large d the vehicle undergoes a "roundabout" transient but settles quickly into the residual annulus. For smaller values of d the vehicle goes straight to the source but overshoots it many times before settling into the residual annulus. The overshoot is the result of being "too good" at turning the vehicle towards the source and of being constrained to maintain a positive velocity V_c (as in aircraft). The trade-off between the two types of behavior indicate that the user can employ the scheme in two ways: with low d for "chase/pursuit" tasks and with d large for

"hovering/coverage/surveillance" tasks.

Remark 3.2: Based on the last statement of Theorem 3.1, the attractive solutions to the physical system, derived from the stable solutions of the error system, have two competing frequencies. The first frequency, (in the t time variable), is ω and comes from the averaging analysis of the error system and perturbs both the amplitude and phase of $\hat{r}_c$. The second frequency comes from the dominant term in the time-varying part of the exponent of $\hat{r}_c(t)$, $\frac{V_c}{\rho}(1+\alpha_\mu^{\mathrm{eq_i}})$ and drives the vehicle around the attractive annulus. As $\rho = \sqrt{\frac{V_c J_0(a)}{2cq_r R J_1(a)}}$ consists of the square root of the product of Bessel functions and other gains, including q_r which the designer has no control over, it is highly likely that ρ is irrational. Thus it is also highly likely that ω, which the designer does have control over, and $\frac{V_c}{\rho}(1+\alpha_\mu^{\mathrm{eq_i}})$ are incommensurate and therefore the attractive solution of the physical system, though it remains within a bounded annulus centered around the source, is not a periodic orbit.[3]

3.4.2 Collocated Sensor

One of the assumptions of Theorem 3.1 requires R to be strictly positive. This rules out the possibility of a sensor collocated with the vehicle center. However, when the washout filter's time constant is sufficiently small, as in Figure 3.7, namely when the washout filter acts approximately as a differentiator, the scheme retains the same stability properties of the previous scenario with a non-collocated sensor. As we shall see in simulations, the price to be paid for collocating the vehicle's sensor and center is that the vehicle needs to be capable of making much sharper turns.

Theorem 3.2 *Consider the following system*

$$\dot{r}_c = V_c \mathrm{e}^{j\theta} \tag{3.56}$$

$$\dot{\theta} = a\omega\cos(\omega t) + c\xi\sin(\omega t) - d\xi^2\sin(\omega t) \tag{3.57}$$

$$\epsilon\dot{\xi} = -\xi - q_r V_c\left((\bar{r}_c - \bar{r}^*)\exp^{j\theta} + (r_c - r^*)\exp^{-j\theta}\right) \tag{3.58}$$

$$J = f^* - q_r|r_c - r^*|^2 \tag{3.59}$$

[3]We use the term highly likely as the set of rational numbers is countable rendering it a null set in the sense of Lebesgue measure in $\mathbb{R}$.

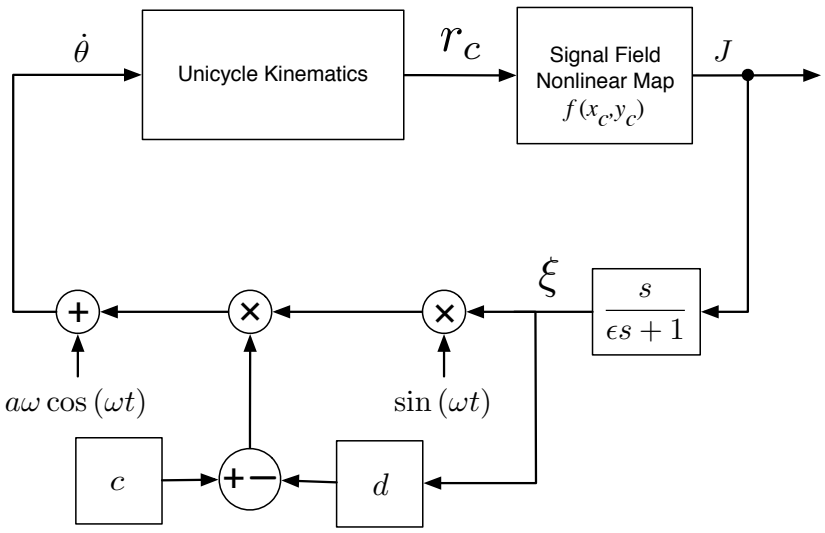

Figure 3.7: Block diagram of source seeking via tuning of angular velocity when the sensor is collocated with the vehicle center.

where $c, d, V_c, q_r > 0$ *and the parameter* a *is chosen such that* $J_1(a), J_0(a), J_1(2a) > 0$. *For sufficiently large* ω *and sufficiently small* $\epsilon \ll 1/\omega$, *if the initial conditions* $r_c(0)$, $\theta(0)$, ξ *are such that the following quantities are sufficiently small*

$$\left| |r_c(0) - r^*| - \rho_J \right|, \qquad |\xi(0)|$$

$$\textit{either } \left|\theta(0) - \arg(r_c(0) - r^*) + \tfrac{\pi}{2}\right| \textit{ or } \left|\theta(0) - \arg(r_c(0) - r^*) - \tfrac{\pi}{2}\right|$$

where

$$\rho_J \;=\; \sqrt{\frac{J_0(a)}{2J_1(a)cq_r}},$$

then the trajectory of the vehicle center $r_c(t)$ *locally exponentially converges to, and remains in, the annulus*

$$\rho_J - O\left(1/\omega\right) - O\left(\epsilon\right) \leq |r_c - r^*| \leq \rho_J + O\left(1/\omega\right) + O\left(\epsilon\right) .$$

and the sensor reading $J(t)$ *locally exponentially converges to a periodic function within* $O(1/\omega) + O(\epsilon)$ *of*

$$f^* - \frac{J_0(a)}{2cJ_1(a)} .$$

Proof: We proceed as in 3.4.1 by shifting the variables as in (3.19)–(3.21) and employing the error variables (3.28), (3.29). The equations of motion for the error system are

$$\begin{aligned}
\frac{d\tilde{r}_c}{d\tau} &= -\frac{V_c}{\omega}\cos(\tilde{\theta} + a\sin(\tau)) && (3.60)\\
\frac{d\tilde{\theta}}{d\tau} &= c\xi\sin(\tau) - d\xi^2\sin(\tau) + \frac{V_c}{\omega}\frac{\sin(\tilde{\theta} + a\sin(\tau))}{\tilde{r}_c} && (3.61)\\
\epsilon\frac{d\xi}{d\tau} &= -\xi + \frac{2V_c q_r}{\omega}\tilde{r}_c\cos(\tilde{\theta} + a\sin(\tau))\,. && (3.62)
\end{aligned}$$

When ϵ is sufficiently small we can apply the singular perturbation method. We define the quasi-steady state

$$\xi^{\mathrm{qs}} = \frac{2V_c q_r}{\omega}\tilde{r}_c\cos(\tilde{\theta} + a\sin(\tau))\,, \qquad (3.63)$$

the reduced model

$$\begin{aligned}
\frac{d\tilde{r}_c^{\mathrm{red}}}{d\tau} &= -\frac{V_c}{\omega}\cos(\tilde{\theta}^{\mathrm{red}} + a\sin(\tau)) && (3.64)\\
\frac{d\tilde{\theta}^{\mathrm{red}}}{d\tau} &= \frac{2V_c c q_r}{\omega}\tilde{r}_c^{\mathrm{red}}\cos(\tilde{\theta}^{\mathrm{red}} + a\sin(\tau))\sin(\tau)\\
&\quad -\frac{4V_c^2 d q_r^2}{\omega}\tilde{r}_c^{\mathrm{red}^2}\cos^2(\tilde{\theta}^{\mathrm{red}} + a\sin(\tau))\sin(\tau) + \frac{V_c}{\omega}\frac{\sin(\tilde{\theta}^{\mathrm{red}} + a\sin(\tau))}{\tilde{r}_c^{\mathrm{red}}}\,, && (3.65)
\end{aligned}$$

and the boundary layer model

$$\frac{d\xi^{\mathrm{bl}}}{d\tilde{\tau}} = -\xi^{\mathrm{bl}}\,. \qquad (3.66)$$

We see that the origin is an exponentially stable equilibrium of the boundary layer. The use of averaging shows that the reduced model has an exponentially stable periodic solution. The averaged reduced model of the error system is

$$\begin{aligned}
\frac{d\tilde{r}_c^{\mathrm{red-ave}}}{d\tau} &= -\frac{V_c J_0(a)}{\omega}\cos(\tilde{\theta}^{\mathrm{red-ave}}) && (3.67)\\
\frac{d\tilde{\theta}^{\mathrm{red-ave}}}{d\tau} &= \frac{V_c}{\omega}\sin(\tilde{\theta}^{\mathrm{red-ave}})\Big(\frac{J_0(a)}{\tilde{r}_c^{\mathrm{red-ave}}} - 2J_1(a)cq_r\tilde{r}_c^{\mathrm{red-ave}}\Big)\\
&\quad + \frac{2V_c^2 J_1(2a)dq_r^2}{\omega}\tilde{r}_c^{\mathrm{red-ave}^2}\sin(2\tilde{\theta}^{\mathrm{red-ave}})\,. && (3.68)
\end{aligned}$$

The equilibria of (3.67), (3.68), similarly to the equilibria, (3.37), (3.38) of the system (3.34)–(3.36) are

$$\left[\tilde{r}_c^{\text{red}-\text{ave}^{\text{eq}_1}}, \tilde{\theta}^{\text{red}-\text{ave}^{\text{eq}_1}}\right] = \left[\sqrt{\frac{J_0(a)}{2J_1(a)cq_r}}, \frac{\pi}{2}\right] \tag{3.69}$$

$$\left[\tilde{r}_c^{\text{red}-\text{ave}^{\text{eq}_2}}, \tilde{\theta}^{\text{red}-\text{ave}^{\text{eq}_2}}\right] = \left[\sqrt{\frac{J_0(a)}{2J_1(a)cq_r}}, -\frac{\pi}{2}\right]. \tag{3.70}$$

The Jacobians which correspond to (3.69), (3.70) are

$$A^{\text{eq}_1} = \frac{V_c}{\omega}\begin{bmatrix} 0 & J_0(a) \\ -4J_1(a)cq_r & -\frac{V_cJ_1(2a)J_0(a)dq_r}{J_1(a)c} \end{bmatrix} \tag{3.71}$$

$$A^{\text{eq}_2} = \frac{V_c}{\omega}\begin{bmatrix} 0 & -J_0(a) \\ 4J_1(a)cq_r & -\frac{V_cJ_1(2a)J_0(a)dq_r}{J_1(a)c} \end{bmatrix}. \tag{3.72}$$

Also similarly to the noncollocated case, the characteristic polynomial is the same for both Jacobians

$$s^2 + \frac{V_c}{\omega}\frac{V_cJ_1(2a)J_0(a)dq_r}{J_1(a)c}s + \left(\frac{V_c}{\omega}\right)^2 4J_0(a)J_1(a)cq_r\,. \tag{3.73}$$

This polynomial produces stable eigenvalues as the coefficients are both positive according to the assumptions. As both Jacobians are Hurwitz, both equilibria (3.69) and (3.70) are exponentially stable. Using the same reasoning as in 3.4.1, we conclude that, for sufficiently large ω, the reduced model of the error system (3.60)–(3.62) has two distinct, exponentially stable periodic solutions within $O(1/\omega)$ of the equilibria (3.69) and (3.70). By using the same method in the nonlinear system section of [5] to shift the system about these solutions and noting that the boundary layer is also exponentially stable we conclude that, for sufficiently small ϵ, the full error system has two distinct, exponentially stable periodic solutions within $O(1/\omega) + O(\epsilon)$ of the equilibria (3.69) and (3.70). This indicates that the distance between the vehicle center r_c and the source r^* converges to within $O(1/\omega) + O(\epsilon)$ of the value $\rho_J = \sqrt{\frac{J_0(a)}{2J_1(a)cq_r}}$, defining the annulus in Theorem 3.2. ■

Remark 3.3: Note that the convergence rate of the system depends on the roots of the characteristic polynomial of the Jacobian of the average system. The best time response of the system is achieved when the system is critically damped, i.e.

when $d = \frac{4}{V_c J_1(2a)} \sqrt{\frac{J_1^3(a)c^3}{J_0(a)q_r}}$ and both roots are $s_{1,2} = -2\frac{V_c}{\omega}\sqrt{J_0(a)J_1(a)cq_r}$. This gives a convergence rate of $\mathrm{e}^{-2V_c\sqrt{J_0(a)J_1(a)cq_r}\,t}$.[4] This "best decay rate" can be understood as a performance limit. However, as this rate and the corresponding value of d both depend on q_r, (which is unknown), one cannot provide an exact recipe for the best parameter choices. Even so, based on the above discussion, we can say that sharp signal fields (high q_r) improve the convergence rate, as well as high forward velocity V_c, high gain c, and to some extent a unity probing amplitude a. The optimal damping gain d grows with c but decays with V_c and q_r.

Simulations: Figure 3.8 shows the trajectory of a vehicle with a sensor collocated on the vehicle center. The washout filter approximates $\dot{J}$. As in the case of a non-collocated sensor, the vehicle converges to an annulus around the source. However, the motion of the vehicle center differs. With a collocated center and sensor, the entire vehicle needs to be employed in the probing of the field instead of the tip of the vehicle alone. This leads to the"lawn mowing" pattern seen in the figure. Lower values of the parameter c can certainly lessen this pattern, however it will always be evident to some extent given the necessity of some sort of probing.

3.4.3 Unstable Solutions

Having discussed the (locally) attractive solutions of the closed-loop system, we now discuss its unstable solutions. The existence of unstable solutions is seen in Figure 3.9. It shows trajectories stemming from a very small initial orientation interval. While moving through this interval, the trajectories switch from turning to the right to turning to the left. This indicates that there is some theoretical initial orientation (though not possible in a digital computer) that result in the vehicle never turning around. It is also indicated in the fact that the $(\tilde{r}_c, \tilde{\theta}, e)$ average error system has two distinct equilibria, both of which are exponentially stable. The regions of attraction of these equilibria are separated by two separatrices, $\tilde{\theta}^{\text{ave}} = 0$ and $\tilde{\theta}^{\text{ave}} = \pi$, which define the following (unstable) solutions of the averaged error

[4]Note that we went from the τ time scale back to the $t = \tau/\omega$ timescale.

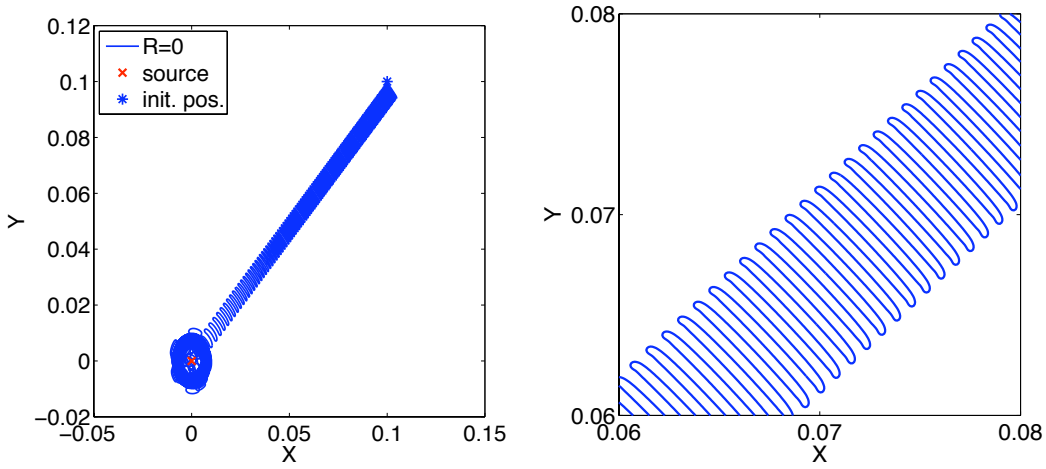

(a) (b)

Figure 3.8: A simulation with a collocated sensor ($R = 0$) and $\epsilon = .001$. (a) The trajectory of the vehicle center converges to an annulus around the source (at the origin). (b) A zoomed in section of the vehicle trajetory, displaying the vehicle motion more clearly. The other simulation parameters are $V_c = 0.1, c = 10^5, d = 10, a = 0.5, \omega = 40, f^* = 0, q_r = 1$.

system (3.34)–(3.36):

$$\tilde{\theta}^{\text{ave}}(\tau) = 0 \tag{3.74}$$

$$\tilde{r}_c^{\text{ave}}(\tau) = \tilde{r}_c^{\text{ave}}(0) - \frac{V_c J_0(a)}{\omega}\tau \tag{3.75}$$

$$\begin{aligned} e^{\text{ave}}(\tau) = {} & 2q_r\left(\tilde{r}_c^{\text{ave}}(0)RJ_0(a) - \frac{R^2 + \tilde{r}_c^{\text{ave}^2}}{2} - \frac{V_c J_0(a)}{h}\left(\tilde{r}_c^{\text{ave}}(0) - RJ_0(a)\right)\right. \\ & \left. - \frac{V_c^2 J_0^2(a)}{h^2}\right)\left(1 - \mathrm{e}^{-\frac{h}{\omega}\tau}\right) \\ & + \frac{2q_r V_c J_0(a)}{\omega}\left(\tilde{r}_c^{\text{ave}}(0) - RJ_0(a) + \frac{V_c J_0(a)}{h}\right)\tau - \frac{q_r V_c^2 J_0^2(a)}{\omega^2}\tau^2 \\ & + e^{\text{ave}}(0)\mathrm{e}^{-\frac{h}{\omega}\tau} \end{aligned} \tag{3.76}$$

and

$$\tilde{\theta}^{\text{ave}}(\tau) = \pi \tag{3.77}$$

$$\tilde{r}_c^{\text{ave}}(\tau) = \tilde{r}_c^{\text{ave}}(0) + \frac{V_c J_0(a)}{\omega}\tau \tag{3.78}$$

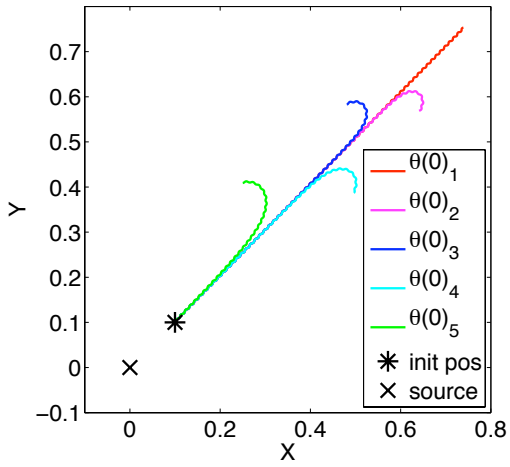

Figure 3.9: An unstable solution.
Five trajectories are shown starting from the same initial position but each with a slightly different initial orientation ranging from $\theta(0)_4 = .9335$ to $\theta(0)_5 = .9436$. They each turn around at some time t. In simulations, numerical error always induces a turn. However, in theory, there does exist a solution which goes to infinity. The simulation parameters are $V_c = 0.1, c = 100, d = 0, a = 0.5, \omega = 40, R = 0.1, h = 1, f^* = 0, q_r = 1$.

$$\begin{aligned} e^{\text{ave}}(\tau) &= 2q_r\left(\tilde{r}_c^{\text{ave}}(0)RJ_0(a) + \frac{R^2 + \tilde{r}_c^{\text{ave}^2}}{2} - \frac{V_cJ_0(a)}{h}\left(\tilde{r}_c^{\text{ave}}(0) + RJ_0(a)\right)\right. \\ &\quad \left. + \frac{V_c^2J_0^2(a)}{h^2}\right)\left(\mathrm{e}^{-\frac{h}{\omega}\tau} - 1\right) \\ &\quad - \frac{2q_rV_cJ_0(a)}{\omega}\left(\tilde{r}_c^{\text{ave}}(0) + RJ_0(a) - \frac{V_cJ_0(a)}{h}\right)\tau - \frac{q_rV_c^2J_0^2(a)}{\omega^2}\tau^2 \\ &\quad + e^{\text{ave}}(0)\mathrm{e}^{-\frac{h}{\omega}\tau}\,. \end{aligned} \tag{3.79}$$

These separatrices $\tilde{\theta}^{\text{ave}} = 0$ and $\tilde{\theta}^{\text{ave}} = \pi$ partition the phase space $\mathbb{R}_+ \times [-\pi, \pi] \times \mathbb{R}$ of the system and separate the equilibria of the averaged error system, (3.37), (3.38). The behavior of the first separatrix is characterized by $\tilde{r}_c^{\text{ave}}$ decreasing along $\tilde{\theta}^{\text{ave}} = 0$, while the behavior of the second separatrix is characterized by $\tilde{r}_c^{\text{ave}}$ increasing along $\tilde{\theta}^{\text{ave}} = \pi$. Note the discontinuity in $\frac{d\tilde{\theta}^{\text{ave}}}{d\tau}$ when $\tilde{r}_c^{\text{ave}} = 0$ and that the equilibria are away from this discontinuity. The effect of the discontinuity is a jump from the first solution to the second at $\tau = \frac{\omega}{V_cJ_0(a)}\tilde{r}_c^{\text{ave}}(0)$. While the separatices define lines in the two-dimensional $(\tilde{r}_c^{\text{ave}}, \tilde{\theta}^{\text{ave}})$ subspace, Figure 3.10 shows the manifold (surface)

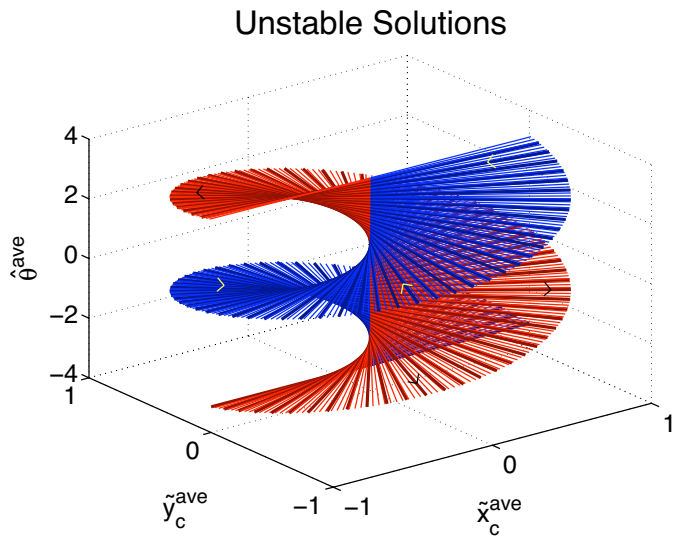

Figure 3.10: Set of unstable solutions.
Blue: The part of "head-on" trajectory pointing towards the source. Red: The part of the "head-on" trajectory pointing away from the source.

those lines create in $(\hat{r}_c^{\text{ave}}, \hat{\theta}^{\text{ave}})$ space. Recall $\hat{r}_c^{\text{ave}}$ is the vehicle position with respect to the source and $\hat{\theta}^{\text{ave}}$ is the vehicle heading. When $\tilde{\theta}^{\text{ave}} = 0$ the vehicle is heading directly toward the source, while when $\tilde{\theta}^{\text{ave}} = \pi$ the vehicle is heading directly away from the source. Along these paths, the vehicle effectively cannot decide which way to turn, and thus remains pointing in the same direction for all time, as indicated by the solutions (3.74)–(3.79). The discontinuity at $(\tilde{x}_c^{\text{ave}} = 0, \tilde{y}_c^{\text{ave}} = 0) = \tilde{r}_c^{\text{ave}} = 0$ can clearly be seen in the figure, as can the jump from the $\tilde{\theta}^{\text{ave}} = 0$ separatrix to the $\tilde{\theta}^{\text{ave}} = \pi$ separatrix. The jump in $\tilde{\theta}$, as a result of passing over the origin, is caused by a reversal of the argument of the vector $\hat{r}_c^{\text{ave}}$ and not a jump in actual vehicle behavior. It is important to realize that, while initial conditions which correspond to the unstable solutions (3.74)–(3.79) exist, the set of these initial conditions is measure zero.

3.4.4 Effect of the d Parameter

We now discuss the last term, $-d\xi^2 \sin(\omega t)$ of the control law (3.3) for $\dot{\theta}$. The standard extremum seeking scheme does not contain this term [86]. Its incorporation

into the scheme was motivated by the need to enable stable hovering around the source, in addition to convergence towards the source. The effect of this term is seen in the transient behavior of the vehicle. Without the d term, the vehicle moves directly toward the source and, having a constant forward velocity, overshoots the source and turns around. The vehicle continues this behavior and the amount of overshoot never decreases. Adding the d term perturbs the vehicle off this path. When d is small the vehicle simply decreases the amount of overshoot each time it turns around until it settles into the system attractor. As d is increased the overshooting decreases more rapidly and the vehicle settles into the system attractor much faster. Examining the averaged error system (3.34)–(3.36) and its equilibria (3.37), (3.38), we see that the location of the equilibria are independent of d.

$$\frac{d\tilde{r}_c^{\text{ave}}}{d\tau} = -\frac{V_c J_0(a)}{\omega}\cos(\tilde{\theta}^{\text{ave}}) \tag{3.80}$$

$$\frac{d\tilde{\theta}^{\text{ave}}}{d\tau} = \frac{1}{\omega}\sin(\tilde{\theta}^{\text{ave}})\left\{\frac{V_c J_0(a)}{\tilde{r}^{\text{ave}}} - 2cq_r R J_1(a)\tilde{r}_c^{\text{ave}}\right\} \tag{3.81}$$

$$\frac{de^{\text{ave}}}{d\tau} = \frac{h}{\omega}\left(2q_r R\tilde{r}^{\text{ave}} J_0(a)\cos(\tilde{\theta}^{\text{ave}}) - q_r R^2 - q_r \tilde{r}^{\text{ave}^2} - e^{\text{ave}}\right) \tag{3.82}$$

However, upon inspection of the characteristic polynomial (3.41) it is clear that the eigenvalues depend on d, specifically, when $d = 0$, the characteristic polynomial becomes

$$\begin{aligned} 0 &= (\omega s)^3 + h(\omega s)^2 + \frac{2V_c^2 J_0(a)^2}{\rho^2}\omega s + h\frac{2V_c^2 J_0(a)^2}{\rho^2} \\ &= (\omega s + h)\left((\omega s)^2 + \frac{2V_c^2 J_0(a)^2}{\rho^2}\right), \end{aligned} \tag{3.83}$$

thus the system has one stable eigenvalue and two purely imaginary eigenvalues, rendering it neutrally stable instead of exponentially stable. Thus the *exponential* convergence results for the system (3.5)–(3.9) derived in Section 3.4 do not hold when $d = 0$. We added the term $-d\xi^2\sin(\omega t)$ to the standard extremum seeking control law in order to achieve exponential stability of the averaged system, without changing its equilibria, and from that exponential convergence of the original system.

The effect of the gain d is readily analyzed by the root locus method. The characteristic equation derived from the characteristic polynomial (3.41) in root

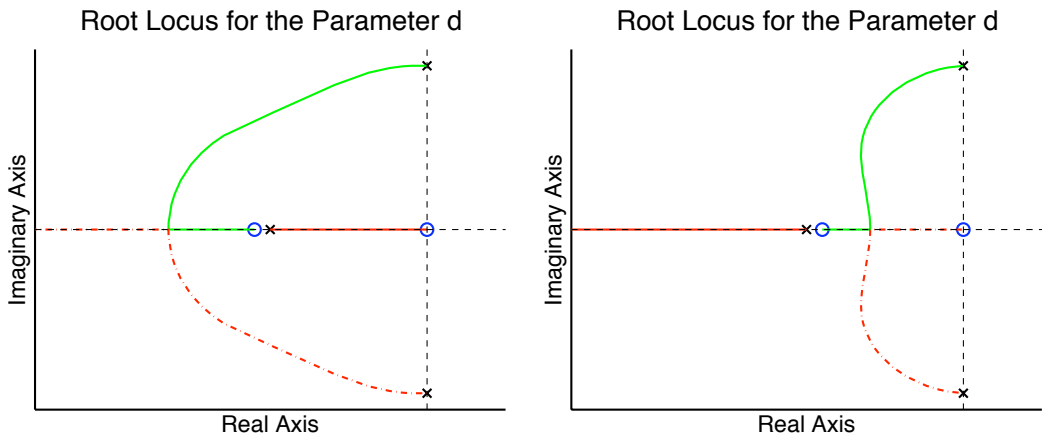

(a) (b)

Figure 3.11: Root locus of parameter d when (a) $\frac{V_c}{R} > h$ and (b) $\frac{V_c}{R} < h$.

locus form is

$$\begin{aligned} 0 &= 1 + d4\rho^2 q_r^2 R(a + O(a^3)) \frac{R(\omega s)^2 + V_c \omega s}{(\omega s + h)\left((\omega s)^2 + \frac{2V_c^2(1+O(a^2))}{\rho^2}\right)} \\ &\approx 1 + d4\rho^2 q_r^2 Ra \frac{R(\omega s)^2 + V_c \omega s}{(\omega s + h)\left((\omega s)^2 + \frac{2V_c^2}{\rho^2}\right)}. \end{aligned} \tag{3.84}$$

Figure 3.11 shows the root locus for the cases $\frac{V_c}{R} > h$ and $\frac{V_c}{R} < h$. In both cases the equilibria change from centers into stable foci and later into stable nodes as d increases. The phase portrait shown in Figure 3.12 contains stable foci, indicated by the spirals converging on the equilibria. The phase portrait shown in Figure 3.13 also depicts exponentially stable equilibria. In this case d has been increased to the point that the eigenvalues are all on the real axis and the equilibria become stable nodes.

Figure 3.14 shows the effect d has on vehicle behavior. As d is increased the vehicle behavior changes from being characterized by moving almost directly toward the source, overshooting and then turning around to being characterized by moving in circles with decreasing radius around the source. In the first case the distance between the vehicle and the source oscillates, as expected by the focus equilibrium in the averaged system. In the second case the distance between the vehicle and the

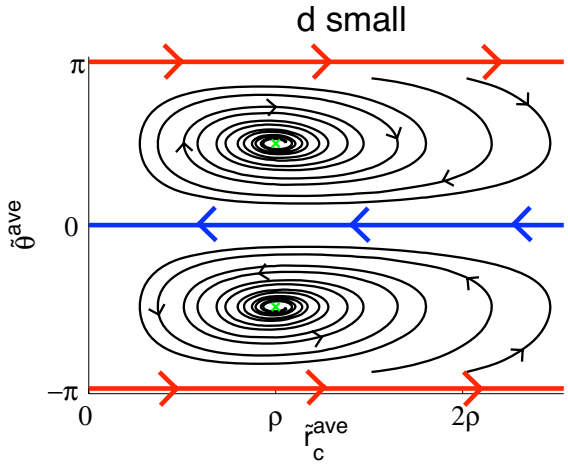

Figure 3.12: Phase portrait of averaged system with d small

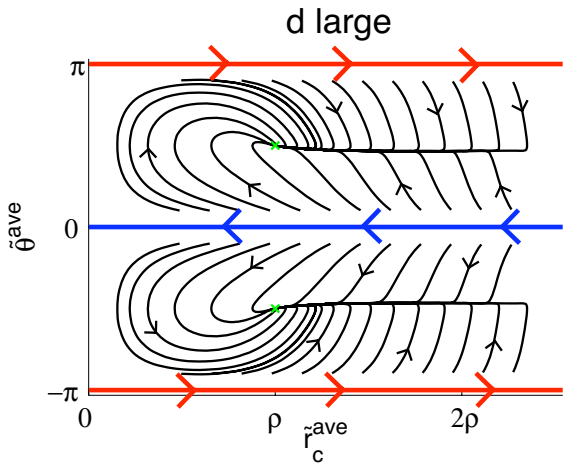

Figure 3.13: Phase portrait of averaged system with d large

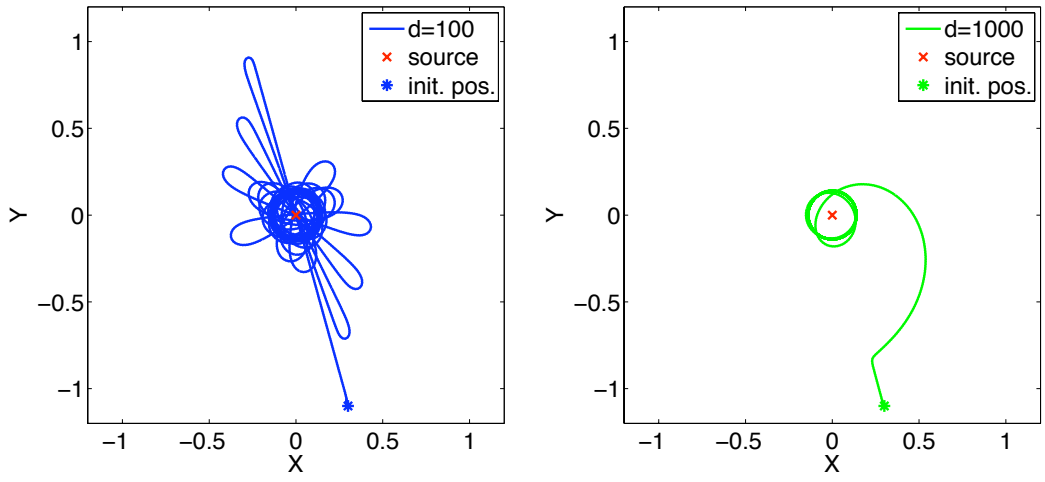

Figure 3.14: Both (a) and (b) show the trajectory of a vehicle with the same initial conditions and same parameters.
The only difference between the two simulations is the value of d. In (a) the value of d is low, while in (b) the value of d has been increased. The other simulation parameters are $V_c = 0.1, c = 100, d = 100, a = 0.5, \omega = 40, R = 0.1, h = 1, q_r = 1$.

source mainly decreases as would be expected by the stable node equilibrium of the averaged system.

3.5 System Properties With $d = 0$

While setting d to zero indicates the system, driven by a map with circular level sets, is not exponentially convergent, interesting behavior still emerges. In this section we discuss first the behavior of the vehicle seen when setting d to zero in the presence of a map with circular level sets. We then consider the behavior of the vehicle in the presence of maps with elliptical level sets. [5]

[5]Unlike the previous two sections, the behavior discussed in this section has no direct corollary to the case with a collocated sensor and a washout filter with a small time constant.

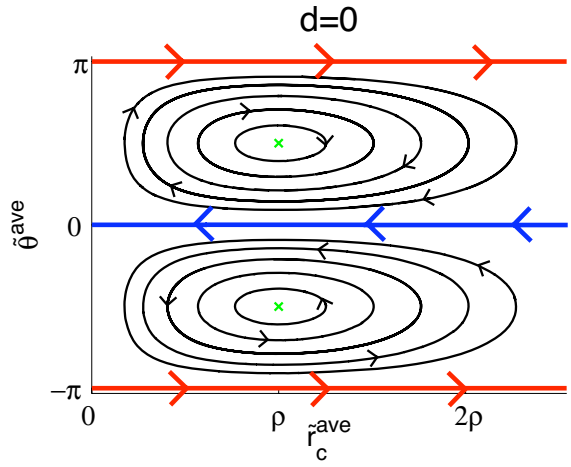

Figure 3.15: Phase portrait of averaged system with $d = 0$

3.5.1 Circular Level Sets

As stated in Section 3.4.4, the averaged error system with d set to zero, (3.80)–(3.82), is only marginally stable about the equilibria (3.37), (3.38). Figure 3.15 shows the phase portrait of $(\tilde{r}_c^{\text{ave}}, \tilde{\theta}^{\text{ave}})$ when $d = 0$. The two equilibria are centers in this case and the orbits surrounding these centers are separated by the separatrices (3.74)–(3.79) discussed above. The orbits are defined by the relationship $W(t) \equiv W(0), \forall t \geq 0$, where W is a Lyapunov function

$$W = \frac{\tilde{r}^{\text{ave}^2}}{2\rho^2} - \ln(\tilde{r}^{\text{ave}} |\sin(\tilde{\theta}^{\text{ave}})|)\,. \tag{3.85}$$

This function is found as an invariant of the system by solving the differential equation

$$\frac{d\tilde{\theta}^{\text{ave}}}{dr^{\text{ave}}} = \tan(\tilde{\theta}^{\text{ave}}) \left\{ \frac{\tilde{r}^{\text{ave}}}{\rho^2} - \frac{1}{\tilde{r}^{\text{ave}}} \right\} \tag{3.86}$$

derived from the quotient of (3.80) and (3.81). The initial conditions of the system determine which orbit $W = const$ the vehicle travels along. Though the averaging theory does not allow us to say anything about the original system as the averaged system (3.80)–(3.82) is not exponentially stable (only neutrally stable), periodic orbits around the source and the dependence on the initial conditions are both still

seen in simulations of the original system. Figure 3.16 depicts the trajectory of the vehicle for $d = 0$ according to both the averaged system equations and the original system equations when starting from different initial conditions. As seen, the original system closely follows the averaged system, but the trajectories are initial condition dependent.

3.5.2 Elliptical Level Sets

While, in the case of a map with circular level sets the absence of the d term in the control law eliminates convergence to an annulus about the source and generates a different "attractor" for each initial condition, the same is not seen when the map has elliptical level sets. In this case, simulations show convergence to specific attractors, which are seen in both averaged simulations and full system simulations.

When the map has elliptical level sets instead of circular ones, the definition of J must be augmented,

$$\begin{aligned} J &= f^* - q_r|r_s|^2 - q_p(r_s^2 + \bar{r}_s^2) = f^* - (q_r + 2q_p)x_s^2 - (q_r - 2q_p)y_s^2 \quad (3.87) \\ &= f^* - q_r|r_c + Re^{j\theta}|^2 - q_p\left(\left(r_c + Re^{j\theta}\right)^2 + \left(\bar{r}_c + Re^{-j\theta}\right)^2\right), \quad (3.88) \end{aligned}$$

where $q_r > 0, q_r \pm 2q_p > 0$. This leads to a modification of ξ, which expressed using $\tilde{r}_c$, θ^*, $\hat{\theta}$, and e defined by (3.28), (3.23), (3.20) and (3.4) is,

$$\begin{aligned} \xi &= J - f^* - e \quad (3.89) \\ &= -R^2\left(q_r + 2q_p\cos\left(2(\hat{\theta} + a\sin(\omega t)\right)\right) - \tilde{r}_c^2\left(q_r + 2q_p\cos\left(2\theta^*\right)\right) \\ &\quad +2R\tilde{r}_c\left(q_r\cos\left(\hat{\theta} - \theta^* + a\sin(\omega t)\right) + 2q_p\cos\left(\hat{\theta} + \theta^* + a\sin(\omega t)\right)\right) \quad (3.90) \end{aligned}$$

The shifted error system, now still in four states as the variables θ^* and $\hat{\theta}$ cannot be combined, is

$$\begin{aligned} \frac{d\tilde{r}_c}{d\tau} &= -\frac{V_c}{\omega}\cos(\hat{\theta} - \theta^* + a\sin(\tau)) \quad (3.91) \\ \frac{d\theta^*}{d\tau} &= -\frac{V_c}{\omega}\frac{\sin(\hat{\theta} - \theta^* + a\sin(\tau))}{\tilde{r}_c} \quad (3.92) \\ \frac{d\hat{\theta}}{d\tau} &= \frac{1}{\omega}c\xi\sin(\tau) \quad (3.93) \\ \frac{de}{d\tau} &= \frac{1}{\omega}h\xi\,. \quad (3.94) \end{aligned}$$

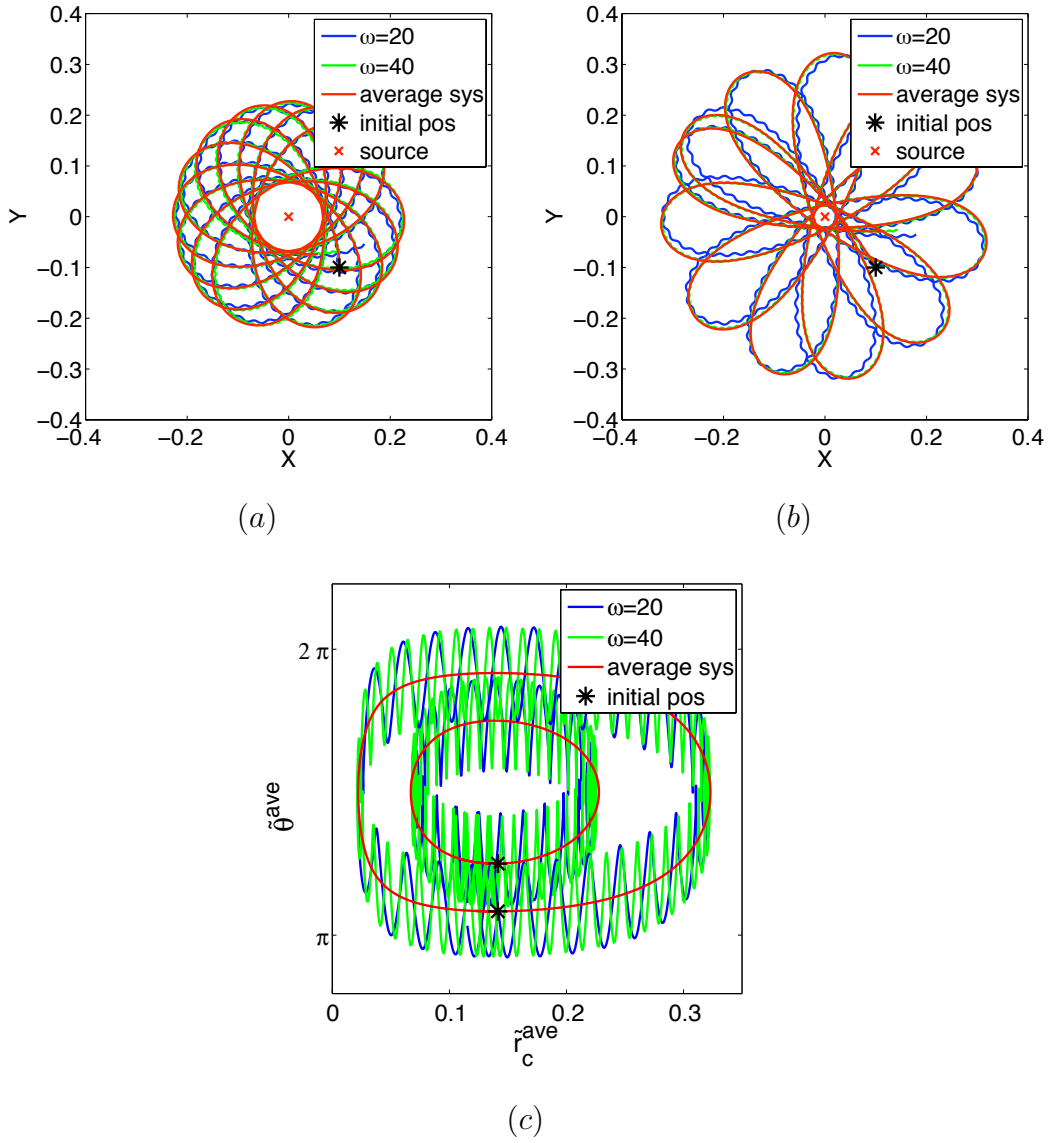

Figure 3.16: Trajectory of the averaged system and the original system with $d = 0$. Image (a) depicts two trajectories of the vehicle center according to the original system equations (one with $\omega = 20$ and the other with $\omega = 40$ and the trajectory of the vehicle center according to the averaged system equations, all in physical space. Image (b) depicts the same thing, but with a different initial orientation, and thus the different resulting "flower pattern". Image (c) depicts all trajectories in error coordinates. The other system parameters are $V_c = 0.1, c = 50, d = 0, a = 0.5, R = 0.1, h = 1, f^* = 0, q_r = 1$.

The averaged error system is

$$\frac{d\tilde{r}_c^{\text{ave}}}{d\tau} = -\frac{V_c J_0(a)}{\omega}\cos(\hat{\theta}^{\text{ave}} - \theta^{*^{\text{ave}}}) \tag{3.95}$$

$$\frac{d\theta^{*^{\text{ave}}}}{d\tau} = -\frac{V_c J_0(a)}{\omega}\frac{\sin(\hat{\theta}^{\text{ave}} - \theta^{*^{\text{ave}}})}{\tilde{r}_c^{\text{ave}}} \tag{3.96}$$

$$\begin{aligned}\frac{d\hat{\theta}^{\text{ave}}}{d\tau} = &-\frac{1}{\omega}c\Bigg(2RJ_1(a)\tilde{r}_c^{\text{ave}}\Bigg(q_r\sin(\hat{\theta}^{\text{ave}} - \theta^{*^{\text{ave}}}) + 2q_p\sin(\hat{\theta}^{\text{ave}} + \theta^{*^{\text{ave}}})\Bigg)\\ &-2R^2J_1(2a)q_p\sin(2\hat{\theta}^{\text{ave}})\Bigg)\end{aligned} \tag{3.97}$$

$$\begin{aligned}\frac{de^{\text{ave}}}{d\tau} = &\frac{1}{\omega}h\Bigg(-R^2(q_r + 2J_0(a)q_p\cos(2\hat{\theta}^{\text{ave}})) - \tilde{r}_c^2\left(q_r + 2q_p\cos\left(2\theta^{*^{\text{ave}}}\right)\right)\\ &+2RJ_0(a)\tilde{r}_c^{\text{ave}}\Bigg(q_r\cos(\hat{\theta}^{\text{ave}} - \theta^{*^{\text{ave}}}) + 2q_p\cos(\hat{\theta}^{\text{ave}} + \theta^{*^{\text{ave}}})\Bigg) - e^{\text{ave}}\Bigg)\end{aligned} \tag{3.98}$$

This averaged system cannot be simplified to three states as in the case of circular level sets, nor does it have an equilibrium to analyze (in the present coordinates), though it does have unstable solutions characterized by

$$\hat{\theta}^{\text{ave}} = n\frac{\pi}{2} \tag{3.99}$$

$$\theta^{*^{\text{ave}}} = \hat{\theta}^{\text{ave}} + m\pi \tag{3.100}$$

where n and m are integers. However, the evolution of the original system closely matches the evolution of the averaged system in simulations. Figure 3.17 shows the initital positions of the vehicle and the attractor to which the trajectories converge for simulations of both the original system (for $\omega = 20$ and $\omega = 40$) and the averaged system. Each initial condition settles to one of two symmetric attractors. The shape of the attractor is the same in all three situations, which indicates the averaged system closely approximates the actual system. However, the initial conditions alone do not determine into which of the two attractors the system settles. By changing the value of ω, the system sometimes settles to the other attractor. This behavior of settling to one of two distinct attractors is seen again and again in simulations of the system indicating that when $d = 0$ and the system map has elliptical level sets, there exist convergent attractors of the system, though this is not seen when the system map has circular level sets.

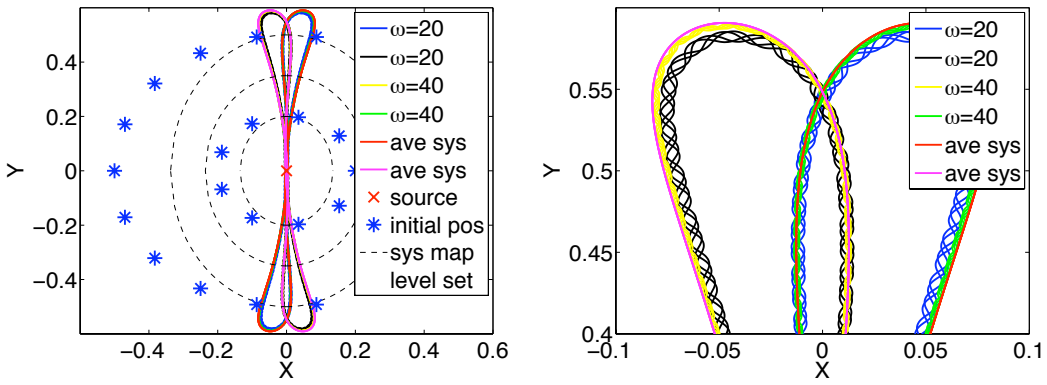

(a) (b)

Figure 3.17: Initial conditions and attractors.
Simulations for $d = 0$ and a range of initial positions are shown. Image (a) depicts the attractor "pair" to which the trajectory of the vehicle center converges. The simulations evolve according to the original system equations with $\omega = 20$ and $\omega = 40$ and according to the averaged system equations. Image (b) depicts a zoomed in version of image (a). The source is located at the origin. The other system parameters are $V_c = 0.1, c = 100, a = 0.5, R = 0.1, h = 1, f^* = 0, q_r = 1.6, q_p = 0.3$.

3.6 System Properties with Elliptical Level Sets and $d > 0$

As mentioned in Section 3.4.1, the value of d affects the general shape, size and number of the system attractors when the system map has elliptical level sets and does not affect the shape, size or number when the system map has circular level sets. In the case of circular level sets, the two system attractors are clockwise and counter clockwise perturbed circular orbits. Figure 3.18 shows the progression of system attractors in the case of elliptical level sets as d increases in value. The attractor progression starts with $d = 0$ and increases to very large d values. While d is small to medium, its increase causes the attractor to move away from the origin and shrink in vertical size - the perturbed figure-eight is being pulled and squashed. When d is large enough, we start seeing attractors that look like elliptical orbits. As d continues to increase, these orbits rotate toward the orientation of the map level sets while decreasing in size. Once these orbits reach that orientation, they continue

to rotate, but now start increasing in size. Figure 3.19 shows another progression of attractors. When d is small the system only exhibits two attractors which resemble perturbed figure-eights. When d is medium valued, we see four different attractors, two perturbed figure eights (smaller than the two seen for small d) and two rotated elliptical orbits. When d is large, we once again find only two attractors, this time two elliptical orbits which are smaller and at a different orientation than the two seen for medium d.

We already know that the V_c parameter affects the size, but not the shape of the attractors in the case of circular level sets. Figure 3.20 shows that, in the case of elliptical level sets, not only does V_c affect the size of the system attractors, it also affects the shape. As V_c increases the vertical size of the attractor first increases, then decreases and finally increases again. The shape of the attractor is first stretched, then squashed and pulled, then stretched again.

3.7 Conclusion

We have shown the results of applying extremum seeking to source seeking with nonholonomic autonomous agents which are denied postion information. We have proved local convergence to an "orbit-like" attractor around the source when the signal map is quadratic with circular level sets and characterized non-local behaviors, including a zero-measure set of unstable trajectories. Simulations show convergent vehicle behavior for elliptical level sets as well.

Future companion publications will present applications to other scenarios, including tracking diffusive sources, extensions to 3-D [24, 21], extensions to fish-like locomotion models, and experimental results with prototype mobile robots and underwater vehicles which move according to the developed control law and track light or sound sources.

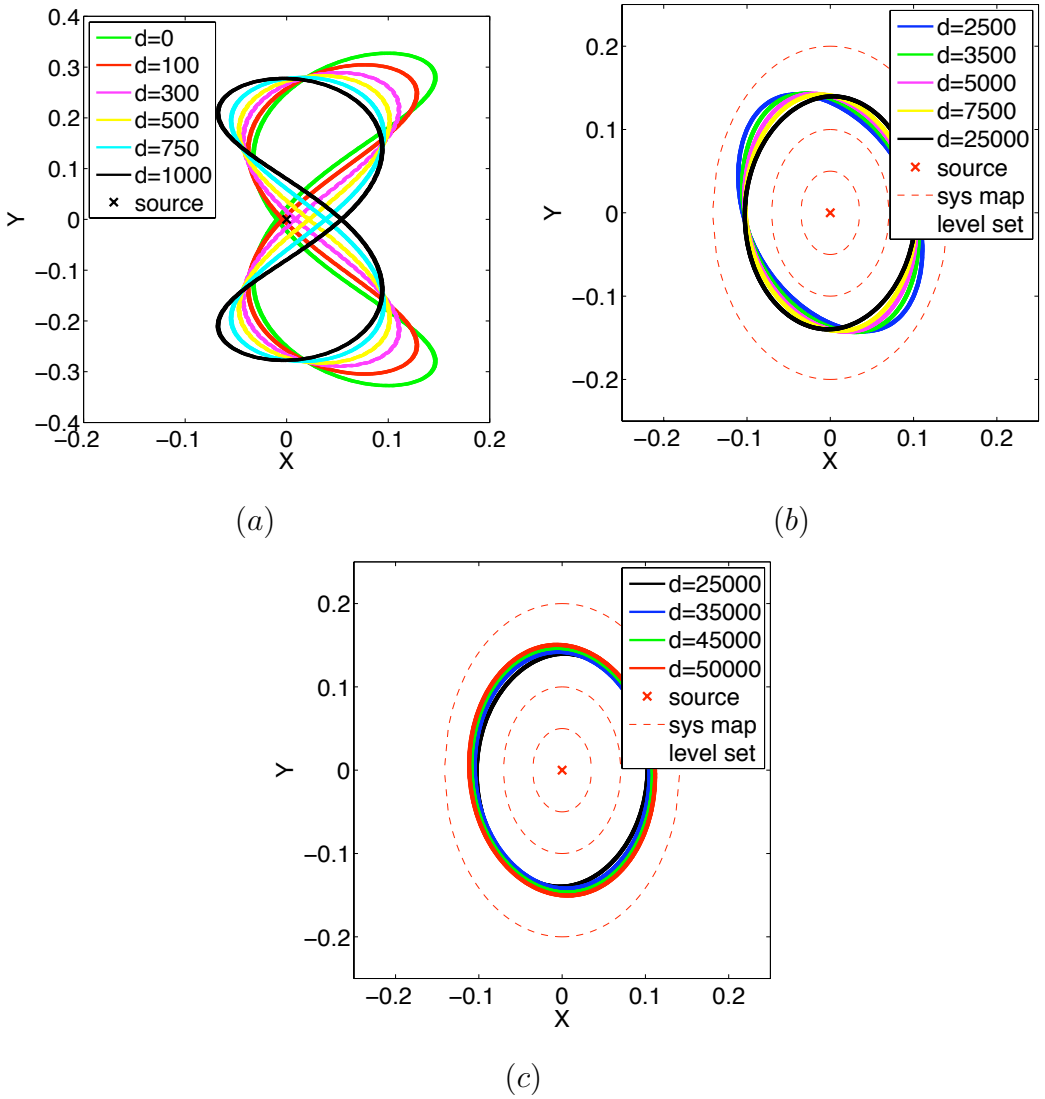

Figure 3.18: System attractors as d progresses.
Simulations for various d and a source located at the origin. (a) As d increases, the attractor crossing in x, y space moves further from the origin while the attractor shape decreases in vertical size. (b) As d continues to increase, the attractors change from morphed figure-eights to rounded orbits. These orbits rotate toward the system map level set orientation and decrease in size as d continues to increase. (c) For large enough d, while the attractor orbits continue to rotate as d increases, the size stops decreasing and starts increasing. The other system parameters are $V_c = 0.1, c = 100, a = 0.5, \omega = 40, R = 0.1, h = 1, f^* = 0, q_r = 1.5, q_p = 0.25$.

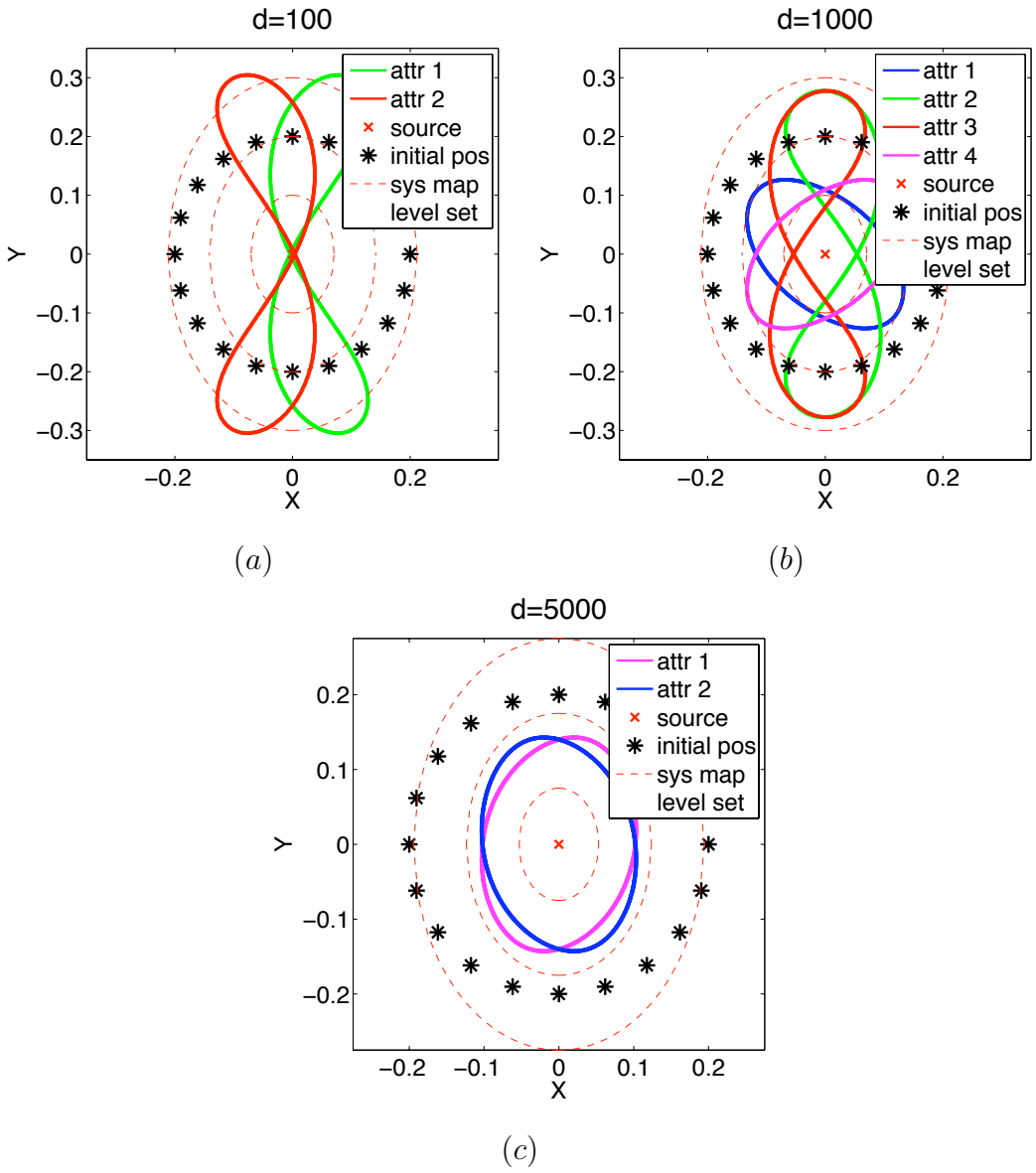

Figure 3.19: Initial conditions and attractors.
Simulations for $d = 100, 1000, 5000$ a range of initial vehicle positions and a source located at the origin are shown. (a) The two attractors which exist when d is small. (b) The four attractors that are seen when d is medium. (c) The two attractors which exist when d is large. The other system parameters are $V_c = 0.1, c = 100, a = 0.5, \omega = 40, R = 0.1, h = 1, f^* = 0, q_r = 1.5, q_p = 0.25$.

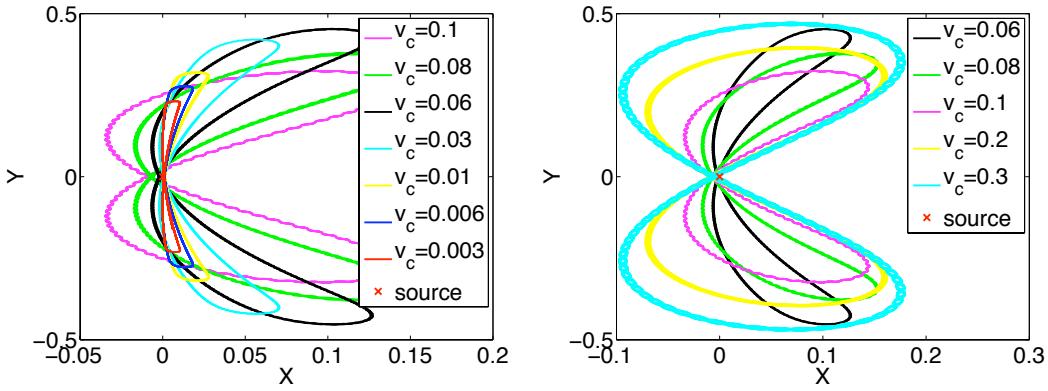

(a) (b)

Figure 3.20: System attractors as V_c progresses.
Simulations for various V_c and a source located at the origin. (a) As V_c increases in the range $0.003 \leq V_c \leq 0.01$ the attractor increases in size but does not change the general shape. As V_c increases in the range $0.01 \leq V_c \leq 0.1$ the attractor changes shape and increases in horizontal size. (b) As V_c increases in the range $0.06 \leq V_c \leq 0.1$ the attractor decreases in vertical size and increases in horizontal size. As V_c increases in the range $0.1 < V_c$ the attractor does not change the general shape, but increases in size. The other system parameters are $c = 100, d = 10, a = 0.5, \omega = 40, R = 0.1, h = 1, f^* = 0, q_r = 1.5, q_p = 0.25$.

3.8 Acknowledgements

We acknowledge fruitful discussions with Andy Teel regarding the topological obstacles to global solvability of the source seeking problem.

This chapter is in full a reprint of the material as it will appear in:
J. Cochran and M. Krstic, "Nonholonomic Source Seeking With Tuning of Angular Velocity," *IEEE Transactions on Automatic Control*, to appear.

The dissertation author was the primary investigator and author of this publication.

4

Applications of Nonholonomic Source Seeking With Tuning of Angular Velocity

4.1 Abstract

We present results for autonomous vehicles operating in GPS-denied environments while performing several different tasks. These vehicles employ extensions of extremum seeking to accomplish their goals. Previously, extremum seeking has successfully been applied to vehicles seeking the source of some signal, while operating in such environments. This chapter considers the objectives of tracking a diffusive signal, tracing a level set of a signal field, and modification of the algorithm for use on a vehicle with limited movement capabilities. We present each scenario, detail each control scheme and, in addition, present simulation results.

4.2 Introduction

Research directed at the many applications that make use of autonomous vehicles is wide, varied and constantly growing. In particular, the field of research dealing with vehicles deprived of position information is rapidly gaining interest.

These vehicles must navigate and perform a desired task without the use of GPS or inertial navigation. The lack of available positioning information can be due to the costs of implementation and computation, or due to the operating environment where such information is unavailable, such as urban, underground and underwater environments. While many groups have used the extremum seeking method outside the field of autonomous vehicles, including [61], [60], [17], [73], [14], [74], [28], [48] and [88], the method has also successfully been applied to autonomous vehicles operating in such environments when the objective is to locate a target which emits some signal [86, 20]. Chapter 3 presents theoretical results for the basic scheme, while this chapter extends those results by presenting the application of extremum seeking to vehicles with different objectives and different configurations from those which the theory covers. The objectives we consider here are tracking a diffusive signal, tracing a level set of a signal field, and modification of the algorithm for use on a vehicle with limited movement capabilities.

Past work with source seeking has focused on signal fields which are static with respect to the target emitting them. The signal field does not change its shape in time, and it moves in unison with the target. While this is a valid representation of certain types of signals (light sources, magnetic fields), there are other types of signals which do change in time. The type of signal we focus on in this chapter is a diffusive signal. In this scenario, the target emits a chemical or biological agent into its surrounding medium as it moves around. This agent, governed by a diffusion equation, disperses throughout the medium. A source modeled in such a way allows for the possibility of local extrema within the signal field. When the target lingers in one location, the local concentration increases and becomes a local maximum when the target leaves. In addition, at different locations around the signal field, the concentration can either be decreasing or increasing in time. The concentration along the target trajectory increases as the target passes over, and then decreases as the signal diffuses away. The concentration in areas adjacent to the trajectory increases as the signal diffuses toward the area and then starts to decrease after enough time has passed. The ability to track this type of process is important for plume tracking applications and has been explored in [62, 58, 32]. That work makes

use of multiple sensors on a single agent or multiple agents communicating between each other. Extremum seeking allows a single autonomous vehicle with only one sensor to track the target, even though the signal field is so complex. In addition to considering diffusive sources, we also consider diffusive *anti-sources* which motivate our results for "cleaning-up" after the target as the vehicle follows it. In this setup, the vehicle can release a cleaning agent which counters the signal that the target releases, thus cleaning while still continuing to track the target.

While oftentimes the objective is to locate the source of a signal, the objective can also be to provide more information about a signal field. One way of doing this is to trace out level sets of the field. There are many ways of performing this task, as seen in [37]. However, these methods often rely on position information, complex communication or multiple coordinating agents. Extremum seeking provides a simple yet effective solution that has no need for GPS information or outside communication, and can be performed by a single autonomous agent. It is also desirable over other methods because it can both find the level set and track it. Other methods must start relatively close to the level set in order to track properly.

Extremum seeking employs a periodic probing motion of the vehicle to search the signal space, which then provides the necessary information to orient the vehicle in the correct direction. There exist applications for which this probing motion is undesirable, in which case extremum seeking can still be applied via a slight modification. This modified method separates the desired tuning of the vehicle orientation from the undesirable periodic probing. The concept behind decoupled extremum seeking is that the sensor can move along the vehicle body, providing the necessary probing motion, while the vehicle itself moves in a smooth fashion. Implementing decoupled extremum seeking does not hinder the vehicle's capability to perform any of the aforementioned tasks, including source seeking, tracking diffusive signals, and level set tracing.

Section 4.3 provides an overview of the basic extremum seeking (source seeking) algorithm. Sections 4.4, 4.5 and 4.6 present results for tracking diffusive sources, tracing level sets, and implementing decoupled extremum seeking respectively. We conclude in section 4.7 with our future intentions.

4.3 Overview of Extremum Seeking for Autonomous Vehicles

The extremum seeking method employs periodic probing to perform non-model based gradient estimation [5]. The vehicles to which we consider applying extremum seeking are kinematically constrained, must navigate to perform a desired task, and have no available position information. Considering these constraints, one of the advantages of the method is being able to simultaneously solve a non-holonomic steering problem while also solving an adaptive optimization problem.

The extremum seeking method applied to source seeking works under the assumptions that a target creates some signal field and that the vehicle can sense that field. The shape of the signal field is unknown, though the strength of the signal is assumed to be a maximum at the target location and to decay with distance away from the target. This signal field could be electromagnetic, acoustic, chemical, biological or any other signal that displays the assumed properties. A vehicle employing extremum seeking uses only the scalar measure of the signal field at the position of its sensor (at the tip of the vehicle) as the input to the control loop. The vehicle uses a periodic probing motion to search the space and a bias term to turn in the correct direction. This combination allows it to perform on-line gradient estimation to converge to the vicinity of the target. As previously mentioned, all of this is achieved without the use of positioning information such as GPS or inertial navigation, and without the use of communication with other entities. Therefore this method is extremely useful in environments, such as urban, underground and underwater environments, where GPS is unavailable, and in applications where inertial navigation is too expensive to implement.

Figure 4.1 shows a general nonholonomic vehicle configuration, also known as the unicycle model. The vehicle moves with forward velocity v, heading angle θ, and angular velocity Ω. The vehicle center and sensor are located at r_c and r_s respectively. The sensor must be a nonzero distance R, away from the center.

Throughout this chapter, the vehicles considered are governed by the unicycle

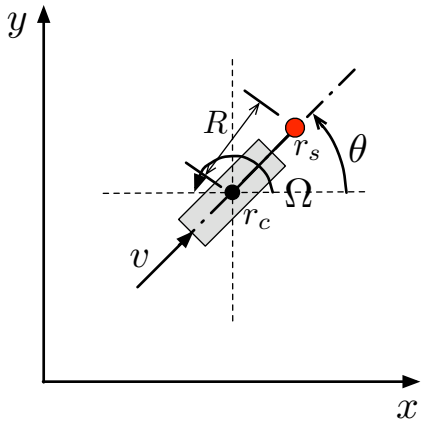

Figure 4.1: Basic vehicle configuration.
The measure R is the distance between the vehicle center located at r_c and the sensor located at r_s. The vehicle moves in the direction θ, with velocity v and angular velocity Ω.

model with a constant forward velocity, V_c.

$$\dot{r}_c \;=\; V_c e^{j\theta} \tag{4.1}$$

This unicycle model with a constant forward velocity is applicable to many agents, including aircraft. We use extremum seeking to tune the vehicles' angular velocity with the basic control law

$$\dot{\theta} \;=\; a\omega\cos(\omega t) + c\frac{s}{s+h}\,[J]\sin(\omega t)\,, \tag{4.2}$$

where J is the sensor reading, $\frac{s}{s+h}\,[J]$ is a washout filter, and the parameters a, c, w, h and R are chosen to give desired performance properties. The term $a\omega\cos(\omega t)$ provides the periodic probing to the vehicle, which allows it to continuously search the signal field and enables the algorithm to determine which way to turn. The turning is accomplished by the second term, $c\frac{s}{s+h}\,[J]\sin(\omega t)$, obtained by passing the sensor signal J through a high-pass filter $\frac{s}{s+h}$, then demodulating the filtered signal by $\sin(\omega t)$ and multiplying the demodulated signal by the gain c. The sensor reading, J, is a function of the sensor position r_s. In this configuration, the sensor position, as a function of the vehicle center r_c and heading θ, is

$$r_s \;=\; r_c + Re^{j\theta}\,. \tag{4.3}$$

The first extension we examine, tracking diffusive signals, applies this scheme to targets which emit a signal which dynamically changes in time and space. The second extension we examine, tracing level sets, modifies the input to the control law, while the last extension we present, decoupled sensor architecture, modifies the control input $\dot{\theta}$.

4.4 Diffusive Source

The previous focus on source seeking has been on targets with signal fields that remain unchanged in time and space, with respect to the target. However, some targets emit signals which create more dynamic signal fields. A primary example of this is a contaminant which diffuses through a medium, be it air or water. This diffusive field differs from previously studied fields, referred to as static fields, in two ways. The first way has already been mentioned, a static field remains unchanged with respect to the source, while the diffusive field changes depending on where the target has traversed. The next difference is where the signal can be sensed. In a static field there is a fully connected area surrounding the source where a sensor can detect the signal. There are no gaps and the shape of this area never changes. This area is defined solely by the position of the source. However, for a diffusive source, this area is determined by both the path that the source follows and the time at which the source passed over a location.

The source will leave a "scent" whereever it goes, which will diffuse into the surrounding areas. After enough time, the signal will diffuse to a low enough concentration that a sensor will not be able to detect it. However, before this low level is reached, a sensor can still detect the signal after the source has moved away. The extremum seeking method allows a vehicle to follow this trail to locate and track the target. Figure 4.2 shows a source moving in two dimensions while leaving behind a contaminant trail. The concentration is indicated by the shading of the footprint, where darker shading indicates a higher concentration. The contaminant diffuses after it has been released, causing its footprint to both widen in space and lighten

in color. The dynamics of the contaminant are governed by a diffusion equation

$$\frac{\partial c}{\partial t} = \frac{\partial^2 c}{\partial x^2} + \frac{\partial^2 c}{\partial y^2} + F\delta\left(x - x_{tg}(t), y - y_{tg}(t)\right) \tag{4.4}$$

where $c = c(t, x, y)$ is the concentration of the contaminant at time t and point (x, y), $(x_{tg}(t), y_{tg}(t))$, is the position of the target/source at time t, and F, a constant scalar, is the strength of the point source defined by $\delta\left(x - x_{tg}(t), y - y_{tg}(t)\right)$. The vehicle, represented by the arrow, starts out pointing toward the trail. The solid line behind the arrow shows the path that the vehicle takes as it completes its task. The snake-like curves in the trail are a product of the sinusoidal perturbation applied directly to the vehicle, which is required to make the sensor search the space in which it operates and for extremum seeking to tune the angular velocity. Once the vehicle finds the trail it continues to turn, "sniff", while finding the edge of the trail, and then heads in the correct direction. The top row of Figure 4.3 shows the source, contaminant, vehicle and vehicle path at a later time in the simulation. The vehicle continues to use the contaminant trail to follow the source, while being able to follow turns which the source made. The turns are significant, as the target spends more time in that area, building up a high concentration, and creating a local maximum that the vehicle must overcome while tracking. The vehicle correctly continues to move along the path of the target, and tracking is successful.

A useful extension to contaminant source tracking is contaminant cleaning. A vehicle that uses the extremum seeking method to follow a source could feasibly clean as it moves along. The top row of Figure 4.3 depicts a source releasing a diffusive contaminant as it moves. The bottom row shows the field after the tracking vehicle, as it moves along, leaves a cleaning agent which counters the contaminant. As seen, the concentration of the contaminant is reduced while the vehicle continues to successfully track the target.

4.5 Level Sets

An alternative goal to tracking is to learn more about the signal field in which the vehicle is operating. One way to accomplish this is to trace out the curves

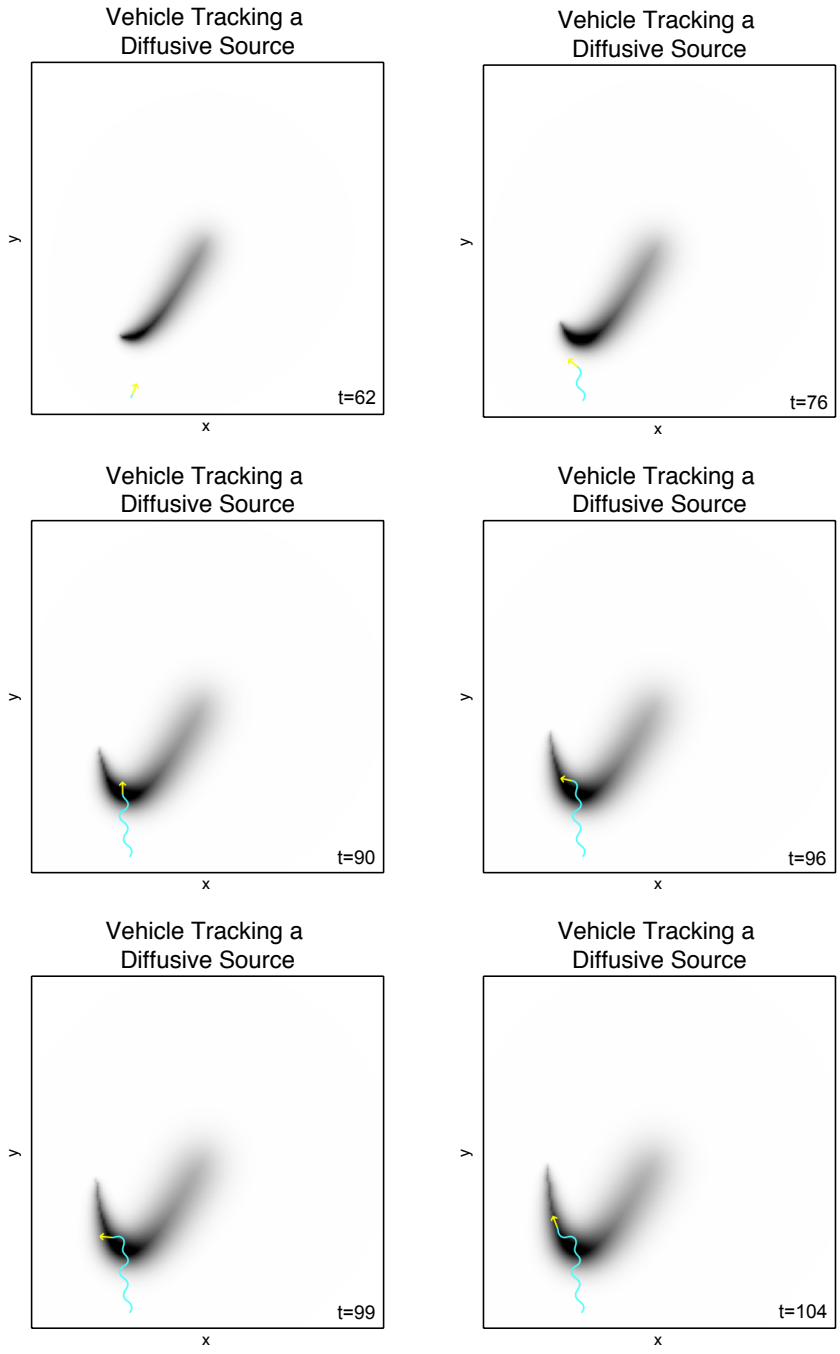

Figure 4.2: Sequence of images from a vehicle employing extremum seeking to tracking a diffusive signal.
The target moves along creating the footprint defined by the shading. The vehicle is represented by the arrow.

which define a specific value of the signal. This curve is referred to as an isoline or level set. Following one constitutes level set tracing. A simple modification to the extremum seeking algorithm produces a simple solution for the implementation of an autonomous vehicles to perform level set tracing. The basic algorithm uses the sensor reading as the input to the control law (4.2), and as the vehicle moves around according to this law it maximizes the sensor signal. The control law, modified for level set tracing, is

$$\dot{\theta} \;=\; a\omega\cos(\omega t) + c\frac{s}{s+h}\left[-\left|J - J_d\right|\right]\sin(\omega t)\,. \tag{4.5}$$

The modified control law uses the absolute value of the difference of the sensor reading J and the desired level set value J_d. The absolute value is multiplied by a negative gain (usually unity) before being used in the control loop. As the vehicle moves, it maximizes $-|J - J_d|$, which is equivalent to the minimization of the error between J and J_d, and in turn implies tracking of the desired level set. Figure 4.4 (a) shows a vehicle tracking a simple elliptical level set. Figure 4.4 (b) shows the signal value at the vehicle center, indicating the vehicle is closely tracking the correct level set.

Extremum seeking also allows vehicles to track more complicated signal fields, as seen in Figure 4.5. This field was constructed with the union of several sources which emit fields with elliptic level sets. The last two sets of images show what happens where there are local maxima in the signal field, causing two distinct curves defined by the same value. Depending of the initial position and orientation of the vehicle, it will converge one of these two curves defined by J_d.

4.6 Actuated Sensor

The basic vehicle configuration used for extremum seeking assumes the vehicle itself can readily perform the movement caused by the periodic perturbation used to search the space, and that this period probing motion can be tolerated in the application. In cases where this type of vehicle movement is not desirable, an actuated sensor can be implemented to decouple the sensor movement from the vehicle center

movement. Figure 4.6 depicts the sensor moving side to side along the vehicle body so that the sensor position as a function of heading θ and the angle θ_s (the angle between the sensor and the centerline of the vehicle) is,

$$r_s = r_c + R\mathrm{e}^{j(\theta+\theta_s)}\,. \tag{4.6}$$

The sensor is actuated according to

$$\theta_s = a\sin(\omega t) \tag{4.7}$$

or

$$\dot{\theta}_s = a\omega\cos(\omega t)\,, \tag{4.8}$$

and the heading control reduces to

$$\dot{\theta} = c\frac{s}{s+h}\,[J]\sin(\omega t)\,. \tag{4.9}$$

The decoupled control law clearly shows that the perturbation $a\omega\cos(\omega t)$ no longer enters directly into the vehicle dynamics, providing for smooth (rather than snaking) trajectories.

Figures 4.7 and 4.8 show the difference in vehicle trajectories between an actuated sensor (decoupled sensor) and one that is fixed to the vehicle. Each simulation was run with exactly the same parameters, the only difference being the actuation of the sensor. In the basic configuration, Figure 4.7, the center is coupled to the sensor and the control law follows (4.2). In the modified configuration, Figure 4.8, the center is decoupled from the sensor motion and the control law follows (4.8) and (4.9). Figure 4.9 shows the distance from the vehicle center to the target as time progresses. The difference in slope, and therefore average speed, is a result of the decoupling of sensor dynamics. With a coupled sensor and center, the vehicle must itself move side to side which reduces its average forward velocity. This does not happen when the sensor is actuated, though this extra speed is of course paid for with the actuation of the sensor.

4.7 Conclusions and Future Work

Extremum seeking applied to autonomous vehicles allows for the completion of a variety of tasks, such as source seeking, level set tracing and modification of vehicle capabilities. Results for basic source seeking are presented in other papers. The results for some of the remaining applications were presented here with simulations to illustrate the capabilities of the method. In the future, we plan to highlight the applications of extremum seeking to collision avoidance, navigating around obstacles and multiple vehicle and multiple target scenarios. We also plan to present stability analysis for some of the aforementioned applications and experimental results with prototype mobile robots and underwater vehicles.

This chapter is in full a reprint of the material as it appears in: J. Cochran, A. Siranosian, N. Ghods, and M. Krstic, "Source Seeking with a Nonholonomic Unicycle without Position Measurements and with Tuning of Angular Velocity — Part II: Applications," *Proceedings of IEEE Conference on Decision and Control*, 2007.

The dissertation author was the primary investigator and author of this paper.

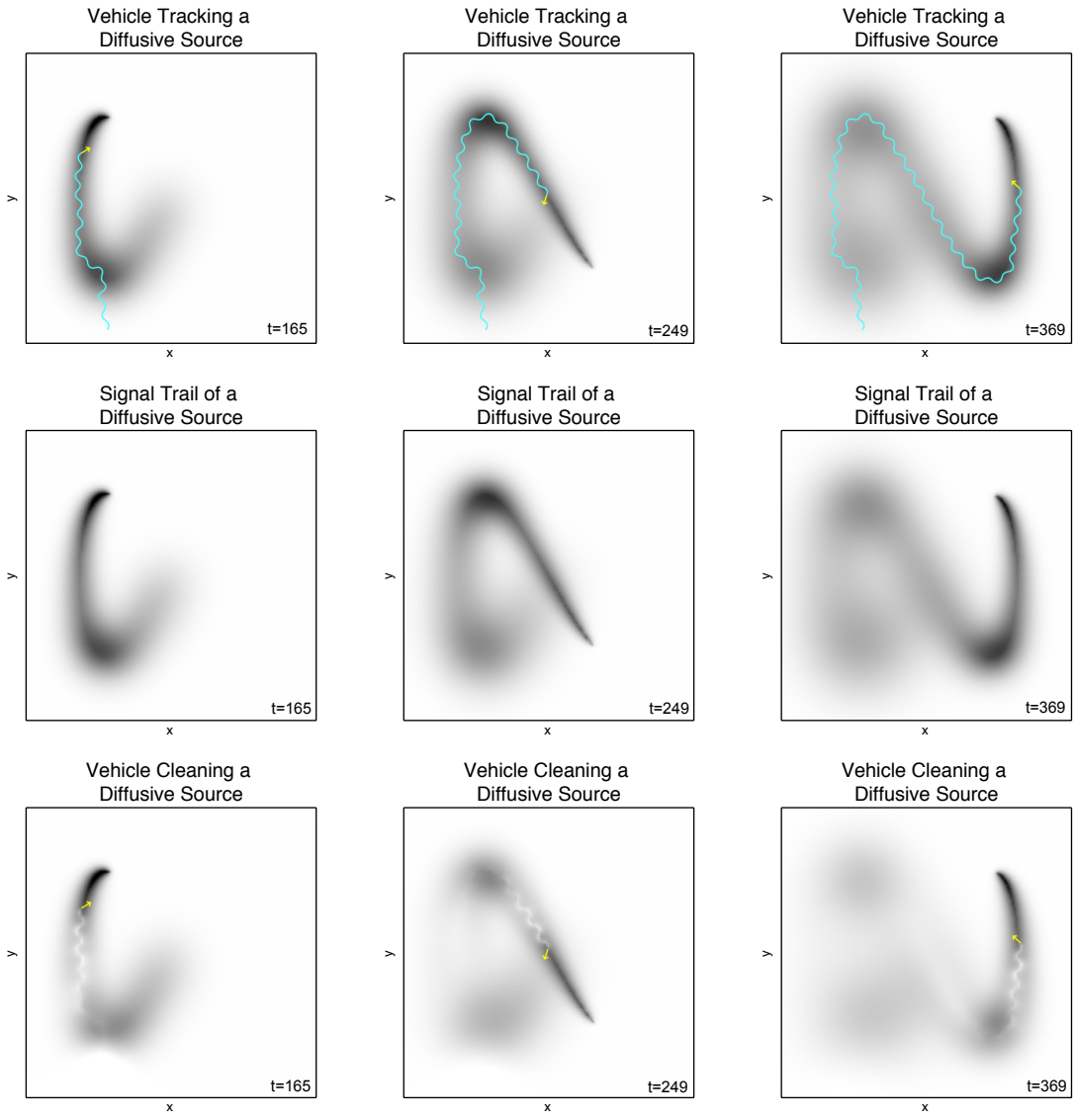

Figure 4.3: Sequence of images from a vehicle tracking a diffusive signal. The top row shows the target has created a curving footprint which the vehicle (arrow) follows successfully. The middle row of images picture a source by itself without a following vehicle moving along and releasing a diffusive contaminant. The bottom row of images show the reduced footprint resulting from a vehicle tracking the source and cleaning as it moves along.

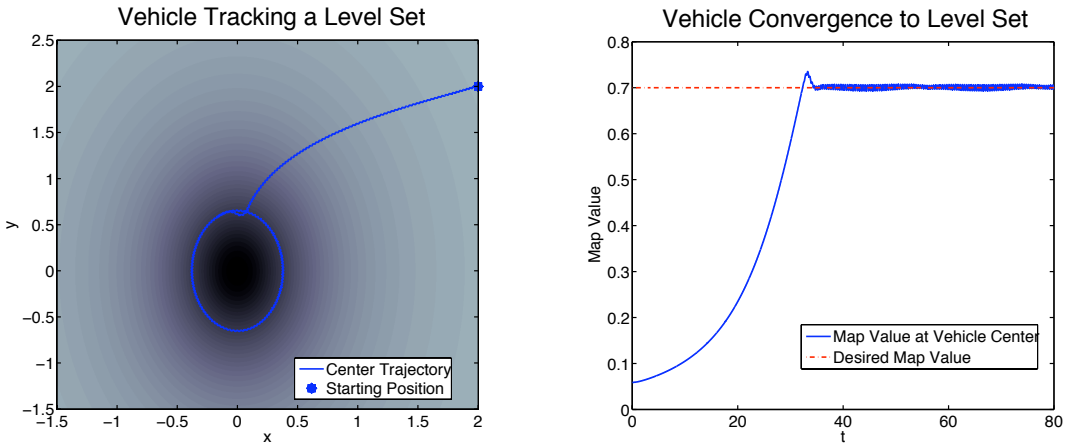

(a) (b)

Figure 4.4: (a) Trajectory of a vehicle employing extremum seeking to trace an elliptical level set. (b) Evolution of the map value at the vehicle center.

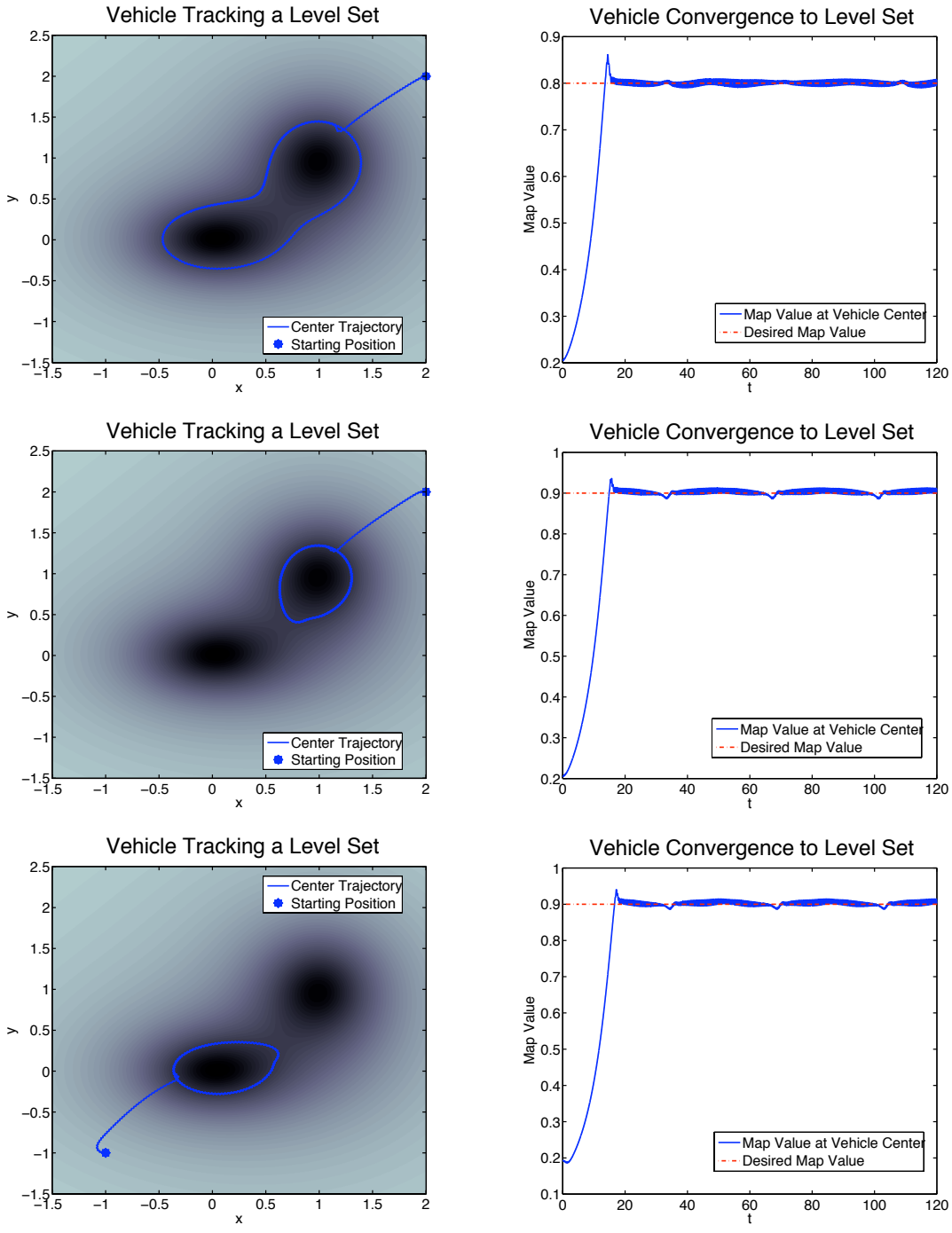

Figure 4.5: Trajectories of vehicles tracing level sets and the evolution of map values at the vehicle center.

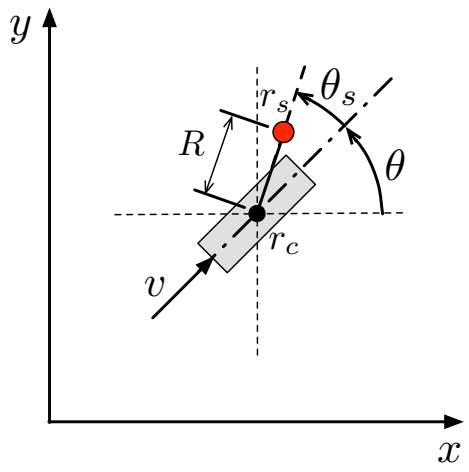

Figure 4.6: Vehicle configuration for decoupled sensor and center. θ_s is the angle between the sensor and the vehicle centerline.

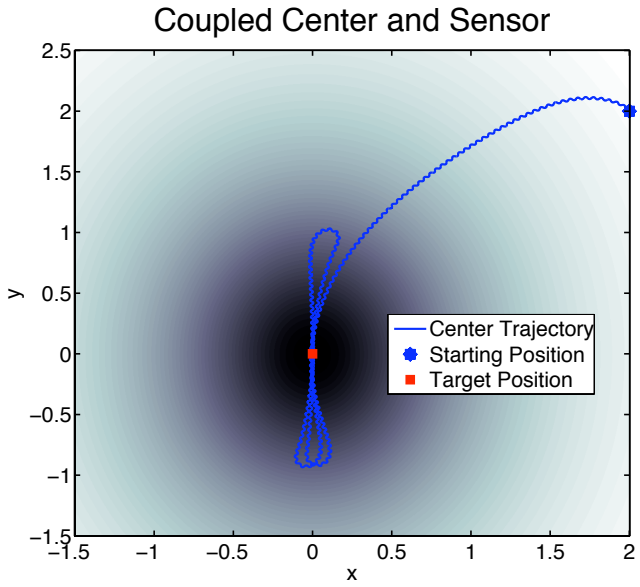

Figure 4.7: Trajectory of vehicle with coupled center and sensor dynamics.

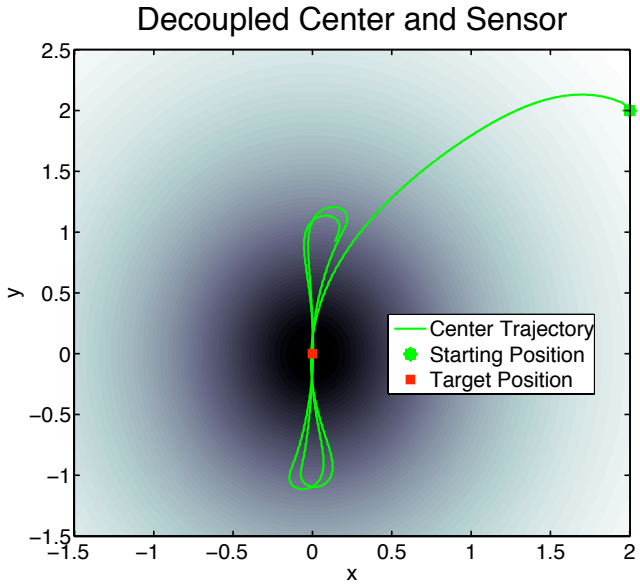

Figure 4.8: Trajectory of vehicle with decoupled center and sensor dynamics.

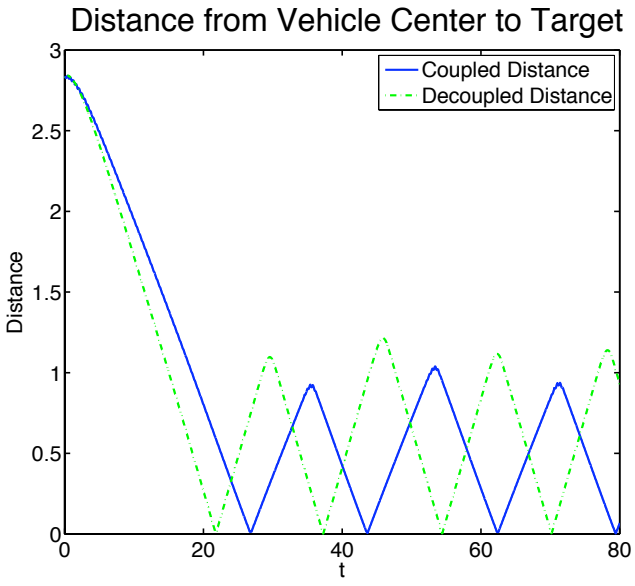

Figure 4.9: Distance between the center of the vehicle and the target.

5

GPS Denied Source Seeking For Underactuated Autonomous Vehicles in 3D

5.1 Abstract

The previous chapters introduced source seeking methods for GPS-denied autonomous vehicles using only local signal measurement and operating in two dimensions. In this chapter we extend these results to three dimensions. The 3D extensions introduce many interesting challenges, including the choice of vehicle models in 3D, sensor placement to allow probing-based gradient estimation of an unknown signal field in 3D, the question of what type of gait can be produced in an underactuated 3D vehicle to allow tuning by single-loop or multi-loop extremum seeking, and the shape of attractors, which become very complex in 3D. We present two control schemes which address these questions. The first scheme focuses on vehicles with a constant forward velocity and the ability to actuate pitch and yaw velocities. The second scheme employs vehicles with constant forward and pitch velocities and actuate only the roll velocity. Our results include convergence analysis and simulation results.

5.2 Introduction

Motivation. The field of study for autonomous vehicles operating without GPS or inertial navigation is an area of rapidly growing interest. In environments where GPS is unavailable and inertial navigation is too costly, such as urban, underground and underwater environments, other methods must be employed to navigate vehicles. Extremum seeking applied to source seeking has been presented as a method for autonomous vehicles to locate a target which emits some sort of measurable signal [22, 86, 20]. This signal could be electromagnetic, acoustic or the concentration of a chemical or biological agent. The extremum seeking method uses only the measurement of the signal from the vehicle's sensor and then employs a periodic probing movement for the vehicle to navigate the field and locate the target. Results of applying this method to vehicles operating in two dimensions show its great potential for use in many applications [23].

Contribution. In this chapter we explore the use of extremum seeking for the navigation of vehicles operating in three dimensions and present the first solution to the problem of localization and pursuit of signal sources using only local signal measurement and without position measurement in three dimensions. The extension of source seeking from two dimensions to three is interesting for several reasons, including the choice of vehicle models in 3D, sensor placement to allow probing-based gradient estimation of an unknown signal field in 3D, the question of what type of gait can be produced in an underactuated 3D vehicle to allow tuning by single-loop or multi-loop extremum seeking, and the shape of attractors that are challenging to characterize in 3D. We choose a model which is easy to relate to several different types of vehicles, and we explore different types of actuation for these vehicles.

Literature. Other researchers have considered source seeking problems: [62] looked at using vehicles modeled as point sources to track vapor emitting sources, [67] explored pursuit and evasion trajectories, and [58] and [42] looked at coordination of multiple vehicles for gradient climbing and target tracking respectively. This work is different in that the vehicle has no knowledge of its position or the position of the source, there is no communication between it and other entities, and

it has nonholonomic dynamics. While we apply the extremum seeking methods to autonomous vehicles, many groups have used the extremum seeking method in their work outside of this field, including [61] in the soft landing of valve actuators, [60] and [17] in plasma current profiles for fusion reactors, [73] in non-local stability properties, [41] in adaptive flow control, [14] in separation control, [74] in active braking systems, [48] in thermoacoustic coolers, and [88] in human exercise machines.

Models and Control Schemes Designed. We present two control schemes for actuating an autonomous vehicle operating in three dimensions whose task is to locate a target which emits a signal that the vehicle can sense. The first scheme addresses vehicles which have a constant forward velocity and can actuate both yaw and pitch velocities. We refer to this vehicle as the VYPa (Vehicle Yaw and Pitch actuated). The second scheme addresses vehicles which also have a constant forward velocity, as well as a constant pitch velocity, but can only actuate the roll velocity. We refer to this vehicle as the VeRa (Vehicle Roll actuated).

Organization of the Chapter. We start in Section 5.3 with an overview of the extremum seeking method applied to source seeking and then continue with Section 5.4, in which the vehicle model is discussed. Sections 5.5 and 5.8 detail the VYPa and VeRa control schemes respectively. Sections 5.7 and 5.8 present simulation results for each scheme. The nonlinearities in these systems give rise to interesting and complex behaviors. To analytically quantify some of these, Section 5.6 includes a local stability result and Section 5.8 includes further analysis of the final trajectories seen in simulations of the VeRa scheme. We continue with Section 5.9 where we present the application of the method to level set tracing, a problem studied in [12]. Section 5.10 concludes the chapter with our intentions for future work.

5.3 Overview of Source Seeking in 2D

Extremum seeking employs periodic forcing of a plant to perform non-model based gradient estimation [5]. In its application to autonomous vehicles [22], the vehicles considered are kinematically constrained and have no position information

available. It is assumed that a target creates some spatially distributed signal field whose shape is unknown, though its strength is known to be maximal at the target and to be decreasing away from it. Extremum seeking employs only a scalar measurement of the signal at the tip of the vehicle, periodic probing to search the vehicle's surroundings, and a demodulating signal that produces a bias input to turn the vehicle in the correct net direction. This combination has a built-in gradient estimation capability. One of the method's successes is simultaneously solving nonholonomic steering and adaptive optimization problems.

Our previous work was for vehicles in 2D, modeled as the nonholonomic unicycle, $\dot{r}_c = v e^{j\theta}$, $\dot{\theta} = \Omega$, where r_c is the vector position of the vehicle center, θ is the vehicle orientation and v and Ω are the forward and angular velocity inputs [20, 23]. These vehicles are given a constant forward velocity, $v = V_c$, while the angular velocity is tuned by extremum seeking, $\Omega(t) = a\omega\cos(\omega t) + c\sin(\omega t)\frac{s}{s+h}[J(t)]$, where a, c, h and ω are parameters of the control law and $J(t)$ is the signal reading from the vehicle sensor located at $r_s = r_c + Re^{j\theta}$. The first term $a\cos(\omega t)$ is a continuous periodic excitation of the angular velocity which allows the vehicle to probe the area and record differences in signal readings. The second term is a bias which turns the vehicle in the correct net direction and it is in fact an estimate of $\partial J(r_c, \theta)/\partial\theta$. The gain c is adjusted to make the vehicle's reaction to the signal field more or less aggressive. The result of applying this control law to the unicycle model is the exponential convergence of the vehicle to the vicinity of the signal source [22].

5.4 Vehicle Model

When extending the vehicle model from two dimensions to three, we must consider how to accurately represent a kinematically constrained vehicle which could support different vehicle configurations. We chose a kinematic model, depicted in Fig. 5.1(a). This figure shows a vehicle whose actuators, shown as cylinders with half arrows, can be used to impart surge, yaw, pitch and roll velocities. The center of the vehicle is labeled r_c, the front of the vehicle is labeled r_f. The sensor, shown as a small sphere, is located above r_f at r_s. Figure 5.1(b) contains a geometric inter-

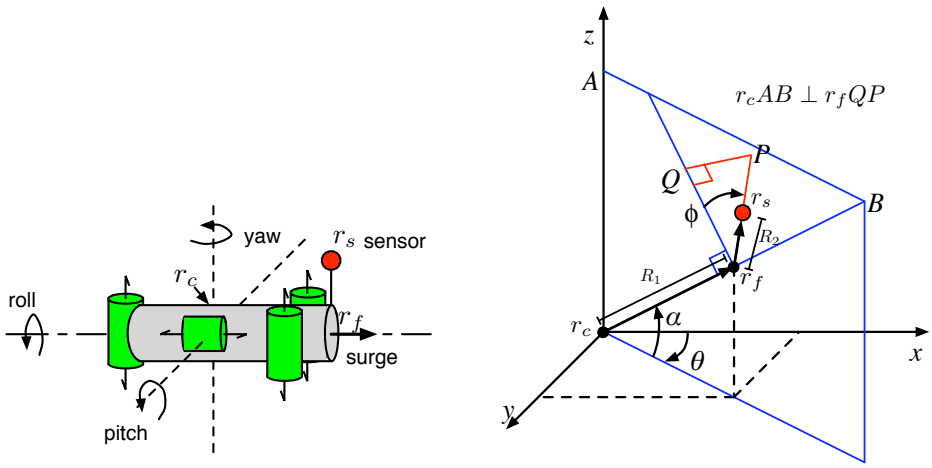

(a) (b)

Figure 5.1: (a) Pictorial drawing of the 3D vehicle. (b) Graphical interpretation of vehicle in 3D.

pretation of the drawing in Fig. 5.1(a). In the coordinate system shown, R_1 is the distance between the center r_c and the front r_f, while R_2 is the distance between the front r_f and the sensor r_s. The vector between r_f and r_s is always perpendicular to the vector between r_c and r_f. The pitch of the vehicle is defined by α, the azimuthal angle. The yaw of the vehicle is defined by θ, the polar angle. The third possible vehicle rotation, roll, is defined by ϕ, and is measured in the plane containing r_fQP relative to the plane containing r_cAB. The surge velocity, V_c, acts in the direction of $\overline{r_cr_f}$ while the pitch velocity V_2 acts in the direction of $\overline{r_fr_s}$. The azimuthal velocity $\dot{\alpha}$ and polar velocity $\dot{\theta}$, or roll velocity $\dot{\phi}$ are available as control inputs.

The differential equation governing the center of the vehicle model depicted in Fig. 5.1 is

$$\dot{r}_c = V_c \begin{bmatrix} \cos(\alpha)\cos(\theta) \\ \cos(\alpha)\sin(\theta) \\ \sin(\alpha) \end{bmatrix} \tag{5.1}$$

where $r_c = (x_c, y_c, z_c)$. The sensor position is

$$\begin{aligned} r_s &= r_c + R_1 \begin{bmatrix} \cos\alpha\cos\theta \\ \cos\alpha\sin\theta \\ \sin\alpha \end{bmatrix} \\ &\quad + R_2 \begin{bmatrix} -\cos\phi\sin\alpha\cos\theta + \sin\phi\sin\theta \\ -\cos\phi\sin\alpha\sin\theta - \sin\phi\cos\theta \\ \cos\phi\cos\alpha \end{bmatrix}, \end{aligned} \tag{5.2}$$

where $r_s = (x_s, y_s, z_s)$.

This model is used for both control schemes presented. The similarities and differences will be summarized here and expanded in the next sections. In both schemes, the surge velocity, V_c, is set to a positive constant. In the first scheme, applied to the VYPa, the sensor is placed at the tip of the vehicle, i.e., $R_2 = 0$, so the roll velocity and angle play no role. Extremum seeking is used to tune the two control inputs, the pitch and yaw velocities. In the second scheme, applied to the VeRA, the pitch velocity, V_2, is also set to a non-zero constant and extremum seeking only tunes the roll velocity for control. The distance R_2 between the r_f tip of the vehicle and r_s the sensor, must be nonzero in this case.

5.5 VYPa Vehicles

The first scheme we address is for the Vehicle Yaw and Pitch actuated – VYPa. This vehicle has a constant forward velocity, V_c, a constant roll angle of zero, and, as the name indicates, is equipped for actuation of its pitch and yaw velocities. The sensor is located at the tip of the vehicle, which equates to setting $R_2 = 0$ and results in $r_f = r_s$. Its position with respect to the vehicle center reduces to

$$r_s = r_c + R_1 \begin{bmatrix} \cos\alpha\cos\theta \\ \cos\alpha\sin\theta \\ \sin\alpha \end{bmatrix}. \tag{5.3}$$

As the surge velocity is constrained to one axis in the body frame and the angular velocity is always around an axis orthogonal to that of the surge velocity, this is the 3D analog of the unicycle.

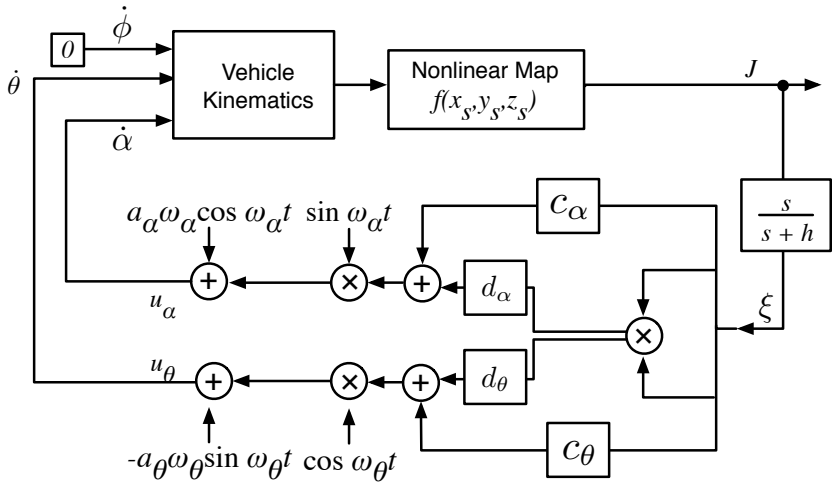

Figure 5.2: Block diagram of ES control applied to the pitch and yaw velocities of the VYPa.

Figure 5.2 shows a block diagram of the control applied to the VYPa, with extremum seeking used to tune the pitch and yaw velocities. When the roll angle is not actuated, tuning the pitch velocity is equivalent to tuning $\dot{\alpha}$, and tuning the yaw velocity is equivalent to tuning $\dot{\theta}$. The designer is free to choose the perturbation amplitudes a_α, a_θ, the perturbation frequencies ω_α, ω_θ, the extremum seeking gains c_α, $c_\theta, d_\alpha, d_\theta$, and the break frequency h of the filter. It should be noted that, by construction, ω_θ can be the same as ω_α. The perturbation amplitude a can be increased to achieve better performance with flat gradients. The higher the perturbation frequencies the more accurate the gradient estimation becomes, however, with a slower convergence rate. The VYPa model equations remain (5.1), while the control inputs, following from Figure 5.2, are

$$\dot{\alpha} = a_\alpha\omega_\alpha\cos(\omega_\alpha t) + \sin(\omega_\alpha t)(c_\alpha\xi + d_\alpha\xi^2) \tag{5.4}$$

$$\dot{\theta} = -a_\theta\omega_\theta\sin(\omega_\theta t) + \cos(\omega_\theta t)(c_\theta\xi - d_\theta\xi^2) \tag{5.5}$$

$$\dot{\phi} = 0 \tag{5.6}$$

where $\frac{s}{s+h}[J]$ is a washout filter applied to the sensor reading J.

As usual, the extremum seeking tuning consists of both 1) periodic perturbations, $a_\alpha\omega_\alpha\cos(\omega_\alpha t)$ and $-a_\theta\omega_\theta\sin(\omega_\theta t)$, which continuously probe the signal field, and

2) bias terms, $\sin(\omega_\alpha t)(c_\alpha \xi + d\xi^2)$ and $\cos(\omega_\theta t)(c_\theta \xi - d\xi^2)$, which turn the vehicle in the correct direction. The bias terms are composed of the sensor measurement which has been high-pass filtered, demodulated, and multiplied by the appropriate gains.

5.6 Convergence of VYPa Vehicle

The dynamics of the closed loop are intricate. The complexity comes from the trigonometric nonlinearities in the vehicle model, the polynomial nonlinearity in the signal map, and from the time varying forcing applied by extremum seeking. The complexity of the system increases compared to the two dimensional case as two extra states must be added to account for the dynamics in the extra dimension.

We assume the nonlinear map defining the distribution of the signal field is quadratic and takes the form $J = f(r_s) = f^* - q_r|r_s - r^*|^2$ where r^* is the unknown maximizer, $f^* = f(r^*)$ is the unknown maximum and q_r is an unknown positive constant. We define an output error variable $e = \frac{h}{s+h}[J] - f^*$ where $\frac{h}{s+h}[J]$ is a high-pass filter applied to the sensor reading J, which allows us to express ξ, the signal from the washout filter, as $\xi = \frac{s}{s+h}[J] = J - \frac{h}{s+h}[J] = J - f^* - e$. As a consequence ξ and $\dot{e}$ take the following form

$$\xi = -\left(q_r|r_s - r^*|^2 + e\right) \tag{5.7}$$

$$\dot{e} = h\xi\,. \tag{5.8}$$

Before stating our main result, we introduce the set $\mathcal{T}_\delta$ defined by

$$\begin{aligned}\mathcal{T}_\delta = &\left\{\rho - \delta \leq \sqrt{(x_c - x^*)^2 + (y_c - y^*)^2} \leq \rho + \delta\right\} \\ &\times\left\{|z_c - z^*| \leq \delta\right\}\end{aligned} \tag{5.9}$$

where

$$\rho = \sqrt{\frac{V_c J_0(\sqrt{2}a)}{\sqrt{2}c_\theta q_r R_1 J_1(\sqrt{2}a)}}\,, \tag{5.10}$$

and point out that all of the parameters $c_\theta, c_\alpha, d_\theta, d_\alpha, h, R_1, V_c, q_r$ are positive, the parameters $\omega_\alpha, \omega_\theta$ are chosen such that $\omega_\alpha = \omega_\theta = \omega$ and $J_0(a)$ and $J_1(a)$ are Bessel functions of the first kind.

Theorem 5.1 *Consider the system defined by* (5.1), (5.3)–(5.5) *and* (5.7), (5.8) *where the parameter a is chosen such that*

$$4V_c\, J_0(\sqrt{2}a) > hR_1\left(4J_0(\sqrt{2}a) - \frac{\left(\sqrt{2}J_1(2a) + J_1(2\sqrt{2}a)\right)}{J_1(\sqrt{2}a)}\right). \tag{5.11}$$

For sufficiently large ω, if $(x_c(0), y_c(0), z_c(0)) \in \mathcal{T}_\delta$ for sufficiently small $\delta > 0$, and if the quantities $|\alpha(0)|$, $\left|e(0) + q_r R_1^2 + \frac{V_c J_0(\sqrt{2}a)}{\sqrt{2}c_\theta R_1 J_1(\sqrt{2}a)}\right|$, and either $\left|\theta(0) - \arctan\frac{y_c - y^*}{x_c - x^*} + \frac{\pi}{2}\right|$ or $\left|\theta(0) - \arctan\frac{y_c - y^*}{x_c - x^*} - \frac{\pi}{2}\right|$, are all sufficiently small, then the trajectory of the vehicle center, $r_c(t)$, exponentially converges to, and remains in the set $\mathcal{T}_{O(1/\omega)}$, and the sensor reading $J(t)$ converges exponentially to a periodic function of period $2\pi/\omega$ within $O(1/\omega)$ of

$$f^* - q_r R_1^2 - \frac{V_c J_0(\sqrt{2}a)}{\sqrt{2}c_\theta R_1 J_1(\sqrt{2}a)}. \tag{5.12}$$

Furthermore, the vehicle center locally exponentially converges to a solution of the form

$$x_c^{\mathrm{attr}_i}(t) = x^* + \tilde{r}_c^{\mathrm{attr}_i}(t)\cos(\theta^{*\mathrm{attr}_i}(t))\cos(\alpha^{*\mathrm{attr}_i}(t)) \tag{5.13}$$

$$y_c^{\mathrm{attr}_i}(t) = y^* + \tilde{r}_c^{\mathrm{attr}_i}(t)\sin(\theta^{*\mathrm{attr}_i}(t))\cos(\alpha^{*\mathrm{attr}_i}(t)) \tag{5.14}$$

$$z_c^{\mathrm{attr}_i}(t) = z^* + \tilde{r}_c^{\mathrm{attr}_i}(t)\sin(\alpha^{*\mathrm{attr}_i}(t)) \tag{5.15}$$

where $i \in \{0, 1\}$ and

$$\tilde{r}_c^{\mathrm{attr}_i}(t) = \left(\rho + \tilde{r}_\mu^{\mathrm{eq_i}} + \tilde{r}_{c_0}^{\frac{2\pi}{\omega}\,\mathrm{eq_i}}(t)\right) \tag{5.16}$$

$$\theta^{*\mathrm{attr}_i}(t) = (-1)^i\left(\frac{V_c}{\rho}\left(1 + \lambda_\mu^{\mathrm{eq_i}}\right)t + \frac{V_c}{\rho}\beta_0^{\frac{2\pi}{\omega}\,\mathrm{eq_i}}(t) + \gamma^{\mathrm{eq}_i}\right) \tag{5.17}$$

$$\alpha^{*\mathrm{attr}_i}(t) = \left(\alpha_\mu^{*\mathrm{eq_i}} + \alpha_0^{*\frac{2\pi}{\omega}\,\mathrm{eq_i}}(t)\right) \tag{5.18}$$

$$\tag{5.19}$$

and where $\tilde{r}_\mu^{\mathrm{eq}_i}, \alpha_\mu^{*\mathrm{eq}_i}$ are $O(1/\omega)$, $\tilde{r}_{c_0}^{\frac{2\pi}{\omega}\,\mathrm{eq}_i}(t), \alpha_0^{*\frac{2\pi}{\omega}\,\mathrm{eq}_i}(t)$ are periodic with frequency ω, zero mean and $O(1/\omega)$, $\lambda_\mu^{\mathrm{eq}_i}$ is $O(a^2) + O(1/\omega)$, $\beta_0^{\frac{2\pi}{\omega}\,\mathrm{eq}_i}(t)$ is periodic with frequency ω, zero mean and $O(a^2) + O(1/\omega)$ and γ^{eq_i} is a constant.

Proof: We start the proof by defining the shifted variables

$$\hat{r}_c = r_c - r^* \tag{5.20}$$

$$\hat{\alpha} = \alpha - a\sin(\omega t) \tag{5.21}$$

$$\hat{\theta} = \theta - a\cos(\omega t) \tag{5.22}$$

$$\tau = \omega t \tag{5.23}$$

and noting their dynamics

$$\frac{d\hat{r}_c}{d\tau} = \frac{V_c}{\omega}\begin{bmatrix} \cos(\hat{\alpha} + a\sin(\tau))\cos(\hat{\theta} + a\cos(\tau)) \\ \cos(\hat{\alpha} + a\sin(\tau))\sin(\hat{\theta} + a\cos(\tau)) \\ \sin(\hat{\alpha} + a\sin(\tau)) \end{bmatrix} \tag{5.24}$$

$$\frac{d\hat{\alpha}}{d\tau} = \frac{1}{\omega}\Big(c_\alpha \xi \sin(\tau) + d_\alpha \xi^2 \sin(\tau)\Big) \tag{5.25}$$

$$\frac{d\hat{\theta}}{d\tau} = \frac{1}{\omega}\Big(c_\theta \xi \cos(\tau) - d_\theta \xi^2 \cos(\tau)\Big)\,. \tag{5.26}$$

We now redefine r_c by its polar coordinates

$$\tilde{r}_c = |\hat{r}_c| = \sqrt{\hat{x}_c^2 + \hat{y}_c^2 + \hat{z}_c^2} \tag{5.27}$$

$$\hat{r}_c = \tilde{r}_c \begin{bmatrix} \cos(\alpha^*)\cos(\theta^*) \\ \cos(\alpha^*)\sin(\theta^*) \\ \sin(\alpha^*) \end{bmatrix} \tag{5.28}$$

$$\tan(\theta^*) = \frac{\hat{y}_c}{\hat{x}_c} \tag{5.29}$$

$$\tan(\alpha^*) = \frac{\hat{z}_c}{\sqrt{\hat{y}_c^2 + \hat{x}_c^2}}\,. \tag{5.30}$$

Using these new definitions, the expression for ξ is

$$\xi = -q_r(\tilde{r}_c^2 + R_1^2 + 2\tilde{r}_c R_1 \xi_c) - e \tag{5.31}$$

$$\begin{aligned} \xi_c = {} & \cos(\hat{\alpha} + a\sin(\tau))\cos(\alpha^*)\cos(\hat{\theta} - \theta^* + a\cos(\tau)) \\ & + \sin(\hat{\alpha} + a\sin(\tau))\sin(\alpha^*) \end{aligned} \tag{5.32}$$

and the resulting dynamics are

$$\frac{d\tilde{r}_c}{d\tau} = \frac{\frac{d\hat{x}_c}{d\tau}\hat{x}_c + \frac{d\hat{y}_c}{d\tau}\hat{y}_c + \frac{d\hat{z}_c}{d\tau}\hat{z}_c}{\tilde{r}_c} \tag{5.33}$$

$$= \frac{V_c}{\omega}\xi_c \tag{5.34}$$

$$\frac{d\alpha^*}{d\tau} = \frac{\frac{d\hat{z}_c}{d\tau}\sqrt{\hat{y}_c^2 + \hat{x}_c^2} - \hat{z}_c\frac{d\sqrt{\hat{y}_c^2+\hat{x}_c^2}}{d\tau}}{\tilde{r}_c^2} \tag{5.35}$$

$$= \frac{V_c}{\omega}\left(\frac{\sin(\hat{\alpha} + a\sin(\tau))\cos(\alpha^*)}{\tilde{r}_c} - \frac{\cos(\hat{\alpha} + a\sin(\tau))\sin(\alpha^*)}{\tilde{r}_c} \times \cos(\hat{\theta} - \theta^* + a\cos(\tau))\right) \tag{5.36}$$

$$\frac{d\theta^*}{d\tau} = \frac{\frac{d\hat{y}_c}{d\tau}\hat{x}_c - \hat{y}_c\frac{d\hat{x}_c}{d\tau}}{\hat{y}_c^2 + \hat{x}_c^2} \tag{5.37}$$

$$= \frac{V_c}{\omega}\frac{\cos(\hat{\alpha} + a\sin(\tau))}{\tilde{r}_c\cos(\alpha^*)} \times \sin(\hat{\theta} - \theta^* + a\cos(\tau))\,. \tag{5.38}$$

The system order can be reduced from six to five by combining $\hat{\theta}$ and θ^* into the error variable

$$\tilde{\theta} = \hat{\theta} - \theta^* \tag{5.39}$$

resulting in

$$\xi_c = \cos(\hat{\alpha} + a\sin(\tau))\cos(\alpha^*)\cos(\tilde{\theta} + a\cos(\tau)) + \sin(\hat{\alpha} + a\sin(\tau))\sin(\alpha^*) \tag{5.40}$$

and the error system

$$\frac{d\tilde{r}_c}{d\tau} = \frac{V_c}{\omega}\xi_c \tag{5.41}$$

$$\frac{d\alpha^*}{d\tau} = \frac{V_c}{\omega}\left(\frac{\sin(\hat{\alpha} + a\sin(\tau))\cos(\alpha^*)}{\tilde{r}_c} - \frac{\cos(\hat{\alpha} + a\sin(\tau))\sin(\alpha^*)}{\tilde{r}_c}\right)$$

$$\times \cos(\tilde{\theta} + a\cos(\tau)) \tag{5.42}$$

$$\frac{d\hat{\alpha}}{d\tau} = \frac{1}{\omega}\Big(c_\alpha \xi \sin(\tau) + d_\alpha \xi^2 \sin(\tau)\Big) \tag{5.43}$$

$$\frac{d\tilde{\theta}}{d\tau} = \frac{1}{\omega}\Big(c_\theta \xi \cos(\tau) - d_\theta \xi^2 \cos(\tau)\Big) - \frac{V_c}{\omega}\frac{\cos(\hat{\alpha} + a\sin(\tau))\sin(\tilde{\theta} + a\cos(\tau))}{\tilde{r}_c \cos(\alpha^*)} \tag{5.44}$$

$$\frac{de}{d\tau} = \frac{h}{\omega}\xi\,. \tag{5.45}$$

$$\tag{5.46}$$

As the system equations are periodic in 2π, the average error system is

$$\frac{d\tilde{r}_c^{\text{ave}}}{d\tau} = \frac{V_c}{\omega}\xi_c^{\text{ave}} \tag{5.47}$$

$$\frac{d\alpha^{*\text{ave}}}{d\tau} = \frac{V_c}{\omega}\left(\frac{J_0(a)\sin(\hat{\alpha}^{\text{ave}})\cos(\alpha^{*\text{ave}})}{\tilde{r}_c^{\text{ave}}} - \frac{J_0(\sqrt{2}a)\cos(\hat{\alpha}^{\text{ave}})\sin(\alpha^{*\text{ave}})\cos(\tilde{\theta}^{\text{ave}})}{\tilde{r}_c^{\text{ave}}}\right) \tag{5.48}$$

$$\frac{d\hat{\alpha}^{\text{ave}}}{d\tau} = -\frac{2q_r R_1 \tilde{r}_c^{\text{ave}} \overset{\text{sin}}{\xi}_c^{\text{ave}}}{\omega}\Big(c_\alpha - 2d_\alpha(q_r(\tilde{r}_c^{\text{ave}^2} + R_1^2) + e^{\text{ave}})\Big) + \frac{4d_\alpha q_r^2 R_1^2 \tilde{r}_c^{\text{ave}^2} \overset{\text{sin}}{\xi}_c^{2\text{ave}}}{\omega} \tag{5.49}$$

$$\frac{d\tilde{\theta}^{\text{ave}}}{d\tau} = -\frac{2q_r R_1 \tilde{r}_c^{\text{ave}} \overset{\text{cos}}{\xi}_c^{\text{ave}}}{\omega}\Big(c_\theta + 2d_\theta(q_r(\tilde{r}_c^{\text{ave}^2} + R_1^2) + e^{\text{ave}})\Big) - \frac{4d_\theta q_r^2 R_1^2 \tilde{r}_c^{\text{ave}^2} \overset{\text{cos}}{\xi}_c^{2\text{ave}}}{\omega} - J_0(\sqrt{2}a)\frac{V_c}{\omega}\frac{\cos(\hat{\alpha}^{\text{ave}})\sin(\tilde{\theta}^{\text{ave}})}{\tilde{r}_c^{\text{ave}}\cos(\alpha^{*^{\text{ave}}})} \tag{5.50}$$

$$\frac{de^{\text{ave}}}{d\tau} = -\frac{h}{\omega}\Big(\Big(q_r(\tilde{r}_c^{\text{ave}^2} + R_1^2) + e\Big) + 2q_r R_1 \tilde{r}_c^{\text{ave}} \xi_c^{\text{ave}}\Big) \tag{5.51}$$

where[1]

$$\begin{aligned}
\xi_c^{\text{ave}} &= J_0(\sqrt{2}a)\cos({\alpha^*}^{\text{ave}})\cos(\hat{\alpha}^{\text{ave}})\cos(\tilde{\theta}^{\text{ave}}) \\
&\quad + J_0(a)\sin({\alpha^*}^{\text{ave}})\sin(\hat{\alpha}^{\text{ave}}) \qquad (5.52)\\
\xi_c^{\sin\text{ave}} &= -\frac{J_1(\sqrt{2}a)}{\sqrt{2}}\cos({\alpha^*}^{\text{ave}})\sin(\hat{\alpha}^{\text{ave}})\cos(\tilde{\theta}^{\text{ave}}) \\
&\quad + J_1(a)\sin({\alpha^*}^{\text{ave}})\cos(\hat{\alpha}^{\text{ave}}) \qquad (5.53)\\
\xi_c^{\cos\text{ave}} &= -\frac{J_1(\sqrt{2}a)}{\sqrt{2}}\cos({\alpha^*}^{\text{ave}})\cos(\hat{\alpha}^{\text{ave}})\sin(\tilde{\theta}^{\text{ave}}) \qquad (5.54)\\
\xi_c^{\sin 2\text{ave}} &= -\frac{\cos^2({\alpha^*}^{\text{ave}})}{4}\Big(J_1(2a)\sin(2\hat{\alpha}^{\text{ave}}) \\
&\quad + \frac{J_1(2\sqrt{2}a)}{\sqrt{2}}\sin(2\hat{\alpha}^{\text{ave}})\cos(2\tilde{\theta}^{\text{ave}})\Big) \\
&\quad + J_1(2a)\frac{\sin^2({\alpha^*}^{\text{ave}})}{2}\sin(2\hat{\alpha}^{\text{ave}}) \\
&\quad + 2\frac{J_1(\sqrt{5}a)}{\sqrt{5}}\frac{\sin(2{\alpha^*}^{\text{ave}})}{2}\cos(2\hat{\alpha}^{\text{ave}})\cos(\tilde{\theta}^{\text{ave}}) \qquad (5.55)\\
\xi_c^{\cos 2\text{ave}} &= -\frac{\cos^2({\alpha^*}^{\text{ave}})}{4}\Big(J_1(2a)\sin(2\tilde{\theta}^{\text{ave}}) \\
&\quad + \frac{J_1(2\sqrt{2}a)}{\sqrt{2}}\cos(2\hat{\alpha}^{\text{ave}})\sin(2\tilde{\theta}^{\text{ave}})\Big) \\
&\quad - \frac{J_1(\sqrt{5}a)}{\sqrt{5}}\frac{\sin(2{\alpha^*}^{\text{ave}})}{2}\sin(2\hat{\alpha}^{\text{ave}})\sin(\tilde{\theta}^{\text{ave}}). \qquad (5.56)
\end{aligned}$$

The average system (5.47)–(5.51) has equilibria defined by

$$\begin{aligned}
&\left[\tilde{r}_c^{\text{ave}^{\text{eq}_i}}, {\alpha^*}^{\text{ave}^{\text{eq}_i}}, \hat{\alpha}^{\text{ave}^{\text{eq}_i}}, \tilde{\theta}^{\text{ave}^{\text{eq}_i}}, e^{\text{ave}^{\text{eq}_i}}\right] \\
&= \left[\rho, 0, 0, (-1)^i\frac{\pi}{2}, -q_r\left(\rho^2 + R_1^2\right)\right] \qquad (5.57)
\end{aligned}$$

for $i \in \{0, 1\}$. The equilibria have the corresponding Jacobians

$$A^{\text{eq}_i} =$$

[1]Note that $\int_0^{2\pi} \mathrm{e}^{aj\sin(t)}dt = 2\pi J_0(a)$ and $\int_0^{2\pi} \mathrm{e}^{aj\sin(t)-jt}dt = 2\pi J_1(a)$.

$$\frac{1}{\omega}\begin{bmatrix} 0 & 0 & 0 & (-1)^{i+1}m_{14} & 0 \\ 0 & -m_{22} & -m_{23} & 0 & 0 \\ 0 & m_{32} & 0 & 0 & 0 \\ (-1)^i m_{41} & 0 & 0 & -m_{44} & (-1)^i m_{45} \\ -m_{51} & 0 & 0 & (-1)^i m_{54} & -h \end{bmatrix} \tag{5.58}$$

where

$$\begin{aligned} m_{14} &= V_c\, J_0(\sqrt{2}a) && (5.59)\\ m_{22} &= \frac{d_\alpha\, q_r\, R_1 V_c\, J_0(\sqrt{2}a)}{c_\theta\, J_1(\sqrt{2}a)} \\ &\quad \times \Big(\sqrt{2}J_1(2a) - J_1(2\sqrt{2}a)\Big) && (5.60)\\ m_{23} &= 2c_\alpha\, q_r\, R_1 \rho J_1(a) && (5.61)\\ m_{32} &= V_c\, J_0(a)\, \frac{\sqrt{\sqrt{2}}}{\rho} && (5.62)\\ m_{41} &= m_{41a} + m_{41b} && (5.63)\\ m_{41a} &= 4\, c_\theta\, q_r\, R_1 \frac{J_1(\sqrt{2}a)}{\sqrt{2}} && (5.64)\\ m_{41b} &= 4\, \frac{d_\theta\, q_r\, V_c\, J_0(\sqrt{2}a)}{c_\theta} && (5.65)\\ m_{44} &= \frac{d_\theta\, q_r\, R_1 V_c\, J_0(\sqrt{2}a)}{c_\theta\, J_1(\sqrt{2}a)} \\ &\quad \times \Big(\sqrt{2}J_1(2a) + J_1(2\sqrt{2}a)\Big) && (5.66)\\ m_{45} &= 4\, d_\theta\, q_r\, R_1 \rho \frac{J_1(\sqrt{2}a)}{\sqrt{2}} && (5.67)\\ m_{51} &= 2hq_r\, \rho && (5.68)\\ m_{54} &= 2hq_r\, R_1 \rho J_0(\sqrt{2}a) && (5.69) \end{aligned}$$

The characteristic polynomial for these equilibria is

$$\begin{aligned} 0 = &\Big((\omega s)^2 + m_{22}\omega s + m_{32}m_{23}\Big)\Big((\omega s)^3 + \Big(h + m_{44}\Big)(\omega s)^2 \\ &+\Big(hm_{44} + m_{41}m_{14} - m_{54}m_{45}\Big)\omega s + hm_{14}m_{41a}\Big). \end{aligned}$$

The second order polynomial has roots with negative real parts as both m_{22} and $m_{32}m_{23}$ are positive. The third order polynomial has roots with negative real parts

as, according to the assumptions in Theorem 5.1, all the coefficients are positive and the product of the s^2 and s^1 coefficients is greater than the s^0 coefficient. Therefore, the Jacobians (5.58) are Hurwitz given the assumptions in Theorem 5.1. As such, the equilibria (5.57) are exponentially stable. By applying Theorem 10.4 from [40] to this result, we conclude that the error system (5.47)–(5.51) has distinct, exponentially stable periodic solutions within $O(1/\omega)$ of the equilibria (5.57) defined by

$$\tilde{r}_c^{\text{attr}_i}(\tau) = \rho + \tilde{r}_c^{2\pi^{\text{eq}_i}}(\tau) \tag{5.70}$$

$$\alpha^{*\text{attr}_i}(\tau) = \alpha^{*2\pi^{\text{eq}_i}}(\tau) \tag{5.71}$$

$$\hat{\alpha}^{\text{attr}_i}(\tau) = \hat{\alpha}^{2\pi^{\text{eq}_i}}(\tau) \tag{5.72}$$

$$\tilde{\theta}^{\text{attr}_i}(\tau) = (-1)^i\frac{\pi}{2} + \tilde{\theta}^{2\pi^{\text{eq}_i}}(\tau) \tag{5.73}$$

$$e^{\text{attr}_i}(\tau) = -q_r\left(\rho^2 + R_1^2\right) + e^{2\pi^{\text{eq}_i}}(\tau) \tag{5.74}$$

where $\tilde{r}_c^{2\pi^{\text{eq}_i}}(\tau)$, $\alpha^{*2\pi^{\text{eq}_i}}(\tau)$, $\hat{\alpha}^{2\pi^{\text{eq}_i}}(\tau)$, $\tilde{\theta}^{2\pi^{\text{eq}_i}}(\tau)$, $e^{2\pi^{\text{eq}_i}}(\tau)$ are periodic with period 2π and are $O(1/\omega)$. This indicates the angle α^* remains within $O(1/\omega)$ of $m\pi$ and the distance between the vehicle center r_c and the source r^* converges to within $O(1/\omega)$ of the value $\rho = \sqrt{\frac{V_c J_0(\sqrt{2}a)}{\sqrt{2}c_\theta q_r R_1 J_1(\sqrt{2}a)}}$. The set $\mathcal{T}_{O(1/\omega)}$ defined in Theorem 5.1 can be derived from this set. As the attractive solution of e is a periodic function within $O(1/\omega)$ of $-q_r R_1^2 - \frac{V_c J_0(\sqrt{2}a)}{\sqrt{2}c_\theta R_1 J_1(\sqrt{2}a)}$, the sensor reading $J(t)$ converges to a periodic function within $O(1/\omega)$ of $f^* - q_r R_1^2 - \frac{V_c J_0(\sqrt{2}a)}{\sqrt{2}c_\theta R_1 J_1(\sqrt{2}a)}$. To prove the last part of the theorem, we first note that, while the error system (5.47)–(5.51) has five states, the (shifted) physical system from which the error system was derived has six, the three state vector $\hat{r}_c$, the two angles $\hat{\alpha}, \hat{\theta}$ and e. To study the attractive solutions of $\hat{r}_c$ and thus x_c, y_c, z_c, we start by determining first the θ^* part of the attractor solution from $\frac{d\theta^*}{d\tau} = \frac{V_c}{\omega}\frac{\cos(\hat{\alpha}+a\sin(\tau))\sin(\tilde{\theta}+a\cos(\tau))}{\tilde{r}_c\cos(\alpha^*)}$ .We substitute the attractor solution (5.70)–(5.74) of the error solution and find

$$\theta^{*\text{attr}_i}(t) = (-1)^i\left(\frac{V_c}{\rho}\left(1+\lambda_\mu^{\text{eq}_i}\right)t + \frac{V_c}{\rho}\beta_0^{\frac{2\pi}{\omega}^{\text{eq}_i}}(t) + \gamma^{\text{eq}_i}\right)$$

where γ^{eq_i} is a constant, $\lambda_\mu^{\mathrm{eq}_i} = \frac{1}{2\pi}\int_0^{2\pi} \lambda^{2\pi^{\mathrm{eq}_i}}(\tau)d\tau$ is the mean of[2]

$$
\begin{aligned}
\lambda^{2\pi^{\mathrm{eq}_i}}(\tau) = & \\
& -2\sin^2\left(\frac{\tilde{\theta}^{2\pi^{\mathrm{eq}_i}}(\tau) + a\cos(\tau)}{2}\right) \\
& -2\sin^2\left(\frac{\hat{\alpha}^{2\pi^{\mathrm{eq}_i}}(\tau) + a\sin(\tau)}{2}\right) \\
& \times \cos\left(\tilde{\theta}^{2\pi^{\mathrm{eq}_i}}(\tau) + a\cos(\tau)\right) \\
& + \frac{\cos\left(\hat{\alpha}^{2\pi^{\mathrm{eq}_i}}(\tau) + a\sin(\tau)\right)}{1 - 2\sin^2\left(\alpha^{*2\pi^{\mathrm{eq}_i}}(\tau)/2\right)} \\
& \times \cos\left(\tilde{\theta}^{2\pi^{\mathrm{eq}_i}}(\tau) + a\cos(\tau)\right) \\
& \times \left(2\sin^2\left(\alpha^{*2\pi^{\mathrm{eq}_i}}(\tau)/2\right) - \frac{\tilde{r}_c^{2\pi^{\mathrm{eq}_i}}(\tau)}{\rho + \tilde{r}_c^{2\pi^{\mathrm{eq}_i}}(\tau)}\right)
\end{aligned}
$$

and it is $O(a^2) + O(1/\omega)$. The quantity $\lambda_0^{\frac{2\pi}{\omega}^{\mathrm{eq}_i}}(t) = \lambda^{\frac{2\pi}{\omega}^{\mathrm{eq}_i}}(t) - \lambda_\mu^{\mathrm{eq}_i}$ is the zero-mean part of $\lambda^{\frac{2\pi}{\omega}^{\mathrm{eq}_i}}(t)$, and $\beta_0^{\frac{2\pi}{\omega}^{\mathrm{eq}_i}}(t)$ is the integral of $\lambda_0^{\frac{2\pi}{\omega}^{\mathrm{eq}_i}}(t)$, is periodic with frequency ω and is zero mean. Both $\lambda_0^{\frac{2\pi}{\omega}^{\mathrm{eq}_i}}(t)$ and $\beta_0^{\frac{2\pi}{\omega}^{\mathrm{eq}_i}}(t)$ are $O(a^2) + O(1/\omega)$. By splitting $\tilde{r}_c^{\frac{2\pi}{\omega}^{\mathrm{eq}_i}}(\tau)$ and $\alpha^{*\frac{2\pi}{\omega}^{\mathrm{eq}_i}}(\tau)$ into $\tilde{r}_\mu^{\mathrm{eq}_i} + \tilde{r}_{c0}^{\frac{2\pi}{\omega}^{\mathrm{eq}_i}}(t)$ and $\alpha_\mu^{*\mathrm{eq}_i} + \alpha_0^{*\frac{2\pi}{\omega}^{\mathrm{eq}_i}}(t)$ where $\tilde{r}_\mu^{\mathrm{eq}_i} = \frac{1}{2\pi}\int_0^{2\pi} \tilde{r}_c^{2\pi^{\mathrm{eq}_i}}(\tau)d\tau$ is $O(1/\omega)$ and the mean of $\tilde{r}_c^{\frac{2\pi}{\omega}^{\mathrm{eq}_i}}(t)$, $\alpha_\mu^{*\mathrm{eq}_i} = \frac{1}{2\pi}\int_0^{2\pi} \alpha^{*2\pi^{\mathrm{eq}_i}}(\tau)d\tau$ is $O(1/\omega)$ and the mean of $\alpha^{*\frac{2\pi}{\omega}^{\mathrm{eq}_i}}(t)$ and both $\tilde{r}_{c0}^{\frac{2\pi}{\omega}^{\mathrm{eq}_i}}(t) = \tilde{r}_c^{\frac{2\pi}{\omega}^{\mathrm{eq}_i}}(t) - \tilde{r}_\mu^{\mathrm{eq}_i}$ and $\alpha_0^{*\frac{2\pi}{\omega}^{\mathrm{eq}_i}}(t) = \alpha^{*\frac{2\pi}{\omega}^{\mathrm{eq}_i}}(t) - \alpha_\mu^{*\mathrm{eq}_i}$ are periodic, zero-mean and $O(1/\omega)$, we find (5.13)–(5.15). ■

Remark 5.1: The attractor seen in this 3D scenario is similar to the attractor seen in the 2D unicycle with a constant forward velocity and tuned angular velocity. In the 2D case the vehicle moves within an annulus, whereas in the 3D case it moves within the set $\mathcal{T}_{O(1/\omega)}$, which is inside a horizontal torus of minor radius $O(1/\omega)$ with major radius ρ.

[2]To avoid confusion between functions with period 2π, $f^{2\pi}(\tau)$, and functions with period $2\pi/\omega$, $f^{\frac{2\pi}{\omega}}(t)$, recall the transformation $\tau = \omega t$.

5.7 Illustration of VYPa Vehicle Behavior

The behavior exhibited by the vehicle is very interesting in terms of how it changes with the chosen parameters. We start this section by illustrating the behavior predicted by Theorem 5.1. We then examine scenarios which have parameter combinations that the theory does not address.

The following figures illustrate the behavior predicted in Theorem 5.1. Fig. 5.3 shows the vehicle converging to a "pseudo-orbit" around a static source which produces a signal field with spherical level sets. Fig. 5.4 illustrates the different attractors seen when the parameter c is varied within the assumptions of Theorem 5.1. The radii of the attractors decrease as c increases, as predicted by the inverse dependence of ρ on c. Fig. 5.4 also shows the local residual behavior of the vehicle center that is averaged out in the proof. Fig. 5.5 shows the vehicle converging to an attractor around a static source which produces a signal field with ellipsoidal level sets. Though the theory presented here does not include ellipsoidal level sets, the convergence to an attractor in these cases is similar to the convergence seen in the 2D cases where the target signal field is made up of elliptical level set [22]. The control law (5.4)–(5.5) also allows the vehicle to seek a moving source as seen in Fig. 5.6 where the source follows a saddle pattern and produces spherical level sets which move with the source.

The proof of Theorem 5.1 relies on both d_α and d_θ being positive, however, convergent behavior is still seen when both are negative and when d_α is made negative. The fourth combination, when d_θ is negative and d_α is positive results in unstable behavior. Fig. 5.7 illustrates the convergent behavior when both d_α and d_θ are negative. In this case the attractor seen when both parameters are positive rotates and is twisted slightly. The attractor in this case is still similar to an "orbit". This differs from the third case, illustrated in Fig. 5.8, where the attractor is no longer of an "orbit" type. In this case the vehicle moves around the surface of a sphere, staying within an $O(1/\omega)$ distance from the sphere.

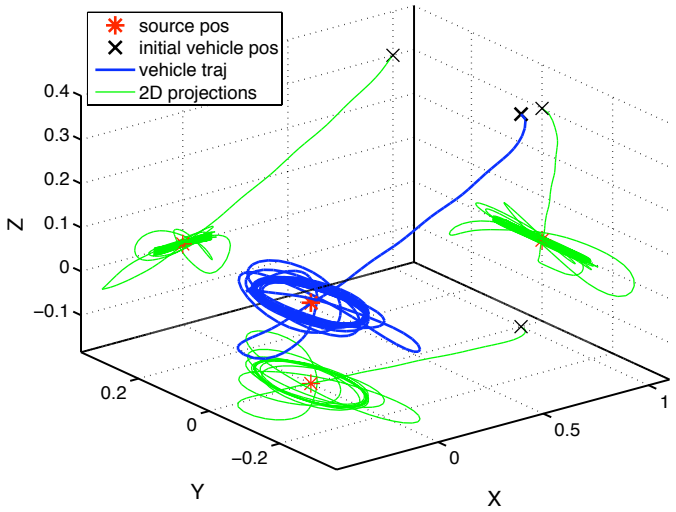

Figure 5.3: Vehicle locating a static source which creates a signal field with spherical level sets.
$V_c = 0.1, c_\theta = c_\alpha = 100,\ d_\theta = d_\alpha = 300, a = 0.5, \omega = 40, R_1 = 0.1,\ f^* = 1, q_r = 1,$ $h = 1$.

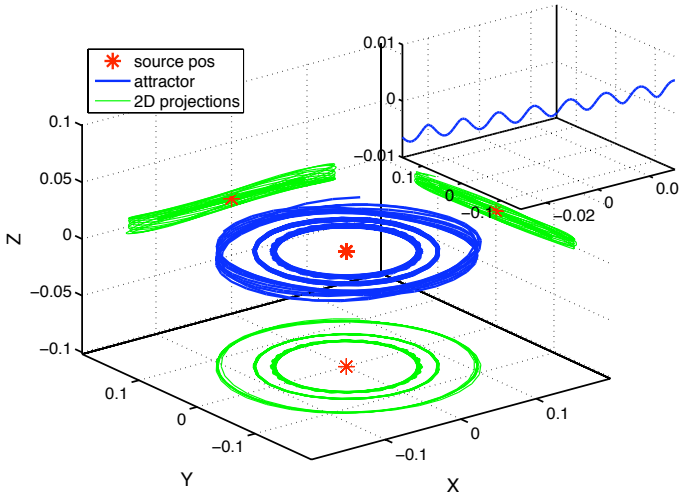

Figure 5.4: Attractors resulting from different parameter configurations.
The inset reveals the close-up behavior of the vehicle center. $V_c = 0.1, a = 0.5,\ \omega = 40,\ R_1 = 0.1,\ f^* = 1, q_r = 1, h = 1$. outer attractor: $c_\theta = c_\alpha = 100, d_\theta = d_\alpha = 300$. middle attractor: $c_\theta = 200, c_\alpha = 100, d_\theta = 600, d_\alpha = 300$. inner attractor: $c_\theta = 300,$ $c_\alpha = 100,\ d_\theta = 600, d_\alpha = 300$.

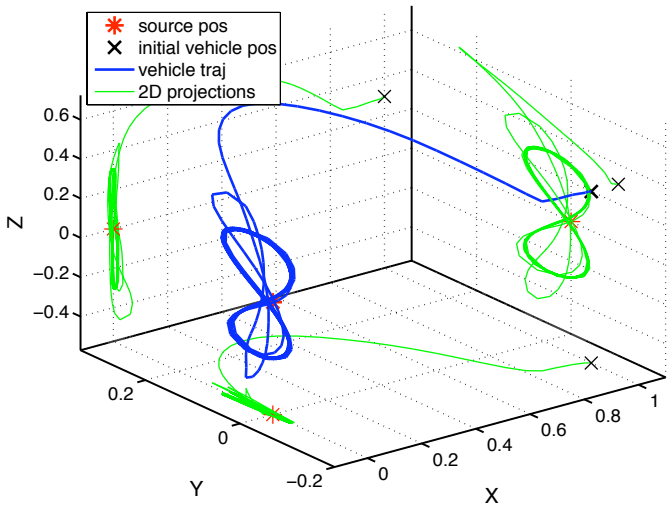

Figure 5.5: Vehicle locating a target from a signal field with ellipsoidal level sets. The attractor seen has elements similar to the attractors seen in the 2D case. $V_c = 0.1$, $c_\theta = c_\alpha = 100$, $d_\theta = 300$, $d_\alpha = 200$, $a = 0.5$, $\omega = 40$, $R_1 = 0.1$, $f^* = 1$, $q_x = 3$, $q_y = 2$, $q_z = 1$, $h = 1$.

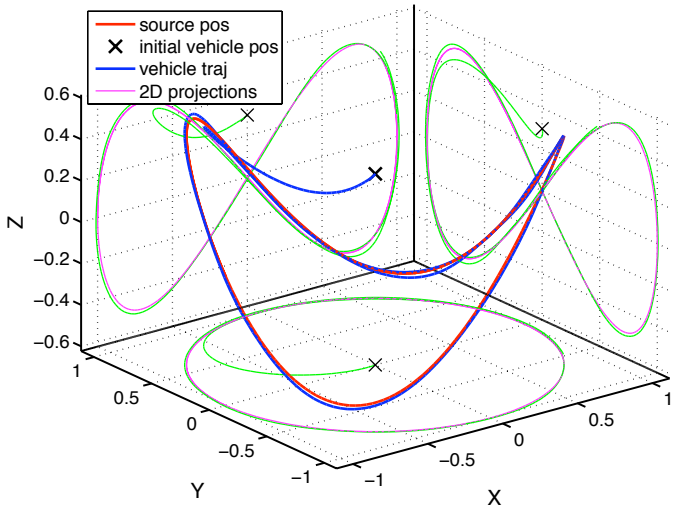

Figure 5.6: The vehicle follows the moving source which creates a signal field with spherical level sets which move with the target.

The target moves according to $(x_t(t), y_t(t), z_t(t)) = \Big(\cos(0.05t),\ \sin(0.05t),\ 0.5\sin(0.1t)\Big)$. $V_c = 0.07$, $c_\theta = c_\alpha = 100$, $d_\theta = d_\alpha = 300$, $a = 0.5$, $\omega = 10$, $R_1 = 0.1$, $f^* = 1$, $q_r = 1$, $h = 1$.

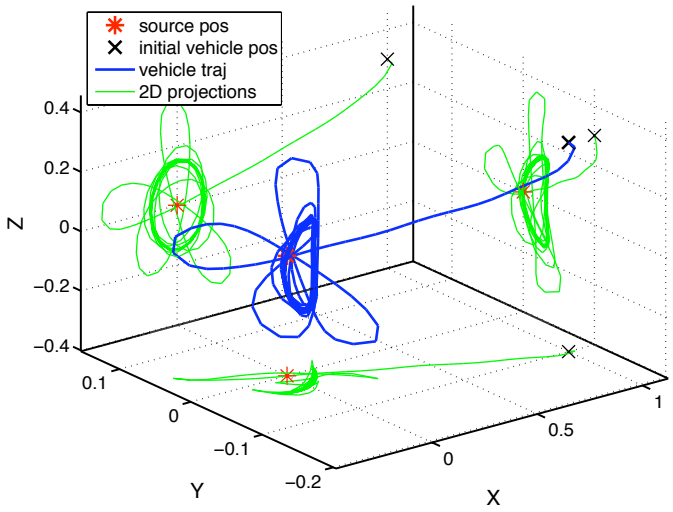

Figure 5.7: Vehicle locates a source.
Signal field has spherical level sets. The final attractor is rotated compared to other cases, but is still of an "orbit-like" form. $V_c = 0.1, c_\theta = c_\alpha = 100$, $d_\theta = 300, = d_\alpha = -300$, $a = 0.5$, $\omega = 40$, $R_1 = 0.1, f^* = 1, q_r = 1, h = 1$.

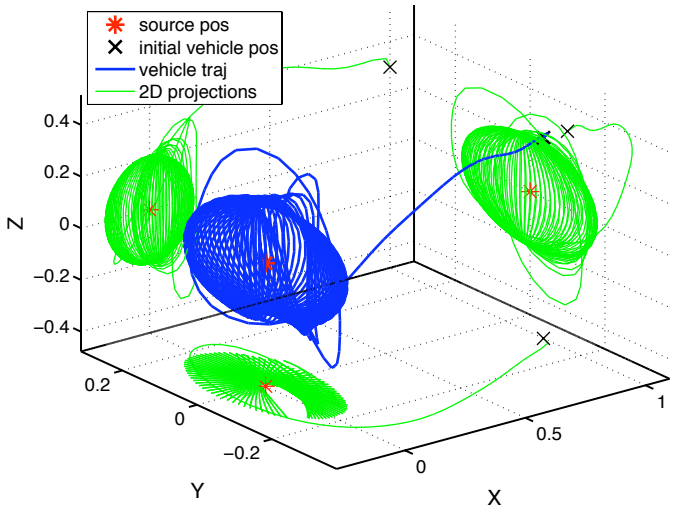

Figure 5.8: Vehicle locates a source.
Signal field has spherical level sets. The attractor is $O(1/\omega)$ within the surface of a sphere instead of an "orbit" type. $V_c = 0.2$, $c_\theta = c_\alpha = 100$, $d_\theta = 300, d_\alpha = -300$, $a = 0.5$, $R_1 = 0.1, \omega = 40, f^* = 1, q_r = 1, h = 1$.

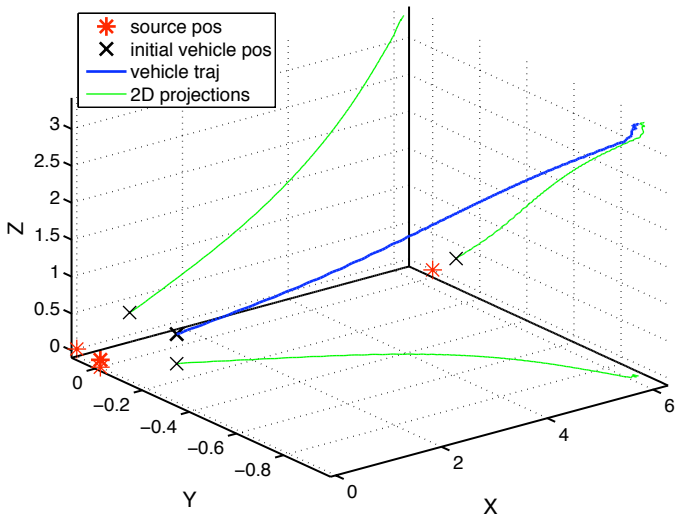

Figure 5.9: Vehicle does not locate the source – parameters produce an unstable result.
Signal field has spherical level sets. $V_c = .1$, $R_1 = .1$, $a = .5$, $\omega = 40$, $c_\theta = c_\alpha = 100$, $d_\theta = -300$, $d_\alpha = 300$.

5.8 VeRa Vehicles

The second scheme presented is for the Vehicle Roll actuated –VeRa. We consider this vehicle configuration to show both the broad applicability of extremum seeking and its use for extremely underactuated vehicles. This vehicle has both a constant forward velocity V_c and a constant pitch velocity V_2. The only tunable input, as the name indicates, is the roll velocity. In this case the sensor must be mounted off of the tip of the vehicle, which indicates $R_2 \neq 0$. When the pitch velocity V_2 is constant, the azimuthal and polar velocities become

$$\dot{\alpha} = \frac{V_2}{R_1}\cos\phi \tag{5.75}$$

$$\dot{\theta} = -\frac{V_2}{R_1}\frac{\sin\phi}{\cos\alpha}\,. \tag{5.76}$$

The VeRa model dynamics remain (5.1) with (5.75) and (5.76) governing the angles α and θ and where u_ϕ is tuned by extremum seeking. The sensor coordinates also remain (5.2).

Figure 5.10 shows a block diagram of the control applied to the VeRa, with

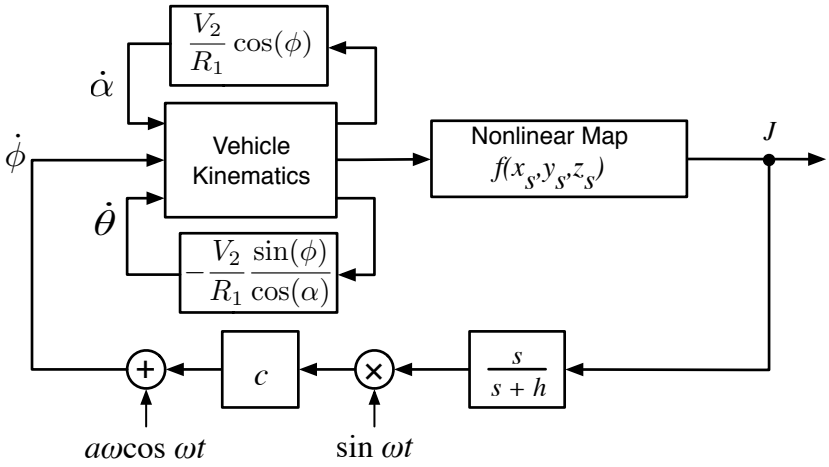

Figure 5.10: Block diagram of ES control applied to the roll velocity of the VeRa.

extremum seeking used to tune the roll velocity according to the following algorithm:

$$\dot{\phi} \;=\; a\omega\cos(\omega t) + c\sin(\omega t)\frac{s}{s+h}[J]\,. \tag{5.77}$$

For a fuller understanding of the behavior displayed while employing the scheme (5.77), we look to averaging theory again.

Proposition 5.1 *Over a finite time interval* $[0, O(\omega)]$*, the solutions of the system* (5.1), (5.75)–(5.77) *remain within* $O(1/\omega)$ *of the solutions of the following system*

$$\begin{aligned}
\frac{d\tilde{r}_c^{\text{ave}}}{d\tau} &= \frac{V_c}{\omega}\Big(\cos(\alpha^{\text{ave}})\cos(\alpha^{*\text{ave}})\cos(\tilde{\theta}^{\text{ave}}) \\
&\quad + \sin(\alpha^{\text{ave}})\sin(\alpha^{*\text{ave}})\Big) && (5.78)\\
\frac{d\alpha^{*\text{ave}}}{d\tau} &= \frac{V_c}{\omega}\frac{1}{\tilde{r}_c^{\text{ave}}}\Big(\sin(\alpha^{\text{ave}})\cos(\alpha^{*\text{ave}}) \\
&\quad - \cos(\alpha^{\text{ave}})\sin(\alpha^{*\text{ave}})\cos(\tilde{\theta}^{\text{ave}})\Big) && (5.79)\\
\frac{d\tilde{\theta}^{\text{ave}}}{d\tau} &= \frac{-1}{\omega}\left(\frac{V_2 J_0(a)}{R_1}\frac{\sin(\hat{\phi}^{\text{ave}})}{\cos(\alpha^{\text{ave}})}\right. \\
&\quad \left. + \frac{V_c}{\tilde{r}_c^{\text{ave}}}\frac{\cos(\alpha^{\text{ave}})}{\cos(\alpha^{*\text{ave}})}\sin(\tilde{\theta}^{\text{ave}})\right) && (5.80)\\
\frac{d\alpha^{\text{ave}}}{d\tau} &= \frac{1}{\omega}\frac{V_2 J_0(a)}{R_1}\cos(\hat{\phi}^{\text{ave}}) && (5.81)
\end{aligned}$$

$$
\begin{aligned}
\frac{d\hat{\phi}^{\text{ave}}}{d\tau} &= -\frac{2cq_rR_2J_1(a)\tilde{r}_c^{\text{ave}}}{\omega} \\
&\quad \times\Bigg(\cos(\alpha^{*\text{ave}})\cos(\hat{\phi}^{\text{ave}})\sin(\tilde{\theta}^{\text{ave}}) \\
&\quad -\sin(\hat{\phi}^{\text{ave}})\Big(\sin(\alpha^{*\text{ave}})\cos(\alpha^{\text{ave}}) \\
&\quad -\cos(\alpha^{*\text{ave}})\sin(\alpha^{\text{ave}})\cos(\tilde{\theta}^{\text{ave}})\Big)\Bigg) \qquad (5.82) \\
\frac{de^{\text{ave}}}{d\tau} &= -\frac{hq_r}{\omega}\Bigg(\tilde{r}_c^{\text{ave}^2} + R_1^2 + R_2^2 \\
&\quad +2R_1\tilde{r}_c^{\text{ave}}\Big(\cos(\alpha^{*\text{ave}})\cos(\alpha^{\text{ave}})\cos(\tilde{\theta}^{\text{ave}}) \\
&\quad +\sin(\alpha^{*\text{ave}})\sin(\alpha^{\text{ave}})\Big) \\
&\quad +2R_2J_0(a)\tilde{r}_c^{\text{ave}} \\
&\quad \Big(\cos(\hat{\phi}^{\text{ave}})\Big(\sin(\alpha^{*\text{ave}})\cos(\alpha^{\text{ave}}) \\
&\quad -\cos(\alpha^{*\text{ave}})\sin(\alpha^{\text{ave}})\cos(\tilde{\theta}^{\text{ave}})\Big) \\
&\quad +\cos(\alpha^{*\text{ave}})\sin(\hat{\phi}^{\text{ave}})\sin(\tilde{\theta}^{\text{ave}})\Big)\Bigg) \\
&\quad -\frac{h}{\omega}e^{\text{ave}}. \qquad (5.83)
\end{aligned}
$$

where $\tilde{r}_c = \sqrt{(x_c-x^*)^2+(y_c-y^*)^2+(z_c-z^*)^2}$, $\alpha^* = \arctan\left(\frac{z_c-z^*}{\sqrt{(x_c-x^*)^2+(y_c-y^*)^2}}\right)$, $\theta^* = \arctan\left(\frac{y_c-y^*}{x_c-x^*}\right)$, $\tilde{\theta} = \theta-\theta^*$, $\tau = \omega t$, $\hat{\phi} = \phi - a\sin(\omega t)$.

Proof: To prove this proposition, we start from the original error system,

$$
\begin{aligned}
\dot{\tilde{r}}_c &= V_c\Big(\cos(\alpha)\cos(\alpha^*)\cos(\tilde{\theta}) + \sin(\alpha)\sin(\alpha^*)\Big) \\
\dot{\alpha}^* &= \frac{V_c}{\tilde{r}_c}\Big(\sin(\alpha)\cos(\alpha^*) - \cos(\alpha)\sin(\alpha^*)\cos(\tilde{\theta})\Big) \\
\dot{\tilde{\theta}} &= -\left(\frac{V_2}{R_1}\frac{\sin(\phi)}{\cos(\alpha)} + \frac{V_c}{\tilde{r}_c}\frac{\cos(\alpha)}{\cos(\alpha^*)}\sin(\tilde{\theta})\right) \\
\dot{\alpha} &= \frac{V_2}{R_1}\cos(\phi) \\
\dot{\phi} &= a\omega\cos(\omega t) + c\sin(\omega t)\xi \\
\dot{e} &= h\xi
\end{aligned}
$$

$$
\begin{aligned}
\xi = -q_r\Bigg(&\tilde{r}_c^2 + R_1^2 + R_2^2 \\
&+2R_1\tilde{r}_c\Big(\cos(\alpha^*)\cos(\alpha)\cos(\tilde{\theta})+\sin(\alpha^*)\sin(\alpha)\Big) \\
&+2R_2\tilde{r}_c\Big(\cos(\alpha^*)\sin(\phi)\sin(\tilde{\theta}) \\
&+\cos(\phi)\Big(\sin(\alpha^*)\cos(\alpha)-\cos(\alpha^*)\sin(\alpha)\cos(\tilde{\theta})\Big)\Big)\Bigg) \\
&-e
\end{aligned}
$$

and after shifting the variables by $\tau = \omega t$, $\hat{\phi} = \phi - a\sin(\omega t)$ and noting that the system equations are periodic in 2π, we find the average system (5.78)–(5.83). ■

We now use Proposition 5.1 to study approximate, finite-time behavior of the system. The equilibria,

$$
\begin{aligned}
&\left[r_c^{\text{ave}^{\text{eq}_i}}, \alpha^{*\text{ave}^{\text{eq}_i}}, \tilde{\theta}^{\text{ave}^{\text{eq}_i}}, \alpha^{\text{ave}^{\text{eq}_i}}, \hat{\phi}^{\text{ave}^{\text{eq}_i}}, e^{\text{ave}^{\text{eq}_i}}\right] \\
=&\left[\frac{V_c R_1}{V_2 J_0(a)}, 0, (-1)^i\frac{\pi}{2}, 0, (-1)^{(i+1)}\frac{\pi}{2},\right. \\
&\left.-q_r\left(\frac{V_c^2 R_1^2}{V_2^2 J_0(a)^2} + R_1^2 + R_2^2 - 2R_2\frac{V_c R_1}{V_2 J_0(a)}\right)\right], \qquad (5.84)
\end{aligned}
$$

where $i \in \{0, 1\}$, have a characteristic polynomial given by

$$
\begin{aligned}
&\left((\omega s)^2 + \frac{V_2^2 J_0(a)^2}{R_1^2}\right)\left(\omega s + h\right) \\
&\quad\times\left((\omega s)^3 + \frac{cV_c R_1}{V_2 J_0(a)}(\omega s)^2 + c\frac{V_c V_2 J_0(a)}{R_1}\right) = 0\,. \qquad (5.85)
\end{aligned}
$$

As these equilibria are unstable, averaging theory does not yield a full characterization of the system attractors. However, this does not necessarily rule out a more complex attractor. We note that the following form of exact solutions to the average system (5.78)–(5.83),

$$\tilde{\theta}^{\text{ave}}(t) = m\pi \qquad (5.86)$$

$$\hat{\phi}^{\text{ave}}(t) = n\pi \qquad (5.87)$$

$$\alpha^{\text{ave}}(t) = (-1)^n\frac{V_2 J_0(a)}{R_1}t + c_1 \qquad (5.88)$$

$$\tilde{r}_c^{\text{ave}}(t) = \sqrt{\begin{array}{l}\left((-1)^{n+1}\frac{V_c R_1}{V_2 J_0(a)}\cos(\alpha^{\text{ave}}(t))+c_2\right)^2 \\ +\left((-1)^{n+m}\frac{V_c R_1}{V_2 J_0(a)}\sin(\alpha^{\text{ave}}(t))+c_3\right)^2\end{array}} \tag{5.89}$$

$$\alpha^{*\text{ave}}(t) = \arctan\left(\frac{(-1)^{n+1}\frac{V_c R_1}{V_2 J_0(a)}\cos(\alpha^{\text{ave}}(t)) + c_2}{(-1)^{n+m}\frac{V_c R_1}{V_2 J_0(a)}\sin(\alpha^{\text{ave}}(t)) + c_3}\right) \tag{5.90}$$

$$e^{\text{ave}}(t) = \mathrm{e}^{-ht}\left(\int_0^t f(\hat{t})\mathrm{e}^{h\hat{t}}d\hat{t} + c_4\right) \tag{5.91}$$

$$\begin{aligned} f(\hat{t}) = -hq_r\Bigg(&\tilde{r}_c^{\text{ave}}(\hat{t})^2 + R_1^2 + R_2^2 \\ &+2R_1\Big((-1)^m c_3\cos(\alpha^{\text{ave}}(\hat{t})) \\ &+c_2\sin(\alpha^{\text{ave}}(\hat{t}))\Big) \\ &+2R_2J_0(a)(-1)^n\Big(c_2\cos(\alpha^{\text{ave}}(\hat{t})) \\ &+(-1)^{m+1}c_3\sin(\alpha^{\text{ave}}(\hat{t})) - \frac{V_cR_1}{V_2J_0(a)}\Big)\Bigg) \end{aligned} \tag{5.92}$$

where n, m are integers and c_1, c_2, c_3, c_4 are constants, are very close to solutions observed by simulation of the full system. Fig. 5.11 shows the trajectory of the vehicle according to the full system equations as well as the trajectory of $\tilde{r}_c$ according to both the full system and average system equations. The solution (5.86)–(5.92) defines a single repeating "loop" with radius $\frac{V_c R_1}{V_2 J_0(a)}$ and unknown center. The drifting of these loops that is seen in the full simulation is presumably due to the system dynamics that are averaged out, similar to the drifting in the VYPa and 2D solutions which lead to the attractors not being periodic. The frequency of r_c^2 is predicted by the known parameters $\frac{V_2 J_0(a)}{R_1}$, while the point that the solution for $\tilde{r}_c^2$ oscillates about, $\left(\frac{V_c R_1}{V_2 J_0(a)}\right)^2 + c_2^2 + c_3^2$, and the amplitude of those oscillations, $2\frac{V_c R_1}{V_2 J_0(a)}\sqrt{c_2^2 + c_3^2}$, depend on unknown constants c_2, c_3. This leads to the question, is a bound on c_2, c_3, and thus the trajectories, seen in simulations? Figure 5.12 shows the path $\tilde{r}_c$ takes given different initial conditions. Each trajectory appears to be bounded

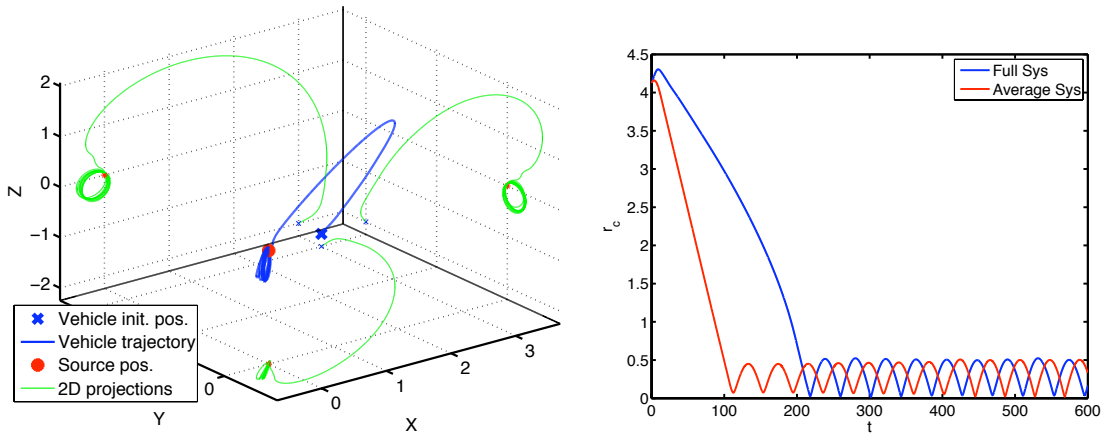

(a) (b)

Figure 5.11: VeRa locates a static source.
(a) The vehicle trajectory according to the full system equations is shown in a 3D space, with 2D projections shown on the grid walls. (b) The distance from the vehicle to the source is shown according to both the full system equations and the average system equations. $V_c = 0.04, V_2 = 0.02, c = 800, a = 1, \omega = 40, R_1 = 0.1, R_2 = 0.05, f^* = 1, q_r = 1, h = 1$.

by $2\frac{V_c R_1}{V_2 J_0(a)}$. This explanation is enforced by the observation that when $V_c < V_2$ the vehicle trajectory is tight and curly, whereas when $V_c > V_2$ the trajectory consists of wide turns as seen in Figs. 5.13 and 5.14.

Though in the case of a VYPa vehicle, the addition of a d term to the control law changes the qualitative behavior of the system (from having marginally stable attractor to having an exponentially stable attractor), the addition of a d term to the VeRa vehicle control law

$$\begin{aligned} \dot{\phi} &= a\omega\cos(\omega t) + \sin(\omega t)(c\xi - d\xi^2) \\ \xi &= \frac{s}{s+h}[J] \end{aligned}$$

does not have the same effect. The effect of this additional term is seen only in the transient and is readily seen when $V_c \ll V_2$. Figure 5.15 highlights the difference. Without a d term, the point in the middle of the vehicle, r_f, makes an unusual but consistent quadruple figure eight pattern while the vehicle is on its way to the source. With the d term, the pattern shrinks to a single figure eight pattern.

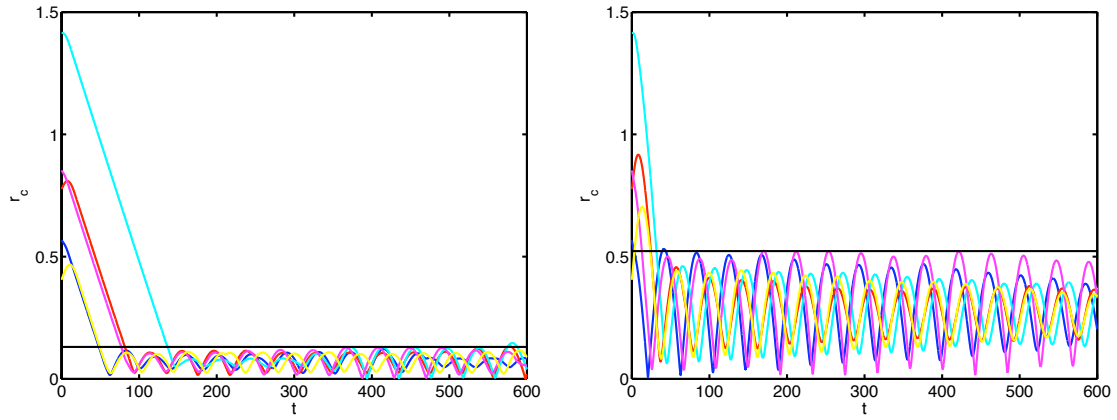

(a) (b)

Figure 5.12: VeRa distance to source.
Both (a) and (b) show the vehicle locating a static source. The different lines indicated different initial conditions. The runs appear to be bounded by the quantity: $2\frac{V_1 R_1}{V_2 J_0(a)}$, which is shown as the black line above the distance oscillations, enforcing the observation that the ratio of $V_c : V_2$ determines tight or wide turns. For all runs $c = 800, a = 1, \omega = 40, R_1 = 0.1, R_2 = 0.05, f^* = 1, q_r = 1, h = 1$. (a) $V_c = 0.01, V_2 = 0.02$. (b) $V_c = 0.04, V_2 = 0.02$.

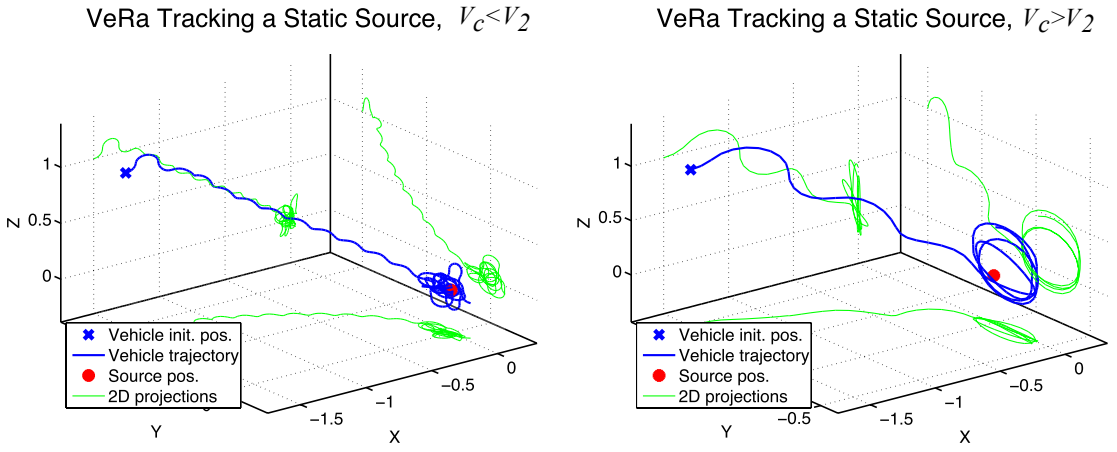

(a) (b)

Figure 5.13: VeRa tracking a static source.
For both runs $c = 400, a = 1, \omega = 30, R_1 = 0.1, R_2 = 0.05, f^* = 1, q_x = 1, q_y = 0.5, q_z = 0.75, h = 1$. (a) The tight curly trajectory of the vehicle center are a result of $V_c < V_2$. $V_c = 0.028, V_2 = 0.055$. (b) The wide turns of the vehicle center trajectory are a result of $V_c > V_2$. $V_c = 0.04, V_2 = 0.02$.

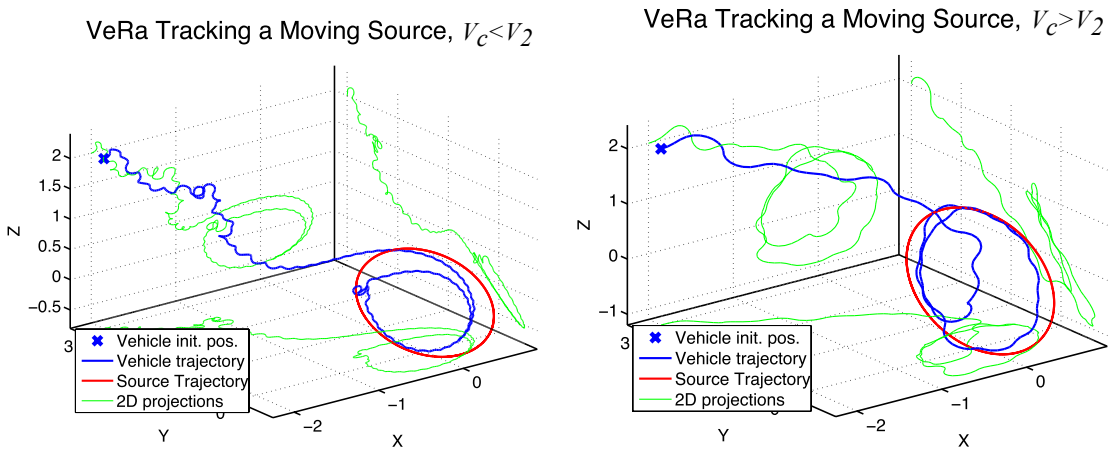

(a) (b)

Figure 5.14: Trajectory of the center of a VeRa vehicle tracking a moving source. The source moves according to $(x_t(t), y_t(t), z_t(t)) = \Big(a_t\cos(\omega_t t),\ a_t\sin(\omega_t t),\ a_{tz}\sin(\omega_{tz}t)\Big)$. For both runs $c = 400, a = 1, \omega = 30, R_1 = 0.1, R_2 = 0.05, f^* = 1, q_x = 1, q_y = 0.5, q_z = 0.75, h = 1$. (a) $V_c = 0.028, V_2 = 0.055, a_t = 0.7, a_{tz} = 0.6, \omega_t = 0.035, \omega_{tz} = 0.035$. (b) $V_c = 0.04, V_2 = 0.02, a_t = 0.75, a_{tz} = 1, \omega_t = 0.0385, \omega_{tz} = 0.0385$.

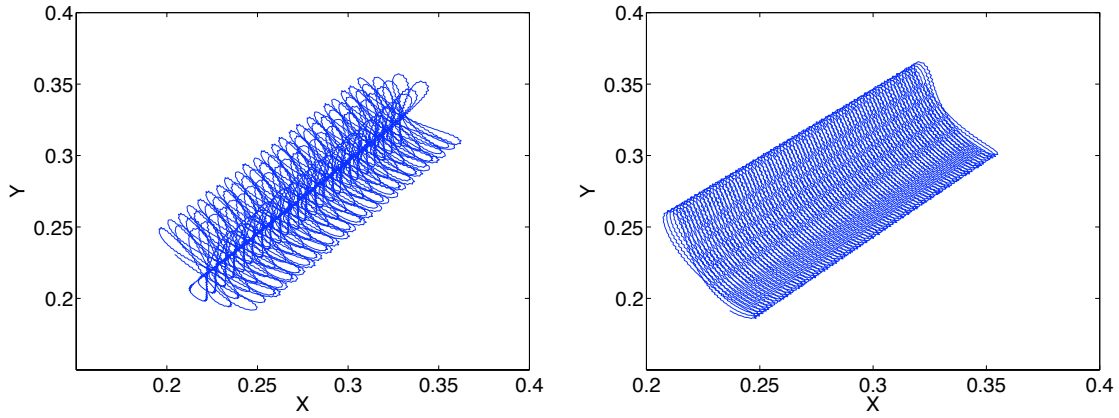

Figure 5.15: Motion of vehicle front, r_f, during transitive journey toward the source. The addition of the d term to the control law changes the pattern r_f makes as it moves. (a) d=0 (b) d=1200 The other system parameters are $V_c = 0.002, V_2 = 0.02, c = 400, a = 1, \omega = 30, R_1 = 0.1, R_2 = 0.05, f^* = 1, q_x = 1, q_y = 0.5, q_z = 0.75, h = 1$.

However, once the vehicle finds the source and starts moving around it the vehicle enters a fundamentally different motion and the d term has no useful effect.

5.9 Other Applications

The use of extremum seeking for navigation of vehicles in three dimension extends beyond source seeking. This method can also be used to explore the domain of the signal field. Other groups have looked at isoline/boundary/level set tracing [37]. However these methods require either multiple agents which must communicate, or require multiple sensors on a single agent. A PD control strategy for level set tracing without position measurement in 2D was analyzed in [12].

By employing a simple modification to the extremum seeking tuning, both the VYPa and VeRa can find and trace three dimensional level sets with only one sensor and without communication with other entities. This modification changes the input to the control laws from the sensor reading, J, to the quantity $-|J - J_d|$, where J_d is the desired level set value. The absolute value operator is used to retain

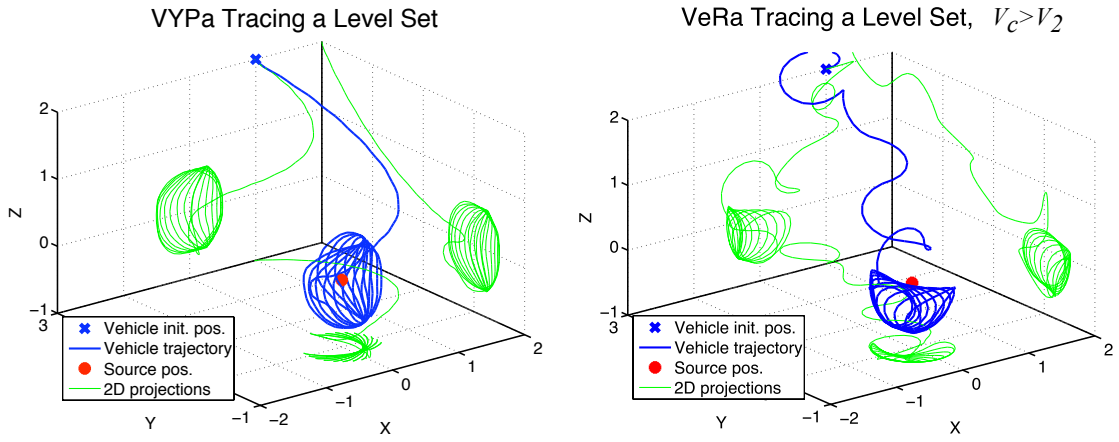

(a) (b)

Figure 5.16: Trajectories of the center of vehicles tracing level sets are shown. For both runs $f^* = 1, q_x = 1, q_y = 1, q_z = 0.5, J_d = 0.8$. (a) VYPa tracing a levelset. $V_1 = 0.11, c = 50, a = 0.5, \omega = 10, R_1 = 0.1, h = 1$. (b) VeRa tracing a levelset. $V_c = 0.07, V_2 = 0.02, c = 500, a = 0.75, \omega = 10, R_1 = 0.1, R_2 = 0.05, h = 1$.

the shape of the original signal field, as opposed to another operator, such as a the square of the difference. The control law in each case then becomes $u_k(t) = a_k\omega_k \cos(\omega_k t) + c_k \sin(\omega_k t)\frac{s}{s+h}\left[-|J(t) - J_d|\right]$ for $k \in \{\theta, \alpha, \phi\}$. Figs. 5.16(a,b) show the differences in how the VYPa and VeRa trace out the same level set on the same signal field. Notice that the vehicles naturally move around the entire three dimensional space instead of repeatedly tracing out the same curve within the level set.

5.10 Conclusions

We have shown how the extremum seeking method can be extended to vehicles with various actuating capabilities operating in three dimensions for carrying out tasks such as source seeking and level set tracing. The stability results presented extend the two dimensional work done previously and highlight the areas in which the three dimensional schemes are more complex and introduce new challenges in analysis.

In case of the VeRa design, it seems very hard to prove stability of an attractor for the motion of the vehicle near the source, though the simulation evidence is overwhelming regarding the existence of such an attractor, which is very complex, as the vehicle performs "loop" motions near the source with varying azimuthal and polar orientations and varying positions of the center of the loop relative to the position of the source. The reason for this complexity, compared to the VYPa system, is that only a single input (roll rate) is used to pursue source seeking with the 6-state kinematic VeRA system. While the value of the averaging method is in simultaneously determining the existence of a periodic solution for a (part of, or an entire) system, for the VeRa system it seems that the existence of an attractor would require one to find an analytical periodic solution of the entire nonlinear time-varying system (5.1), (5.2), (5.75)–(5.77) *before* applying averaging.

In the future we plan to explore 3D boundary/levelset tracing for processes governed by diffusion and/or convection.

This chapter is in full a reprint of the material as it has been submitted to: J. Cochran, A. Siranosian, N. Ghods, and M. Krstic, "GPS Denied Source Seeking For Underactuated Autonomous Vehicles in 3D," *IEEE Transactions on Robotics*, to appear.

The dissertation author was the primary investigator and author of this paper.

6

Fish Locomotion

6.1 Abstract

We present a method of locomotion control for underwater vehicles which are propelled by a periodic deformation of the vehicle body, similar to the way a fish moves. The control law employs extremum seeking, which is a non-model based method that has been used recently in "source seeking" control for nonholonomic mobile robots. We develop control laws for two different "fish" models which are distinguished by their respective underlying methods of propulsion. The first fish model consists of three rigid body links and relies on a two degree of freedom, *non-reciprocal*, movement which propels the fish through a perfect fluid without the use of a Kutta condition to shed vortices. The second fish model is for a fish modeled by a Joukowski airfoil which has only one degree of freedom in its movement, and thus relies on vortex shedding to move through a perfect fluid. With the use of extremum seeking, we achieve the same results in each case: The fish is capable of performing 'source seeking' in GPS-denied underwater environments, and, if position measurement is available, it is capable of navigating from point A to point B, as well as along a predetermined path.

6.2 Introduction

The literature on underwater vehicles has started to address vehicles which are propelled forward not by a traditional motor, but rather by other means - such as mimicking the movement of fish and other aquatic creatures. This chapter addresses locomotion control for underwater vehicles which employ a periodic deformation of the vehicle body, similar to the way a fish moves, to move forward. The motivation for this work comes from our previous work on source seeking for the nonholonomic unicycle with constant forward velocity [18]. In that work we use the extremum seeking method to design a control law which drives the vehicle to the vicinity of a source. We have shown that the scheme is locally exponentially convergent both in two dimensions and in three [18, 19].

Over the course of studying this control law, which employs periodic forcing, we began looking for the most suitable application, which we found in underwater vehicles which employ periodic movement for locomotion. The advantage of using extremum seeking over other control methods is that extremum seeking is a non-model based method — and thus much simpler to employ for systems, such as underwater vehicles and fish models, which do not have simple models.

In this chapter apply the same extremum seeking method to two different "fish" models and achieve the same results in each case: The fish is capable of performing 'source seeking' in GPS-denied underwater environments, and, if position measurement is available, it is capable of navigating from point A to point B, as well as along a predetermined path, depending on the designer's choice.

The fish models are distinguished by their respective underlying methods of propulsion. The first fish model, developed by [38], relies on a two degree of freedom, *non-reciprocal*, movement which propels the fish through a perfect fluid without the use of a Kutta condition to shed vortices. The second fish model, developed by [84] (and studied by [52]), has only one degree of freedom in its movement, and thus relies on vortex shedding to move through a perfect fluid. In both cases a specific periodic movement of the fish body will propel the fish forward. A slight modification to this movement, and the fish will turn. We study how to use a combination of these two "gaits" to enable the fish to move from an originating point to a desired destination

point or along a prespecified path.

Much work has been done in the area of modelling fish movement - both for the understanding of fluid dynamics and for the purpose of building more efficient vehicles that operate underwater. [27, 49, 77, 13, 50, 75, 78] have all examined locomotion by swimming and the role of vortices. References [38, 84, 52, 25] have taken the lessons learned from this previous work and extended it to the development of computational fish models in fluid systems. Unlike earlier methods, [38] uses conservation of circulation and ideas from reduction theory to build a model for a rigid body three link fish without the explicit use the fluid variables. This enables [38] to explicitly derive the equations of motion for the fish model and to study the locomotion due solely from body shape changes and not from vorticity. The model developed in [84], [52] spans the gap between studies which look at deformable bodies moving through a fluid without the use of vortex shedding and studies examining systems with rigid bodies and vortices. The Joukowski airfoil fish model relies on only one input and exploits the presence of vortices for both propulsion and steering. Both models were developed with the underlying motivation to build a platform to develop motion-planning algorithms for underwater vehicles. [76, 53, 52, 56, 39] and other research groups have developed underwater vehicles modelled after biological entities which use sinusoid-dominated movements to propel the vehicle forward. In related work, [63] and references therein have studied stabilization of vortex shedding – an area which can also lead to useful ideas for vehicle control.

A common theme in all this work is the periodic movement of the body. Any control scheme applied to these types of models/vehicles must take this periodic movement into account in order to be efficient. This immediately brings the extremum seeking method to mind as it takes advantage of periodic signals to probe a signal field. Thus we take lessons learned from previous work to combine the natural gait of the fish model with the extremum seeking method to control where the fish moves.

The chapter is structured as follows: We review our work on source seeking with the nonholonomic unicycle in Section 6.3. Section 6.4 discusses the motion of the fish and fluid systems. Section 6.5 specifically discusses a three link body moving in

a fluid, while Section 6.6 is concerned with a deformable Joukowski foil moving in a fluid with discrete vortex shedding. In each of these two sections we introduce the extremum seeking control law and discuss the results of applying the control law to the fish models. We conclude in Section 6.7.

We give a preview of our results here to help motivate the reader, as the model and control developments are lengthy and difficult to appreciate outside of the context of the problem that is eventually solved. Figures 6.1(a) and 6.1(b) display the two fish models we are considering, shown within their velocity field environments. Figure 6.2 shows a typical source seeking transient that our control algorithms in Sections 6.5 and 6.6 achieve.

A note is in order on the two models that we consider in this paper and on the notation we employ. These models are quite non-standard as control theoretic models as they consist of ODEs (the fish subsystem, with forces acting on it included, plus vortex locations and strengths in the case of Joukowski foil fish) and of an infinite-dimensional output map (the fluid potential field). The three-link fish has five states and two inputs, whereas the Joukowski foil fish has a large number of states (growing to infinity in a 'countable' manner as time goes to infinity) and one input. We develop our notation in the paper so that the two models, which are given in the spirit of geometric mechanics in the original literature [38, 52, 84], are presented here as control-oriented (input-state-output) models.

6.3 Review of Source Seeking with a Nonholonomic Unicycle

In [18] we focus on the problem of seeking the source of a scalar signal using a nonholonomic unicycle with constant forward velocity and no position information. The vehicle relies on locally sensing a scalar signal which emanates from the source it seeks. The strength of the signal is assumed to decay with distance away from the source, though other information about the signal's spatial distribution is unknown. The control law, designed using extremum seeking, jointly estimates the gradient of the signal field and drives the vehicle toward the source.

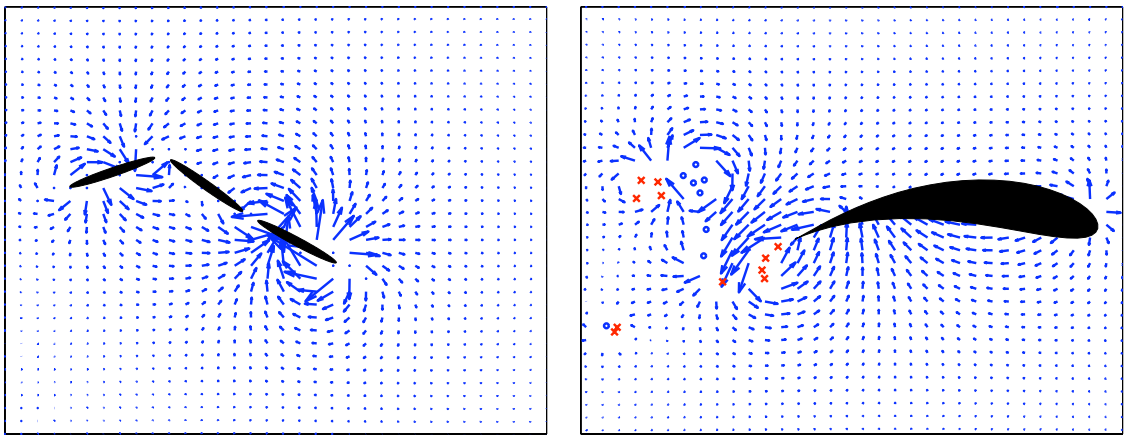

(a) (b)

Figure 6.1: A snapshow in time showing (a) the three link fish moving in a potential flow and (b) a Joukowski foil fish moving in a potential flow with point vortices. The arrows represent the velocity vectors of the fluid. The 'x's are point vortices which rotate counter clockwise, while the 'o's are point vortices which rotate clockwise.

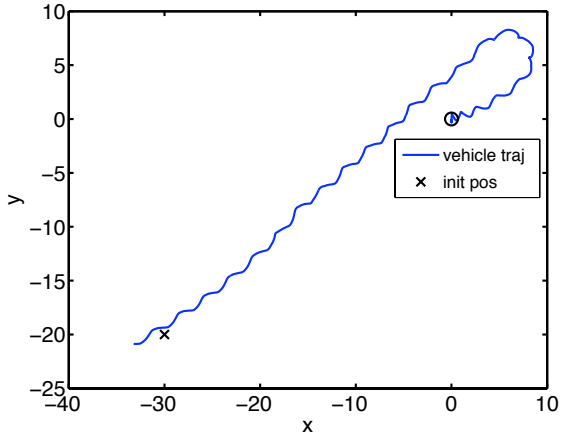

Figure 6.2: A typical trajectory of a fish-like vehicle seeking the source of some signal and being driven by our extremum seeking based control law.

While other groups have considered source seeking problems, [62] and [58], this work was different in that the vehicle has no knowledge of its position or the position of the source, there is no communication between it and other entities, and it has nonholonomic dynamics. Many groups have also employed unicycle models in their work, including [36] and [43], while others have also used the extremum seeking method in their work outside of the field of autonomous vehicles, including [61], [60], [17], [73], [41], [14], [74], [48] and [88].

The center r_c of the unicycle is governed by $\dot{r}_c = V_c e^{i\theta}$ where θ is its orientation and V_c is its constant forward velocity. The sensor position is $r_s = r_c + Re^{i\theta}$. The control is applied through angular velocity forcing $\dot{\theta} = u$, and the control law is given by

$$\dot{\theta} = u = a\omega\cos(\omega t) + c\xi\sin(\omega t) \tag{6.1}$$

$$\xi = \frac{s}{s+h}J(r_s)\,, \tag{6.2}$$

where ξ is a washout filter applied to the signal J sensed at the vehicle sensor r_s, located at a distance R away from the center and a, ω, c, h are parameters which effect performance. The control law is made of two terms which serve two different functions. The first term $a\omega\cos(\omega t)$ is a persistent excitation which allows the vehicle to probe the signal space. The second term $c\xi\sin(\omega t)$ is a bias term which jointly estimates the gradient and drives the vehicle to turn up the gradient — in essence maximizing the signal on average.

In [18] we consider a measured signal with an (unknown) spatial distribution

$$J = -q_r|r^* - r_s|^2\,, \tag{6.3}$$

where r^* is the location of the signal source, and prove convergence to a small set near the source using averaging. A detailed simulation study indicates that the controller is also stabilizing for non-circular level sets and sources which move around.

6.4 Equations of Motion in a Perfect Fluid

Though they go about it in different ways, both [84] and [38] use the same general ideas to derive the equations of motion for the fish/fluid system. In the end, they

use variations of Kirchhoffs equations for the motion of a rigid body in an ideal fluid

$$\frac{d\mathbf{L}}{dt} + \Omega\mathbf{k} \times \mathbf{L} = 0 \tag{6.4}$$

$$\frac{dA}{dt} + \mathbf{k} \cdot ([U\ V]^T \times \mathbf{L}) = 0 \tag{6.5}$$

where $\mathbf{L}$ and A are the linear and angular momentum of the fluid/body system and U, V, and Ω are the translational and rotational velocities of the body [55]. The theme of these derivations is conservation of momentum and starting the system from rest, which in turn implies $\mathbf{L} = 0$ and $A = 0$ for all time. This allows one to solve for U, V, and Ω at each time step and then integrate to derive the locomotion of the fish.

To find $\mathbf{L}$ and A, both [84] and [38] first find the kinetic energy of the system which they then differentiate to find the momentum $\mathbf{L} = \left[\frac{\partial T}{\partial U}\frac{\partial T}{\partial V}\right]^T, A = \frac{\partial T}{\partial \Omega}$ where T is the kinetic energy of the system. To find T, each group sums the kinetic energy of the fluid, T_f, plus the kinetic energy of the fish model, T_b. In the case of the Joukowski foil fish, [84], the momentum from the vortices is also taken into account.

In both cases the fluid is modeled by potential flow. The flow is assumed to be incompressible, inviscid, irrotational and at rest at infinity. In this case the velocity field $\mathbf{u}$ can be expressed in term of a potential function ϕ:

$$\nabla^2\phi = 0 \tag{6.6}$$

$$\mathbf{u} = \nabla\phi\,. \tag{6.7}$$

The boundary conditions result from two assumptions:

1) The ambient flow (flow not resulting from the fish movement) is quiescent, and thus the velocity goes to zero at ∞.

2) The fluid velocity normal to the body surface must match the velocity of the body surface in the normal direction.

These conditions are expressed as

$$\nabla\mathbf{u}|_\infty = 0 \tag{6.8}$$

$$\mathbf{u} \cdot \mathbf{n} = \dot{\mathcal{B}}|_{\mathcal{S}} \cdot \mathbf{n} \tag{6.9}$$

where $\mathcal{B}$ is the fish body and $\mathcal{S}$ is the surface of the body (touching the fluid). In the three link case [38], each link is modeled as a rigid body and the velocity of the body at its surface is straightforward to find. The potential itself is found through a boundary element method [71] as a function of the configuration of the body and its velocities. In the case of the Joukowski airfoil [84, 52], the fish is modeled as a deformable body - yet at each timestep its shape and thus the velocity of the body at its surface can be found analytically. Using complex analysis, the full velocity potential is found in closed form, also as a function of the configuration of the body and its velocities.

Using Green's theorem, the quantity

$$T_f = \frac{1}{2}\int_{\mathcal{D}} \mathbf{u}^2 dv\,, \tag{6.10}$$

where $\mathcal{D}$ is the domain and dv is the standard volume element, can be changed to

$$T_f = -\frac{1}{2}\int_{\partial S} \phi \nabla\phi \cdot \mathbf{n} ds \tag{6.11}$$

where ∂S is the surface of the fish body. In this way, as ϕ is expressed in terms of the body configuration and related velocities, and the integral is over the body surface, we have two useful occurrences: T_f is also expressed in terms of the body variables and ϕ only needs to be calculated along the surface of the body and not everywhere in the domain.

As [38] and [84] use different fish models, the kinetic energy of the fish body is found and expressed in different ways. However, in both cases the kinetic energy can be expressed solely in terms of the body configuration and velocities.

6.5 Locomotion and Source Seeking for a Three Link Fish

The *scallop theorem* discussed by [65], states that reciprocal motion in a Stokes flow does not allow for forward movement. The reasoning for this can also be applied to potential flow, thus we must take this result into account when considering fish models. Entities with one degree of freedom can only produce reciprocal motion. To

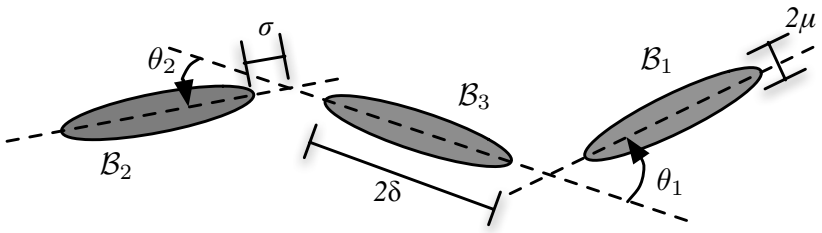

Figure 6.3: Configuration of the three link fish model.

move they must achieve separation (not possible in Stokes or potential flow) — for instance, scallop opens slowly and closes very fast to move itself forward. The three link fish developed in [38], which is mentioned in [65] and is considered here, has two degrees of freedom and can produce non-reciprocal motion. It moves forward without the use of separation (or vorticity). Depicted in Figure 6.3, each link $\mathcal{B}_i$ of the fish is an ellipse with major semi-axis of length δ and minor semi-axis of length μ. The joints which connect the links are located at a distance σ away from the tips of the ellipses and their angles are defined as θ_α, $\alpha = 1, 2$. The two inputs to the system are the angular velocities of the two joints $\dot{\theta}_1, \dot{\theta}_2$. Certain combinations of these inputs allow the fish to move forward, while others allow the fish to turn.

To build the model without the explicit use of the fluid variables, [38] In addition to exploiting the fluid system symmetry through reduction theory, [38] also formulates the problem in such as way that the net motion of the fish is equivalent to a sum of geometric and dynamic phases over closed curves in phase space. Thus, without the explicit use of the fluid variables, [38] derives the equations of motion for the fish model. This further allows [38] to show that net locomotion can result from body shape changes and not solely from vorticity. More importantly, the model is formulated in a way that allows one to apply control theory methods for motion planning and control.

We will first summarize the equations of motion for this three-link fish. This allows us to concretely discuss and depict through figures the basic gaits to move forward and to turn. We then present our control law which allows the fish to move

from an initial location to a desired one and to move along a predetermined path.

6.5.1 ODE Model with an Infinite Dimensional Output Map for a Three Link Fish in a Potential Flow

The five state variables which we use to describe the three link system are

$$\Xi = [\theta_1 \ \theta_2 \ g_3^T]^T \tag{6.12}$$

$$g_3 = [\theta_f \ f_x \ f_y]^T \tag{6.13}$$

where θ_1 and θ_2 are the angles between the links and (f_x, f_y) and θ_f are, respectively, the location of the center of the middle ellipse and the orientation of the middle ellipse with respect to the fixed inertial frame. The inputs to the system are the angular velocities of the joints,

$$\Psi = [\Psi_1 \ \Psi_2]^T , \tag{6.14}$$

i.e., $\dot{\theta}_1 = \Psi_1$, $\dot{\theta}_2 = \Psi_2$, while the infinite dimensional output map is the potential field

$$\phi(x, y) = \eta[\Xi, \Psi](x, y) , \tag{6.15}$$

which is goverened by the Laplace equation (6.6) with boundary conditions (6.8) and (6.9), and where the solution operator $\eta[\Xi, \Psi]$ is defined below. To complete this description we explain the governing ODE for $\dot{g}_3$. Reference [38] develops the motion of the three link fish using geometric phases, holonomy, and symmetry. Here we present only a summary into the equations which drive the fish, and do not redo the derivations in [38].

Each link $\mathcal{B}_i$ is defined by an orientation and position $g_i = [\theta_{\mathcal{B}_i} \ \mathcal{B}_{ix} \ \mathcal{B}_{iy}]^T$ with respect to a fixed inertial frame. The angular and translational velocities are expressed with respect to the fixed inertial frame as $\dot{g}_i$ or with respect to their own body frame as $\xi_i = \begin{bmatrix} \Omega_i \\ U_i \\ V_i \end{bmatrix}$, $i = 1, 2, 3$. As the derivation of $\dot{g}_3$ is made simpler when considering the movement with respect to the $\mathcal{B}_3$ fixed frame, instead of the inertial

frame, we make use of ξ_1 and ξ_2, not g_1 and g_2. The relationship between $\dot{g}_3$ and ξ_3 is defined by

$$\dot{g}_3 = \begin{bmatrix} 1 & 0 & 0 \\ 0 & \cos(\theta_f) & -\sin(\theta_f) \\ 0 & \sin(\theta_f) & \cos(\theta_f) \end{bmatrix} \xi_3 \,, \tag{6.16}$$

where we still must explain the relationship between ξ_3 and (Ξ, Ψ). [38] shows that the entire configuration can be defined through the movement of one link (the middle link $\mathcal{B}_3$ is the link of choice) plus the movement of the joints, i.e. the entire system can be defined by the state variables Ξ. With this in mind, the velocities of the other two links relative to the third link, but expressed with respect to their respective fixed frames, are

$$\zeta_1 = \xi_1 - \mathrm{Ad}_{x_1^{-1}} \xi_3 \tag{6.17}$$

$$\zeta_2 = \xi_2 - \mathrm{Ad}_{x_2^{-1}} \xi_3 \,, \tag{6.18}$$

where

$$\mathrm{Ad}_{x_1^{-1}}(\theta_1) = \begin{bmatrix} 1 & 0 & 0 \\ (\delta+\sigma)\sin(\theta_1) & \cos(\theta_1) & \sin(\theta_1) \\ (\delta+\sigma)(1+\cos(\theta_1)) & -\sin(\theta_1) & \cos(\theta_1) \end{bmatrix} \tag{6.19}$$

$$\mathrm{Ad}_{x_2^{-1}}(\theta_2) = \begin{bmatrix} 1 & 0 & 0 \\ -(\delta+\sigma)\sin(\theta_2) & \cos(\theta_2) & \sin(\theta_2) \\ -(\delta+\sigma)(1+\cos(\theta_2)) & -\sin(\theta_2) & \cos(\theta_2) \end{bmatrix} \tag{6.20}$$

denote the matrices that transform ξ_3 from the $\mathcal{B}_3$-fixed frame to the respective $\mathcal{B}_1$-fixed and $\mathcal{B}_1$-fixed frames. The variables ζ_1, ζ_2 are given by

$$\zeta_1 = \Pi_1 \dot{\theta}_1 = \Pi_1 \Psi_1 \tag{6.21}$$

$$\zeta_2 = \Pi_2 \dot{\theta}_2 = \Pi_2 \Psi_2 \tag{6.22}$$

$$\Pi_1 = \begin{bmatrix} 1 & 0 & +(\delta+\sigma) \end{bmatrix}^T \tag{6.23}$$

$$\Pi_2 = \begin{bmatrix} 1 & 0 & -(\delta+\sigma) \end{bmatrix}^T . \tag{6.24}$$

To continue, we examine the kinetic energy of the fluid

$$T_f = -\frac{1}{2}\int_{\partial S} \phi \nabla\phi \cdot \mathbf{n} ds \tag{6.25}$$

where $\partial S = \sum_1^3 \partial\mathcal{B}_i$ is the boundary over all three bodies, which can be expressed in terms of "added inertias" $\mathbb{M}_{ij}^f$ and ξ_i as

$$T_f = \frac{1}{2}\sum_{i=1}^{3}\sum_{j=1}^{3} \xi_i^T \mathbb{M}_{ij}^f(\Xi)\xi_j. \tag{6.26}$$

The "added inerties" $\mathbb{M}_{ij}^f$ depend on the configuration of the three link body Ξ and are derived in [38]. This is a consequence of being able to express ϕ solely in terms of the body configuration and velocities:

$$\phi = \sum_{i=1}^{3}\left(\Omega_i\mathcal{X}_i + \begin{bmatrix} U_i \\ V_i \end{bmatrix} \cdot \varphi_i\right) = \sum_{i=1}^{3}[\mathcal{X}_i \ \varphi_i^T]\xi_i \tag{6.27}$$

where $\mathcal{X}_i(x, y, \Xi)$ and $\varphi_i(x, y, \Xi)$ define potential functions which depend *only* on θ_1, θ_2 and g_3 and the spatial coordinates (x, y). The quantities $\mathcal{X}_i$ and φ_i depend on coefficients which are found using a boundary element method [71] and depend only on Ξ, and do not depend on the spatial coordinates. These coefficients are used to find $\mathbb{M}_{ij}^f(\Xi)$. The kinetic energy of the bodies $T_{\mathcal{B}_i} = \frac{1}{2}\left(\mathcal{I}\Omega_i^2 + m\left(U_i^2 + V_i^2\right)\right)$ can also be expressed in terms of ξ_i

$$T_{\mathcal{B}_i} = \frac{1}{2}\xi_i^T \mathbb{M}_i^b \xi_i \tag{6.28}$$

$$\mathbb{M}_i^b = \begin{pmatrix} \mathcal{I} & 0 & 0 \\ 0 & m & 0 \\ 0 & 0 & m \end{pmatrix} \tag{6.29}$$

where m is the mass of the ellipse and $\mathcal{I} = m(a^2 + b^2)/4$ is the body moment of inertia. The total kinetic energy of the system is then expressed as

$$T = \frac{1}{2}\sum_{i=1}^{3}\sum_{j=1}^{3} \xi_i^T \mathbb{I}_{ij}\xi_j \tag{6.30}$$

$$\mathbb{I}_{ij} = \mathbb{M}_{ij}^f(\Xi) \qquad \text{for } i \neq j \tag{6.31}$$

$$\mathbb{I}_{ii} = \mathbb{M}_{ii}^f(\Xi) + \mathbb{M}_i^b\,. \tag{6.32}$$

The total effective momentum, expressed with respect to the $\mathcal{B}_3$ fixed frame is

$$h_s = \sum_{i=1}^{3}\sum_{j=1}^{3} \mathrm{Ad}^T_{x_i^{-1}} \mathbb{I}_{ij}\xi_j \tag{6.33}$$

where $\mathrm{Ad}^T_{x_i^{-1}}(\theta_i)$ transforms from the $\mathcal{B}_i$-fixed frame to the $\mathcal{B}_3$-fixed frame. (Note that $\mathrm{Ad}^T_{x_3^{-1}}$ is the identity operator.) Equation (6.33) can now be rewritten as

$$h_s = \sum_{i=1}^{3} \mathrm{Ad}^T_{x_i^{-1}} \mathbb{I}_{i3}\xi_3 + \sum_{i=1}^{3}\sum_{\alpha=1}^{2} \mathrm{Ad}^T_{x_i^{-1}} \mathbb{I}_{i\alpha}\Big(\zeta_\alpha + \mathrm{Ad}_{x_\alpha^{-1}}\xi_3\Big) \tag{6.34}$$

The quantity h_s is governed by Kirchhoff-like equations and as we assume that the system starts from rest, h_s remains zero for all time. This leads to an equation for ξ_3

$$\begin{aligned}
\xi_3(\Xi,\Psi) &= -\Big(\sum_{i=1}^{3} \mathrm{Ad}^T_{x_i^{-1}} \mathbb{I}_{i3} + \sum_{i=1}^{3}\sum_{\alpha=1}^{2} \mathrm{Ad}^T_{x_i^{-1}} \mathbb{I}_{i\alpha}\mathrm{Ad}_{x_\alpha^{-1}}\Big)^{-1} \sum_{i=1}^{3}\sum_{\alpha=1}^{2} \mathrm{Ad}^T_{x_i^{-1}} \mathbb{I}_{i\alpha}\zeta_\alpha \\
&= -\Big(\sum_{i=1}^{3} \mathrm{Ad}^T_{x_i^{-1}} \mathbb{I}_{i3} + \sum_{i=1}^{3}\sum_{\alpha=1}^{2} \mathrm{Ad}^T_{x_i^{-1}} \mathbb{I}_{i\alpha}\mathrm{Ad}_{x_\alpha^{-1}}\Big)^{-1} \sum_{i=1}^{3}\sum_{\alpha=1}^{2} \mathrm{Ad}^T_{x_i^{-1}} \mathbb{I}_{i\alpha}\Pi_\alpha\Psi_\alpha
\end{aligned} \tag{6.35}$$

Thus evolution equation governing the system is

$$\dot{\Xi} = \begin{bmatrix} \Psi_1 \\ \Psi_2 \\ l\Big(\Xi,\Psi\Big) \end{bmatrix} \tag{6.36}$$

where the vector field $l = \Big[l_1\ l_2\ l_3\Big]^T$ is defined by the right hand side of (6.16). The infinite dimensional output map $\eta[\Xi,\Psi](x,y)$ defined in (6.27), which describes the fluid field throughout the domain is given in a more detailed form as

$$\eta[\Xi,\Psi](x,y) = \tau_1(\Xi,\Psi)^T\Pi_1\Psi_1 + \tau_2(\Xi,\Psi)^T\Pi_2\Psi_2 + \sum_{i=1}^{3}\tau_i(\Xi,\Psi)^T\Gamma_i(\Xi)\xi_3(\Xi,\Psi) \tag{6.37}$$

where $\tau_i(\Xi,\Psi) = [\mathcal{X}_i(x,y,\Xi)\ \ \varphi_i^T(x,y,\Xi)]^T$ and $\Gamma_1 = \mathrm{Ad}_{x_1^{-1}}(\theta_1)$, $\Gamma_2 = \mathrm{Ad}_{x_2^{-1}}(\theta_2)$ and $\Gamma_3 = I$. Thus the complete dynamic system is given by the five-dimensional state equation (6.36) and the infinite-dimensional output map (6.37).

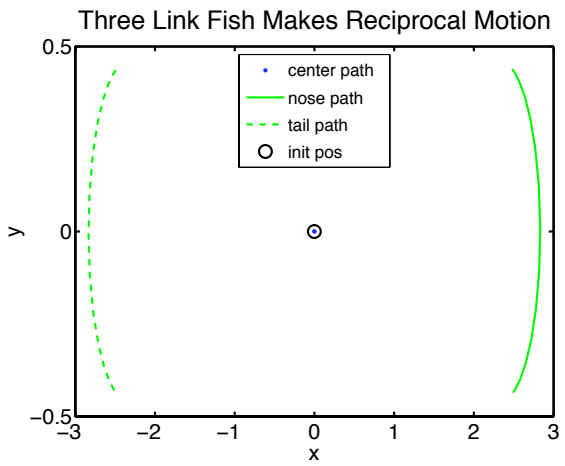

Figure 6.4: Reciprocal motion of the three link fish: $\beta_0 = 1$, $\theta_1|_{t=0} = 0$, $\theta_2|_{t=0} = 0$.

6.5.2 Reciprocal Motion

Though the three link fish can produce non-reciprocal motion as shown by [38], all allowable motions of the fish do not necessarily have that property — a fact which we highlight here. The movement of the three link fish is determined by the two inputs which are the angular velocities of the two joints. Examples of inputs which produce reciprocal motion are

$$\dot{\theta}_1 = \cos(t) \tag{6.38}$$

$$\dot{\theta}_2 = \beta_0 \cos(t) \tag{6.39}$$

for $\beta_0 \in \Re$. Figures 6.4, 6.5 and 6.6 show the motion of the center and far edges of the fish when executing this kind of motion. In the first case the center link simply rotates about its center while in the second case the center fish link moves up and down. Figure 6.7 depicts a sequence of snap shots in time of reciprocal fish motion when $\beta_0 = 1$, $\theta_1|_{t=0} = -1$, $\theta_2|_{t=0} = 0$. The arrows indicating the fluid motion highlight the symmetry of the motion and thus the fluid field causing the fish to make no net forward locomotion.

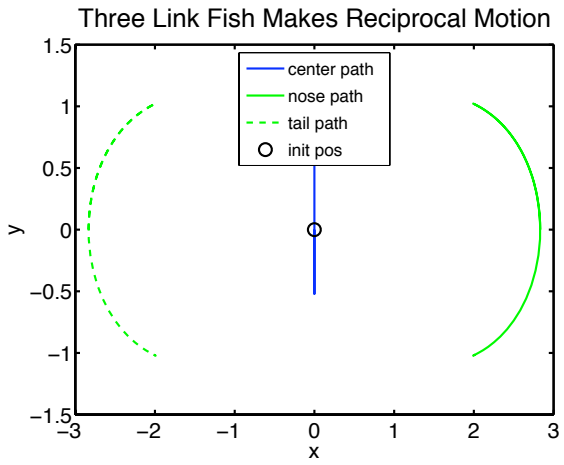

Figure 6.5: Reciprocal motion of the three link fish: $\beta_0 = -1$, $\theta_1|_{t=0} = 0$, $\theta_2|_{t=0} = 0$.

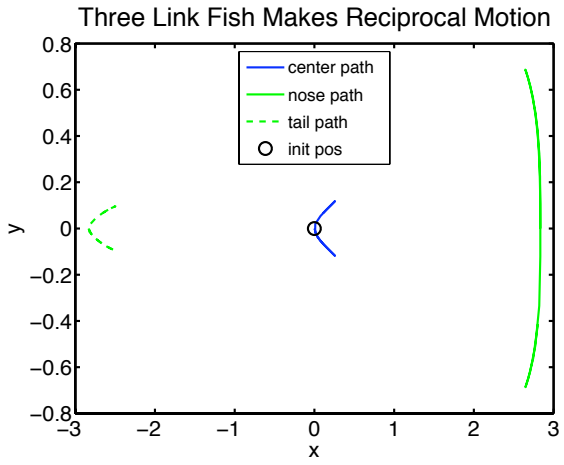

Figure 6.6: Reciprocal motion of the three link fish: $\beta_0 = 1/2$, $\theta_1|_{t=0} = 0$, $\theta_2|_{t=0} = 0$.

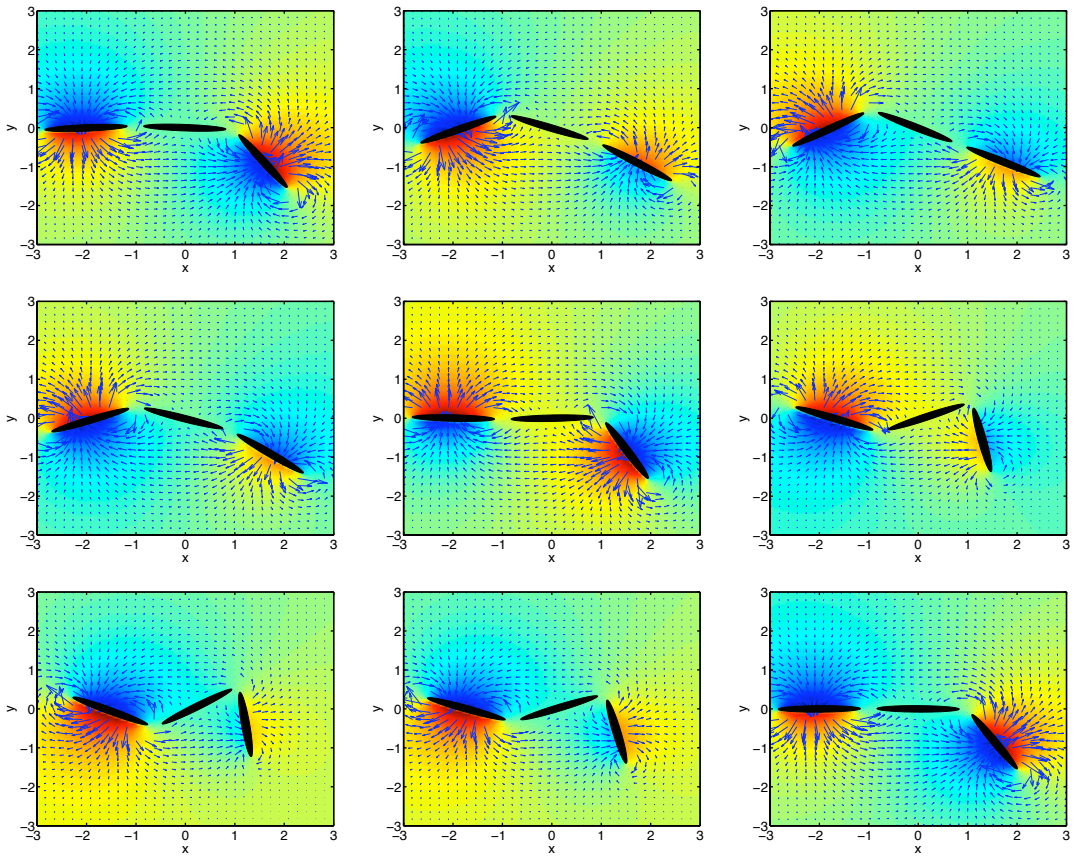

Figure 6.7: Snapshots in time of reciprocal motion.
The background color field represents the potential field ϕ with red representing positive values and blue representing negative values. $\beta_0 = 1$, $\theta_1|_{t=0} = -1$, $\theta_2|_{t=0} = 0$

6.5.3 Basic Gaits for Three Link Fish

We consider two basic gaits: moving forward and turning, which were first studied by [38]. The angular velocities for both gaits are the same

$$\dot{\theta}_1 = a\omega \sin(\omega t) \tag{6.40}$$

$$\dot{\theta}_2 = a\omega \cos(\omega t) \tag{6.41}$$

but the initial condition differs; The initial conditions for moving forward are

$$\theta_1|_{t=0} = -a \tag{6.42}$$

$$\theta_2|_{t=0} = 0 \tag{6.43}$$

leading to

$$\theta_1 = -a \cos(\omega t) \tag{6.44}$$

$$\theta_2 = \sin(\omega t)\,. \tag{6.45}$$

However, the initial conditions for turning are

$$\theta_1|_{t=0} = \beta - a \tag{6.46}$$

$$\theta_2|_{t=0} = -\beta \tag{6.47}$$

leading to

$$\theta_1 = -a \cos(\omega t) + \beta \tag{6.48}$$

$$\theta_2 = a \sin(\omega t) - \beta\,. \tag{6.49}$$

Note that $\beta = a = \omega = 1$ in [38]. Figure 6.8 shows the fish moving forward for different parameter combinations, while Figure 6.9 shows the fish turning in circles for different parameter combinations. Figure 6.10 shows snapshots in time of the fish moving forward. The subtle difference in the fluid field that results from this movement verses the fluid field that results from the reciprocal motion in Figure 6.7 highlights how the fish moves itself forward.

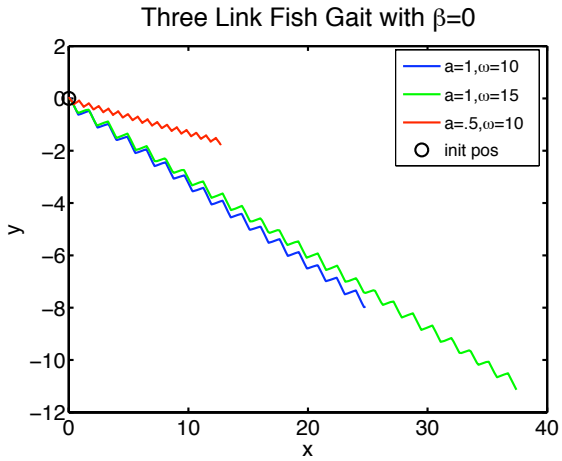

Figure 6.8: Forward gaits of a three link fish. $\beta = 0$.

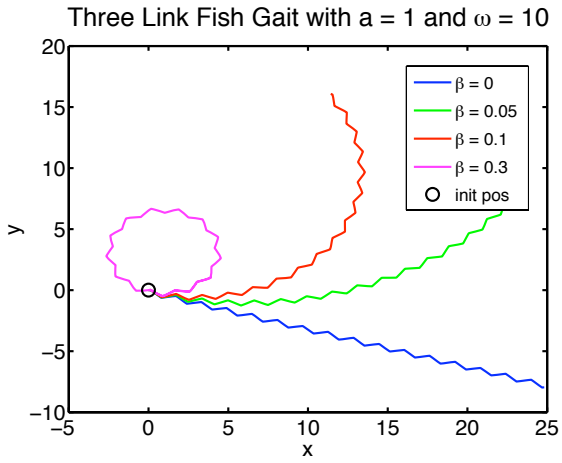

Figure 6.9: Turning gaits of a three link fish. $a = 1$, $\omega = 10$.

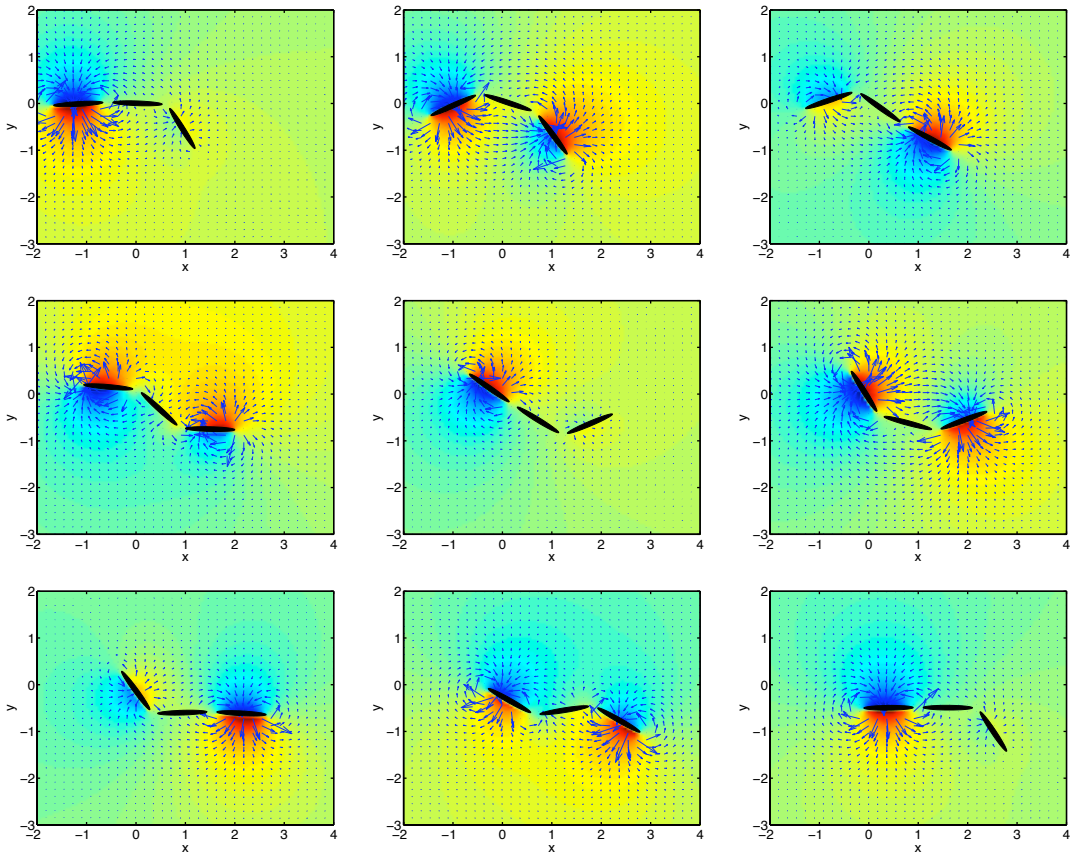

Figure 6.10: Snapshots in time of the fish moving forward.
The background color field represents the potential field ϕ with red representing positive values and blue representing negative values. The subtle difference in the fluid field that results from this movement versus the fluid field that results from the reciprocal motion in Figure 6.7 highlights how the fish moves itself forward. $a = 1$, $\theta_1|_{t=0} = -1$, $\theta_2|_{t=0} = 0$

6.5.4 Source Seeking With a Three Link Fish

We take the basic gaits of the three link fish and modify them to enable the fish to move both from an initial location to a desired location in space and along a predetermined path. There are two parts to our control law: 1) how to apply extremum seeking to the gaits and 2) what function to optimize with extremum seeking.

As explained in Section 6.3, the control law for the nonholonomic unicycle (6.1) is made up of two parts: a persistent excitation $a\omega\cos(\omega t)$ which allows the entity to probe the space and a feedback term $c\xi\sin(\omega t)$ which allows the entity to turn and move up the gradient. The persistent excitation $a\omega\cos(\omega t)$ is exactly what we see in (6.40), modulo a phase shift. If we assume β depends on time instead of being constant, then, following (6.48)–(6.49) we find

$$\dot{\theta}_1 = a\omega\sin(\omega t) + \dot{\beta} \tag{6.50}$$

$$\dot{\theta}_2 = a\omega\cos(\omega t) - \dot{\beta}\,. \tag{6.51}$$

By equating $\dot{\beta} = -c\xi\cos(\omega t)$ we arrive at our control law

$$\dot{\theta}_1 = a\omega\sin(\omega t) - c\xi\cos(\omega t) \tag{6.52}$$

$$\dot{\theta}_2 = a\omega\cos(\omega t) + c\xi\cos(\omega t)\,. \tag{6.53}$$

$$\xi = \frac{s}{s+h}[J] \tag{6.54}$$

Thus the turing parameter β depends on the function J we wish to optimize and the fish moves in such a way to maximize the value output value of J.

The question now becomes, what exactly is J? The ultimate goal is to move the fish either from an initial location in space to desired one (x^*, y^*) in space or along a path P^*. In the first case, if we assume the fish can somehow sense the distance between itself and the goal location (x^*, y^*), then we wish to minimize that distance and, similar to (6.3), we can define J as the function

$$J = -q_r\Big(\big(f_{sx} - x^*\big)^2 + \big(f_{sy} - y^*\big)^2\Big) \tag{6.55}$$

$$f_s = \begin{bmatrix} f_x + \cos(\theta_f)(\delta+\sigma) + \cos(\theta_1+\theta_f)(2\delta+\sigma) \\ f_y + \sin(\theta_f)(\delta+\sigma) + \sin(\theta_1+\theta_f)(2\delta+\sigma) \end{bmatrix} \tag{6.56}$$

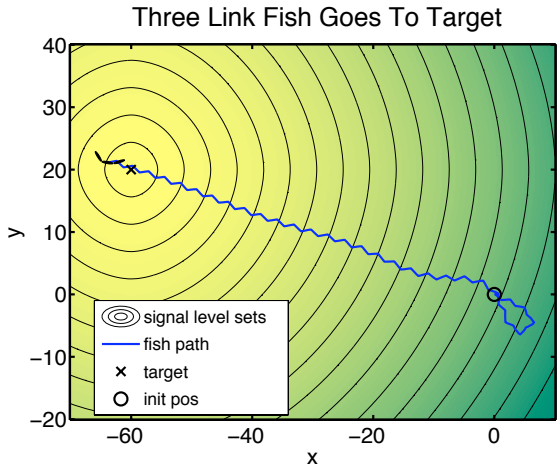

Figure 6.11: Source seeking for a three link fish.
The background color field represents the "concentration" of the signal field J with yellow representing higher values than green. $a = 1$, $c = 2$, $\omega = 10$, $h = 10$, $q_r = 1/100$, $\delta = 5/6$, $\sigma = 1/6$.

where $f_s = (f_{sx}, f_{sy})$ is the location of the sensor which we assume to be at the tip of the forward ellipse, i.e. the fish nose. Figure 6.11 shows a typical simulation of the fish moving to a desired location under the algorithm (6.52)–(6.54). This simulation was made while enforcing the constraint that the tuning variable β does not exceed a certain value — the amplitude of the probing signal a. This ensures the links do not cross themselves as the fish moves.

From (6.55), (6.56) it may appear that the fish needs the information about the target's position and about its own position. This is not always the case. With measurement of $J(t)$ alone, the fish can be guided by the algorithm (6.52)–(6.54) to reach a local maximum J^* on physical space, as in [18, 19].

6.5.5 Path Following for a Three Link Fish

The function J, optimized by extremum seeking, can be modified so that the fish can not only move from to a desired location, but also so that the fish can follow a predefined path. There are a myriad of ways to construct J for this purpose, however, the one we choose to use here is fairly simple. We define a path

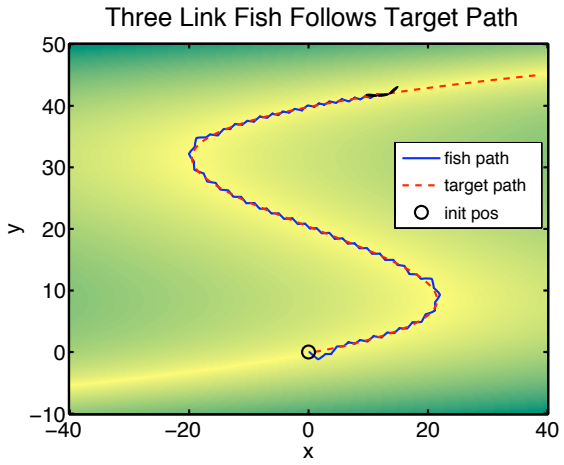

Figure 6.12: Three link fish following a predetermined path.
The background color field represents the "concentration" of the signal field J with yellow representing higher values than green. $a = 1$, $c = 2$, $\omega = 10$, $h = 10$, $\delta = 5/6$, $\sigma = 1/6$.

parametrically and use the error to define J. For instance, we define the target path $x = a_1 y^3 + a_2 y^2 + a_3 y + a_4$ and define J as a function of the error between f_{sx} and $a_1 f_{sy}^3 + a_2 f_{sy}^2 + a_3 f_{sy} + a_4$. The error can be multiplied by a gain and can be raised to a power to obtain different gradient fields. Figure 6.12 shows the fish following the path defined by $x = 2/300y^3 - 2/5y^2 + 16/3y + 1$. The fish optimizes

$$J = -5\sqrt{|f_{sx} - 2/300 f_{sy}^3 - 2/5 f_{sy}^2 + 16/3 f_{sy} + 1|} \tag{6.57}$$

to follow this path.

6.6 Locomotion and Source Seeking for a Joukowski Foil Fish

We now move to the discussion of locomotion for a deformable Joukowski foil. [84, 52] have used the Joukowski transformation, a class of conformal maps, to study a fish modelled as an airfoil. The transformation

$$z = F(\zeta) = \zeta + \zeta_c + \frac{\alpha}{\zeta + \zeta_c} \tag{6.58}$$

allows the parameterization of a circle $\zeta = r_c e^{i\theta}$ in the ζ-plane to describe an airfoil in the $z = x + iy$ plane. The parameters $\zeta_c = \zeta_x + i\zeta_y \in \mathbb{C}$ and $\alpha \in \mathbb{R}$ determine the foil shape. Varying the imaginary part $\Im\{\zeta_c\} = \zeta_y$ while enforcing the constraint $r_c = |\zeta_c - \alpha|$ with r_c constant, as is done in [84, 52] and in this work, causes the camber of the foil to vary as well. This variation allows for one degree of freedom, which, by itself, will not allow the fish to make forward progress in a potential flow. To counter this, [84, 52] add discrete point vortices to the system, modelled after vortex shedding by actual fish. (The potential function in this case encompasses the domain of the fluid minus small circles at the locations of the vortices.) The vortices are shed at discrete time instants from the trailing edge of the fish. When this happens, an exchange of momentum ensues and the fish is capable of moving forward. By periodically varying $\dot{\zeta}_y$ — the single input to the system — in a certain way, the fish will move forward or turn.

The model presented in [84, 52] spans the gap between studies which look at deformable bodies moving through a fluid without the use of vortex shedding and studies examining systems with rigid bodies and vortices. Through the model in [84, 52], the authors successfully address motion planning problems for fish locomotion, using only one input and exploiting the presence of vortices for both propulsion and steering.

Similarly to the three link fish, we will first summarize the equations of motion for the fish foil, though we do not rederive these equations. After discussing the basic gaits to move forward and to turn, we then present our control law which allows the fish to move both to a desired location and along a specific path.

6.6.1 ODE Model With an Infinite Dimensional Output Map for a Joukowski foil fish in a Potential Flow with Point Vortices

The continually growing number of state variables of this system are

$$\Xi \;=\; \left[\zeta_y \; g \; \Lambda^T \, \Gamma^T\right]^T \tag{6.59}$$

where $g = [\theta_f \ f_x \ f_y]^T$, $\Lambda = [\zeta_1 \ \zeta_2 \ ...]^T$, with $\zeta_k \in \mathbb{C}^N$, is a vector of the location of each point vortex and $\Gamma = [\gamma_1 \ \gamma_2 \ ...]^T$, with $\gamma_k \in \mathbb{R}$, is a vector of the strength of each point vortex. The variables θ_f and (f_x, f_y) are the orientation and location of the foil fish with respect to the spatially fixed frame. The number of vortices N continues to grow as time goes on; at periodic discrete points in time another vortex is added. The system has one input, $\dot{\zeta}_y = \Psi$ while the output map defines the potential field and is given in the infinite dimensional form $\phi(x, y) = \eta[\Xi, \Psi](x, y)$, which should not be confused with (6.15) as Ξ defined in (6.12) and (6.59) are different and the inputs Ψ in the two problems are also different. To complete the model description we must develop expressions for the evolution of all the state variables and define the output operate η.

Both [84] and [52] develop the equations of motion for a Joukowski foil in a perfect fluid with point vortices. [52] develops the expression for the potential function which [84] uses (and therefore we use as well). However, [52] uses Newton's second law to derive the motion of the body, while [84] applies conservation laws. We use the motion derived by [84].

The complex potential $W(z) = \phi(z) + i\psi(z)$ is an analytic function where ϕ is the potential function and ψ is the stream function. Similarly to the three link fish case, we use a frame of reference attached to the foil and we express $W(z)$ in terms of the body configuration and velocities as

$$\begin{aligned} w(\zeta) = W(z) \ &= \ U w_1(\zeta) + V w_2(\zeta) + \Omega w_3(\zeta) \\ &\quad + \dot{\zeta}_x w_{s1}(\zeta) + \dot{\zeta}_y w_{s2}(\zeta) + \dot{\alpha} w_{s3}(\zeta) \\ &\quad + \sum_{k=1}^{N} w_{pv}^k(\zeta) \end{aligned} \tag{6.60}$$

where U, V are the translational velocities of the foil, Ω is the rotational velocity, N is the number of vortices in the flow and $w_{pv}^k(\zeta)$ represents the contribution to the potential from the k-th vortex. As noted in [84], the "subscript 's' appears in conjunction with variables describing the shape of the foil." Finding the functions w_i and w_{si} corresponds to satisfying the boundary condition that the normal component of the fluid velocity must match the normal component of the velocity of the foil at its surface. The velocity of the foil at its surface is a combination of the translational

and rotational velocities of the foil *plus* the velocities associated with the change in shape $\dot{\zeta}_x, \dot{\zeta}_y, \dot{\alpha}$, which depends on the input $\Psi = \dot{\zeta}_y$. The full expressions for these functions are listed in Appendix A. The functions w^k_{pv} are found using the *Milne-Thomson circle theorem* [55]

$$w^k_{pv} = i\gamma_k \left(\log(\zeta - \zeta_k) - \log\left(\zeta - \frac{r_c^2}{\bar{\zeta}_k}\right) \right) \tag{6.61}$$

where ζ_k is the location of the k-th point vortex, and γ_k is its strength.

Using the complex potential $W(z)$, the kinetic energy of the fluid can be determined from the same integral used in Section 6.5.1

$$T_f = -\frac{1}{2}\int_{\partial S} \phi(\nabla\phi \cdot \mathbf{n}) ds \tag{6.62}$$

where ∂S is the surface of the foil. Given that ϕ is a function of the body configuration, the body velocities and the point vortices, T_f can be expressed as

$$T_f = \frac{1}{2}[\mathbf{U}^T \ \dot{\mathbf{s}}^T \ \Gamma^T] \begin{bmatrix} & \mathbb{M}^{T_f} & \end{bmatrix} \begin{bmatrix} \mathbf{U} \\ \dot{\mathbf{s}} \\ \Gamma \end{bmatrix} \tag{6.63}$$

$$\mathbf{U} = [\Omega \ U \ V]^T \tag{6.64}$$

$$\mathbf{s} = [\zeta_x \ \zeta_y \ \alpha]^T \tag{6.65}$$

$$\Gamma = [\gamma_1 \ ... \ \gamma_N]^T \tag{6.66}$$

where the body shape $\mathbf{s}(\zeta_y)$ can be determined from ζ_y alone, the matrix $\mathbb{M}^{T_f}(\mathbf{s}, \Lambda)$ depends only on the foil *shape* $\mathbf{s}(\zeta_y)$ and the location of the vortices and the change in body shape $\dot{\mathbf{s}}(\mathbf{s}, \Psi)$ depends only the shape $\mathbf{s}(\zeta_y)$ and the input Ψ. The relationship between ζ_y and ζ_x, a is defined as

$$\zeta_x = \frac{(1-\mu)}{(1+\mu)}\sqrt{r_c^2 - \zeta_y^2} \tag{6.67}$$

$$\begin{aligned} \alpha &= \zeta_x - \sqrt{r_c^2 - \zeta_y^2} \\ &= -\frac{2\mu}{(1+\mu)}\sqrt{r_c^2 - \zeta_y^2} \end{aligned} \tag{6.68}$$

where $\mu \in (0, 1)$ is a constant. The kinetic energy of the foil can also be expressed in term of the body configuration and velocities

$$T_{\mathcal{B}} = \frac{1}{2}[\mathbf{U}^T \ \dot{\mathbf{s}}^T] \begin{bmatrix} & \mathbb{M}^{T_{\mathcal{B}}} & \end{bmatrix} \begin{bmatrix} \mathbf{U} \\ \dot{\mathbf{s}} \end{bmatrix} \tag{6.69}$$

where the matrix $\mathbb{M}^{T_\mathcal{B}}(\mathbf{s})$ depends on only the shape $\mathbf{s}$ of the foil. The total effective momentum of the system is

$$A = \frac{\partial(T_\mathcal{B}+T_f)}{\partial\Omega} - \frac{1}{2}\sum_{k=1}^{N}(-2\pi\gamma_k)(|\mathbf{z}_k|^2 - |\mathbf{z}_0|^2) \tag{6.70}$$

$$\mathbf{L} = \begin{bmatrix} \frac{\partial(T_\mathcal{B}+T_f)}{\partial U} \\ \frac{\partial(T_\mathcal{B}+T_f)}{\partial V} \end{bmatrix} + \sum_{k=1}^{N}(-2\pi\gamma_k)(\mathbf{z}_k+\mathbf{z}_0)\times\mathbf{k} \tag{6.71}$$

where the terms due to the vortices are developed in [70], $\mathbf{z}_k = [\Re\{z_k\}\ \Im\{z_k\}]^T$ is the vector location of the k-th vortex in the foil-fixed frame, and $\mathbf{z}_0$ is the location of the origin of the foil-fixed frame with respect to the spatially-fixed frame. The momentum is governed by (6.4)–(6.5) and the system starts from rest; therefore $\mathbf{L} = [L_x\ L_y]^T = 0$ and $A = 0$ for all time. Thus we have a system of equations

$$\begin{bmatrix} A \\ L_x \\ L_y \end{bmatrix} = I\begin{bmatrix} \Omega \\ U \\ V \end{bmatrix} + B\begin{bmatrix} \dot\zeta_x \\ \dot\zeta_y \\ \dot\alpha \end{bmatrix} + P\begin{bmatrix} \gamma_1 \\ \vdots \\ \gamma_N \end{bmatrix} \tag{6.72}$$

with a solution

$$\mathbf{U}(\Xi,\Psi) = -I^{-1}\left(B\dot{\mathbf{s}} + P\Gamma\right) \tag{6.73}$$

where the matrices $I(\mathbf{s})$ and $B(\mathbf{s})$ depend only on the foil shape $\mathbf{s}$ and the matrix $P(\mathbf{s},\Lambda)$ depends on the shape plus the locations of the vortices.

The remaining two items to summarize are 1) the motion of the point vortices and 2) how to add vortices. The motion of the vortices

$$\dot\zeta_k = p_k(\Xi,\Psi) = \left(\overline{\frac{dW_k}{dz}} - (U+iV+i\Omega z_k) - \frac{\partial F}{\partial\zeta_c}\dot\zeta_c - \frac{\partial F}{\partial\alpha}\dot\alpha\right)\frac{1}{F'(\zeta_k)} \tag{6.74}$$

$$W_k(z) = W(z) - i\gamma_k\log(z-z_k) \tag{6.75}$$

is stated in [84] and is found using *Routh's rule* [57]. The point vortices are added to the system one by one at discrete points in time. [84] chooses the trailing edge of the foil as $(\alpha-\zeta_c)$ while choosing the stagnation point (the location of the new point vortex) as $\zeta_n = 1.5(\alpha-\zeta_c)$. Thus the condition

$$\left.\frac{dw}{d\zeta}\right|_{\zeta=\zeta_n} = 0 \tag{6.76}$$

must be satisfied to guarantee the stagnation point. The addition of the new vortex causes the effective fluid momenta to change, and thus the body momentum must change as well. The discrete change in $\mathbf{U}$, denoted as $\Delta\mathbf{U}$, plus the strength of the new vortex γ_n must satisfy

$$I\Delta\mathbf{U} + P\gamma_n = 0 \tag{6.77}$$

to ensure the conservation of momentum.

The calculation of $\mathbf{U}$ is split into 1) intervals of time where (6.72) is used to find the body's translational and rotational velocities due to the body configuration and its shape velocities and 2) points in time where (6.76) and (6.77) are used to calculate the discrete change in the body velocities.

Thus, the complete dynamic system is given by the evolution equation

$$\dot{\Xi} = \begin{bmatrix} \dot{\zeta}_y \\ \dot{g} \\ \dot{\Lambda} \\ \dot{\Gamma} \end{bmatrix} = \begin{bmatrix} \Psi \\ l(\Xi,\Psi) \\ \Pi(\Xi,\Psi) \\ 0 \end{bmatrix} \tag{6.78}$$

and by the infinite dimensional output map

$$\phi(x,y) = \eta[\Xi,\Psi](x,y) = \Re\Big\{W(z)\Big\}, \tag{6.79}$$

where

$$\Pi(\Xi,\Psi) = [p_1(\Xi,\Psi)\ p_2(\Xi,\Psi)\ ...]^T \tag{6.80}$$

$$l(\Xi,\Psi) = \begin{bmatrix} 1 & 0 & 0 \\ 0 & \cos(\theta_f) & -\sin(\theta_f) \\ 0 & \sin(\theta_f) & \cos(\theta_f) \end{bmatrix} \mathbf{U}(\Xi,\Psi), \tag{6.81}$$

and where $\mathbf{U}(\Xi,\Psi)$ is defined in (6.73), $p_k(\Xi,\Psi)$ is defined in (6.74), and $W(z)$ is defined in (6.60). The initial condition for Λ is arbitrary, while the initial condition for Γ is zero. In this way, until a vortex is initialized, it has no effect on the system. To initialize, each ζ_k in Λ and γ_k in Γ are reset at time $k\Delta t$ where Δt is the time between each shed vortex. Thus the reset is defined as

$$\zeta_k(k\Delta t) = 1.5\Big(\alpha(k\Delta t) - \zeta_c(k\Delta t)\Big) \tag{6.82}$$

$$\gamma_k(k\Delta t) = \nu_k \tag{6.83}$$

where ν_k is the γ_n part of the solution to (6.76), (6.77) at time $k\Delta t$ where $\zeta_n = \zeta_k$ and $\Delta\mathbf{U}$ is added to (6.73) for use in (6.81).

6.6.2 Basic Gaits of the Joukowski Foil Fish

As shown in [84], the Joukowski foil fish, with the help of the shed vortices, will move forward and turn with the same input

$$\dot{\zeta}_y = a\omega\cos(\omega t)\,, \tag{6.84}$$

where the other shape parameters follow from the choice of ζ_y as seen in (6.67), (6.68). The difference between the two gaits lies in the initial condition of ζ_y; The fish will move straight forward with the initial condition $\zeta_y|_{t=0} = 0$ while the fish will move around circles with the initial condition $\zeta_y|_{t=0} = \beta$ with $\beta \neq 0$ leading to

$$\zeta_y(t) = a\sin(\omega t) + \beta\,. \tag{6.85}$$

Figures 6.14 and 6.13 show the fish moving forward and in a circle for various choices of parameters. Figure 6.14 clearly shows the effect of the non-decaying vortices — the fish tail still moves with the same frequency, yet the period of resulting fish locomotion increases. Figure 6.15 shows snapshots in time of the fish moving forward and the vortices that form.

6.6.3 Source Seeking for a Joukowski Foil Fish

The derivation of the control law for the foil fish is very similar to the derivation found in Section 6.5.4. We notice that the forward gait and turning gait both have a sinusoidal term - similar to the persistent excitation term in the unicycle control law (6.1). We make β from (6.85) time dependent and arrive at

$$\dot{\zeta}_y = a\omega\cos(\omega t) + c\xi\sin(\omega t) \tag{6.86}$$

$$\xi = H(s)[J] \tag{6.87}$$

$$H(s) = \left(\frac{s}{s+h}\right)^2 \tag{6.88}$$

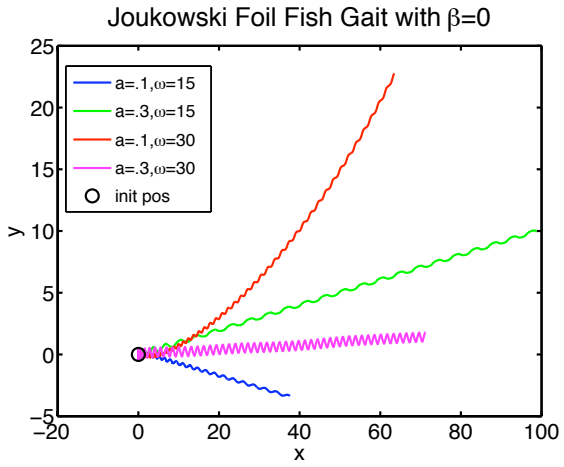

Figure 6.13: Forward gait for Joukowski foil fish. $\beta = 0$.

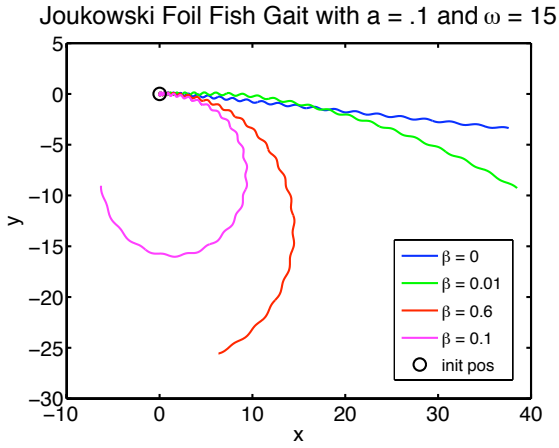

Figure 6.14: Turning gait for Joukowski foil fish. $a = .1$, $\omega = 15$.

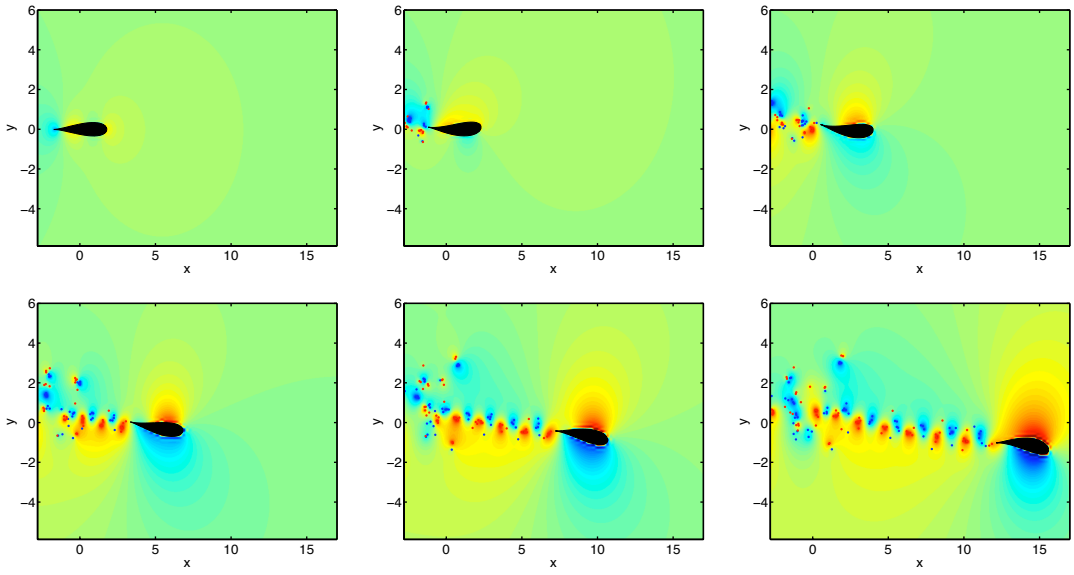

Figure 6.15: Snapshots in time of a Joukowski foil fish moving forward. The background color field represents the stream function ψ with red representing positive values and blue negative. Vortices are also shown as xs moving counter clockwise and os clockwise. $a = .1$, $\beta = 0$.

where our compensator $H(s)$ is a double washout filter. The function J we wish to maximize is

$$J = -q_r\Big(\big(x^* - f_{sx}\big)^2 + \big(y^* - f_{sy}\big)^2\Big) \tag{6.89}$$

$$f_s = \left(\mu + \frac{a^2}{\mu}\right)\mathrm{e}^{j\theta_f} + f_x + if_y \tag{6.90}$$

where $f_s = (f_{sx}, f_{sy})$ is the location of the fish sensor, a forward point of the fish — its "nose". As before (x^*, y^*) is the goal location. Figures 6.16 and 6.17 depict the fish going toward a target under the influence of (6.86) and different parameter choices.

While we constrain only the value of β in the control law for the three link fish, we constrain both the value of β and its time derivative $\dot{\beta}$ in the control law of the Joukowski foil fish. We do this both for physical realism and for computational convergence.

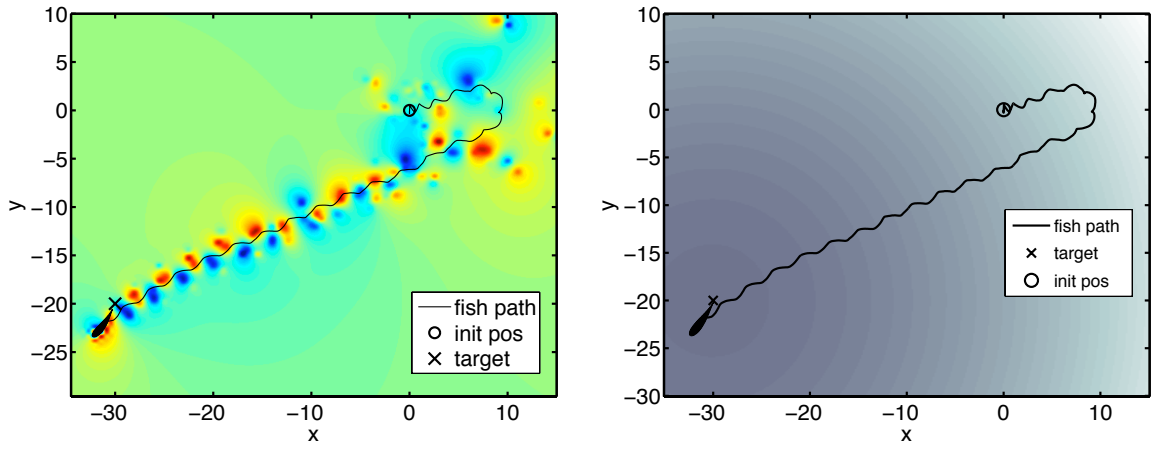

(a) (b)

Figure 6.16: Source seeking for a Joukowski foil fish.
(a) The background color field represents the stream function ψ with red representing positive values and blue negative. (b) The background color field represents the "concentration" of the signal field J with the darker shade representing higher values than the lighter shade. $a = 0.3$, $c = 0.3$, $\omega = 20$, $h = 10$, $q_r = 10.2$, $r_c = 1$, $\mu = 0.74$.

6.6.4 Path Following for a Joukowski foil fish.

We modify the function J in the same way we did in Section 6.5.5 so that the Joukowski foil fish follows a predetermined path. Figure 6.18 shows the path the fish takes when following the path defined by

$$J = 300/\sqrt{1 + \left| f_x - (3/1000 f_y^3 - 4/15 f_y^2 + 16/3 f_y + 1) \right|} \tag{6.91}$$

6.7 Conclusions

We have shown that the extremum seeking method, which performs real-time optimization using periodic perturbations, can perform navigation of underwater vehicles which move through sinusoid-dominated body movement instead of through the use of traditional motors. The control law was demonstrated on two different

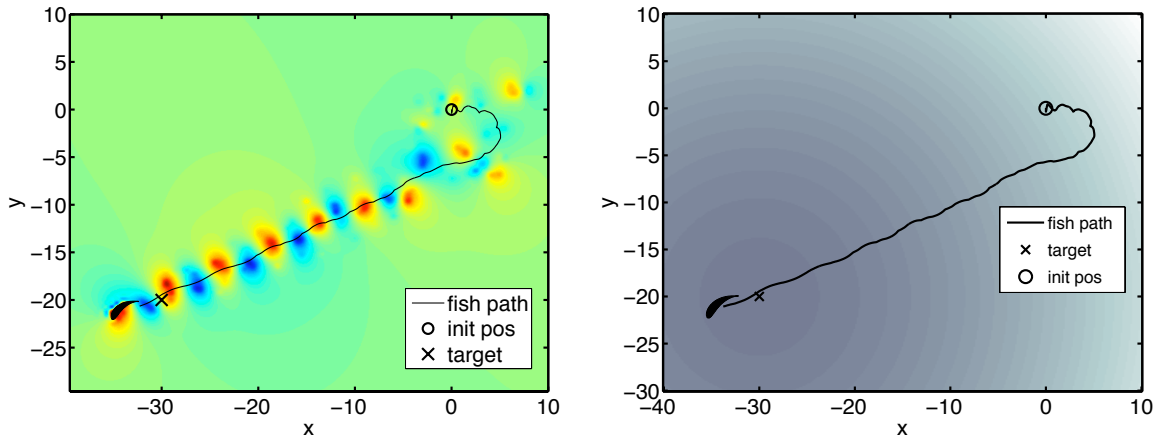

(a) (b)

Figure 6.17: Source seeking for a Joukowski foil fish.
(a) The background color field represents the stream function ψ with red representing positive values and blue negative. (b) The background color field represents the "concentration" of the signal field J with the darker shade representing higher values than the lighter shade. $a = 0.3$, $c = 0.3$, $\omega = 10$, $h = 10$, $q_r = 10.2$, $r_c = 1$, $\mu = 0.74$.

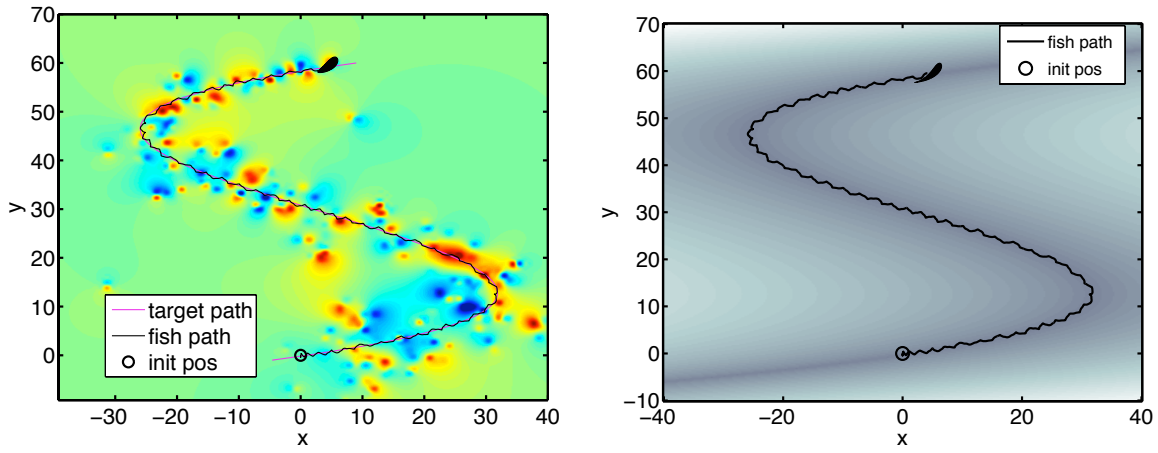

(a) (b)

Figure 6.18: Joukowski foil fish following a predetermined path.
(a) The background color field represents the stream function ψ with red representing positive values and blue negative. (b) The background color field represents the "concentration" of the signal field J with the darker shade representing higher values than the lighter shade. $a = 0.3$, $c = 10$, $\omega = 20$, $h = 20$, $r_c = 1$, $\mu = 0.74$.

computational fish models, a three link model developed by [38] and a fish modeled as an airfoil developed by [84]. The algorithm allows the fish to find the source of a signal, move to a target waypoint and follow a prespecified path. These tools can also be used to guide the vehicle through an obstacle field. This work also serves as validation that methods from control theory can be applied to the models developed in [38] and [84] for navigation control for underwater vehicles.

A reader might like to see a detailed theoretical analysis such as those that we have completed source seeking with nonholonomic vehicles in two dimensions [18] and three dimensions [19]. Such detailed results are beyond reach for the highly complex (and high dimensional) models in this chapter, however, the theoretical intuition from [18, 19] has guided the choices of the control laws (6.52)–(6.54) and (6.86)–(6.88).

In so much as the two models considered are realistic models of body-fluid interaction taking place in locomotion of actual fish, the simple control laws (6.52)–(6.54) and (6.86)–(6.88) seem as plausible feedback strategies that actual fish may be using to navigate gradient fields.

6.8 Acknowledgments

The authors gratefully acknowledge discussions with and initial code from Eva Kanso, Scott Kelly and Hailong Xiong. We would like to sincerely thank them.

This chapter is a reprint of the material as it is being prepared for:
J. Cochran, E. Kanso, S. D. Kelly, H. Xiong, and M. Krstic, "Source Seeking for Two Nonholonomic Models of Fish Locomotion," *IEEE Transactions on Robotics*, under review.

The dissertation author was the primary investigator and author of this paper.

Appendix A

Full Expressions for w_i and w_{si}.

$$w_1(\zeta) = -\frac{r_c^2}{\zeta} + \zeta_c + \frac{\alpha^2}{(\zeta+\zeta_c)} \tag{A.1}$$

$$w_2(\zeta) = -i\left[\frac{r_c^2}{\zeta} + \zeta_c + \frac{\alpha^2}{(\zeta+\zeta_c)}\right] \tag{A.2}$$

$$w_3(\zeta) = \frac{-i}{2}\left[r_c^2 + 2\frac{\zeta_c r_c^2}{\zeta} + \delta^2 + 2\alpha^2\frac{r_c^2/\zeta + \overline{\zeta_c}}{(\zeta+\zeta_c)} + \frac{\alpha^4(\zeta-\zeta_c)}{(\zeta+\zeta_c)(r_c^2-\delta^2)}\right] \tag{A.3}$$

$$\begin{aligned} w_{s1}(\zeta) = \Bigg[& -\frac{r_c^2}{\zeta} + \frac{\alpha^2 r_c^2}{\zeta\zeta_c^2} + \frac{\alpha^2}{(\zeta+\zeta_c)} - \frac{\alpha^4\zeta_c^2}{(\zeta+\zeta_c)(r_c^2-\delta^2)^2} \\ & -\frac{2\alpha^4 r_c^2\zeta_c}{(r_c^2-\delta^2)^3}\log\left(\frac{\zeta+\zeta_c}{r_c}\right) - \left(\frac{\alpha^2 r_c^2}{\zeta_c^3} - \frac{\alpha^2 r_c^2}{\zeta_c(r_c^2-\delta^2)^2}\right)\frac{\zeta}{(\zeta+\zeta_c)} \\ & -2\alpha^2 r_c^2\left(\frac{1}{\zeta_c^3} + \frac{\overline{\zeta_c}\alpha^2}{(r_c^2-\delta^2)^3}\right)\log\left(\frac{\zeta+\zeta_c}{\zeta}\right) + \frac{2\alpha^4 r_c^2(i\zeta_y)}{(r_c^2-\delta^2)^3}\log\left(\frac{\zeta}{r_c}\right)\Bigg] \end{aligned} \tag{A.4}$$

$$\begin{aligned} w_{s2}(\zeta) = (-i)\Bigg[& \frac{r_c^2}{\zeta} - \frac{\alpha^2 r_c^2}{\zeta\zeta_c^2} + \frac{\alpha^2}{(\zeta+\zeta_c)} - \frac{\alpha^4\zeta_c^2}{(\zeta+\zeta_c)(r_c^2-\delta^2)^2} \\ & -\frac{2\alpha^4 r_c^2\zeta_c}{(r_c^2-\delta^2)^3}\log\left(\frac{\zeta+\zeta_c}{r_c}\right) + \left(\frac{\alpha^2 r_c^2}{\zeta_c^3} - \frac{\alpha^2 r_c^2}{\zeta_c(r_c^2-\delta^2)^2}\right)\frac{\zeta}{(\zeta+\zeta_c)} \\ & +2\alpha^2 r_c^2\left(\frac{1}{\zeta_c^3} + \frac{\overline{\zeta_c}\alpha^2}{(r_c^2-\delta^2)^3}\right)\log\left(\frac{\zeta+\zeta_c}{\zeta}\right) + \frac{2\alpha^4 r_c^2\zeta_x}{(r_c^2-\delta^2)^3}\log\left(\frac{\zeta}{r_c}\right)\Bigg] \end{aligned} \tag{A.5}$$

$$w_{s3}(\zeta) = 2\alpha\Bigg[-\frac{r_c^2}{\zeta\zeta_c} - \frac{\alpha^2\zeta_c}{(\zeta+\zeta_c)(r_c^2-\delta^2)} - \frac{\alpha^2 r_c^2}{(r_c^2-\delta^2)^2}\log\left(\frac{\zeta+\zeta_c}{r_c}\right)$$

$$+\frac{r_c^2\Big((r_c^2-\delta^2)^2-\alpha^2\zeta_c^2\Big)}{\zeta_c^2(r_c^2-\delta^2)^2}\log\left(\frac{\zeta+\zeta_c}{\zeta}\right)\Bigg] \tag{A.6}$$

where $\delta = |\zeta_c|$.

Bibliography

[1] O.-M. Aamo and M. Krstic, *Flow Control by Feedback: Stabilization and Mixing*. Springer, 2002.

[2] ——, "Feedback control of particle dispersion in bluff body wakes," *International Journal of Control*, vol. 77, pp. 1001–1018, 2004.

[3] M. J. Ablowitz, M. D. Kruskal, and J. F. Ladik, "Solitary wave collisions," *SIAM J. Applicat. Math.*, vol. 36, pp. 428–437, June 1979.

[4] M. Abramowitz and I. A. Stegun, *Handbook of Mathematical Functions with Formulas, Graphs, and Mathematical Tables*. New York: Dover, 1964.

[5] K. Ariyur and M. Krstic, *Real-Time Optimization by Extremum-Seeking Control*. Hoboken, NJ: Wiley-Interscience, 2003.

[6] J. Baker and P. D. Christofides, "Drag reduction in transitional linearized channel flow using distributed control," *International Journal of Control*, vol. 75, no. 15, pp. 1213–1218, 2002.

[7] A. Balogh, W.-J. Liu, and M. Krstic, "Stability enhancement by boundary control in 2D channel flow," *IEEE Trans. Automatic Control*, vol. 46, pp. 1696–1711, 2001.

[8] B. Bamieh and M. Dahleh, "Energy amplification in channel flows using stochastic exictation," *Physics of Fluids*, vol. 13, no. 11, Nov. 2001.

[9] L. Baramov, O. R. Tutty, and E. Rogers, "Robust control of linearized Poiseuille flow," *Journal of Guidance, Control, and Dynamics*, vol. 25, no. 1, January-February 2002.

[10] ——, "H_∞ control of nonperiodic two-dimensional channel flow," *IEEE Transactions on Control Systems Technology*, vol. 12, no. 1, January 2004.

[11] V. Barbu, "Feedback stabilization of Navier-Stokes equations," *ESAIM: Control, Optim. Cal. Var.*, vol. 9, pp. 197–205, 2003.

[12] D. Baronov and J. Baillieul, "Reactive exploration through following isolines in a potential field," *2007 American Ctrl. Conf.*, 2007.

[13] P. W. Bearman, "Vortex shedding from oscillating bluff bodies," *Annu. Rev. Fluid Mech.*, vol. 16, pp. 195–222, 1984.

[14] R. Becker, R. King, R. Petz, and W. Nitsche, "Adaptive closed-loop separation control on a high-lift configuration using extremum seeking," *3rd AIAA Flow Control Conference*, 2006.

[15] T. R. Bewley, "Flow control: new challenges for a new renaissance," *Progress in Aerospace Sciences*, vol. 37, pp. 21–58, 2001.

[16] T. R. Bewley and S. Liu, "Optimal and robust control and estimation of linear paths to transition," *J. Fluid Mech.*, vol. 365, pp. 305–349, 1998.

[17] C. Centioli, F. Iannone, G. Mazza, M. Panella, L. Pangione, S. Podda, A. Tuccillo, V. Vitale, and L. Zaccarian, "Extremum seeking applied to the plasma control system of the Frascati Tokamak Upgrade," *44th IEEE Conf. on Decision and Ctrl., and the European Ctrl. Conf.*, 2005.

[18] J. Cochran and M. Krstic, "Nonholonomic source seeking with tuning of angular velocity," *IEEE Trans. Automatic Control*, under review.

[19] J. Cochran, A. Siranosian, N. Ghods, and M. Krstic, "3D source seeking for underactuated vehicles without position measurement," *IEEE Trans. Robotics*, under review.

[20] J. Cochran and M. Krstic, "Source seeking with a nonholonomic unicycle without position measurements and with tuning of angular velocity — part I: Stability analysis," *2007 Conf. on Decision and Control*, 2007.

[21] ——, "3D nonholonomic source seeking without position measurement," *2008 Amer. Ctrl. Conf.*, 2008.

[22] ——, "Nonholonomic source seeking with tuning of angular velocity," *IEEE Trans. Automat. Contr.*, accepted with minor revision.

[23] J. Cochran, A. Siranosian, N. Ghods, and M. Krstic, "Source seeking with a nonholonomic unicycle without position measurements and with tuning of angular velocity — part II: Applications," *2007 Conf. on Decision and Control*, 2007.

[24] ——, "GPS denied source seeking for underactuated autonomous vehicles in 3D," *2008 Intl. Conf. Robotics and Automation*, 2008.

[25] J. D. Eldridge, "Numerical simulation of the fluid dynamics of 2D rigid body motion with the vortex particle method," *Journal of Computational Physics*, vol. 221, pp. 626–648, 2007.

[26] A. Glezer and M. Allen, "U.S. patent 5758823: Micromachined synthetic jet actuators and applications thereof," 2002.

[27] J. Gray, "Studies in animal locomotion: VI. the propulsive powers of the dolphin," *Journal of Experimental Biology*, vol. 13, pp. 192–199, 1936.

[28] M. Guay, M. Perrier, and D. Dochain, "Adaptive extremum seeking control of nonisothermal continuous stirred reactors," *Chem. Eng. Science*, vol. 60, pp. 3671–3681, 2005.

[29] M. D. Gunzburger and H. C. Lee, "Feedback control of karman vortex shedding," *Journal of Applied Mechanics*, vol. 63, no. 3, pp. 828–835, Sept. 1991.

[30] M. Hogberg, T. R. Bewley, and D. S. Henningson, "Linear feedback control and estimation of transition in plane channel flow," *Journal of Fluid Mechanics*, vol. 481, pp. 149–175, 2003.

[31] M. Ilak and C. W. Rowley, "Modeling of transitional channel flow using balanced proper orthogonal decomposition," *Physics of Fluids*, July 2007, submitted.

[32] H. Ishida, K. Suetsugu, T. Nakamoto, and T. Moriizumi, "Plume-tracking robots: A new application of chemical sensors," *The Biological Bulletin*, vol. 200, pp. 222–226, April 2001.

[33] A. Isidori, *Nonlinear Control Systems*. Springer-Verlag, 1995.

[34] S. S. Joshi, J. L. Speyer, and J. Kim, "A systems theory approach to the feedback stabilization of infinitesimal and finite-amplitude disturbances in plane Poiseuille flow," *J. Fluid Mech.*, vol. 332, pp. 157–184, 1997.

[35] M. Jovanovic and B. Bamieh, "Componentwise energy amplification in channel flows," *Journal of Fluid Mechanics*, vol. 534, pp. 145–183, Jun. 2005.

[36] E. Justh and P. Krishnaprasad, "Equilibria and steering laws for planar formations," *Systems and Control Letters*, vol. 52, pp. 25–38, 2004.

[37] S. Kalantar and U. Zimmer, "Control of open contour formations of autonomous underwater vehicles," *International Journal of Advanced Robotic Systems*, vol. 2, no. 4, pp. 309–316, Dec. 2005.

[38] E. Kanso, J. E. Marsden, C. W. Rowley, and J. B. Melli-Huber, "Locomotion of articulated bodies in a perfect fluid," *Journal of Nonlinear Science*, vol. 15, pp. 255–289, 2005.

[39] S. D. Kelly and R. B. Hukkeri, "Mechanics, dynamics, and control of a single-input aquatic vehicle with variable coefficient of lift," *IEEE Trans. Robotics*, vol. 22, no. 6, pp. 1254–1264, 2006.

[40] H. Khalil, *Nonlinear Systems*, 3rd ed. Upper Saddle Rive, NJ: Prentice Hall, 2002.

[41] R. King, R. Becker, G. Feuerbach, L. Henning, R. Petz, W. Nitsche, O. Lemke, and W. Neise, "Adaptive flow control using slope seeking," *14th IEEE Mediterranean Conf. on Ctrl. Automation*, 2006.

[42] D. J. Klein, C. Matlack, and K. A. Morgansen, "Cooperative target tracking using oscillator models in three dimensions," *200t American Ctrl. Conf.*, 2006.

[43] D. Klein and K. Morgansen, "Controlled collective motion for trajectory tracking," *2006 American Ctrl. Conf.*, 2006.

[44] M. Krstic, J. Cochran, and R. Vazquez, "Backstepping controllers for stabilization of turbulent flow pdes," in *Modeling and Control of Complex Systems*, P. Ioannou and I. Pitsilides, Eds. CRC Press, 2008.

[45] M. Krstic, I. Kanellakopoulos, and P. Kokotovic, *Nonlinear and Adaptive Control Design*. John Wiley and Sons, 1995.

[46] B. Laroche and P. Martin, "Motion planning for a 1-D diffusion equation using a Brunovsky-like decomposition," *14th Intl. Symp. of Mathematical Theory of Networks and Systems*, 2000.

[47] B. Laroche, P. Martin, and P. Rouchon, "Motion planning for the heat equation," *Intl Journal of Robust and Nonlinear Control*, vol. 10, pp. 629–644, 2000.

[48] Y. Li, A. Rotea, G. T.-C. Chiu, L. Mongeau, and I.-S. Paek, "Extremum seeking control of a tunable thermoacoustic cooler," *IEEE Trans. Contr. Syst. Technol.*, vol. 13, pp. 527–536, 2005.

[49] S. J. Lighthill, *Mathematical Biofluiddynamics*. SIAM, 1975.

[50] P. F. Linden and J. S. Turner, "'optimal' vortex rings and aquatic propulsion mechanisms," *Proc. Royal Soc. Lond. B.*, vol. 241, pp. 647–653, 2004.

[51] J. Marshall, M. Broucke, and B. Francis, "Pursuit formations of unicycles," *Automatica*, vol. 42, pp. 3–12, 2006.

[52] R. J. Mason, *Fluid Locomotion and Trajcetory Planning for Shape-Changing Robots*. PhD thesis, California Institute of Technology, 2002.

[53] E. Mbemmo, Z. Chen, S. Shatara, and X. Tan, "Modeling of biomimetic robotic fish propelled by an ionic polymer-metal composite actuator," *IEEE International Conf. on Robotics and Automation*, 2008.

[54] T. Meurer and M. Zeitz, "Feedforward and feedback tracking control of nonlinear diffusion – convection – reaction systems using summability methods," *Industrial and engineering chemistry research*, vol. 44, no. 8, pp. 2532–2548, 2005.

[55] L. M. Milne-Thomson, *Theoretical Hydrodynamics*. Dover, 1996.

[56] K. Morgansen, V. Duindam, R. Mason, J. Burdick, and R. Murray, "Nonlinear control methods for planar carangiform robot fish locomotion," *Proc. of the IEEE Inter. Conf. on Robotics and Automation*, 2001.

[57] P. K. Newton, *The N-vortex problem*. Springer-Verlag, 2001.

[58] P. Ogren, E. Fiorelli, and N. Leonard, "Cooperative control of mobile sensor networks: adaptive gradient climbing in a distributed environment," *IEEE Trans. Automat. Contr.*, vol. 29, pp. 1292–1302, 2004.

[59] F. Ollivier and A. Sedoglavic, "A generalization of flatness to nonlinear systems of partial differential equations. Application to the command of a flexible rod." *5th IFAC Symp on Nonlinear Control Systems*, 2001.

[60] Y. Ou, C. Xu, E. Schuster, T. Luce, J. R. Ferron, and M. Walker, "Extremum-seeking finite-time optimal control of plasma current profile at the DIII-D Tokamak," *2007 American Ctrl. Conf.*, 2007.

[61] K. Peterson and A. Stefanopoulou, "Extremum seeking control for soft landing of and electromechanical valve actuator," *Automatica*, vol. 29, pp. 1063–1069, 2004.

[62] B. Porat and A. Neohorai, "Localizing vapor-emitting sources by moving sensors," *IEEE Trans. Signal Processing*, vol. 44, pp. 1018–1021, 1996.

[63] B. Protas, "Center manifold analysis of a point-vortex model of vortex shedding with control," *Physica D*, vol. 228, pp. 179–187, 2007.

[64] B. Protas and A. Styczek, "Optimal rotary control of the cylinder wake in the laminar regime," *Physics of Fluids*, vol. 14, pp. 2073–2087, 2002.

[65] E. M. Purcell, "Life at low Reynolds number," *Am. J. Phys.*, vol. 45, no. 1, January 1977.

[66] J.-P. Raymond, "Feedback boundary stabilization of the two dimensional Navier-Stokes equations," *SIAM Journal on Control and Optimization*, vol. 45, pp. 790–828, 2006.

[67] P. Reddy, E. Justh, and P. Krishnaprasad, "Motion camouflage in three dimensions," *45th IEEE Conf. Decision and Ctrl.*, 2006.

[68] P. Rouchon, "Motion planning, equivalence, infinite dimensional systems," *Intl Journal of Applied Mathematics and Computer Science*, vol. 11, no. 1, 2001.

[69] P. J. Schmid and D. S. Henningson, *Stability and Transition in Shear Flows*. Springer, 2001.

[70] B. N. Shashikanth, J. E. Marsdend, J. W. Burdick, and S. D. Kelly, "The Hamiltonian structure of a 2-D rigid circular cylinder interacting dynamically with N point vortices," *Physics of Fluids*, vol. 14, pp. 1214–1227, 2002.

[71] A. M. O. Smith and J. L. Hess, "Calculation of potential flow about arbitrary bodies," *Prog. Aeronaut. Sci.*, vol. 8, pp. 1–139, 1966.

[72] A. Smyshlyaev and M. Krstic, "Closed-form boundary state feedback for a class of 1-D partial integro-differential equations," *IEEE Trans. Automatic Control*, vol. 49, pp. 2185–2202, Dec. 2004.

[73] Y. Tan, D. Nesic, and I. M. Y. Mareels, "On non-local stability properties of extremum seeking controllers," *Automatica*, vol. 42, pp. 889–903, 2006.

[74] M. Tanelli, A. Astolfi, and S. Savaresi, "Non-local extremum seeking control for active braking control systems," *Conference on Control Applications*, 2006.

[75] G. Taylor, "Analysis of the swimming of long and narrow animals," *Proc. Royal Soc. Lond. A.*, vol. 214, no. 1117, pp. 158–183, August 1952.

[76] M. S. Triantafyllou and G. S. Triantafyllou, "An efficient swimming machine," *Scientific American*, vol. 272, pp. 64–70, March 1995.

[77] M. S. Triantafyllou, G. S. Triantafyllou, and D. K. P. Yue, "Hydrodynamics of fishlike swimming," *Annu. Rev. Fluid Mech.*, vol. 32, pp. 33–53, 2000.

[78] E. D. Tytell and G. V. Lauder, "The hydrodynamics of eel swimming I. wake structure," *Journal of Experimental Biology*, vol. 207, pp. 1825–1841, 2004.

[79] R. Vazquez, J. M. Coron, and E. Trelat, "Stable Poiseuille flow transfer for a Navier-Stokes system," *25th American Ctrl. Conf*, 2006.

[80] R. Vazquez and M. Krstic, "A closed-form feedback controller for stabilization of the linearized 2D Navier-Stokes Poisseuille flow," *IEEE Transactions on Automatic Control*, vol. 52(12), pp. 2298–2312, 2007.

[81] ——, *Control of Turbulent and Magnetohydrodynamic Channel Flows*. Birkhauser, 2007.

[82] R. Vazquez, E. Schuster, and M. Krstic, "A closed-form observer for the 3D inductionless MHD and Navier-Stokes channel flow," *45th IEEE Conf. on Decision and Ctrl,*, pp. 739–746, Dec. 2006.

[83] S. M. Veres, L. Baramov, O. R. Tutty, and E. Rogers, "Iterative design for active control of fluid flow," *International Journal of Control*, vol. 76, no. 14, pp. 1375–1386, 2003.

[84] H. Xiong and S. D. Kelly, "Self-propulsion of a deformable Joukowski foil in a perfect fluid with vortex shedding," *Journal of Nonlinear Science*, under review.

[85] C. C. Yuan, M. Krstic, and T. Bewley, "Active control of jet mixing," *IEE Proceedings: Control Theory and Applications*, vol. 151, pp. 763–772, 2004.

[86] C. Zhang, D. Arnold, N. Ghods, A. Siranosian, and M. Krstic, "Source seeking with nonholonomic unicycle without position measurement and with tuning of forward velocity," *Systems and Control Letters*, vol. 56, pp. 245–252, 2007.

[87] C. Zhang, A. Siranosian, and M. Krstic, "Extremum seeking for moderately unstable systems and for autonomous vehicle target tracking without position measurements," *Automatica*, vol. 43, pp. 1832–1839, 2007.

[88] X. Zhang, D. Dawson, W. Dixon, and B. Xian, "Extremum seeking nonlinear controllers for a human exercise machine," *Proc. 2004 IEEE Conf. Decision and Ctrl.*, 2004.